UC Irvine
UC Irvine Electronic Theses and Dissertations

Title

Understanding the Transformation Leading to Transition Metal-Nitrogen-Carbon (M-N-C) Catalysts during Pyrolysis

Permalink

https://escholarship.org/uc/item/04h9t4g5

Author

Huang, Ying

Publication Date

2023

Copyright Information

Peer reviewed|Thesis/dissertation

UNIVERSITY OF CALIFORNIA,
IRVINE

Understanding the Transformation Leading to Transition Metal-Nitrogen-Carbon (M-N-C)
Catalysts during Pyrolysis

DISSERTATION

submitted in partial satisfaction of the requirements
for the degree of

DOCTOR OF PHILOSOPHY

in Materials Science and Engineering

by

Ying Huang

Dissertation Committee:
Associate Professor Iryna V. Zenyuk, Chair
Professor Plamen Atanassov
Professor Lorenzo Valdevit

2023

DEDICATION

To myself

Man is his own star; and the soul that can
Render an honest and a perfect man,
Commands all light, all influence, all fate;
Nothing to him falls early or too late.
Our acts our angels are, or good or ill,
Our fatal shadows that walk by us still.

(*Epilogue to Beaumont and Fletcher's Honest Man's Fortune*)

To this journey

From hill to hill no bird in flight;
From path to path no man in sight.
A lonely fisherman afloat,
Is fishing snow in lonely boat.

Liu Zongyuan
Translated by Xu Yuanchong

TABLE OF CONTENTS

iii

LIST OF FIGURES

LIST OF TABLES

ACKNOWLEDGEMENTS

I participated a lot of workshops organized by national labs during my PhD. All those workshops benefit me a lot. Thanks for those who put efforts on making those happen, especially the ones held during the pandemic.

I would like to thank my families and friends for the support. I would like to say sorry to my parents, who want me to be around but still support me to do what I wanted to do.

I would like to thank all my colleagues for the support. It is a nice experience to work with you.

I received so many helps in my PhD journey, and I really appreciate all the kindness of everyone. Thank you!

VITA

Ying Huang

2016	B.Eng. in Materials Science and Engineering, South China University of Technology
2017	Master in Materials Science and Engineering, Rice University
2023	Ph.D. in Materials Science and Engineering, University of California, Irvine

FIELD OF STUDY

Materials Science and Engineering

PUBLICATIONS

1. **Huang, Y.**, Chen, Y., Xu, M., Asset, T., Tieu, P., Gili, A., Kulkarni, D., De Andrade, V., De Carlo, F., Barnard, H. S., Doran, A., Parkinson, D. Y., Pan, X., Atanassov, P., & Zenyuk, I. V. (2021, July). Catalysts by pyrolysis: Direct observation of chemical and morphological transformations leading to transition metal-nitrogen-carbon materials. *Materials Today*, 47, 53–68. https://doi.org/10.1016/j.mattod.2021.02.006

2. Chen, Y., **Huang, Y.**, Xu, M., Asset, T., Yan, X., Artyushkova, K., Kodali, M., Murphy, E., Ly, A., Pan, X., Zenyuk, I. V., & Atanassov, P. (2022, March). Catalysts by pyrolysis: Direct observation of transformations during re-pyrolysis of transition metal-nitrogen-carbon

materials leading to state-of-the-art platinum group metal-free electrocatalyst. *Materials Today*, 53, 58–70. https://doi.org/10.1016/j.mattod.2022.01.016

3. Avid, A., Ochoa, J. L., **Huang, Y.**, Liu, Y., Atanassov, P., & Zenyuk, I. V. (2022). Revealing the role of ionic liquids in promoting fuel cell catalysts reactivity and durability. *Nature Communications*, 13(1). https://doi.org/10.1038/s41467-022-33895-5

4. Qi, Y., **Huang, Y.**, Gao, Z., Chen, C. H., Perego, A., Yildirim, H., Odgaard, M., Asset, T., Atanassov, P., & Zenyuk, I. V. (2022, December). Insight into carbon corrosion of different carbon supports for Pt-based electrocatalysts using accelerated stress tests in polymer electrolyte fuel cells. *Journal of Power Sources*, 551, 232209. https://doi.org/10.1016/j.jpowsour.2022.232209

5. Murphy, E., Liu, Y., Matanovic, I., Guo, S., Tieu, P., **Huang, Y.**, Ly, A., Das, S., Zenyuk, I., Pan, X., Spoerke, E., & Atanassov, P. (2022, May 20). Highly Durable and Selective Fe- and Mo-Based Atomically Dispersed Electrocatalysts for Nitrate Reduction to Ammonia via Distinct and Synergized NO2– Pathways. *ACS Catalysis*, 12(11), 6651–6662. https://doi.org/10.1021/acscatal.2c01367

6. Delafontaine, L., Murphy, E., Guo, S., Liu, Y., Asset, T., **Huang, Y.**, Chen, J., Zenyuk, I. V., Pan, X., & Atanassov, P. (2022, September 9). Synergistic Electrocatalytic Syngas Production from Carbon Dioxide by Bi-Metallic Atomically Dispersed Catalysts. *ChemElectroChem*, 9(17). https://doi.org/10.1002/celc.202200647

7. Qi, Y., Liu, J., Sabarirajan, D. C., **Huang, Y.**, Perego, A., Haug, A. T., & Zenyuk, I. V. (2021, April 30). Interpreting Ionic Conductivity for Polymer Electrolyte Fuel Cell Catalyst Layers with Electrochemical Impedance Spectroscopy and Transmission Line Modeling.

Journal of the Electrochemical Society, 168(5), 054502. https://doi.org/10.1149/1945-7111/abf96d

8. Liu, C. P., Saha, P., **Huang, Y.**, Shimpalee, S., Satjaritanun, P., & Zenyuk, I. V. (2021, April 21). Measurement of Contact Angles at Carbon Fiber–Water–Air Triple-Phase Boundaries Inside Gas Diffusion Layers Using X-ray Computed Tomography. *ACS Applied Materials &Amp; Interfaces*, 13(17), 20002–20013. https://doi.org/10.1021/acsami.1c00849

9. Li, J., Sougrati, M. T., Zitolo, A., Ablett, J. M., Oğuz, I. C., Mineva, T., Matanovic, I., Atanassov, P., **Huang, Y.**, Zenyuk, I., Di Cicco, A., Kumar, K., Dubau, L., Maillard, F., Dražić, G., & Jaouen, F. (2020, December 7). Identification of durable and non-durable FeNx sites in Fe–N–C materials for proton exchange membrane fuel cells. *Nature Catalysis*, 4(1), 10–19. https://doi.org/10.1038/s41929-020-00545-2

10. Peng, X., Kulkarni, D., **Huang, Y.**, Omasta, T. J., Ng, B., Zheng, Y., Wang, L., LaManna, J. M., Hussey, D. S., Varcoe, J. R., Zenyuk, I. V., & Mustain, W. E. (2020, July 16). Using operando techniques to understand and design high performance and stable alkaline membrane fuel cells. *Nature Communications*, 11(1). https://doi.org/10.1038/s41467-020-17370-7

11. Pan, Z., **Huang, Y.**, Wang, Y., & Wu, Z. (2017, December). Disintegration of Nannochloropsis sp. cells in an improved turbine bead mill. *Bioresource Technology*, 245, 641–648. https://doi.org/10.1016/j.biortech.2017.08.146

12. Chen, W. F., Koshy, P., **Huang, Y.**, Adabifiroozjaei, E., Yao, Y., & Sorrell, C. C. (2016, November). Effects of precipitation, liquid formation, and intervalence charge transfer on the properties and photocatalytic performance of cobalt- or vanadium-doped TiO_2 thin films.

ABSTRACT OF THE DISSERTATION

Understanding the Transformation Leading to Transition Metal-Nitrogen-Carbon (M-N-C)

Catalysts during Pyrolysis

by

Ying Huang

Doctor of Philosophy in Materials Science and Engineering

University of California, Irvine, 2023

Associate Professor Iryna V. Zenyuk, Chair

With the demand for reducing greenhouse gas emissions and developing diverse energy sources, more and more efforts have been made in the advent of hydrogen fuel energy technologies. Transition metal-nitrogen-carbon materials (M-N-C catalysts) are promising electrocatalysts in the hydrogen fuel energy technologies like polymer electrolyte fuel cells (PEFCs) and electrolyzer applications. High-temperature treatment in the inert atmosphere (pyrolysis) is the most common method for the synthesis of M-N-C catalysts and is critical to achieving high electrocatalytic activity and electronic conductivity. To this day, despite many uses and successful implementations in materials manufacturing, pyrolysis has been an entirely empirical technology, with process control and optimization relying exclusively on the "Edisonian" approach. The knowledge gap in the mechanism about how the precursor is being transformed into catalysts hinders further development of the M-N-C catalysts regardless of the precursor

class and processing protocols. Herein, this dissertation focused on probing the morphological evolution and chemical transformation of the precursors to M-N-C catalysts via a combination of in situ and ex situ synchrotron and laboratory-based diagnostic techniques. The following processes have been observed and analyzed:

i) The pyrolysis process of a mixture of nitrogen-containing charge-transfer organic salt, transition metal (iron) salt, and amorphous silica powder (precursors) leading to M-N-C materials.

ii) The re-pyrolysis process of the above-mentioned M-N-C materials leading to state-of-the-art M-N-C catalysis.

iii) The pyrolysis process of two commercial highly porous metal-organic frameworks (MOFs) leading to the M-N-C catalysts.

It was found that the pyrolyzing temperature might bring an adverse effect on the final product, causing the active sites to decrease and the carbon to be highly graphitized. The carbon graphitization event catalyzed by the metallic particles forming occurs during the heat treatment. The direct observation and thorough fundamental study of the pyrolytic synthesis are expected to benefit in improving the rational design of the M-N-C catalysts.

Chapter 1

Introduction

1.1 Overview

CO_2 emission can cause the greenhouse effects. In 2021, more than 33 billion tons of CO_2 was produced due to the energy production [1]. This is because the current energy system primarily relies on the fossil fuels, which occupied 82.3% of the primary energy consumption in 2021 [1] . The needs to decrease the CO2 emission is consistent with the needs to diversify the energy sources.

The concept of Net-zero emission energy system was thus created[2]. Net-zero emission energy system would not add CO_2 into the atmosphere from the energy and industrial processes, which requires that the annual capture and geological storage of CO_2 should be at least equals to the annual CO_2 generation by energy and industrial processes[3]. More than 70% of the global CO2 from the fossil fuel and industry are from electricity, short-distance light road transportation, residential, commercial, etc. Those CO_2 emissions are straightforward to eliminate since the renewable energy or energy from on-demand nonrenewable sources can be applied. However, there are 27% of the CO2 are emitted from long-distance road transport (1%), aviation (2%), shipping (3%), iron and steel manufacturing, cement manufacturing and highly reliable electricity needs (load-following electricity, 12%) [2]. Those are considered to be difficult-to-eliminate emissions. The strategies to create the net-zero emission energy system is to conduct CO_2 management and use diversifying energy sources, including hydrogen, biofuel, synthetic hydrocarbon, ammonia, and electricity from renewable energy or on-demand nonrenewable energy.

H_2 is one of the most important strategies of the eliminate the CO2 emission from road transportation. It holds a high energy density (120 MJ/kg) and can be converted into electricity by its oxidation *via* fuel cell. Refill hydrogen can be finished in a hydrogen station, which is very similar to the current filling way. Hydrogen can be easily integrated in the current transportation system.

1.2 polymer electrolyte fuel cells (PEFCs)

With the demand for reducing greenhouse gas emission and developing diverse energy sources, more and more efforts have been made in advent of hydrogen fuel energy technologies (polymer electrolyte fuel cells (PEFCs), electrolyzers, electrochemical hydrogen pumps) as a base for potentially zero-carbon footprint economy. PEFCs are used to convert hydrogen to electricity (mechanism shown in **Figure 1-1** Schematic of PEFC and associated transport phenomena and reaction mechanisms on the anode and cathode.) for a variety of applications with a substantial milestone in introduction of commercial and passenger PEFC vehicles, as early as 2014[4]. One of the limiting components of PEFC technology is the oxygen reduction reaction (ORR), as it is sluggish. PEFC cathode catalysts are currently platinum group metal based (PGM), with high cost and limited geographic location of the source, become barriers to broader market introduction of PEFCs and adoption of hydrogen economy as practical alternative to fossil-fuels based economy[5,6].
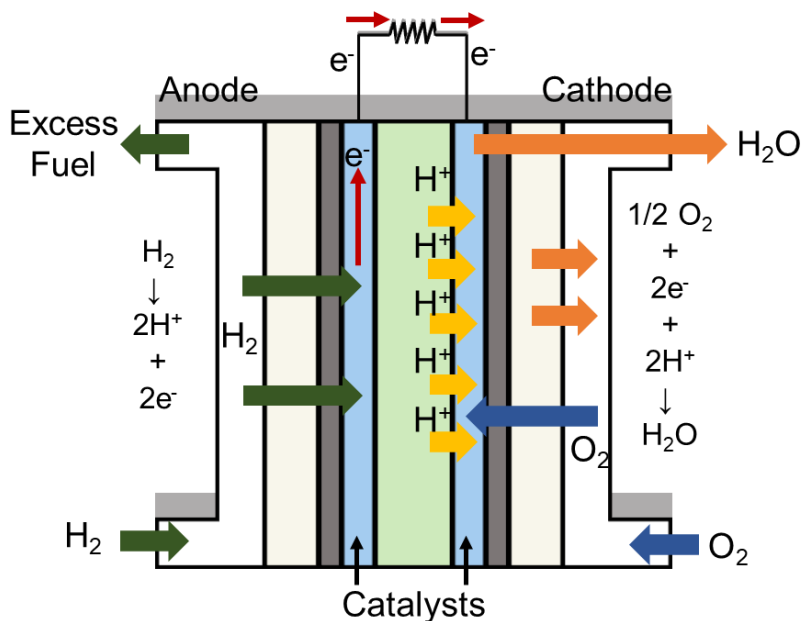
Figure 1-1 Schematic of PEFC and associated transport phenomena and reaction mechanisms on the anode and cathode.

1.3 Platinum Group Metal (PGM) -Free Catalysts

One approach to solve the high-cost issue is to use platinum-group-metal free (PGM-free) catalysts. Substantial efforts in materials, such as functionalizing carbon (with doped iron[7,8] and cobalt[9,10] or without doped metal[11]), carbide[12], nitride[13] and oxide[14] have been made to advance the PGM-free catalysts. The transition metal-nitrogen-carbon (M-N-C) catalysts are being considered as one of the most promising candidates due to their record setting (for their class) activity and notable selectivity to oxygen reduction reaction (ORR).

The most-usual methods to synthesize the M-N-C catalysts are hard-template method, soft-template method, and polymer-derived method[15]. Hard-template method, as the name suggests, is mixing hard-template and the metal, nitrogen, carbon sources together as precursors [16,17]. The hard template used in the precursors is silica. The precursors then are pyrolyzed to form the M-N-C materials. The silica would be removed by KOH or HF after the pyrolysis. The reason of

introducing the hard template is to introduce mesopores into the catalysts, which helps improve the accessibility of the O_2 to active sites.

The soft-template method is using metal-organic frameworks (MOFs) as template. This is a kind of porous materials and is considered as a good nitrogen and carbon sources into precursors to M-N-C catalysts. The metal might be mixed with or doped onto the MOFs[18,19]. The precursors would then be pyrolyzed to form the final products.

The polymer-derived method uses nitrogen-doped polymers together with metal salts. Polyaniline was the one usually used as nitrogen and carbon sources to synthesize M-N-C catalysts [8,20]. They might be used together with the metal salts or used to link the metal first before being pyrolyzed. When the polymer molecules link the metal, the metal can be dispersed[21]. The polymer itself would not exist after the heat treatment process but can hold the dispersed active sites and provide pores. The polymer-derived can be combined with the soft-template method by using electrospinning to synthesis the precursors [22]. In this method, MOFs are supposed to dispersed in the polymer-derived carbon support. By using this method, catalysts with sufficient micropores and macropores can be made. However, the high amount of the macropores can be averse to the catalytic performance since it hinders the transport of protons.

The Fe- and Co- NC has been proved to hold the best ORR activity among most of the $3d$ transition metal, and thus people usually used the mixture of Fe- or Co- salts, the nitrogen sources and carbon sources together as precursors.

1.4 Oxygen reduction reaction (ORR)

The ORR catalyzed by M-N-C catalysts might follow two pathways depending on the catalytic sites and experimental conditions. The pathways are shown as below.

i)   4-electron (4e⁻) pathway: $O_2 + 4e^- + 4H^+ \rightarrow 2H_2O$

ii)   2-electron (2e⁻) pathway: $O_2 + 2e^- + 2H^+ \rightarrow H_2O_2$

The reaction pathway depends on the catalytic active sites. Notice that peroxide (H_2O_2) is an oxidant and can react with the transition metal. In a fuel cell stack, the H_2O_2 can also harm to the ionomer and membrane materials. However, the H_2O_2 can be further reduced to H_2O at some catalytic active sties. In a PEFC system, the electrolyte is acid, and the below discussion about the active sites are all based on acid media. The M-N$_x$ sites can catalyze the direct 4e⁻ pathway where the oxygen is reduced to water directly, or the $2 \times 2e^-$ pathway, where the oxygen is reduced to peroxide first, but then further reduced to water at the same site. The 2e⁻ pathway can happen at N-H sites, including the pyrrolic nitrogen and the protonated pyridinic nitrogen. The further reduction of peroxide to water can happen on another active sites, which are the metallic metal, metal-oxides, encapsulated metal carbide and pyridinic N inside a M-N-C system. This is the 2e⁻ + 2e⁻ pathway. The H_2O_2 can also be disproportioned into O_2 and H_2O. A good M-N-C system should contains mostly M-N$_x$ site since the 4e⁻ pathway is the most efficient one. Also, the ratio between N-H (or pyrrolic N) and pyridinic N should be reasonable (*i.e.* around 1, and better to contain less N-H sites) [23,24].

The classic way to probe the peroxide production is the rotating ring disk electrode (RRDE) experiment. The RRDE includes a disk and a Pt ring, where the disk can be used to deposit the catalyst ink and detect the half-wave potential, limiting current, etc. of the overall reaction. On the disk, the oxygen can be reduced to both water and peroxide. The rotating can transfer all the product to the Pt ring located 5 to 6 mm from the electrode center. At the Pt ring, the peroxide would be further reduced the peroxide to water and detect, and the current would be detected at

the same time. From the current, researchers can learned how much peroxide was yielded on the disk.

1.5 Motivation to Study Pyrolysis

High-temperature pyrolysis is material treatment at elevated temperature, usually above 400 °C, but rarely exceeding 1,200 °C, conducted in inert atmosphere (under N_2 or Ar gas atmosphere), or in controlled reductive (H_2 mixed with inert gas) or oxidative (H_2O vapor mixed with inert gas) atmosphere. Pyrolysis has been generally used as a principal method to create carbonaceous materials from various precursors (synthetic organic chemicals and naturally occurring materials), where activated carbons are the major industrial product. Specialty carbonaceous materials serving as catalysts or catalyst supports (including ORR catalysts) are often synthesized by high-temperature pyrolysis, served as catalysts "backbone", quasi-support or framework and are widely used in this materials class synthesis to provide connectivity and electron conductivity, ensure gaseous and liquid permittivity and improve the catalytic activity, selectivity and stability.

Different nitrogen, carbon and metal precursors were treated under high-temperature pyrolysis to obtain carbonaceous materials as ORR catalysts: low-molecular weight N and C containing organics, polymers, metal-organic framework (MOF) and composites/mixture of above with templating agents, such as metal oxides or salts, removable after the pyrolysis by secondary (post) treatment. However, how the precursor mechanistically transforms during the pyrolysis and how and why pyrolysis specifically benefits activity and morphology of M-N-C catalysts remains largely unknown. Namely, the pyrolysis step is currently treated as a "black box" with precursors as "input" and highly active catalyst as "output". This knowledge gap makes it difficult for scientists to design the materials with better activity. Herein, a study focusing on understanding the transformation of the materials during the high-temperature pyrolysis is essential.

Multiple studies[25-28] have shown that pyrolysis of different precursors leads to formation of a multi-component mixture of carbonaceous materials (at various degree of graphitization), and non-carbon "doping agents". Such "decorative phases" include various transition metal-nitrogen moieties (M-N_x), incorporated in N-doped carbon, which by itself could have select structural features, and inorganic metal-containing nanoparticles (reduced transition metal particles or clusters, metal carbides, nitrides, oxo-carbides, oxo-nitrides, etc.), all present in the pyrolysis product. Great efforts have been made to identify several of these moieties as active sites in ORR, including M-N_x (x = 2-4) along with multitudinous nitrogen moieties (such as pyridinic N, pyrrolic N and graphitic N incorporated in carbons of different level of graphitization) in the pyrolyzed catalyst for catalytic activity[27-30].

Recently, Li *et al.* monitored the formation of $Fe_1(II)$-N_4 sites via *in situ* X-ray absorption spectroscopy (XAS) during the pyrolysis process[31]. The formation of one specific active site, the single-atom $Fe_1(II)$ – N_4 site, was the focus of this study and the vapor-phase single Fe atom transport mechanism has been revealed. Aiyappa *et al.* observed the pyrolysis of a Co-based single metal-organic framework (MOF) nanoparticle to form the oxygen evolution reaction electrocatalyst on a nanoelectrode tip[32]. The above-mentioned studies tried to understand some specific transformation, like metal oxidation status or local environment, during the pyrolysis process. However, a broad view about how the precursor transforms into catalyst from the morphological (materials) and chemical (surface science) perspective is still unexplored and this knowledge is much needed for better understanding the mechanism of the active sites' creation/evolution during the pyrolysis, their stability, mobility and transformation into a less active (inert) moieties at higher temperatures.

1.6 Introduction of the applied techniques

The direct and thorough analysis of the pyrolysis process is based on a series of *in situ* and *ex situ* techniques. In this thesis, multiple techniques were applied.

To have a general understanding of the heat treatment process, thermogravimetric analysis (TGA) was applied to learn the mass changes during the ramping. TGA was also connected with Fourier-transform infrared spectroscopy (FTIR) and mass spectroscopy (MS) to conduct the evolved gas analysis. N_2 sorption was applied to get a general idea about the products' morphology, including the Brunauer-Emmett-Teller (BET) surface area, pore volume and the pore size distribution.

To probe the catalysts' morphological transformation during the pyrolysis, scanning transmission electron microscopy (STEM) was applied. STEM, together with energy-dispersive X-ray spectroscopy (EDS) or electron energy loss spectroscopy (EELS) can provide two-dimensional (2D) high-resolution information of how the element distributed during the process. X-ray computed tomography (CT) allows researchers to observe the morphological evolution of the materials in a 3-D views under micro-scale (micro-CT) or nanoscale (nano-CT). The studies in this thesis are using innovation furnaces, which include X-ray transparent windows to achieve *in situ* observations.

Phase and chemical information cannot be ignored. The crystal transformation in the studies of this thesis were revealed by conducting *in situ* X-ray diffraction (XRD). The carbon in the catalysts can be important, as some extent of the amorphous carbon can help improve the catalytic activity and stability[33], while some extent of the graphitic carbon is beneficial for the electron to move[34]. For this reason, Raman spectroscopy was applied to understanding the

carbon type inside the catalysts. The chemical status and local environment of the metal

disclosed the information about whether metal is highly dispersed and bonded with nitrogen to

form M-N$_x$ sites. If the metal mainly bonded with metal and form particles, researchers

considered it badly dispersed. This information is revealed in this thesis by using X-ray

absorption spectroscopy (XAS). The surface of the catalyst is also important, since the O$_2$ would

contact the surface easily. Thus, the surface is supposed to have sufficient active sites and a

reasonable ratio between the sites catalyzing 2e$^-$ pathway and the sites that can further reduce

peroxide. The surface chemistry is detected by X-ray photoelectron spectroscopy (XPS). This

technique detects the content at the surface (~10 nm) with the limit of 0.1 atom%. All the

deconvolution of the XPS data was based on the reported DFT calculation results.

1.7 Dissertation focus

The studies in this dissertation focus on providing a thorough observation of the pyrolysis that

leads to the formation of M-N-C catalysts. The precursors chosen covered from the state-of-the-

art one (the mixture of the nicarbazins, metal salts and silica as hard template) to the currently

popular ones (ZIF-8 and ZIF-67, both are MOF materials).

The Chapter 2 and Chapter 3 were studying the state-of-the-art catalyst. This catalyst has been

scaled up by a company and requires two pyrolysis process. The Chapter 2 aims to understand

the 1st pyrolysis process, where the precursors transform into M-N-C materials. With more

studies conducting to study M-N-C materials, researchers found that a 2nd pyrolysis process can

help improve the catalytic performance of the materials. This is a pure empirically introduced

process and the reasons behind were not revealed. The Chapter 3 focused on observing the 2nd

pyrolysis (i.e. re-pyrolysis) process. The study reveals the transformation of the materials during

the process from the morphological views, phase view and surface chemical views.

MOFs are promising precursors for transition metal-nitrogen-carbon (M-N-C) catalysts with high catalytic performance. Pyrolysis is the most common way to convert MOFs into electrically conductive MOF derived M-N-C catalysts. The Chapter 4 probed the morphological evolution and spectroscopic transformation of two commercial MOFs with the same sodalite topology, the ZIF-8 and ZIF-67. This Chapter focuses on understanding the similarities and differences when pyrolyzing the MOFs with and without the often-used transition metals. This study aims to understand the pathway of MOF leading to the carbonaceous materials *via* pyrolysis.

The studies in this dissertation provide the direct observation and thorough analysis of "the birth of catalysts" are the foundation, with the goal to provide guidance for the rational design of M-N-C as ORR catalysts.

Chapter 2

Pyrolysis of Precursor to the State-of-the-Art Transition Metal-Nitrogen-Carbon Materials

2.1 Overview

Different N-C precursors have been used in synthesizing M-N-C materials by pyrolysis, including N-containing organics, such as amines, amides and imides, and their more complex adducts, like charge-transfer organic salts[35,36], variety of N-containing polymers[8], variety of biopolymers, biomass-derived materials at different level of purification or product definition[37], and organic materials already incorporating the transition metal such as porphyrins, phthalocyanines and other chelating molecules[38,39], and MOFs[9]. The charge-transfer organic salt precursors have been selected specifically under the hypothesis that their relative stability would facilitate the introduction of the N-doped moieties in the carbon at the early stages of pyrolysis process[17]. It has been suggested that polymer precursors facilitate decrease in the inter-atomic distance between N and C and thus benefit the formation of N-doped carbon[8]. Some authors discuss that specific/select MOF precursors maintain their morphology (physical structure) during the pyrolysis while undergoing multiplicity of chemical formations[22,40,41].

In this study, a charge-transfer N-containing organic salt nicarbazin was chosen as the precursor to undergo pyrolysis. Materials derived from this precursor have been published and empirically studied by our groups by an extensive set of *ex situ* methods[17,31,40,42,43]. Such materials belong to the family of "hard-templated" synthesis for controlled porosity and morphology and have been studied and evaluated for their materials and catalytic properties by a list of researchers[31,38,44-46]. Materials based on nicarbazin pyrolysis have been commercialized as PGM-free ORR catalyst[47]

and N-containing synthetic carbon supports for low-PGM and other specialty applications. Recently, catalysts derived from pyrolyzed nicarbazin have shown activity as heterogeneous (non-electrochemical) catalysts for the selective oxidation of alcohols[48] and on the carbon dioxide electroreduction to CO with high level of selectivity and control.

This study is, to our knowledge, the first systematic study bringing direct observation of the pyrolytic synthesis of carbon-based catalyst with *in situ* techniques. This study introduces monitoring the chemical and morphological transformation during pyrolysis for the synthesis of M-N-C electrocatalysts via a combination of *in situ* synchrotron and lab-based diagnostic techniques including X-ray computed tomography (CT), X-ray diffraction (XRD) and scanning transmission electron microscopy (STEM), with the support of *ex situ* techniques when limited by facility (**Figure 2-1**). These techniques provide substantial evidence to the mechanisms of material transformation during the pyrolysis and enable direct observation of the "birth of electrocatalyst", enabling foundation for the rational design of the M-N-C electrocatalysts.
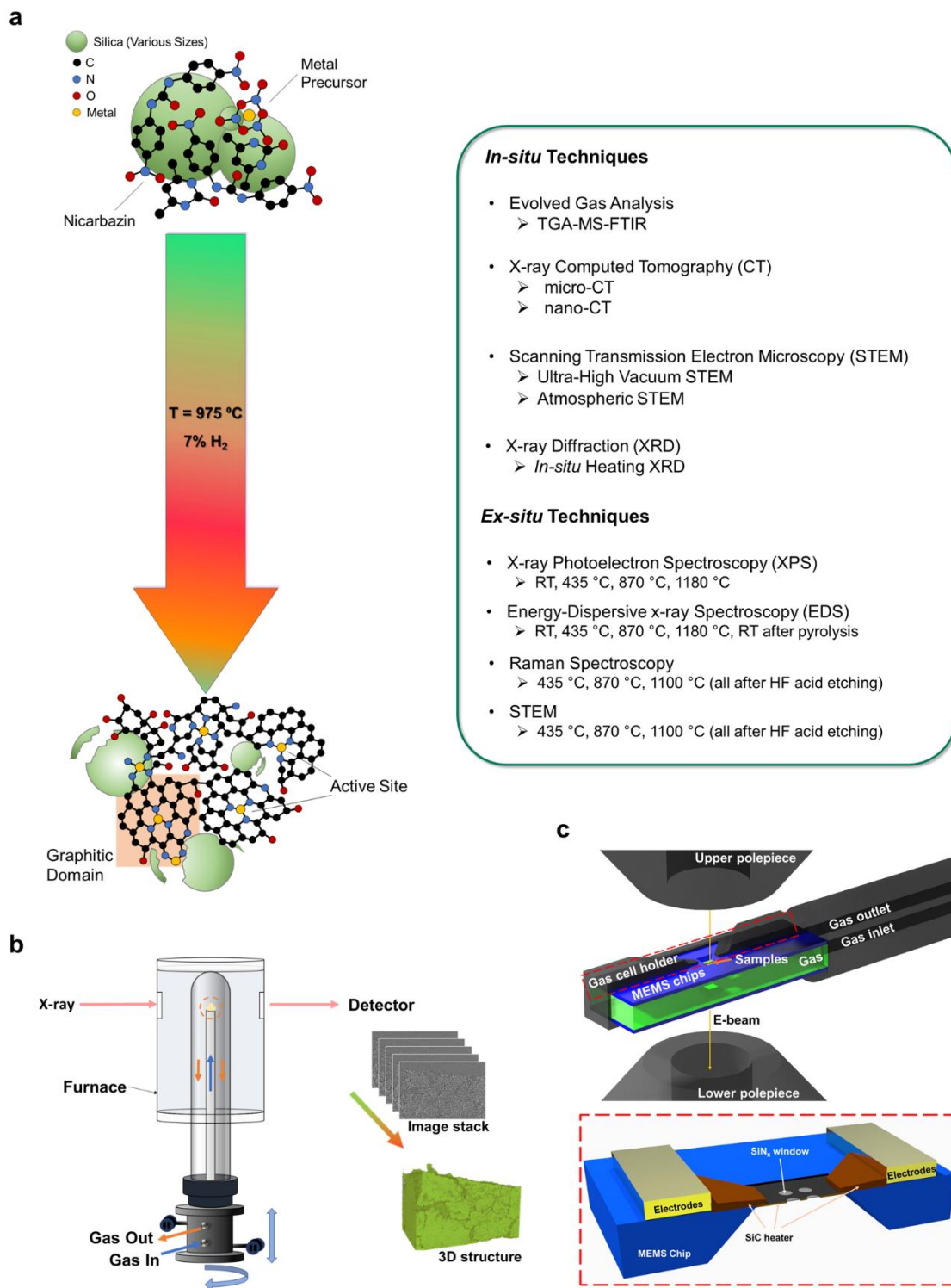
Figure 2-1 Overview of the investigation of the M-N-C catalysts transformation during pyrolysis.

(a) Schematic of the pyrolysis process and list of the diagnostic techniques applied in the study, (b) schematic of an *in situ* X-ray CT experiment using a custom designed furnace, and (c) the sample holder for *in situ* atmospheric STEM experiment and a cross-sectional 3D view of the heating chip.

13

2.2 Methods

2.2.1 Materials Synthesis

The precursors mix, along with the samples used for eX-situ STEM, electrochemistry & Raman spectroscopy were synthesized by the sacrificial support method. Namely, a calculated amount of silica mix (*e.g.* Stöber spheres (1 g), LM-150 (Evonik, 2.5 g) and OX-50 (Cabot, 2.5 g)) was mixed with 1.2 g of iron nitrate nonahydrate (Sigma-Aldrich) and 12.5 g of nicarbazin (Sigma-Aldrich) in water. A wet impregnation was then performed, first during t = 30 min in an ultrasonic bath, then at 45 °C while stirring. The resulting sample was dried overnight at 45 °C and ball-milled for 30 min (45 Hz). The resulting precursor mix was used for the *in situ* characterizations. When needed, the next steps of the synthesis were also undergone, i.e. the sample were pyrolyzed in a tubular furnace using a 5% H_2:95% N_2 flow, with a ramping rate of 10 °C min^{-1} up to 435 °C, 870 °C or 1100 °C, where the temperature was maintained for 30 min, before being ramp down to room temperature. The samples were then ball-milled for 1h (45 Hz) and etched in a 2:1 HF to H_2O solution for 96 h. After the etching, the samples were washed up to neutral pH and ball-milled one last time, for 1h.

2.2.2 *In situ* Micro-Computed Tomography (µCT)

The precursor material was imaged using synchrotron hard X-rays on beamline 8.3.2 at the Advanced Light Source (ALS) at Lawrence Berkeley National Laboratory (LBNL). White light illumination was used, and detection was with a 50 µm LuAG scintillator, 5x lens and a sCMOS PCO Edge camera, yielding a pixel size of 1.3 µm. The precursor material was mounted on the top of a ceramic holder, which was placed inside a quartz tube, where the quartz tube was mounted in an air-tight seal onto a base. The holder and the tube were placed on a rotating stage.

14

5% H_2 and 95% Ar was purged inside the quartz tube and continued flowing at 100 standard cubic centimeters per minute during the whole experiment. The top part of the holder and the tube with precursor material were enveloped by a furnace with an X-ray transparent window[49]. The design of the furnace and detailed drawings are reported previously[49]. For a CT experiment, the sample was rotated by 180 degrees, with 100-300 ms per projection, and 1313 projections per scan.

For the continuous ramping μCT experiment, the precursor material was scanned at pristine state, next at the ramping stages with a rate of 31.25 ℃ min^{-1} and 9.375 ℃ min^{-1}, then scanned three times when being held at 975 ℃ and at the final state after cool down. For the stepped ramping μCT experiment, the precursor material was scanned at pristine state, 150 ℃, 250 ℃, 350 ℃, 450 ℃, 550 ℃, 650 ℃, 750 ℃, 850 ℃, three times at 970 ℃ and at the final status after cool down.

The data was reconstructed using TomyPy and Gridrec algorithm. Our earlier works report parameters details of the reconstructions[50]. Fiji ImageJ was used for reconstructed data pre-processing. Trainable Weka Segmentation Plugin was used for segmentations[51]. Two phases were identified in segmentation: carbonaceous materials and pores. The three-dimensional volume rendered visualization was created by Dragonfly 4.1.

2.2.3 *In situ* X-ray Nano-Computed Tomography (nano-CT)

The precursor material was imaged with the transmission X-ray microscope (TXM) from sector 32-ID at the Advanced Photon Source (APS) at Argonne National Laboratory (ANL). Monochromatic X-rays illuminate the mono-capillary condenser that focuses the beam onto the sample. A 50 nm outermost zone width Fresnel zone plate used as an objective lens projects X-

rays onto a full-field detector. A phase-ring placed in the back focal plane of the zone plate was used to perform imaging in Zernike phase contrast mode to detect low atomic mass elements such as carbonaceous materials[52]. 8 keV energy was chosen, due to phase-ring designed for this energy, yielding a voxel resolution of 44.6 nm and field of view (FOV) of 55 x 46 µm. The precursor material was mounted on the top of a graphite pin, as graphite proved to be stable material with low thermal expansion coefficient at high temperatures. The pin was mounted onto a high accuracy air-bearing rotary stage, necessary to perform computed tomography. The top part of the graphite pin was enveloped by an inductive furnace with X-ray transparent window. The inner environment of furnace was purged by 5% H_2 and 95% N_2, where this gas was flown through the furnace during the whole experiment. A preheat tubing segment that enters the furnace was used to heat the gas to avoid thermal fluctuations, which become relevant for nanometer scale imaging. The precursor material was rotated through 180 degrees and imaged 726 times during 180 degrees rotation, using 0.5-2 s exposure time per projection. Imaging was performed for pyrolysis process at pristine state, 90 ºC, 200 ºC, 435 ºC, 710 ºC, 870 ºC, 1180 ºC and at the final state after cooling down to room temperature.

The data was reconstructed using TomoPy and ASTRA toolbox was used for reconstructions[53-56]. Then image processing was done in Fiji ImageJ. The segmentation and three-dimensional structures were done with Dragonfly 4.1 software. The 3D structures/labels for nano-CT were either done by manual segmentation or deep learning segmentation.

2.2.4 *In situ* Scanning Transmission Electron Microscope (STEM)

The precursor material was used for the *in situ* heating STEM experiment under vacuum environment and under 5% H_2 and 95% N_2 environment. The precursor material was first dispersed in a solvent using ultrasonic bath for around 3 minutes. For *in situ* gas reaction TEM

experiment, a Protochips Atmosphere^{TM} system was used where the suspension was deposited directly on a Micro-electromechanical Systems-based (MEMS-based) E-chip (EAB-33AB, Protochips, Inc.). The chip is comprised of a thin SiC heater of which the temperature is obtained by measuring the electrical resistance. There are a 3x3 array of $\varphi = 8$ μm holes in the center of the SiC heater that are covered by 50 nm SiN$_x$ membrane to provide electron transparent areas for observation. A second window chip and a gasket were used to create an enclosed gas reaction region inside the TEM holder. For the *in situ* heating STEM experiment under vacuum environment, the Protochips Fusion Select^{TM} was used where there is only one heating chip (E-FHDC, Protochips, Inc.) used and the $\varphi = 8$μm holes were covered by holey carbon thin films.

STEM was performed on a JEOL JEM-ARM300CF microscope with probe correctors and 300 kV cold field emission gun. All reported temperatures were calculated by the measured electrical resistance of the heater. For the *in situ* heating experiment under vacuum environment, images were taken at pristine state, 250 ⁰C, 350 ⁰C, 435 ⁰C, 710 ⁰C, 870 ⁰C, 950 ⁰C, 1180 ⁰C and at the final state after cool down. Energy dispersive X-ray spectroscopy (EDS) was done at the pristine state, 250 ⁰C, and at the final state. For the *in situ* heating experiment under 5% H$_2$ and 95% N$_2$ atmosphere, images were taken at pristine state, 100 ⁰C, 150 ⁰C, 250 ⁰C, 300 ⁰C, 350 ⁰C, 435 ⁰C, 710 ⁰C, and 870 ⁰C.

The authors noticed that there is some donut-shape structure in the gas-cell E-chip, which is due to the artificial texture of the SiN$_x$ membrane and was stable throughout the entire experiment. Also, a trace amount of tungsten was observed on the E-chip for the ultra-high vacuum heating experiment. Same issue was present for new chips without any samples hence we believe that the tungsten was a contaminant from the chip. Tungsten may also be an impurity in iron nitrate nonahydrate (even in the one $\geq$99.999% trace metals basis, shown in the certificate of analysis

for product #529303 from Sigma-Aldrich), which was a raw material used in the precursor synthesis.

2.2.5 *In situ* X-ray Diffraction (XRD)

The *in situ* XRD experiment was performed with an incident 20 keV X-rays and 30 s exposure time on beamline 12.2.2 at the ALS at LBNL in an environmental cell previously reported [57,58]. Briefly, around 1 mg of the sample was introduced inside a 0.7 mm outer diameter quartz capillary. A tungsten carbide injection capillary delivered the gas mixture from the mass flow controllers. Both concentric capillaries were mounted and enclosed inside a silicon carbide cylinder, which acted as oven by being heated with two infrared lamps. The silicon carbide oven has two holes to allow for the incident X-ray beam to interact with the sample and move to the detector, a PerkinElmer XRD 1621. A pattern with a LaB_6 standard NIST 660b was acquired for setup calibration before the experiment. Placed few millimeters below the sample, an S-type thermocouple allowed for temperature control. The temperature was changing during X-ray exposure, and the reported temperature was the average temperature during the exposure time. Before the experiment, the temperature was calibrated using a second thermocouple placed in the sample position. The XRD data was collected when the precursor material was heated from room temperature to 934 $^{\circ}$C at the rate of 10 $^{\circ}$C min^{-1}, hold at 934 $^{\circ}$C for 60 minutes and cooled to room temperature at the rate of 60 ºC min^{-1} under 5% H_2 and 95% Ar atmosphere. The total gas was flowing at 5 Nml min^{-1} during the whole process. The patterns containing Debye diffraction rings were processed on-the-fly using Dioptas[59] software to yield intensity as function of 2Theta.

2.2.6 *Ex situ* Energy-Dispersive X-ray Spectroscopy (EDS)

The precursor materials were ramped to 435 °C, 870 °C and 1180 °C under Ar environment. The samples were held at the final temperatures for 10 minutes before naturally cooled down. The samples were then removed from a furnace and placed onto a holey carbon coated copper grid. The *ex situ* EDS were performed on a JEOL JEM-2800 microscope at 200 kV with dual silicon drift detectors EDS.

2.2.7 *Ex situ* X-ray Photoelectron Spectroscopy (XPS)

The precursor materials were ramped to 435 °C, 870 °C and 1180 °C, respectively for the *ex situ* XPS characterization. Samples were held at the final temperatures for 10 minutes before naturally cooled down, removed from the furnace and mounted onto a carbon tape. High resolution XPS was performed on a Kratos AXIS Supra spectrometer with a monochromatic Al Kα source. After characterizing the sample surface, Ar ion gun was used to etch the surface of 1180 °C sample for 30 s with 500 eV Ar250+ cluster setup. CasaXPS software was used to analyze the data, using 70 % Gaussian / 30 % Lorentzian setup. The fitting of N 1s and C 1s was based on our previous calculations and publications, while the fitting of Fe 2p was based on the previous study.

2.2.8 Thermogravimetric Analysis with in-line Mass Spectrometry and Fourier Transform Infrared Spectroscopy (TGA-MS-FTIR)

The precursor materials were mounted in a ceramic crucible. TGA-MS-FTIR characterization was performed on a simultaneous thermal analyzer (Netzsch STA 449 F3 Jupiter), which is connected to a mass spectrometer (NETZSCH Aeolos QMS 403 D) and a FT-IR spectrometer (Bruker ALPHA) at the end of the manifold. Blank experiments were performed for background corrections. All sample were heated under Ar from 25 ºC to 90 ºC, held at 90 ºC for 15 minutes,

then heated to 950 ⁰C with the rate of 5 ⁰C min^{-1}, 10 ⁰C min^{-1} and 20 ⁰C min^{-1} respectively. The evolved gases were transferred to collect simultaneous MS and FT-IR spectra.

For the MS analyses, a secondary electron multiplier and multiple ion detection mode were used to collect the evolution cures of m/z = 12, 17, 18, 28, 30, 44, 46. For the FT-IR spectra, the spectra in the range 4396-650 cm^{-1} IR absorption band was detected. The Rubberband correction method was used to correct the baseline of FT-IR data. NETZSCH Proteus Thermal Analysis and OPUS software were used to analyze the data.

2.2.9 *Ex situ* Raman Spectroscopy

The Raman micrographs were obtained on a Renishaw Raman microscope, using a 532 nm SSDP laser as the excitation source. The fits of the Raman patterns were performed using five peaks, *i.e.* 4 Lorentzian (G, D1, D2, D4) and one gaussian (D3) in the 1000 – 1800 cm^{-1} to efficiently assess the in-plane defectivity of the different electrocatalysts.

2.2.10 Electrochemistry

The electrochemical experiments were performed as follow. Prior to the experiment, all the experimental glassware was washed overnight in a concentrated solution of 96% H_2SO_4: 30% H_2O_2 (equivalent volume). The samples were then thoroughly washed with MilliQ water (18.2 MΩ) and double-boiled to remove any traces of the acid, before the addition of the 0.1 M $HClO_4$ solution (prepared from a Suprapur 70% $HClO_4$). Meanwhile, the working electrode (glassy carbon electrode, S_{geo} = 0.247 cm^2 with a platinum ring) was polished and subsequently cleaned for 5 min in an ultrasonic bath in acetone, isopropanol, and MilliQ H_2O. Then, while rotating at 250 rpm., 2×10 µL of the electrocatalyst ink (a mixture of isopropanol, Nafion®, milliQ H_2O and catalyst powder, aiming for a loading of 800 µg cm$^{-2}_{geo}$ on the electrode, a Nafion®/catalyst

ratio of 0.3 & an isopropanol:water ratio of 0.5) was drop casted on the working electrode, while alloying said electrode to dry under an heat-flux (and while maintain rotation) between each deposition. An RHE (Gaskatel) reference electrode and a carbon rode were used as the reference and the counter electrode, respectively. The electrolyte resistance was measured prior to any experiments and remained between 23 – 25 Ω for all experiments. The electrocatalyst was activated in a N_2-saturated electrolyte, through 100 cycles at 500 mV s^{-1} between 0.05 and 1.23 V *vs.* RHE, followed by 3 cycles at 20 mV s^{-1} and a linear sweep voltammetry between 0.10 and 1.05 V vs. RHE at 5 mV s^{-1} (measured to act as a baseline-correction for the O_2-saturated measurments). O_2 was then bubbled for 20 min and the electrocatalyst performances were measured by a linear sweep voltammetry between 0.10 and 1.05 V vs. RHE at 5 mV s^{-1} and at 1,600 r.p.m. The obtained data were corrected from the ohmic losses in solution, the baseline obtained in N_2-saturated electrolyte and the transport in solution, using the Koutechy-Levich equation.

2.3 Morphological Transformation

The X-ray computed tomography results are sub-divided into morphological observation at micro- and nano- length scales. The real-time porosity changes on a micro-scale during the pyrolysis process were resolved using *in situ* heating X-ray micro-computed tomography (X-ray μCT). The furnace with X-ray transparent windows (**Figure 2-2**) and the environmental gas cell together enable *in situ* pyrolysis X-ray CT experiment. The technique allows tracking morphology changes, as the sample undergoes heat treatment[49]. Using the *in situ* heating X-ray μCT, we interrogated the morphology changes at micrometer-scale, as the sample underwent heat treatment. **Figure 2-3a** shows the temperature profile and corresponding locations of X-ray μCT scans. The segmented 3D images were used to generate the porosity plot in the thru-plane direction (**Figure 2-3b**). The

average porosity of the precursor increased by 17.3 % during the temperature ramping stage, from pristine to location 1-4 (975 °C). After that the porosity decreased by 8.7 %, as the sample was held at 975 °C and then cooled down.

The reason for the porosity increase during the temperature ramp is the breaking of the packed precursor bonds, shrinkage of the sample material, the decomposition of iron nitrate (used as Fe precursor), and most importantly melting and evaporation of nicarbazin (the melting temperature is around 262 °C according to the thermogravimetric analysis TGA results), as well as some impurities. The representative cross-section tomographs and the three-dimensional structures show that most of the void pathways are formed by decomposed material leaving the precursor during the temperature ramping stage (**Figure 2-3c**). **Figure 2-3c** also shows that the formed pathway sizes are on the order of 100 µm, and this is mainly due to fast temperature ramp rate (31.25 °C min^{-1} from 525 °C to 900°C and 9.375 °C min^{-1} from 900 °C to 975 °C. Sample was inserted into the furnace at 525 °C), where the precursor undergoes significant morphological changes in a short period of time, therefore releasing large amount of decomposed products that leave the precursor by convective transport, creating these gas pathways.
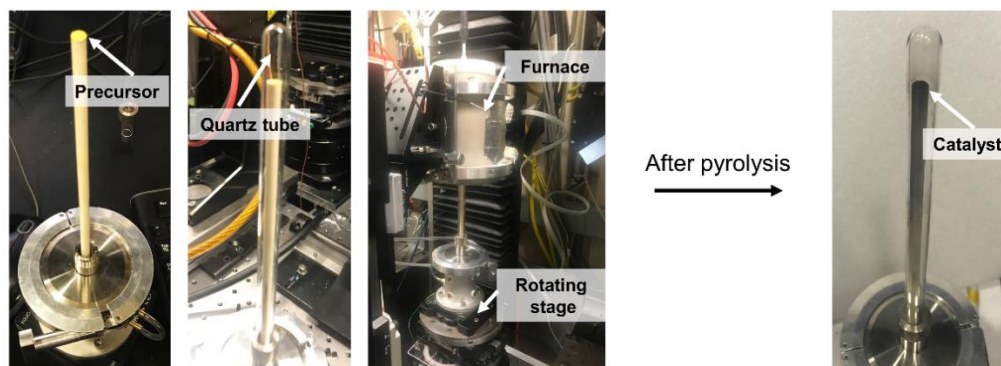
Figure 2-2 Pyrolysis setup for micro-CT experiment
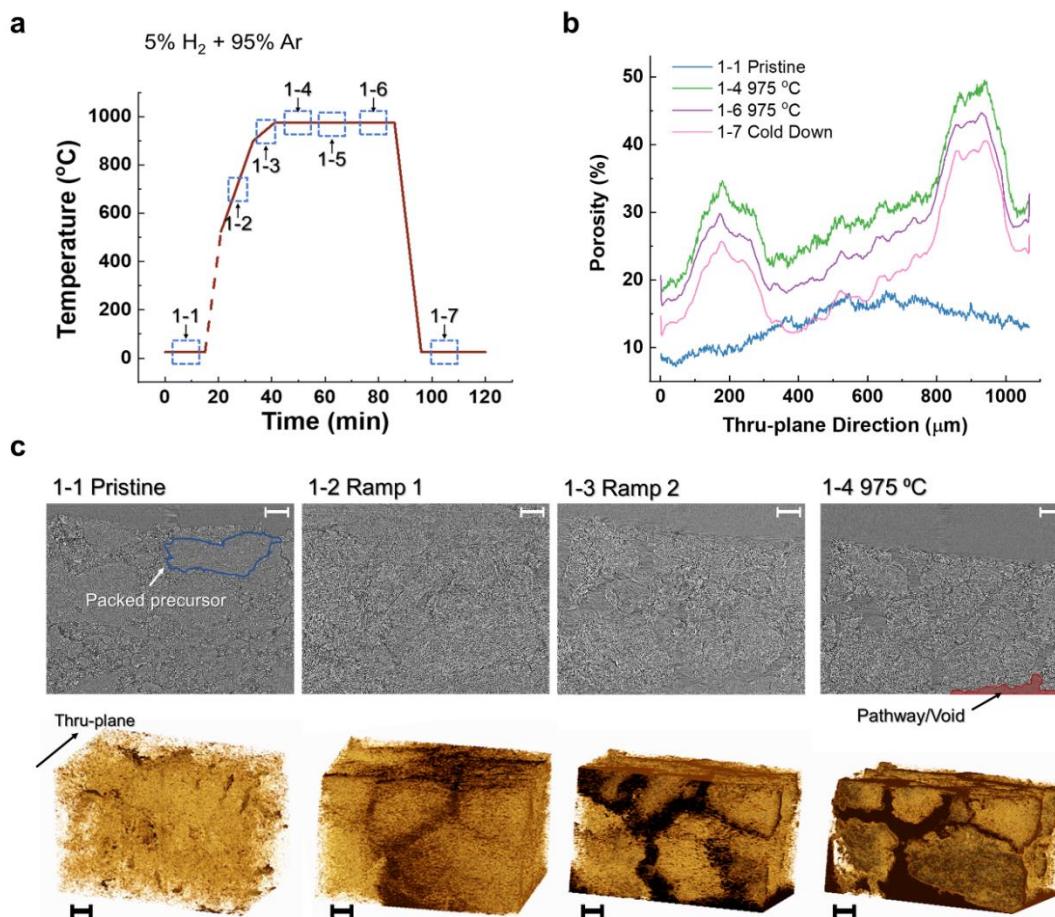
Figure 2-3 *In situ* Ramping micro-CT experiment under 5% H_2 + 95% Ar.

(a) Temperature and image profile used in the experiment, (b) Porosity *vs.* thru-plane direction calculated from the image stack, and (c) Representative cross-section images and 3D structures created based on the image stacks. Scale bar: 100 μm

After the temperature reaches 975 °C and during temperature hold, the morphology at micro-scale did not change significantly (**Figure 2-4 – Figure 2-5**). The tomographs collected during the temperature ramp were not as clear as the other cross-section images due to the rapid changes of the sample morphology during scan under the heat treatment. When using temperature "stepping ramping protocol" rather than "continuous ramping protocol" (**Figure 2-5 – Figure 2-6**), precursor morphological changes were less pronounced. During the stepping ramping protocol, temperature was held constant for 10 min per temperature step and the average ramp rate between each step was about 10 °C min^{-1}, which is 3 times slower compared to the ramp rate of 31.2 °C min^{-1} from 525 °C to 900 °C during continuous ramping protocol. Heat flux is proportional to the ramp rate,

where lower ramp rate indicates lower heat flux to the sample. Comparing the morphological transformations during stepping ramping protocol, we observe minor void pathways formation because the melting and evaporation occurs over a longer period, requiring less decomposed and evaporated species flux through the porous precursor. The void pathways for stepped ramp protocol are on the order of 10 µm in sizes, whereas for the faster ramp of continuous ramping protocol the void/pathways were on the order of 100 µm. According to the previous study[60] of pyrolysis conditions for activated carbon formation, the heating rate is the 2nd most significant (temperature as the 1st) effect to influence the morphological properties: the total pore volume has a volcano-type relationship, while the yield decreases with the increased ramping rate. These micrometer-scale macropores and pathways, if remaining after the purification, will also benefit the diffusion[61] of oxygen and water molecules after the integration into the catalyst layer of the membrane electrode assembly (MEA).
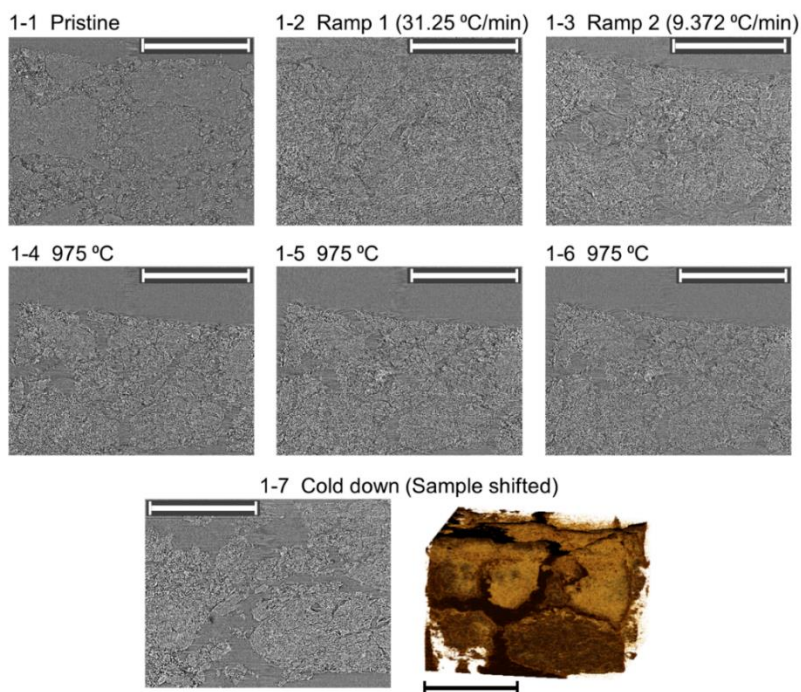
Figure 2-4 *In situ* continuous ramping micro-CT experiment under 5% H_2 + 95% Ar.

Scale bar: 500 µm
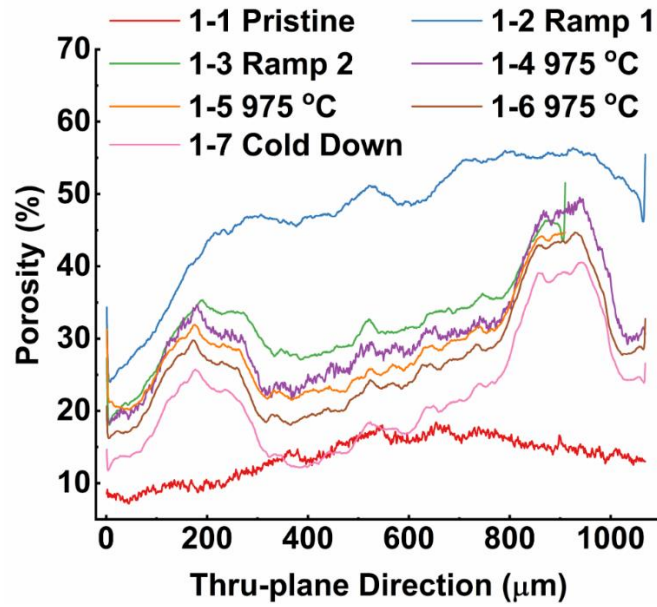
Figure 2-5 Porosity calculated from *in situ* continuous ramping micro-CT experiment data
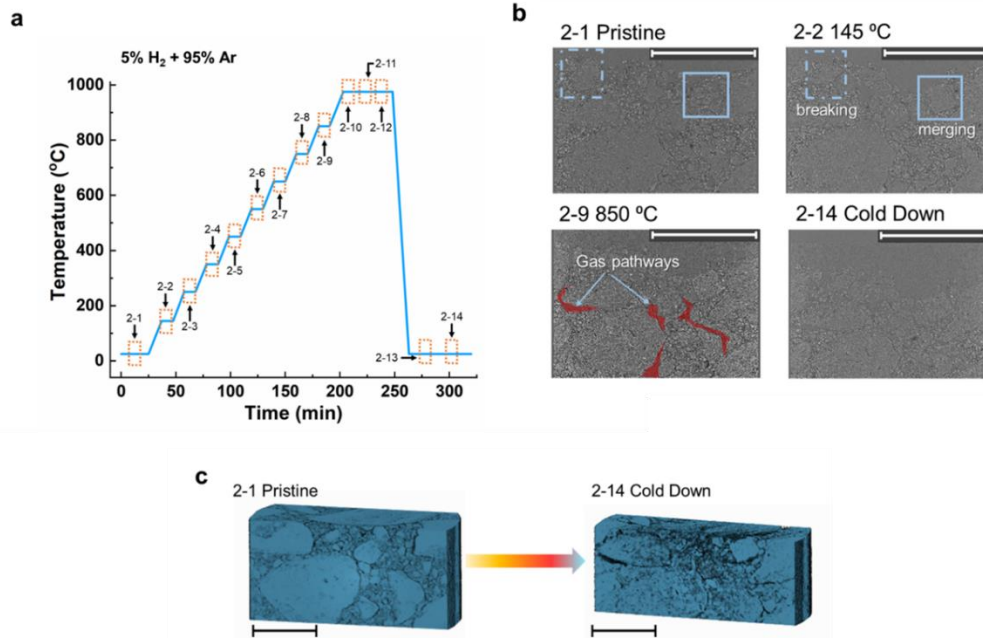
Figure 2-6 *In stiu* stepped ramping micro-CT experiment under 5% H_2 + 95% Ar.

(a) temperature profile of the "stepped ramping" experiment. (b) representative cross-section images at certain temperatures. (c) 3D structures of the sample before and after stepped ramping pyrolysis. Scale bar: 500 µm.
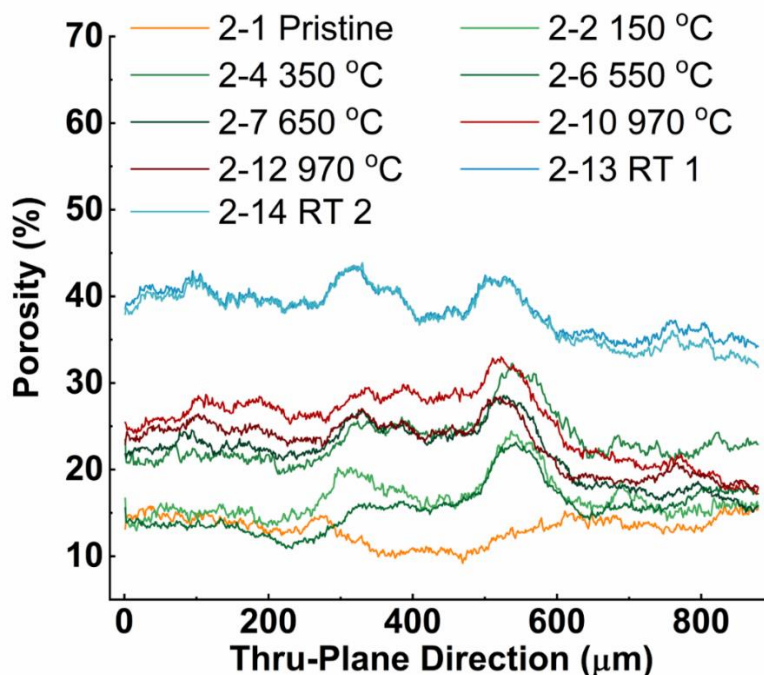
Figure 2-7 Porosity calculated from *in situ* stepped ramping micro-CT experiment data

The morphological transformations on nanoscale were observed by using *in situ* nano-CT technique. Nano-CT achieves a high spatial resolution of 44.5 nm and provides an ability to bridge the scales from micro to nano. The optic configuration of nano-CT is more complex than micro-CT with additional optical components. In nano-CT, x-rays are shaped by condenser and focus onto the sample, then Fresnel zone plates magnify the image onto the detector[56,62]. Using the furnace and the environmental gas cell system (**Figure 2-8**), the transformations of agglomerated precursor particles were observed under 5% H_2 + 95% N_2 environment. A representative cross-section images of two particles are shown in **Figure 2-9**. With temperature raising to 435 °C, the organic compounds and iron nitrate on the surface had evaporated or decomposed, and the larger particle has shrunk by 37.8 % (**Figure 2-10** and Table 2-1). At the same time, the precursor inside the particle was exposed to atmosphere (H_2+N_2). At 870 °C, both particles were observed (**Figure 2-9f**) with further shrinkage and a gap between the internal amorphous precursor phase and the external shell appeared. The internal amorphous carbonaceous phase then completely disappeared

26

after the temperature further increased to 1180 °C, leaving only the external shell. These observations indicate that the transformation of the amorphous carbon began at the edge of the two phases. *In situ* nano-CT experiments were also performed in air environment (**Figure 2-11**) and in the H_2+N_2 environment (**Figure 2-12**) for reproducibility. When the sample was calcinated in the air environment, a similar gap between internal amorphous carbonaceous material and external shell appeared at 560 °C (**Figure 2-11**). This is due to the carbon oxidation and the formation of surface oxides, which are expected due to O_2 environment. These two reactions resulted in obvious morphological change of gap formation between the external shell and internal phase at lower temperature 500 °C. In the H_2+N_2 environment, the low partial pressure of hydrogen gas limited the reduction ability of H_2 at low temperature. Particle shrinkage was also observed at around 300 °C - 350 °C in nano-CT experiments under both air and H_2+N_2 environments (**Figure 2-11** and **Figure 2-12**), which was primarily due to the aforementioned nicarbazin melting.

The bright nanoparticles (ranging from hundreds of nm to several µm) observed in **Figure 2-9** are most likely metal abundant species (due to high brightness). These particles appeared at 200 °C and maintained the same size from 200 °C to 870°C, then grew bigger and agglomerated above 870 °C. The relative position of the bright nanoparticles and the big particle remained roughly the same from room temperature to 870 °C (**Figure 2-10** and Table 2-1). When the larger particle shrunk, the bright nanoparticles moved together with the larger particle, but did not remain in the void area. Melting of organic precursors helps redistribution of the metal species at lower temperature (the moving of Fe precursor below 700 °C), but the agglomeration of metallic species, most likely due to the catalytic graphitization by Fe and the reduction of Fe by carbon, will dominate the morphological change above 870 °C and becomes severe at 1200 °C. The metal agglomeration phenomenon is also observed in air environment (**Figure 2-11**) from 200 °C and

became clearer after the carbonaceous material was oxidized. Nano-CT technique is limited in resolution and can only show the larger Fe abundant particles without insights on the chemical composition. Simultaneous X-ray absorption near edge structure (XANES) measurement was performed during the nano-CT experiments. The data was collected during the above *in situ* pyrolysis experiment, but the concentration of the nanoparticles was below the detection limit[56,62,63] compared with standard XANES measurement on bulk samples and the data was inconclusive.
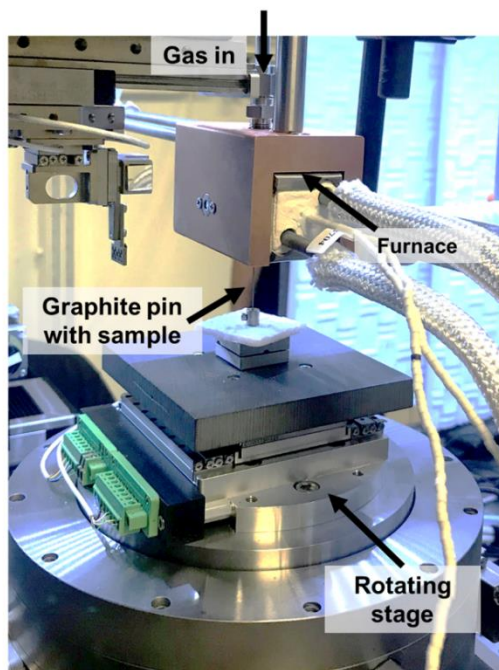
Figure 2-8 Pyrolysis setup for nano-CT experiment
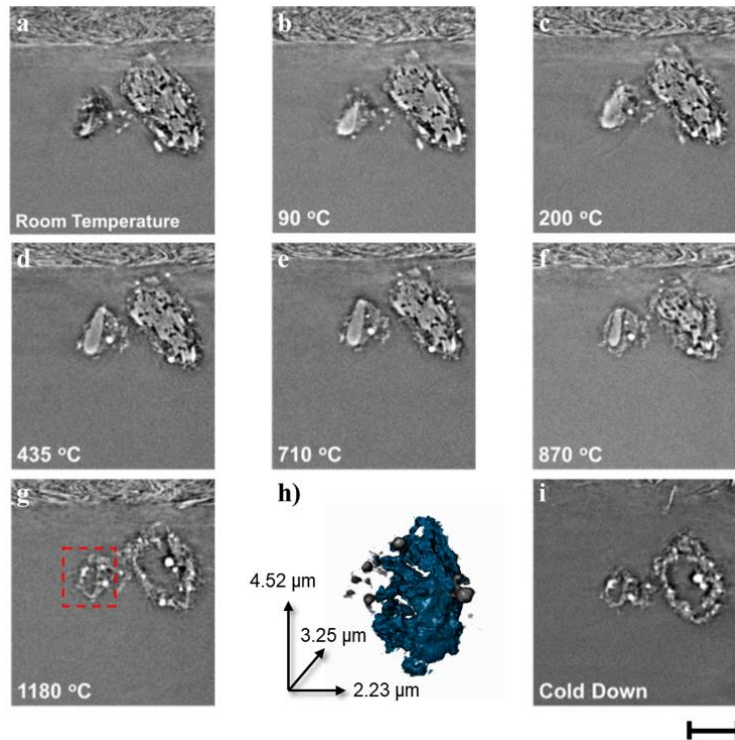
Figure 2-9 *In situ* nano-CT experiment under 5% H_2 + 95% N_2 environment.

(a - g) Representative x-ray cross-section tomographs during the temperature ramping, (h) three-dimensional volume rendering of a particle in the selected area in (g), and (i) representative cross-section tomograph after the sample cool down. Scale bar: 5 μm
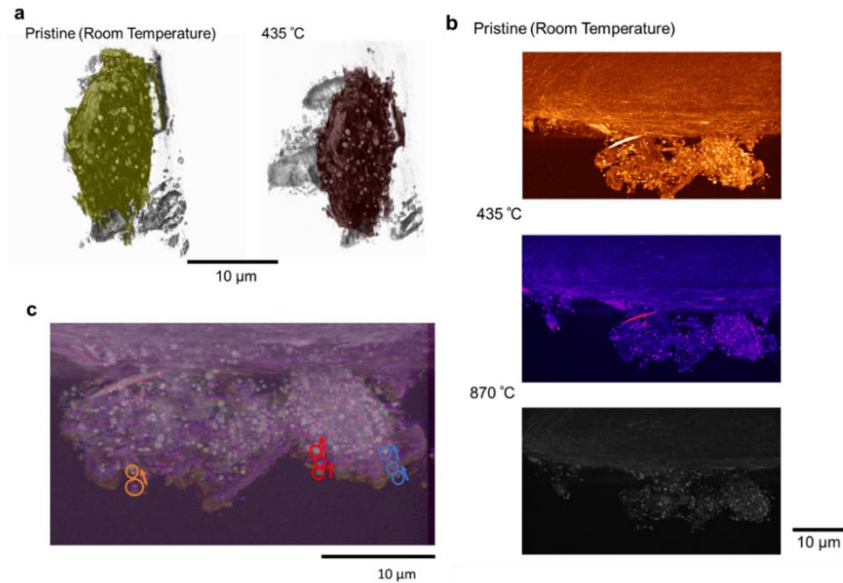
Figure 2-10 Nano-CT (5% H_2 + 95% N_2) processed images for tracking volume and position changes.

(a) segmented images for the data taken at room temperature and 435 ⁰C, the labeled particle was used to track the volume changes during the process. (b) max intensity Z-project for the data taken from room temperature, 435 ⁰C and 870 ⁰C and (c) the overlay images of b. Arrows indicate the particle position changes during the process

Table 2-1 Labeled voxels in Nano-CT images taken in room temperature and 435 ⁰C

Image (shown in Fig. S7a)	Pristine (room temperature)	435 ⁰C
Label voxel	6,416,743	3,965,710
Volume ($\mu m3$)	569.27	351.82
Decreased percentage	37.8 %	
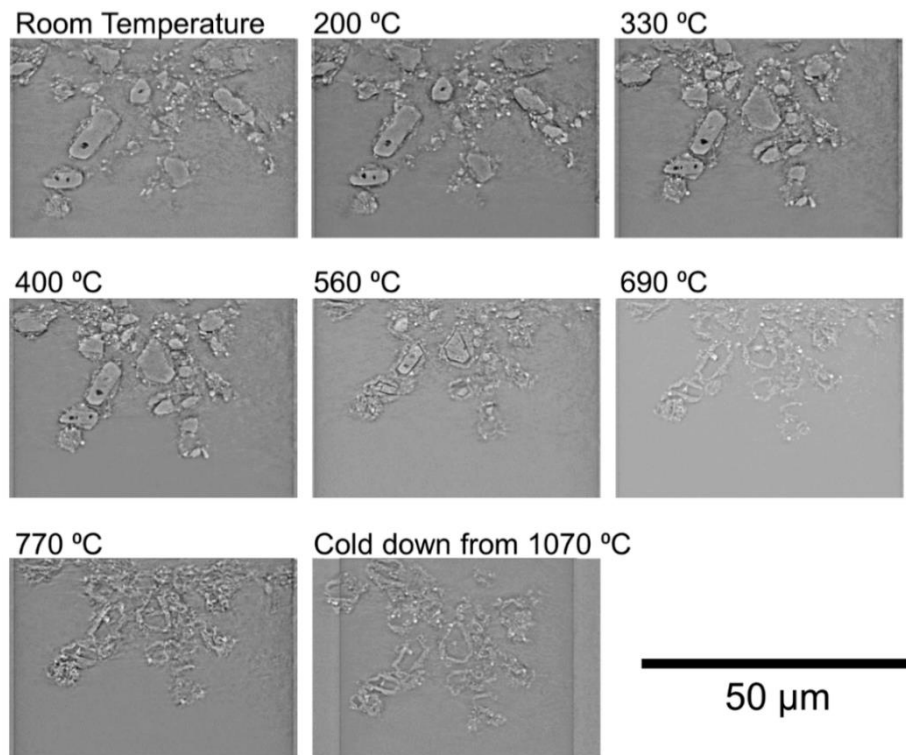
Figure 2-11 Nano-CT experiment under air environment.
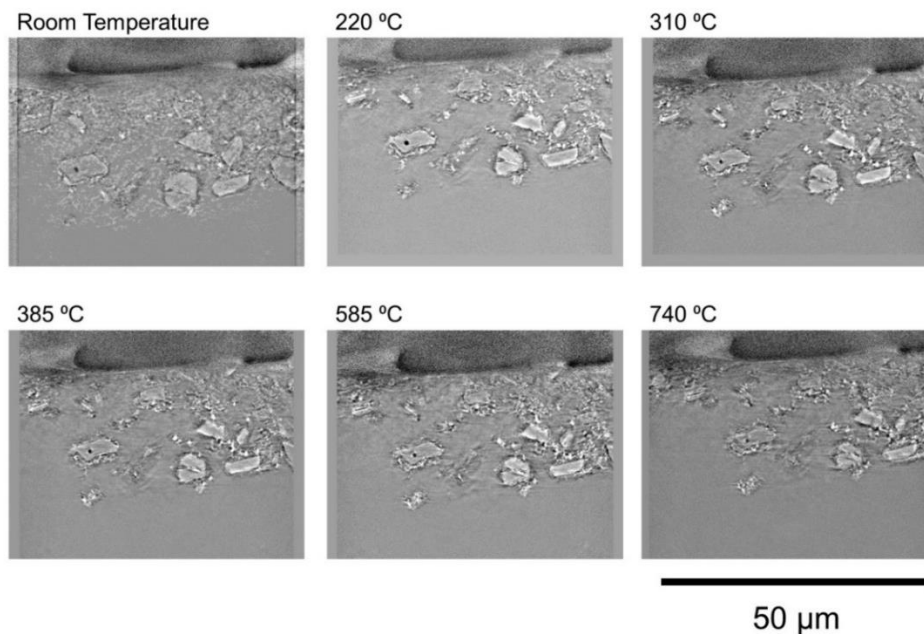
Figure 2-12 Nano-CT experiment under 5% H_2 + 95% N_2 environment (Pyrolysis up to 740 ⁰C)

The *in situ* environmental STEM technique was used to investigate morphological transformations at nanoscale. Identical locations were identified to observe the transformations when the temperature was increased from room temperature to 870 °C under 5% H_2 and 95% N_2 environment (**Figure 2-13**). **Figure 2-13** shows a selected field of view, where fibrous organic matter (long dark stripes, pointed out by blue arrow in **Figure 2-13**) is accompanied by larger nanoparticles that agglomerate into larger clusters of ~100 nm and smaller clusters of ~10 nm. These are metallic species (small and bright) and silica nanospheres (larger and darker than metallic species, but brighter than organic matter). From room temperature to 435 °C and to 710 °C the gradual disappearance of the organic fibers was observed (**Figure 2-13a-c**), which is partially due to nicarbazin melting and evaporation, and further decomposition at high temperature. The metal nanoclusters did not seem to have obvious change in morphology before 710 °C. Majority of the obvious changes in nanoclusters occurred between 710 °C and 870 °C. In this temperature range the large nanoclusters (silica nanospheres) remained intact, whereas the

31

smaller nanoclusters (metallic species, several nm in **Figure 2-13c1, c3 & c4**, and tens of nm in **Figure 2-13c2**) transformed and were no longer detected in this field of view (comparison between **Figure 2-13c2** and **d2**). The nanoclusters are pointed out by orange arrows in **Figure 2-13c** and box in **Figure 2-13c1-c4**, while by red arrows in **Figure 2-13d** and box in **Figure 2-13d1-d4**. This can be considered as evidence that the iron atoms dispersed at high temperature.

Silica nanospheres are frequently used as hard template for the synthesis of M-N-C electrocatalysts, to help the formation of mesopores[17,64]. They are etched by hydrogen fluoride (HF) after the pyrolysis and normally regarded as inactive during the pyrolysis. However, the *in situ* STEM experiment performed under ultra-high vaccum environment (**Figure 2-14**) reveals other functionality of the hard template. The transformation of the sphere, which was confirmed to be an amorphous silica sphere by EDS and Fast Fourier transform (FFT), was observed during the experiment (**Figure 2-14** and **Figure 2-16**). The bright field STEM showed that the silica nanosphere at 250 °C has a thin layer (~5 nm) of organic compounds on its surface. This layer became thinner with the increase of tempearture and disappeared at 1180 °C. Also, a pit or crack within the sphere began to appear when the sample was heated to 1180 °C. It seems that the carbon layer was peeled from the silica nanosphere surface and removed a portion of silica away. This phenomenon is consistent with the "silicon ocean" found near the sphere (**Figure 2-15**), both indicating the silica cracking and dispersing at high temperature. The *ex situ* EDS mapping also supports this statement, which shows the breaking of silica spheres when comparing the samples pyrolyzed at 435 °C, 870 °C and 1180 °C (**Figure 2-17**, **Figure 2-18**, and **Figure 2-19**). These findings reveal that silica hard template, which is designed to form mesopores, also could create micropores during the pyrolysis, leading to larger precursor surface area after etching benefiting electrocatalysis properties.
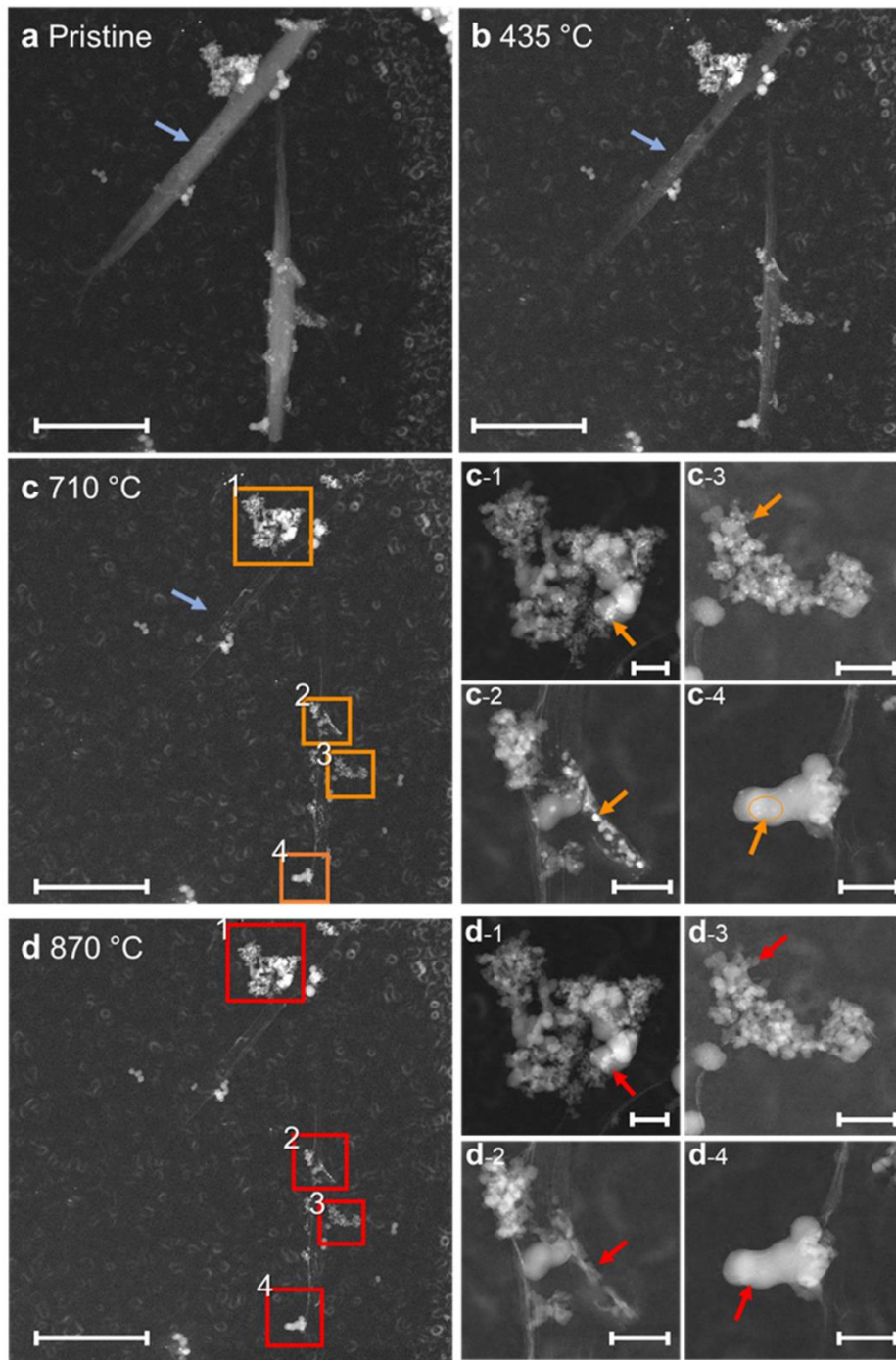
Figure 2-13 *In situ* atmospheric STEM experiment under 5% H_2 and 95% N_2 environment.
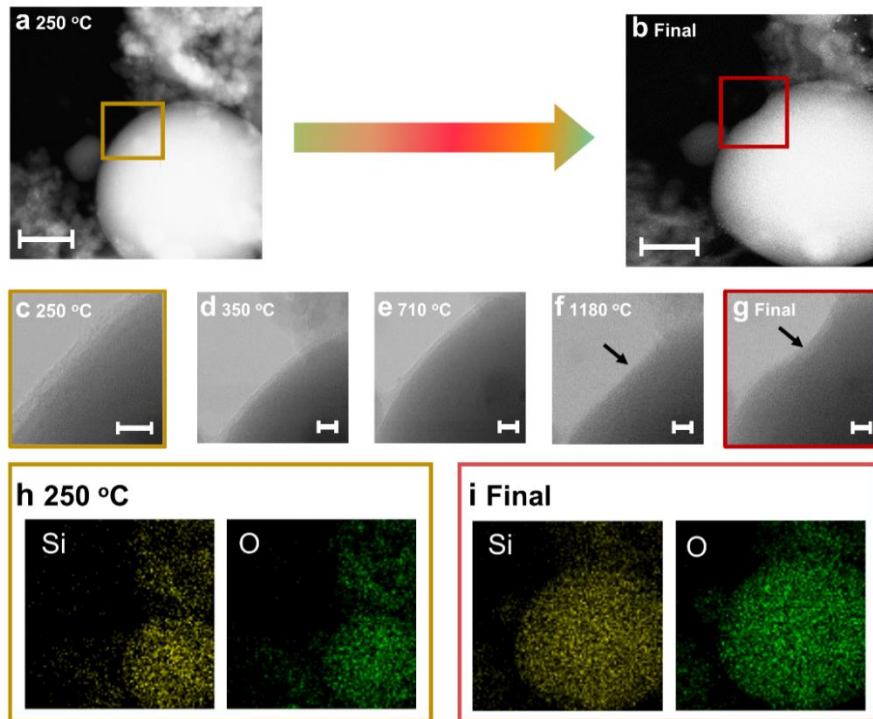
Figure 2-14 *In situ* STEM experiment under ultra-high vacuum environment.
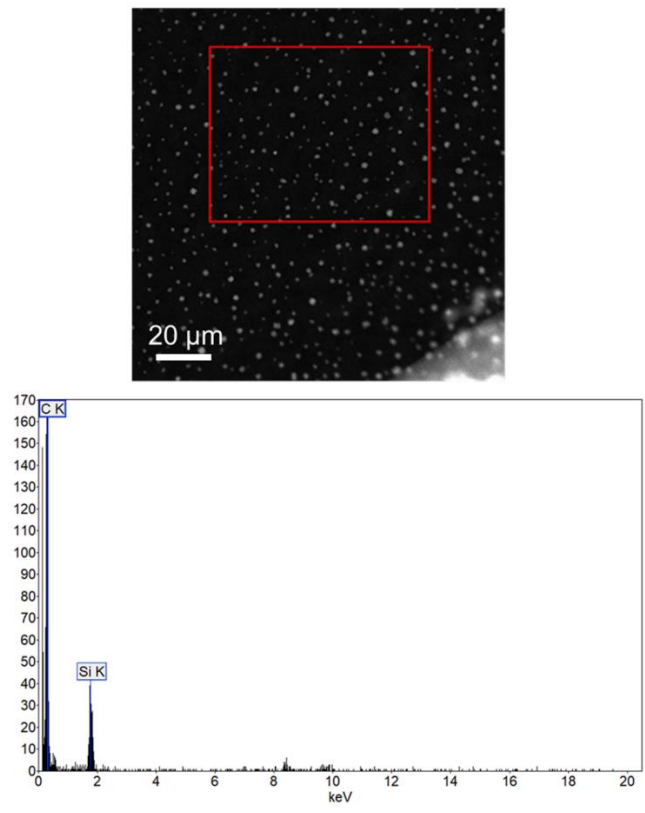
Figure 2-15 STEM image and EDS spectrum of "Silicon Ocean".

The image is taken at the room temperature after the sample was pyrolyzed up to 1180 °C
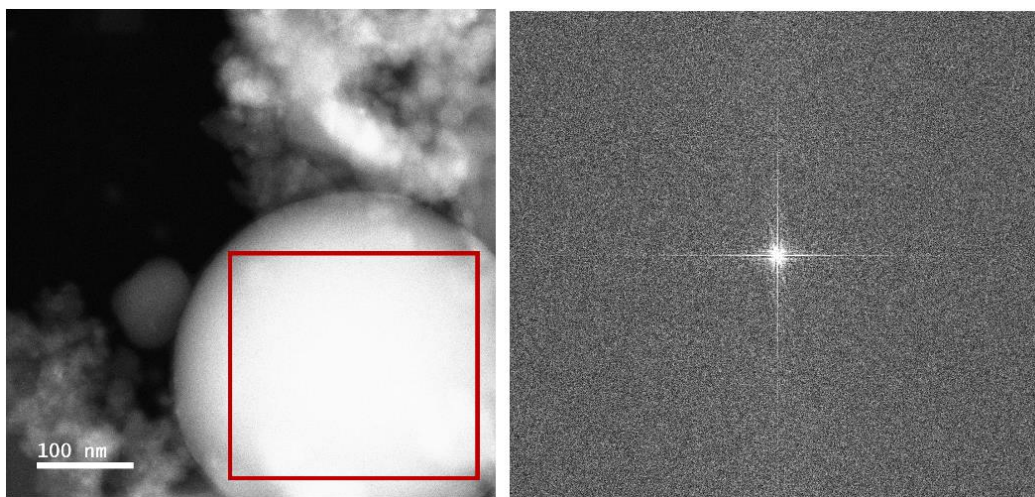
Figure 2-16 FFT of selected region (the silica ball) in the DF-STEM image.

The image is taken at 250 °C under ultra-high vacuum
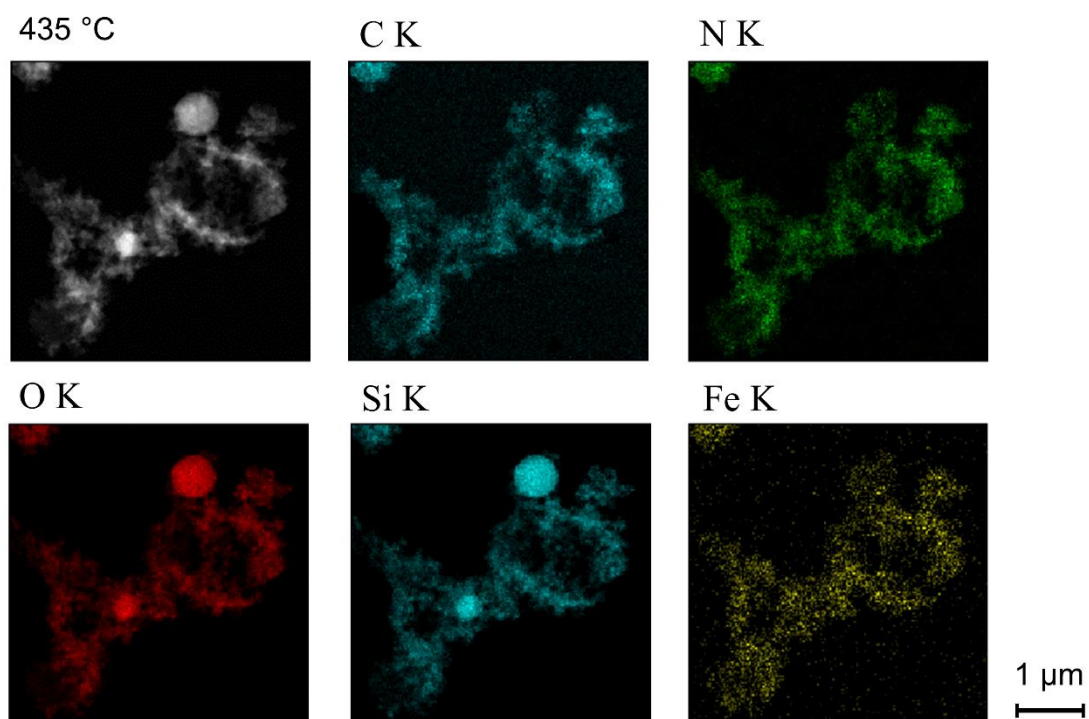
Figure 2-17 *Ex situ* EDS mapping on the sample pyrolyzed up to 435 °C under Ar environment.
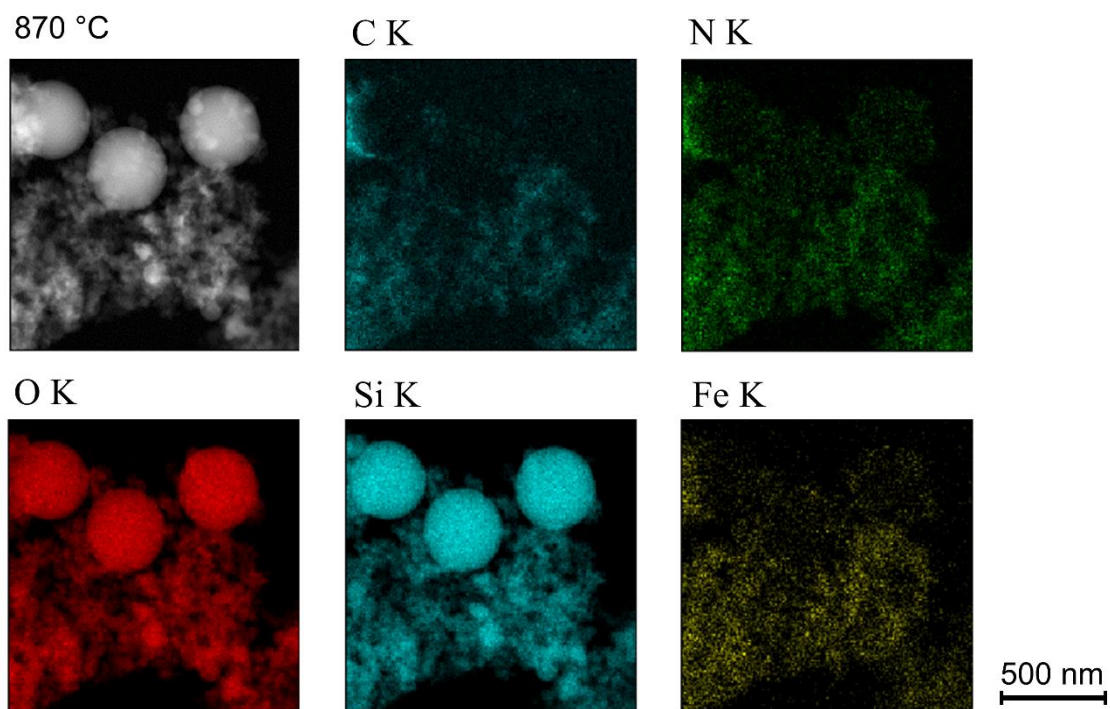
Figure 2-18 *Ex situ* EDS mapping on the sample pyrolyzed up to 870 °C under Ar environment.
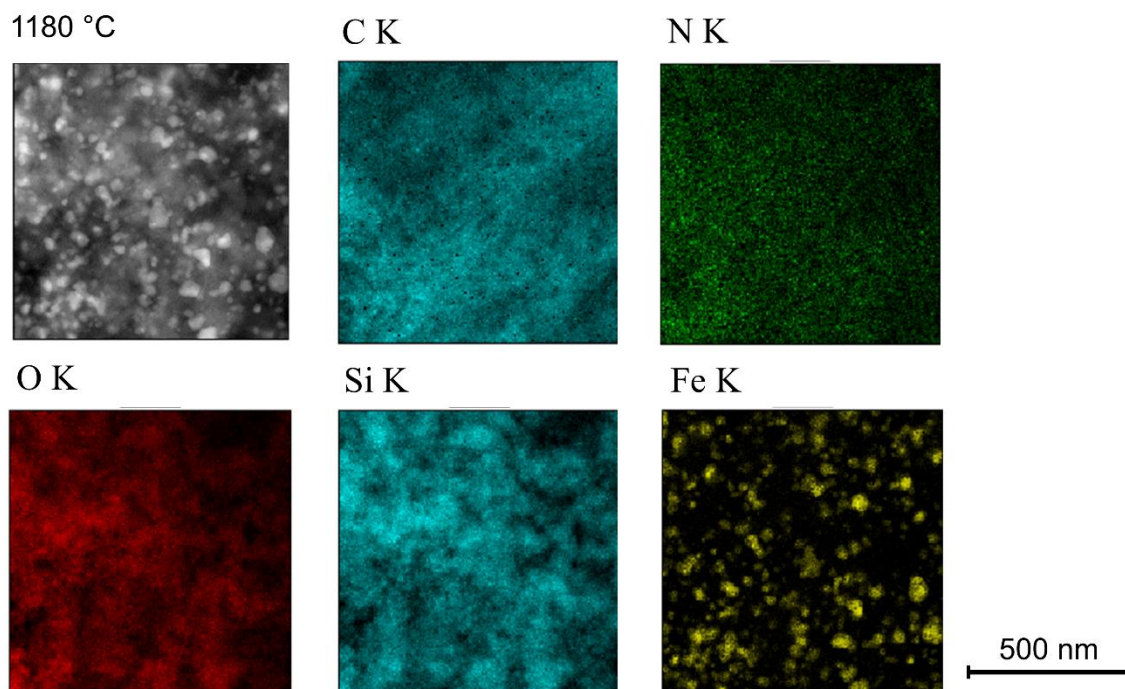
Figure 2-19 *Ex situ* EDS mapping on the sample pyrolyzed up to 1180 °C under Ar environment.

The *in situ* x-ray CT and TEM techniques described above provided insights regarding the morphological transformation during the pyrolysis process from micro-scale to nanoscale, showing the porosity increase, metal element diffusion and the silica spheres breaking. The questions about what reactions occurred during heat treatment resulting in what chemical transformations and whether they correlated to the morphological observations remain. TGA, combined with mass spectroscopy and Fourier transformed infrared spectroscopy (TGA-MS-FTIR) was performed to understand the solid-gas reactions occurring during the pyrolysis and to analyze the evolved gases simultaneously (**Figure 2-20a - c**). The in-line MS-FTIR operated at 200 °C to detect the decomposed molecules escaped from the TGA instrument, locating at the end of manifold which has detection time delay depending on the diffusion speed of a specific gas molecule. The completed FTIR and MS data are provided in Supporting Material (**Figure 2-21 –Figure 2-22**). The largest mass decrease of 30 % was observed at around 262.4 °C, with the main

evolved gas being CO_2 and H_2O. Although assumed, NH_3 presence was not confirmed, due to the overlap of infrared spectra of H_2O and NH_3, as well as their similar m/z in mass spectra. This largest mass loss is due to nicarbazin melting (occurring at 262.4 °C) along with decomposition, which was confirmed by additional observation of CO, NO_2, NO and C in this temperature range. The nicarbazin melting and decomposition phenomena are consistent with the morphological observation in the *in situ* nano-CT and *in situ* TEM under ultra-high vacuum (**Figure 2-20d - e**). The radiography images showed nicarbazin covering the surface of the precursor particles as a wet film during melting and the bubble appearance, as nicarbazin decomposed and left the chamber. The dark-field STEM images of 250 °C & 350 °C present the disappearance of the big "bubbles". In addition, CO is found to be the main evolving gas detected by MS when the temperature reached 800 °C and above. This feature may refer to the reduction of iron by pyrolyzed carbon, the catalytic graphitization by iron, or the formation of iron carbide. Surprisingly, when the TGA crucible reaching high temperature (920 °C, **Figure 2-23**), the in-line FTIR detected abnormal absorbance from 650 cm^{-1} -1800 cm^{-1} in the evolving gas. The vibration feature is similar to the gas-phase IR spectra[65,66] of several nitrobenzene derivatives, (*e.g.* 4-(4-nitrobenzyl)pyridine, 2,2'-dinitrobiphenyl, 5-nitro-o-toluidine and 2-methyl-4-nitroaniline), which could probably come from nicarbazin precursor or its byproduct, originating from 1,3-bis(4-nitrophenyl)-urea and 4,6-dimethyl-1H-pyrimidin-2-one. Due to their large molecular mass (123 for nitrobenzene), these byproducts need longer time to diffuse from the crucible to FTIR detector, which is consistent with the phenomena of bulk pyrolysis in tube furnace (see **Figure 2-23c**).

Additional TGA experiments were performed using different temperature ramping rates (5-20 °C min^{-1}, **Figure 2-24**) and under different inert gas atmosphere (Ar and N_2, **Figure 2-25**). The measured melting temperatures were 259.3 °C, 262.4 °C, 271.5 °C for the sample pyrolyzed under

Ar at 5 ⁰C min^{-1}, 10 ⁰C min^{-1}, and 20 ⁰C min^{-1}, respectively. Under N$_2$ atmosphere, the sample pyrolyzed at 10 ⁰C min^{-1} melted at 269.5 ⁰C. The results show that the ramping rate and the inert gas species do not significantly affect the melting and decomposition point, which indicate that the activation energy of this process was not affected[67]. The shift of measured melting points arises from the different heat transfer rates between the crucibles and thermocouple.
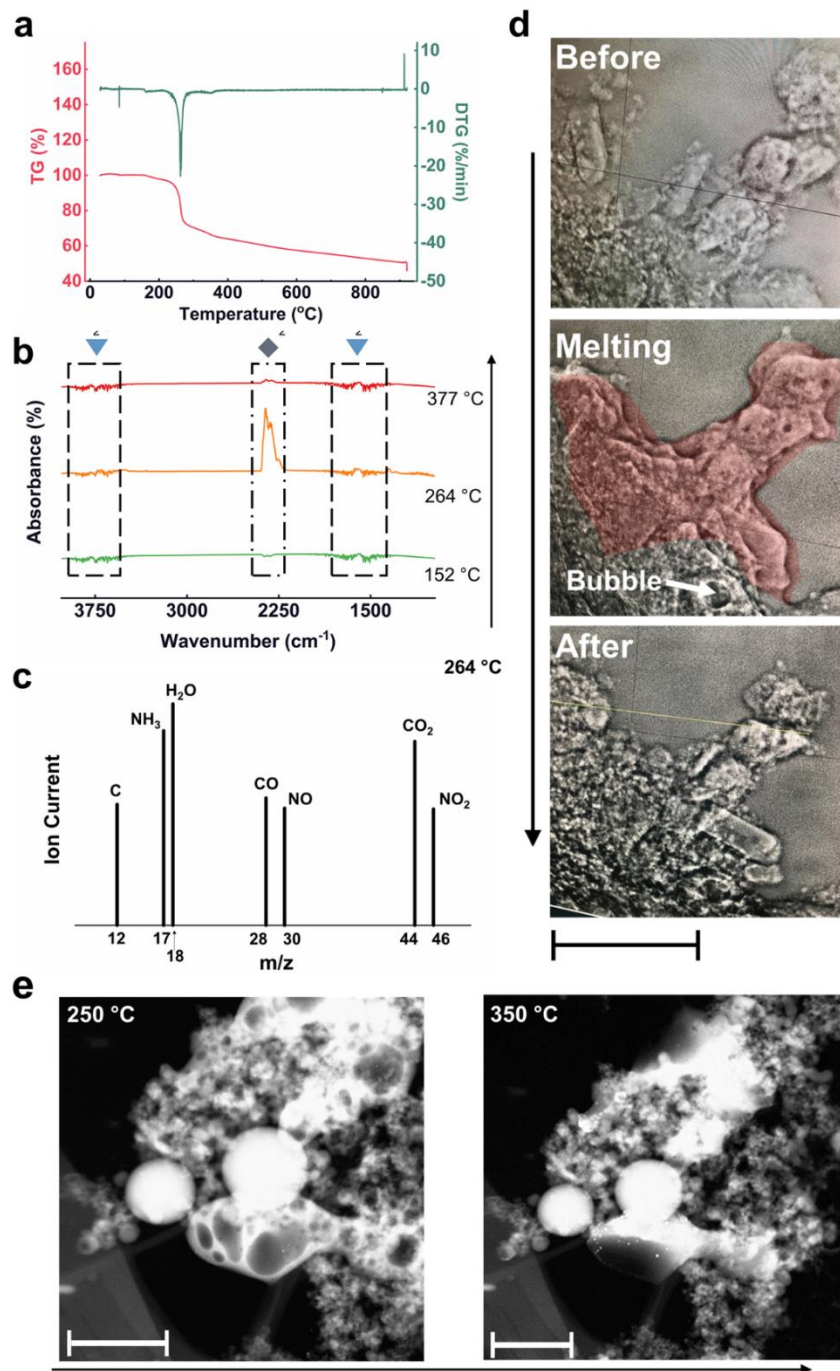
Figure 2-20 Material melting and decomposition during pyrolysis.

(a) TGA and DTG plots from 180 °C to 880 °C of the precursor mixture, with TG and DTG standing for total mass and differential time loss respectively. (B) Corresponding FTIR spectra of the evolved gases when the crucible was at 152 °C, 264 °C, and 377 °C respectively. (c) Corresponding MS when the crucible was at 264 °C. (d) X-ray nano-CT radiographs on the computer screen showing the before, melting and after stage respectively, recorded by external camera. Scale bar: 15 μm (estimated). (e) STEM micrographs showing the melting stage during the *in situ* STEM experiment under ultra-high vacuum. Scale bar: 500 nm.
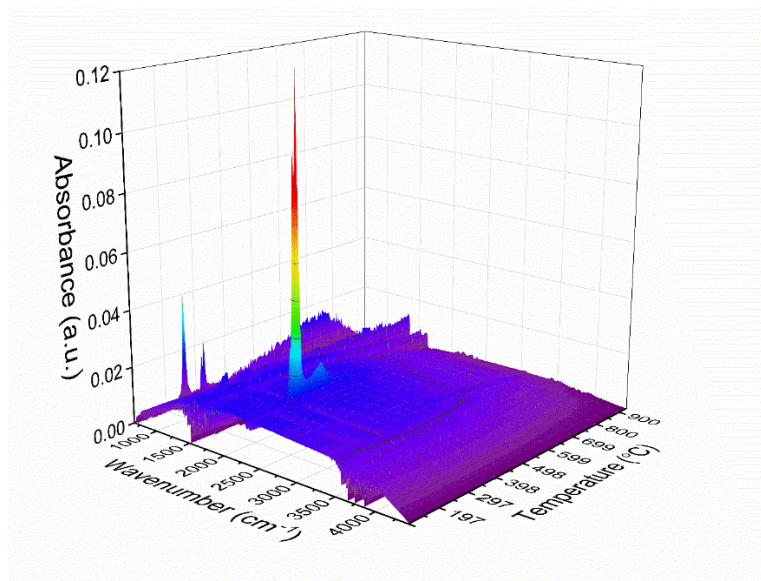
Figure 2-21 FTIR spectra from the evolved gases in the TGA-MS-FTIR experiment.

Note: without the calibration of carrier gas
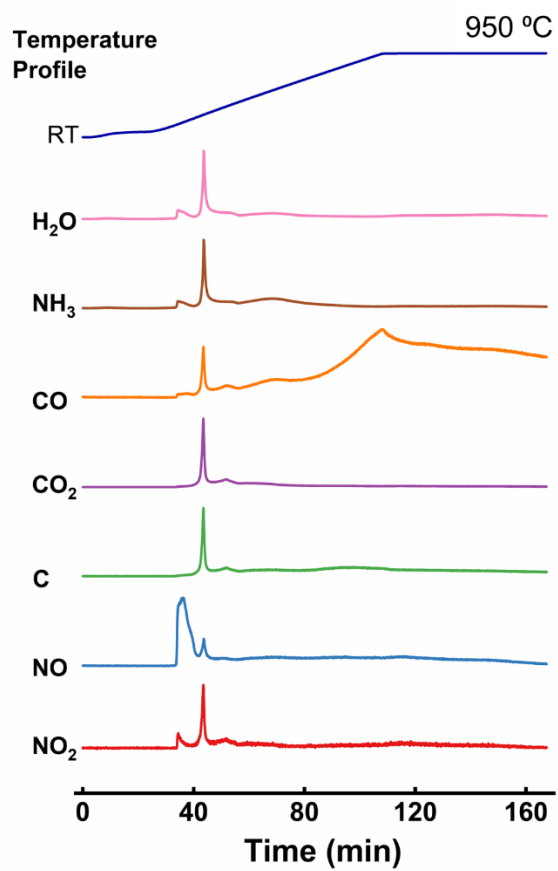
Figure 2-22 MS results from the evolved gases in the TGA-MS-FTIR experiment.

41
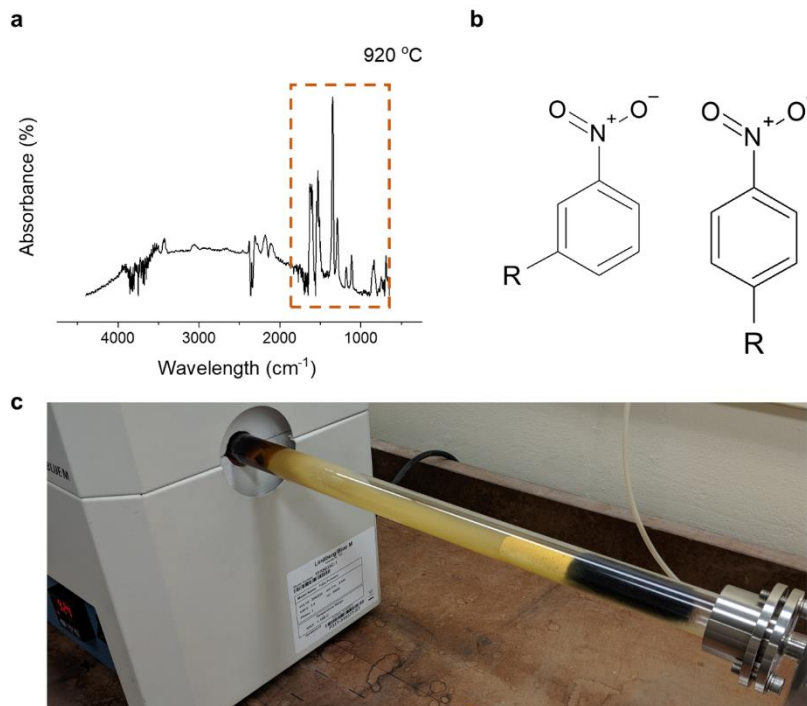
Figure 2-23 Abnormal infrared absorbance of the evolving gas when the TGA crucible was at high temperature.

(a) Selected FTIR spectrum of the evolving gas when the crucible reached 920 °C in the TGA-MS-FTIR experiment. (b) The chemical schemes of $C_6H_4NO_2R$ evolved at 920 °C. (c) The photograph of tube furnace during the pyrolysis of bulk precursor mixture at 924 °C (shown on the LED panel, left bottom). The yellow matter was distributed in the downstream of H2+N2 atmosphere, and absorbed by the porous alumina pellet at the end of quartz tube. The black fire-resistant wool fiber was put at the terminal for filtering
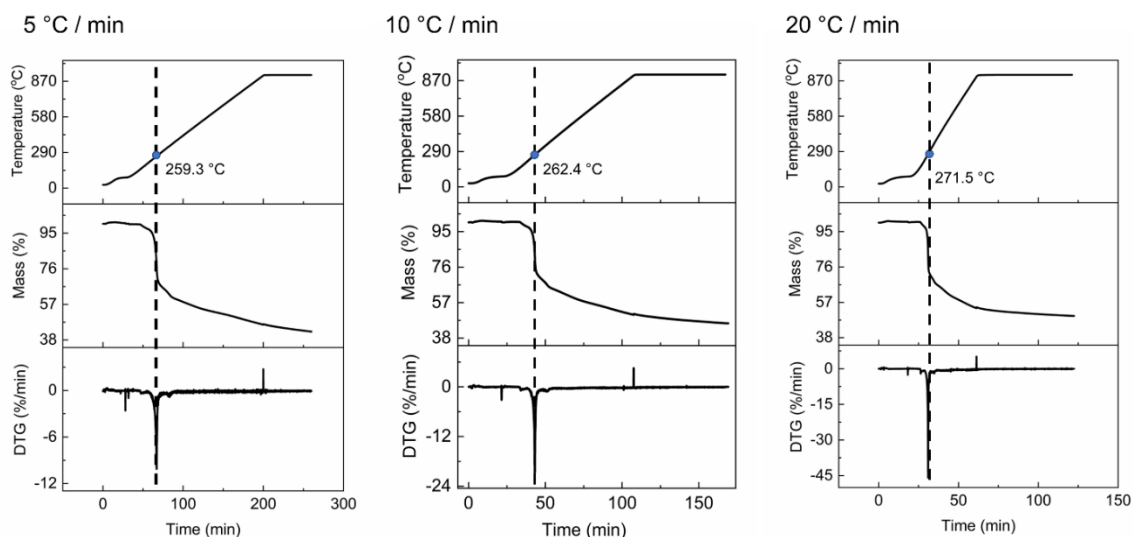
Figure 2-24 TGA results at different ramping rates under Ar environment.
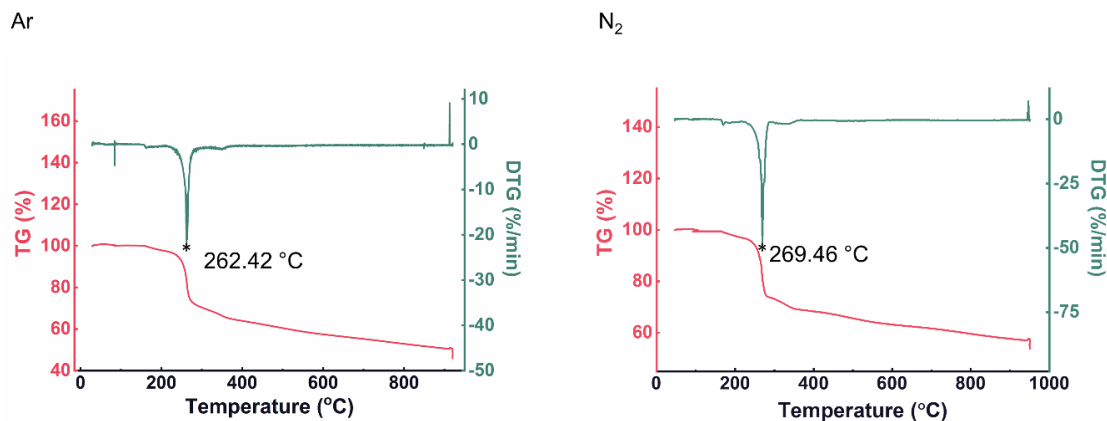
Figure 2-25 TGA results under Ar and N2 atmosphere.

2.4 Spectroscopic and Phase Transformation

In situ XRD experiment was introduced to monitor changes in the crystal structure during the pyrolysis with the rate of 10 ⁰C min^{-1} and under 5 % H$_2$ and 95 % Ar atmosphere, with the corresponding patterns above 650 ⁰C and back to room temperature shown in **Figure 2-26a**. The completed pattern data is provided as **Figure 2-27a**. All pristine narrow peaks disappeared when the temperature reached above ~260 °C, which is consistent with the aforementioned mixture melting phenomenon. The flat patterns from 260 °C to 650 °C suggest that the metal-abundant species observed in nano-CT (**Figure 2-9**) and STEM (**Figure 2-13**) are likely amorphous. Generally, four major peaks at $2\theta \approx 21^\circ$, 26.5°, 43.5°, 50° (Cu Kα, after correction from beamline x-ray energy) and one broad peak at the 2θ range of $18.7^\circ - 23.7^\circ$ appeared above 650 ⁰C. The latter one corresponds to the amorphous silica of the pristine material, as it is already present in the initial diffraction patterns (see **Figure 2-27a**) and, to some extent, has a potential contribution of amorphous carbon formed during the pyrolysis. The peak at $2\theta \approx 26.5$ ° appeared above 900 °C, with d-spacing of around 0.336 nm (calculated on Bragg's law), corresponds to the graphite (002) reflection (symbolized by "♦", JCPDS 41-1487). Graphite was also observed in the *in situ* TEM experiment under ultra-high vacuum when the temperature reached 950 °C, which lattice spacing

was around 0.339 nm (**Figure 2-26d**), showing good consistency between XRD and TEM data. At 849 °C and above, the peaks at 2θ ≈ 43.5° and 50° appeared, indicating the possible formation of iron carbide (symbolized by "♠", JCPDS 35-0772)[68] or complicated Fe alloy (see **Figure 2-27b**). Several publications reported that metallic Fe, FeC alloy and FeSi alloy with body-center cubic structure could both show the reflections of (110) at ~43.5° and (200) at ~67° (JCPDS 71-4409) [69,70]. Theoretical[71] and experimental[72] works also reveal that metallic Fe and Fe alloy with face-center cubic structure could have (111) at 43°-45° and (200) at 51°-53°. It is worth noticing that the formation of graphite and Fe / FeC alloy probably correspond to each other, *i.e.* the catalytic graphitization by Fe at high temperature, which was observed by numerous studies (*e.g.* iron nitrate with microcrystalline cellulose[73], iron films with carbon nanofibers via physical vapor deposition[74], ferrocene with maleic acid[75]). Considering the complicated reducing environment during pyrolysis and relative low concentration of iron, it is difficult to conclude whether metallic iron or iron carbide dominate.

Ex situ XPS was performed on the precursor samples pyrolyzed at 435 °C, 870 °C and 1180 °C, as well as the 1180 °C sample after Ar-etching (fitted results shown in **Figure 2-26b-c** and Error! Reference source not found., curve-fitted high-resolution spectra plots shown in **Figure 2-23**, **Figure 2-24**, and **Figure 2-25**). Argon etching technique was performed on 1180 °C sample to assess the Fe presence as it was not detected on the initial surface. As the survey spectra results showed in **Figure 2-26b** (the completed numerical data shown in Error! Reference source not found.), the surface chemistry changes mainly occurred at the pyrolysis process from room temperature to 435 °C, concomitant with the melting progress observed by the TGA, nano-CT and STEM (**Figure 2-20**). The atomic concentration of C 1s and N 1s increased from 27.3 % to 60.8 % and from 3.8 % to 10.4 %, while O 1s and Si 2p decreased from 42.7 % to 18.8 % and from

26.0 % to 9.8 % respectively. The decreased concentrations of O 1s and Si 2p revealed that after the melting of mixture (i) the oxide species evaporated or were reduced, and (ii) silica nanospheres were covered by organic byproducts, which is consistent with the STEM images shown in **Figure 2-14**. The surface atomic concentration of Fe 2p 3/2 kept around 0.2 % for all samples except 1180 °C, whose Fe concentration dropped to zero. After the Ar-etching on the sample pyrolyzed to 1180 °C, the atomic concentration of Fe 2p increased back to 0.23 %, while Si 2p and O 1s became 23.2 % and 23.4 %, respectively. The disappearance of Fe on the surface of the 1180 °C sample is consistent with the phenomena observed by STEM-EDS as shown in **Figure 2-17**, **Figure 2-18**, and **Figure 2-19**, *i.e.* that iron atoms agglomerated inside the carbon matrix. The curve fitting plots of high resolution Fe 2p spectra shown in **Figure 2-28** (fitting results are shown in **Figure 2-26c**) further revealed that no metallic Fe existed on the surface of the 435 °C and 870 °C samples, and the relative atomic concentration of Fe^{2+} and Fe^{3+} in both samples can be considered the same (slight drop when temperature increased), thus inferring that iron-based nanoparticles observed in the previous sections (i.e. **Figure 2-9** and **Figure 2-13**) are likely iron oxides, which was also suggested by the Li *et al.* using *in situ* XAS[31]. After etching the 1180 °C sample by Ar ions, metallic Fe and Fe^{2+} were found, whose relative atomic concentration increased from 0 % to 28.1 % and from 59.4 % to 71.9 % respectively, compared to the 870 °C sample. No Fe^{3+} was observed after Ar etching. This indicates the reduction of iron occurred above 870 °C, consistent with the appearance of Fe alloy / iron carbide in XRD patterns above 850 °C, as shown in **Figure 2-26a** and **Figure 2-27**. Since Fe and Fe^{2+} were found beneath the sample surface pyrolyzed at 1180 °C, and the relative concentration of graphitic C (fitted from high resolution C 1s spectra, as shown in **Figure 2-29**) is found to increase from 36.0 % to 41.0 % when the temperature is elevated from

870 °C to 1180 °C, it can be implied that the iron nanoparticles catalyzed the graphitization, which is consistent with the phenomenon discovered in the STEM experiment, as **Figure 2-26d** shows.

The high-resolution C 1s and N 1s XPS spectra with curve fitting are shown in **Figure 2-29** and **Figure 2-30**, respectively. The typical carbon framework was found in the 870 °C and 1180 °C samples, while the strong signal between 281 eV to 284 eV indicates that there are still numerous organic compounds and partially decomposed organic byproducts within the sample pyrolyzed at 435 °C. For instance, the C 1s signal of adsorbed ethylene was found to be located around 282.7 eV[76], and it cannot be easily distinguished with CO due to the same molecular mass. The increase of temperature also resulted in the decrease of absolute atomic concentration of O 1s. When the temperature was elevated to 1180 °C, the sp^3 carbon signal at around 285.3 eV was detected on the surface with a relative atomic concentration of 27.0 % and became stronger (33.1 %) inside the surface (*i.e.* after Ar-etching).

Figure 2-30 shows the change of N 1s during the pyrolysis. The relative atomic concentration of N-H (pyrrolic N, as well as hydrogenated pyridinic N[24]) remained ~30 % from 870 °C to 1180 °C. However, most of the N-H was located at the surface and the relative atomic concentration dropped to around 17.8 % when the sample surface was etched by argon. As for the nitrogen coordinated to the iron (Fe-N$_2$, Fe-N$_3$ and Fe-N$_4$ all locate around 399 to 400 eV[24]) or metal-free amine N, the relative atomic concentration fell from 16.9 % to 11.2 % as the temperature raised from 435 °C to 1180 °C. After etching the sample, the number goes back to 33.1 %, implying the sink of the iron moieties into the carbon framework, consistent with Fe 2p shown in **Figure 2-28**. For the spectrum of 435 °C sample, strong signals from 395 eV to 397 eV were detected. Similar to the low binding energy area in C 1s, they probably come from imine structure (C=N) of the nicarbazin as well as partially decomposed organic byproducts. According to the previous study[23] for M-N-C

46

electrocatalyst, in addition to the M-N$_x$ active sites that can undergo either 2e$^-$ or 4e$^-$ pathways for oxygen reduction reaction, N-H could partially reduce oxygen molecule into peroxide while pyridinic N further reduce peroxide to water. Besides, graphitic N performs an important role in proton transfer, essential for ORR. For rational design of a promising M-N-C material, it is essential to reach a balance for these multitudinous nitrogen moieties to achieve better electrochemical performance. The N 1s spectra at 870 °C and 1180 °C fulfilled this target.
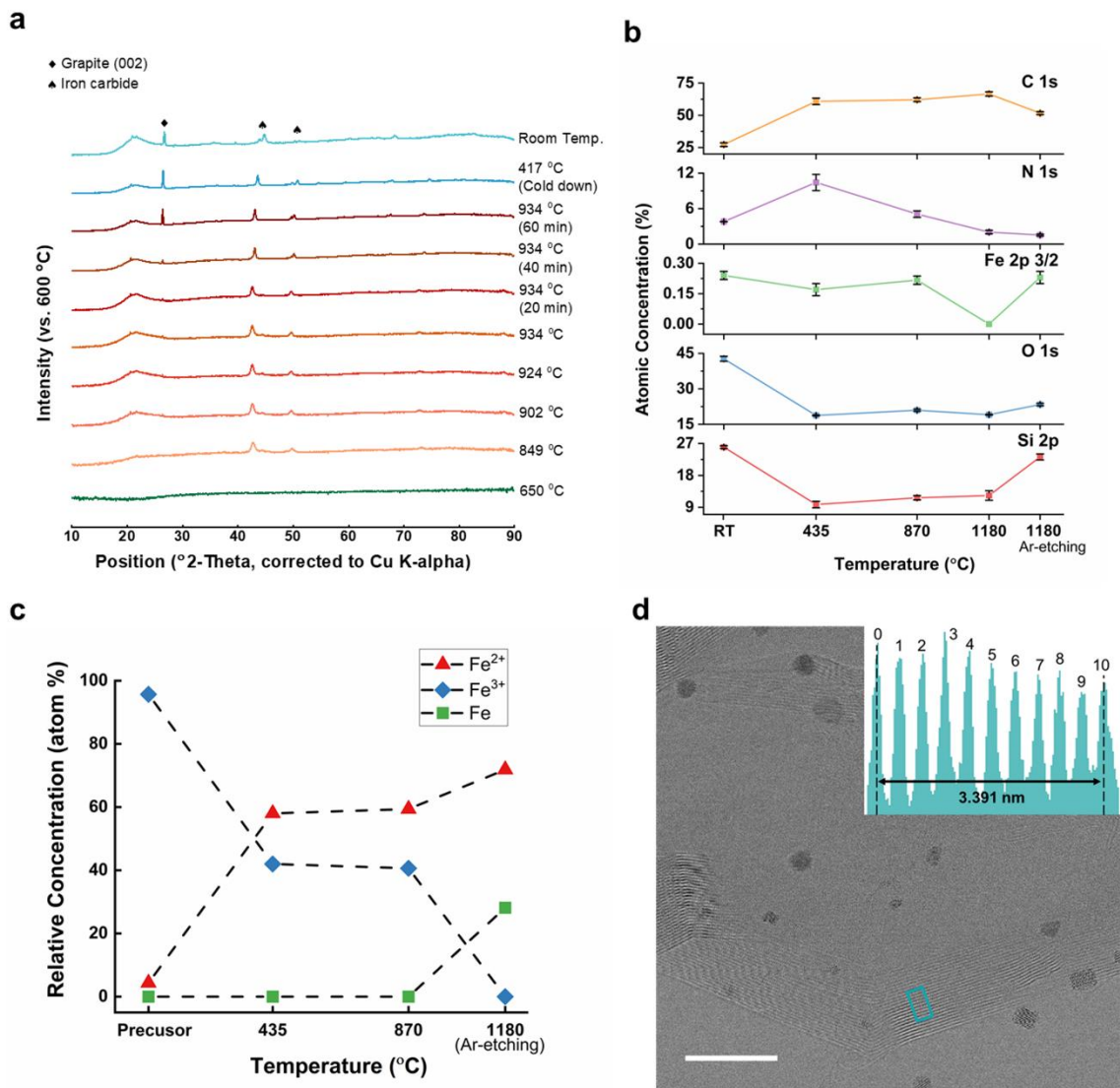
Figure 2-26 Spectroscopic material characterization during pyrolysis.

(a) Selected XRD patterns recorded at selected temperatures beyond 600 °C. All patterns in the figure subtracted the pattern recorded at 600 °C. (b) Atomic concentration of C 1s, N 1s, Fe 2p 3/2, O 1s and Si 2p from XPS. (c) Relative atomic concentration of Fe species in the sample pyrolyzed at 435 °C, 870 °C and 1180 °C (after Ar-etching) from curve-fitted Fe 2p 3/2 spectra. (d) BF-STEM image of graphite at room temperature cold down from 1180 °C in *in situ* STEM experiment and intensity profile of selected area. Scale bar: 10 nm.
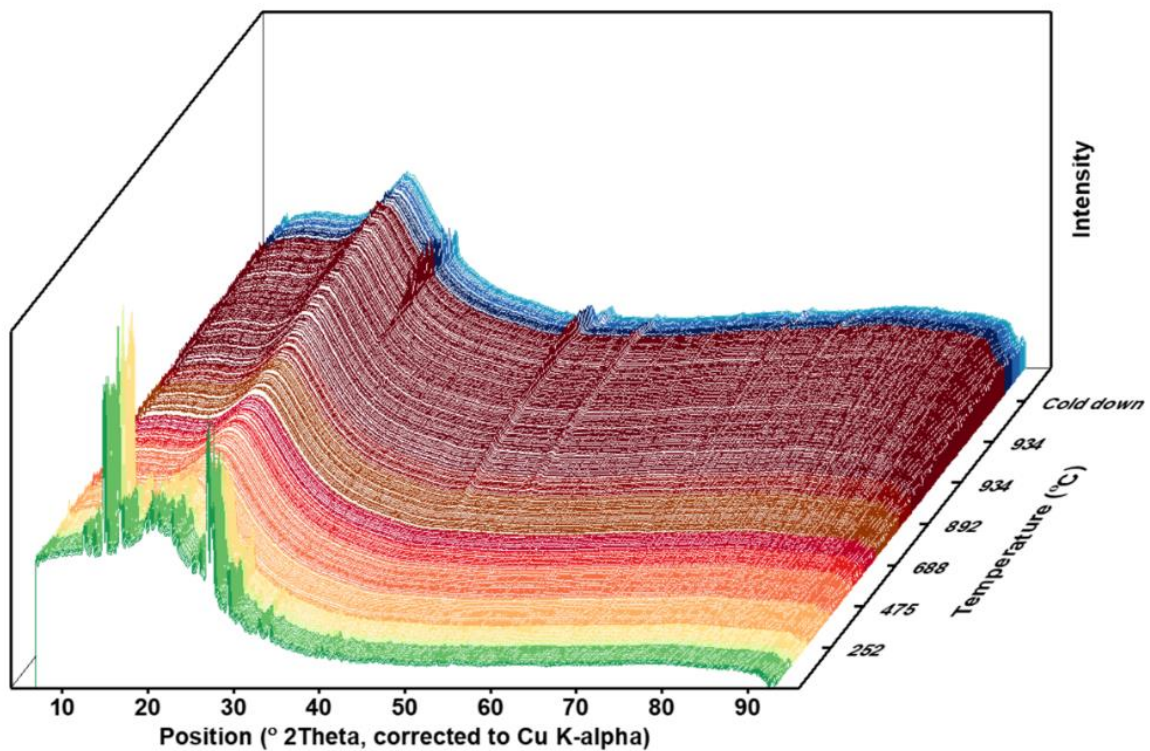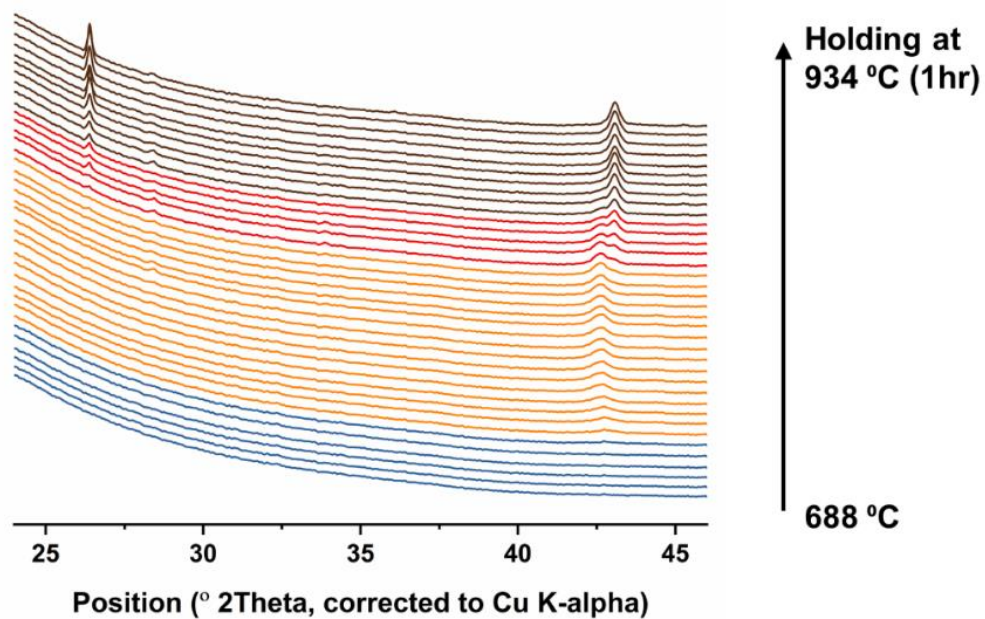
Figure 2-27 XRD results from in-situ XRD experiment under 5% H_2 and 95% Ar.

(a) Completed XRD results. (b)Selective spectra from 688 ⁰C to 934 ⁰C (after holding for an hour), showing the Fe/FeC formation.

Table 2-2 XPS survey results for the precursor and samples pyrolyzed at different temperatures.

	O 1s	C 1s	N 1s	Si 2p	Fe 2p 3/2
Precursor	42.7% ($\pm$1.05%)	27.3% ($\pm$1.38%)	3.8% ($\pm$0.03%)	26.0% ($\pm$0.37%)	0.24% ($\pm$0.02%)
435	18.8% ($\pm$0.20%)	60.8% ($\pm$2.48%)	10.4% ($\pm$1.37%)	9.8% ($\pm$0.91%)	0.17% ($\pm$0.03%)
870	21.0% ($\pm$0.40%)	62.1% ($\pm$1.39%)	5.1% ($\pm$0.55%)	11.7% ($\pm$0.59%)	0.22% ($\pm$0.02%)
1180	19.1% ($\pm$0.15%)	66.6% ($\pm$1.63%)	2.0% ($\pm$0.28%)	12.3% ($\pm$1.34%)	0
1180 Ar-etching	23.4% ($\pm$0.48%)	51.7% ($\pm$1.06%)	1.5% ($\pm$0.15%)	23.2% ($\pm$0.84%)	0.23% ($\pm$0.03%)
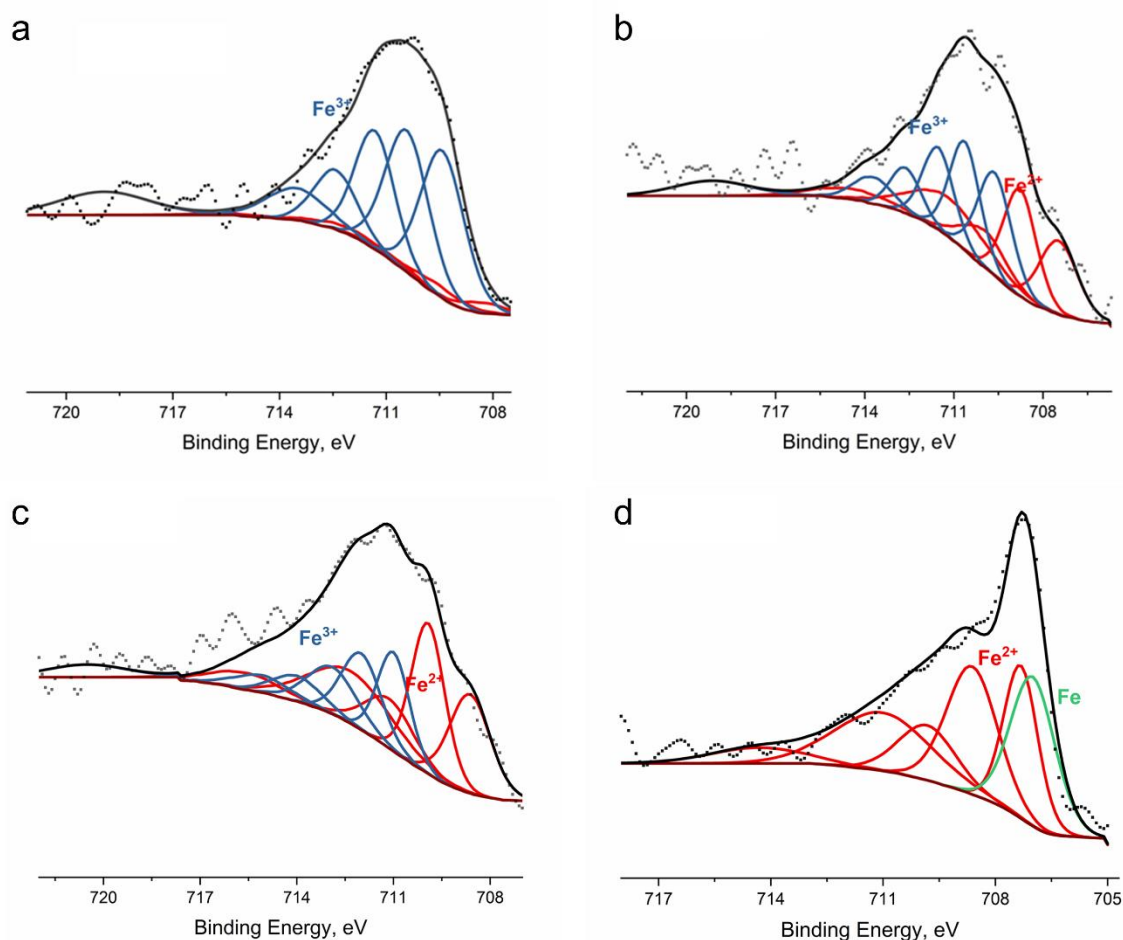
Figure 2-28 XPS Fe 2p 3/2 spectra of the precursor and samples pyrolyzed at different temperatures.

(a) Fe 2p 3/2 spectra for the precursor, (b) the sample pyrolyzed at 435 ºC, (c) the sample pyrolyzed at 870 ºC, and (d) the sample pyrolyzed at 1180 ºC after Ar-etching.

Figure 2-29 XPS C 1s spectra of the precursor and samples pyrolyzed at different temperatures.

(a) the precursor, (b) the sample pyrolyzed at 435 ⁰C, (c) the sample pyrolyzed at 870 ⁰C, (d) the sample pyrolyzed at 1180 ⁰C, (e) the sample pyrolyzed at 1180 ⁰C after Ar-etching, and (f) the relative atomic concentration of different C 1s species.
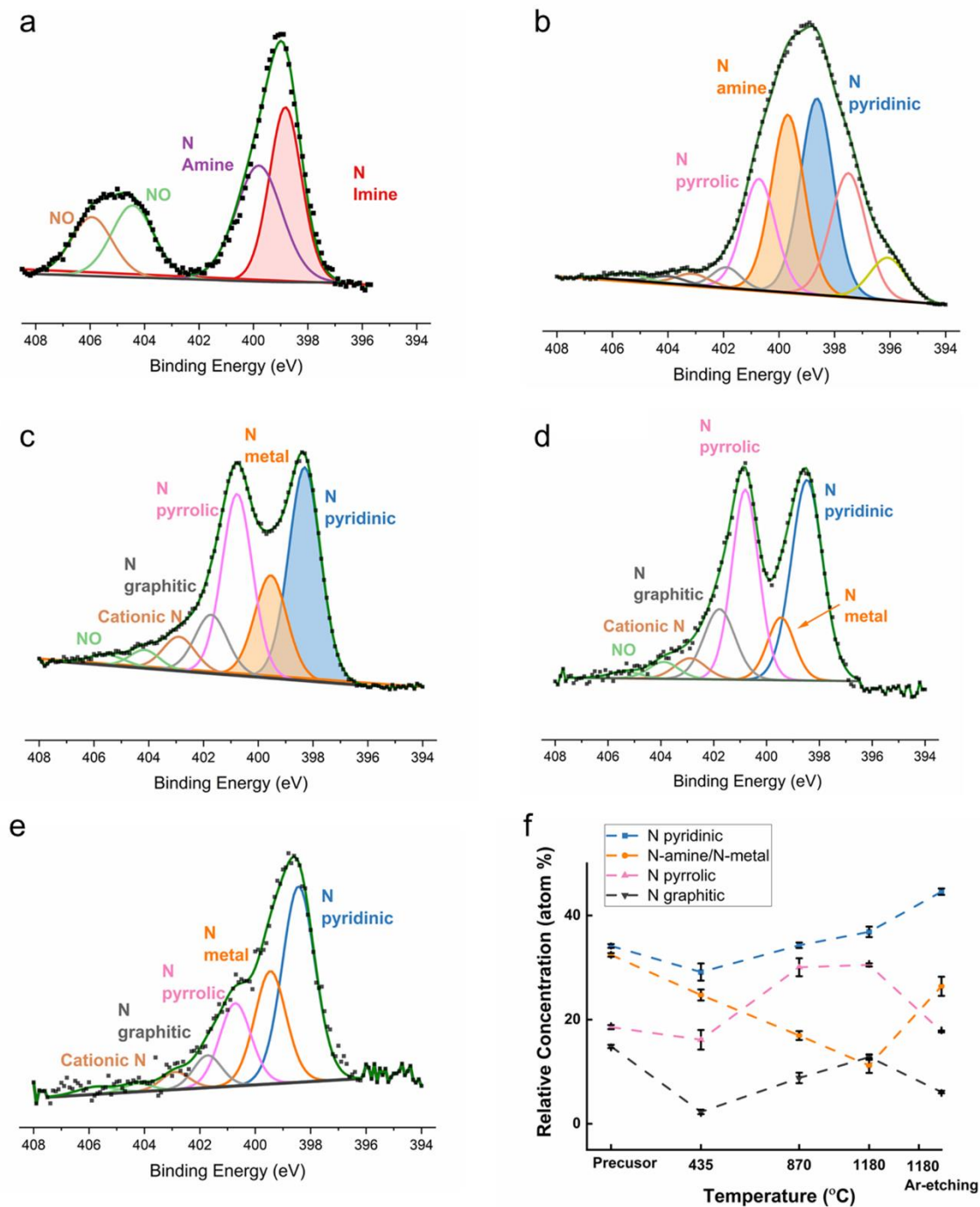
Figure 2-30 XPS N 1s spectra of the precursor and samples pyrolyzed at different temperatures.

(a) the precursor, (b) the sample pyrolyzed at 435 °C, (c) the sample pyrolyzed at 870 °C, (d) the sample pyrolyzed at 1180 °C, (e) the sample pyrolyzed at 1180 °C after Ar-etching, and (f) the relative atomic concentration of different N 1s species.

To learn more about the carbon transformation, *ex situ* Raman spectra were performed on the

samples pyrolyzed at 435 °C, 870 °C and 1100 °C (after HF acid etching and the sequential

purification) The curve-fitting of Raman spectra is shown in **Figure 2-31**, with the corresponding fitted results in Table 2-3. The corresponding *ex situ* STEM micrographs can be found in **Figure 2-32**, **Figure 2-33**, and **Figure 2-34**. The lower temperature (1100 °C vs. 1180 °C in other characterizations) arises from the limitation of the tubular furnace used in this manuscript for bulk sample preparation. Five bands for carbonaceous material was utilized for the curve fitting (G, D1, D2, D3, and D4)[77,78], where the G-band (1580 cm^{-1}) is characteristic of graphitic carbon and the D-bands (D1-D4) are the first-order bands corresponding to the disordered crystal structure or structural defects in the carbon planes. As **Figure 2-31d** shows, the signal for the sample pyrolyzed at 435 °C is dominated by the D1 and D3 peaks, indicating that the formation of carbon structure was not completed yet at this temperature. When comparing the spectra of the samples synthesized at 870 °C and 1100 °C, it can be found the lower temperature derived sample has an obvious right shoulder which can be attributed to the disordered D2-band. The ratio of integrated intensity of D1-band and G-band is calculated to be 2.97 for 870 °C and 1.93 for 1180 °C respectively. This large increase of graphitic carbon at higher temperature is in agreement with the high-resolution C 1s XPS data (**Figure 2-29**) and the discovery of the ordered graphite lattice under 1180 °C in STEM experiment (**Figure 2-26d**). Furthermore, it corroborates with nano-CT data, where external shell is observed that is most likely of graphitic content. The D1/G ratio is higher than 1 even when the sample was pyrolyzed to 1100 °C. This imply that the carbon structure remains highly defective, due to the presence of N, Fe-containing moieties and micropores induced by the breaking of silica (**Figure 2-14** - **Figure 2-15**).
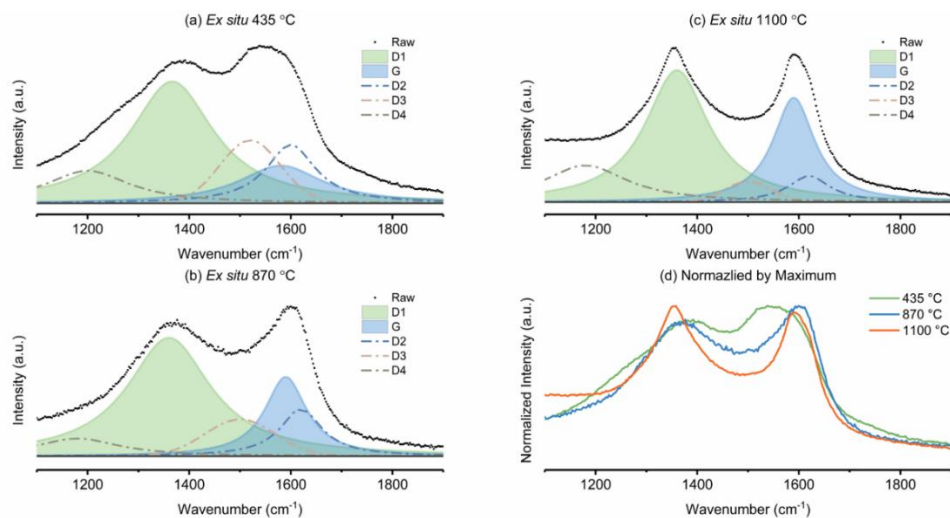
Figure 2-31 Raman spectra of the samples pyrolyzed at different temperatures and etched by HF.

(a) the sample pyrolyzed at 435 ºC, (b) the sample pyrolyzed at 870 °C, (c) the sample pyrolyzed at 1100 °C, and (d) normalized spectra with maximum set to 1.

Table 2-3 Raman fitted results for the samples pyrolyzed at different temperatures and etched by HF.

	D1	D2	D3	D4	G
435 °C	47.48% (±3.54%)	13.46% (±5.63%)	11.64% (±7.05%)	12.67 (±2.49%)	14.75% (±7.76%)
870 °C	53.82% (±3.01%)	10.75% (±1.87%)	9.22% (±1.94%)	8.07% (±1.88%)	18.14% (±1.80%)
1100 °C	47.97% (±3.27%)	6.21% (±2.17%)	3.61% (±1.40%)	17.43% (±2.64%)	24.85% (±1.66%)
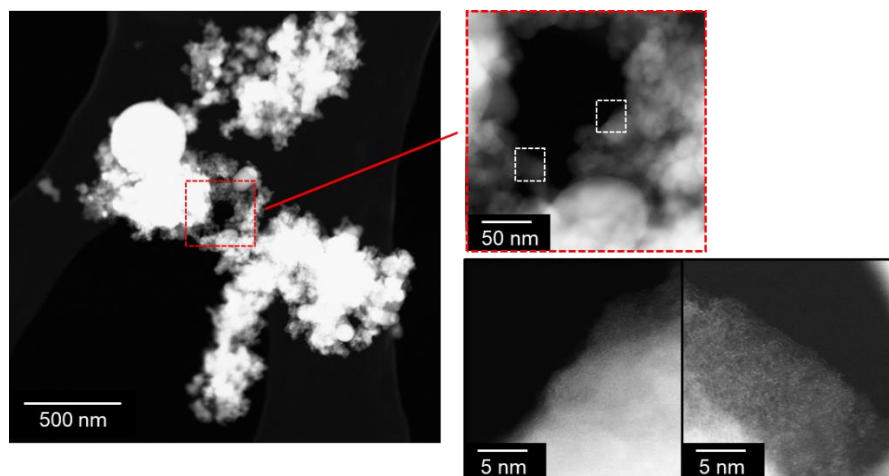
Figure 2-32 Scanning Transmission Electron Micrographs for the sample pyrolyzed at 435°C and subsequently etched by HF.

Note: The presence of silica nanospheres is still observed, despite the etching
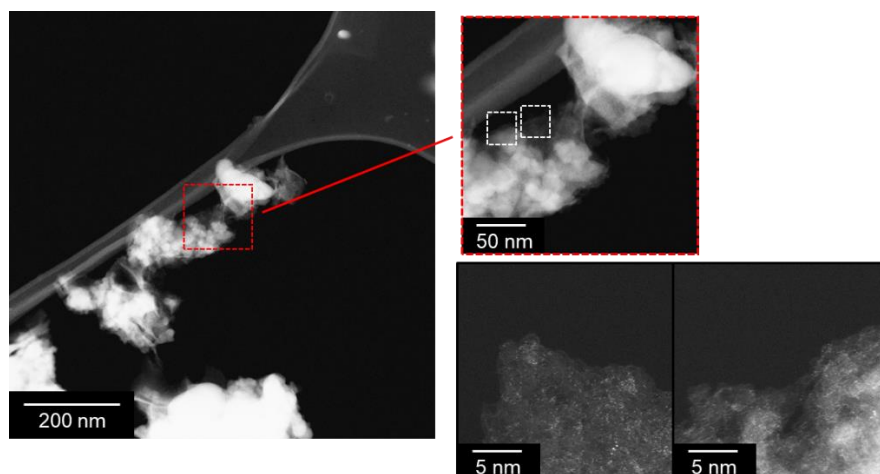
Figure 2-33 Scanning Transmission Electron Micrographs for the sample pyrolyzed at 870°C and subsequently etched by HF.
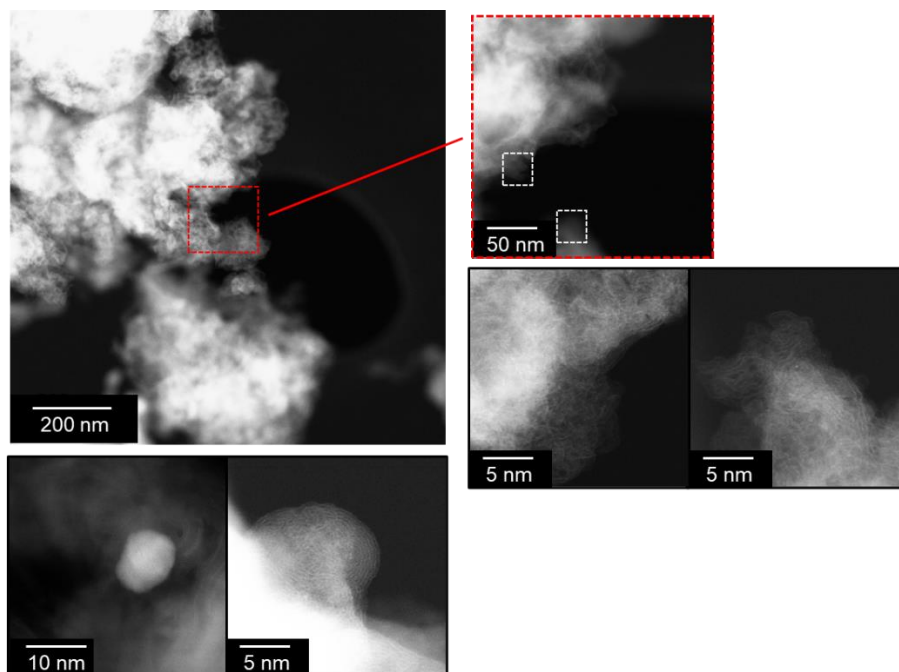
Figure 2-34 Scanning Transmission Electron Micrographs for the sample pyrolyzed at 1100°C and subsequently etched by HF.

2.5 Electrochemical performance

The electrochemical activity of the samples pyrolyzed at 435 °C, 870 °C and 1100 °C (after HF etching to remove silica and the sequential purification, as the same ones used for Raman spectroscopy) was assessed with a rotating ring disk electrode setup (**Figure 2-35** - **Figure 2-36**). The sample pyrolyzed at 435 °C shows negligible capacitance (**Figure 2-36**) with maximum current density in O_2-saturated electrolyte below 30 μA cm^{-1}_{geo}, indicating that both the carbon substrate and the active sites had not formed then. When comparing the electrochemical features of the samples pyrolyzed at 870 °C and 1100 °C, it appears that the higher temperature resulted in decreased performance, due to: (i) the capacitance decreased, which can be attributed to the increased concentration of graphitic C, and a lower surface area; (ii) the formation of inactive metallic iron and iron carbide nanoparticles embedded in the carbon structure (as shown in **Figure 2-19**, which would have been etched during the acid treatment and not exist in the final catalyst),

led to the decrease in the density of iron-containing moieties (as shown in **Figure 2-34**) and a decrease of the half-wave potential about 100 mV. (iii) the aforementioned decrease in the Fe-Nx active site density resulted in insufficient number of active sites able to reduce the peroxide formed by other moieties, such as hydrogenated pyridinic nitrogen, as shown in high-resolution N 1s spectra (**Figure 2-30**), leading to an increased peroxide generation. The electrochemical performance clearly underlined the critical role played by the pyrolysis temperature in the design of an optimal M-N-C electrocatalysts for the oxygen reduction reaction.
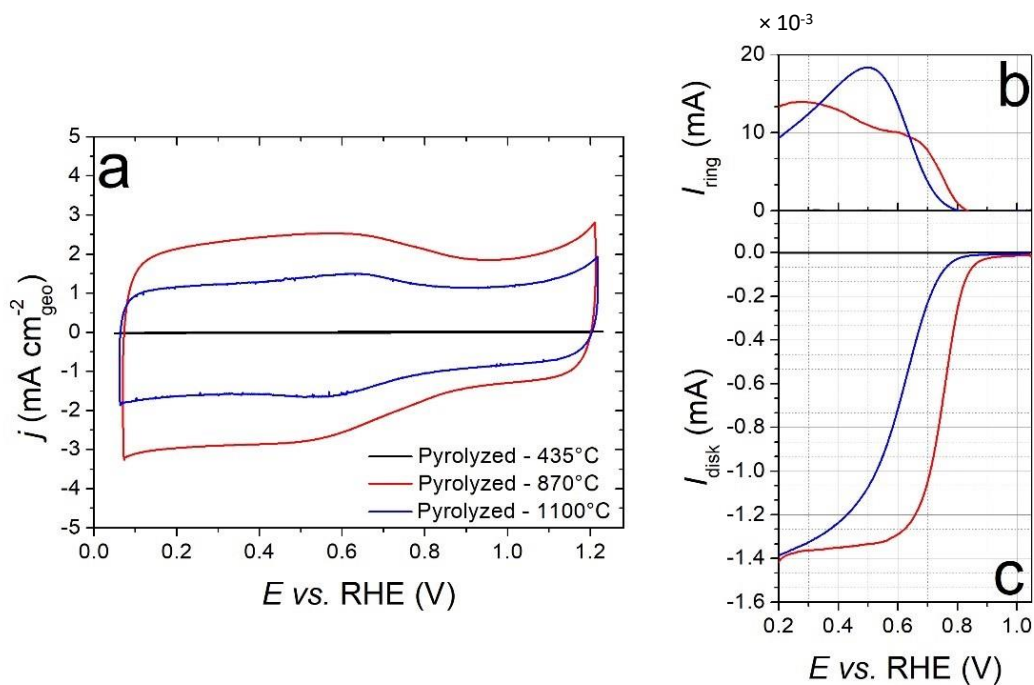
Figure 2-35 Electrochemistry data for the sample pyrolyzed at different temperatures and etched by HF.

The electrolyte is O_2-saturated 0.1 M $HClO_4$. (a) cyclic voltammetry in N_2-saturated electrolyte and a scan rate of 20 mV s^{-1}, (b) ring current density and (c) disk current density in O_2-saturated electrolyte, 1600 rpm and 5 mV s^{-1} scanning rate. The sample loading on the electrode was of 800 μg cm^{-2}$_{geo}$ and the electrode surface was of 0.247 cm[2].
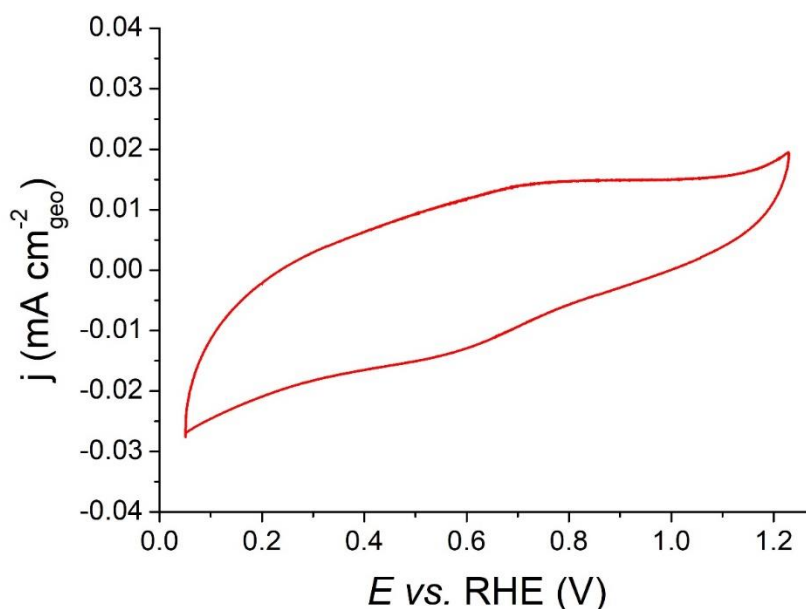
Figure 2-36 Zoomed CV data for the sample pyrolyzed at 435 °C and etched by HF.

2.6 Summary

This work probes the morphological and chemical transformation during the pyrolysis of M-N-C catalysts via a combination of *in situ* synchrotron and lab-based diagnostic techniques from room temperature to 1180 °C. Fe-N-C was synthesized with sacrificial support method using nicarbazin as an organic precursor. Three transformation stages were observed: the melting/decomposition stage below 435 °C, the carbon framework formation stage from 435 °C to 870 °C, and the reduction/graphitization stage above 870 °C. In the melting/decomposition stage, the nitrogen-carbon precursor nicarbazin melted and decomposed, redistributing Fe precursor within the material and increasing the porosity of the precursor. In the carbon framework forming stage, the amorphous carbon was synthesized, whereas the metal-abundant nanoclusters became distributed uniformly, alongside the formation of atomically dispersed Fe-containing moieties. During the reduction/graphitization stage, the internal amorphous phase of the particles gradually disappeared with the graphitized shells left, which was catalyzed by iron, resulting in metal nanocluster and

carbide nanoparticle formation. When the temperature further increased to 1200 °C, the graphitization gradually dominated, leading to more agglomeration of metallic iron / iron carbide, and less M-N$_x$ active sites. As such, the highest ORR activity was observed for the electrocatalyst pyrolyzed at 870 °C: too low pyrolysis temperature resulted in semi-synthesized carbon structure, while too high pyrolysis temperature led to severe Fe particles agglomeration and worse electrochemical performance.

In conclusion, the rational design of M-N-C electrocatalysts requires fundamental research for each specifically selected combination of metal, nitrogen and carbon precursors to identify their unique three pyrolysis stages. The corresponding pyrolysis parameters need to be meticulously chosen to optimize the micrometer-scale pathway formation at melting/decomposition stage, the carbon framework and Fe, N-containing moieties formation at the 2nd stage, as well as the balance for catalyzed graphitization and metal agglomeration when pursuing higher temperature.

Chapter 3

Re-pyrolysis of Transition Metal-Nitrogen-Carbon Materials Leading to State-of-the-Art Platinum Group Metal-free Electrocatalyst

3.1 Overview

The desire to have explicitly atomically dispersed M-N-C catalysts led scientists to attempt a second pyrolysis step. Dual pyrolysis or subsequent two-step pyrolysis methods have been briefly mentioned in previous publications[30,79-82], without additional explanation or specific attention. The "re-pyrolysis" unexpectedly resulted in a much greater positive impact on the overall catalyst performance, allowing the initial activity to be sustained, alleviating some of the degradation modes, and generally improving the durability.[43] Re-pyrolysis, as a materials synthesis method addition, is a way of substantially improving the performance of numerous M-N-C catalysts that performed "below expectations" after the first pyrolysis. This process is less sensitive to variables and can be easily scaled for industrial applications.

This chapter addresses the issues of re-pyrolysis in detail through a plethora of *in situ* techniques. Here, we report observational results as we directly monitor the continuous changes of the M-N-C catalyst during the re-pyrolysis process via several *in situ* heating spectroscopy/microscopy characterization methods: XPS, STEM, EDS, EELS, XRD and X-ray CT. The catalyst tested was a non-specific iron-nitrogen-carbon material that has been constantly researched and reported for several years, which allow for generalized results for revealing the function of the re-pyrolysis.

3.2 Methods

3.2.1 Materials Synthesis

The iron-metal-nitrogen catalysts were synthesized via Sacrificial Support Methods[36], using the recipe from the previous publication[83]. A calculated amount of silica, mixed homemade Stöber spheres, LM-150 and OX-50 (Cabot) (1 g, 2.5 g and 2.5 g respectively), were combined with 1.2 g of iron nitrate nonahydrate (Sigma-Aldrich) and 12.5 g of nicarbazin (Sigma-Aldrich) in water to form a viscous solution. After drying and ball-milling, the mixture was pyrolyzed at 975 ℃ under a 7% H_2-93% N_2 atmosphere. The materials were then etched by hydrofluoric acid (Sigma-Aldrich), washed until the pH reached neutral, dried and ball-milled in sequence to get the pyrolyzed Fe-N-C catalysts. The pyrolyzed Fe-N-C catalysts were then re-pyrolyzed at destinated temperatures (450 ℃, 750 ℃, and 950 ℃) under NH_3 for 1h.

The authors noticed that some particles appeared in the pyrolyzed product. It might be due to the inaccurate temperature setting. The particles usually appear when the pyrolysis temperature is higher than 1000 ℃ with this precursor. With the accurate pyrolysis temperature, the metal in the product should be atomically dispersed.

3.2.2 Electrochemical Measurements

The electrochemical performances were measured by using a rotating ring disk electrode (RRDE) method. For the data in Figure 1, the catalyst inks with a concentration of 5 µg µL^{-1} were prepared by mixing 5 mg of Fe-N-C catalysts, 150 µL of 0.5 wt % Nafion solution (Ion Power) and 850 µL of 4:1 H_2O/Isopropanol (Sigma-Aldrich) under sonication. After dropping a calculated amount of the inks on an RRDE (Pine Research) with a glassy carbon disk of 0.2475 cm^2 area and a platinum ring of 0.1866 cm^2 area, a final electrode layer of 0.175 mg cm^{-2} loading

was derived, which is enough to cover the disk surface. Linear sweep voltammetry (LSV) was then performed by using this RRDE as the working electrode, a graphite rod as the counter electrode and a reversible hydrogen electrode (RHE) as the reference electrode, in 0.5 M H_2SO_4 (in house prepared, Sigma-Aldrich) acid media and 0.1 M KOH (in house prepared, BioXtra) alkaline media respectively. The corresponding LSV parameters were set as follows on a WaveNow potentiostat (Pine Research): rotation speed of 1600 rpm, scanning window of 1.1 V to 0 V *versus* RHE in both media for the disk electrode, the potential held at 1.1 V *versus* RHE for the ring electrode, scanning rate of 5 mV s^{-1}. For the data in Figure S20, the catalyst inks with a concentration of 5 µg µL^{-1} were prepared by mixing 5 mg of Fe-N-C catalysts, 15 µL of 5 wt. % Nafion solution Sigma-Aldrich) and 985 µL of 4:1 H_2O/Isopropanol (Sigma-Aldrich) under sonication. A final layer of 0.174 mg cm^{-2} loading was derived. The electrolyte is 0.1 M $HClO_4$, and the electrolyte resistance was measured prior to any experiments. The catalyst was activated in a N_2-saturated electrolyte through 100 cycles at 500 mV s^{-1} between 0.05 and 1.23 V *vs.* RHE, followed by 3 cycles at 20 mV s^{-1} and a linear sweep voltammetry between 0.05 and 1.05 V *vs.* RHE at 20 mV s^{-1} (as a baseline correction). Then, a linear sweep voltammetry between 0.05 and 1.05 V *vs.* RHE at 20 mV s^{-1} was measured at 900 r.p.m at O_2-saturated electrolyte. The data was corrected from the ohmic losses in solution and the baseline obtained in N_2-saturated electrolyte.

3.2.3 X-ray Photoelectron Spectroscopy Characterization

High resolution XPS was performed on a Kratos AXIS Supra spectrometer with a monochromatic Al Kα source. The catalyst was pressed on the surface of silica/alumina tape using tungsten carbide press die, held inside a molybdenum alloy frame and treated by an e-beam heater to reach a specific temperature under ultra-high vacuum. For *in situ* heating procedure, the sample was first heated to 750 ℃ from room temperature with a ramping rate of 10 ℃ min^{-1},

held at 150 ℃, 250 ℃, 350 ℃, 450 ℃, 550 ℃, 650 ℃ and 750 ℃ respectively for the

measurements of the survey (160 eV pass energy), C 1s and N 1s (20 eV pass energy) spectra. It

was then heated to 950 ℃ without the control of the ramping rate, followed by an immediate

natural cooling down to 150 ℃, and finally held at 150 ℃. Similar spectra measurements were

performed when the temperature reached 950 ℃ and was held at 150 ℃ respectively. For *in situ*

double heating procedure, the sample was heated from 150 ℃ to 750 ℃ with a ramping rate of

10 ℃ min^{-1}, heated from 750 ℃ to 950 ℃ without ramping control, naturally cooled down to

150 ℃ and held at 150 ℃ in sequence. Then it repeated the same procedure once and was finally

held at 150 ℃. The spectra measurements were only performed at three 150 ℃ points (initial,

first cooled and second cooled). Three independent measurements (*i.e.* a freshly prepared sample

for every experiment) were performed for each analysis without the assistance of a charge

neutralizer. CasaXPS software was utilized to analyze the data, using a 70% Gaussian / 30%

Lorentzian line shape for curve fitting and linear background for quantifying atomic composition

(Shirley background for Fe 2p). The corresponding peak position, range and full-width-at-half-

maximum parameters in high resolution C 1s and N 1s spectra were fitted according to the

previous publications[23,24,43,84,85].

3.2.4 Scanning Transmission Electron Microscopy Characterization

Aberration-corrected STEM was performed on a JEOL JEM-ARM300F microscope. High angle

annular dark field (HAADF) (Z-contrast) images were recorded using a convergence semi-angle

of 22 mrad, inner collection angle of 83 mrad and outer collection angle of 165 mrad

respectively. For *in situ* heating STEM, the sample was heated to each specific temperature for

imaging recording from room temperature to 950 ℃ and cooled down without ramping control

under ultra-high vacuum. Energy dispersive X-ray spectroscopy (EDS) maps were only recorded before and after heating.

STEM-EELS was performed on a Nion UltraSTEM 200 HERMES microscope with a high-energy resolution monochromated electron energy loss spectroscopy (EELS) system. The equipment was operated at the accelerating voltage of 60 kV. The sample was vacuum heated at 160 ℃ to get rid of the contamination before putting into the microscope. For imaging, the convergence semi-angle was 33 mrad with a beam current of ~100pA. For spectroscopy, the EELS dispersion and dwell time were 0.4 eV/channel and 0.2 s/pixel, respectively. The background subtraction process for core-loss EELS was carried out by fitting a power-law function in the commercial software package Digital Micrograph. All reported temperatures were calculated by the measured electrical resistance of the heater. For the *in situ* heating experiment under a vacuum environment, images were taken at the pristine state, 650 ℃, one area at 950 ℃, and the final state after cool down. EELS spectra were collected when the images were taken. The Protochips Fusion was used with the heating chip (E-FHDC, Protochips, Inc.). The threshold was done with the Image Processing Toolbox in Dragonfly 4.1.

3.2.5 X-ray diffraction (XRD)

XRD was performed on a Rigaku SmartLab X-ray diffractometer using a Cu Kα source, equipped with an Anton Paar air-cooling heating module. The catalyst was pressed on a silica/alumina tape, held on AlN basement and covered by a graphite dome. Nitrogen gas was filled inside the dome while air blows on the dome surface to cool it down. For in situ heating XRD, two samples were heated from room temperature to 950 ℃ and held at 150 ℃, 250 ℃, 350 ℃, 450 ℃, 550 ℃, 650 ℃, 750 ℃, 850 ℃, 950 ℃ for fast pattern measurements with 2θ

from 10º to 90º and high-resolution scanning with 2θ from 20º to 35º respectively. They were then naturally cooled down to 150 ℃ and held at this point for final measurements.

3.2.6 X-ray computed tomography (CT)

X-ray CT was performed at Beamline 8.3.2 at Advanced Light Source at Lawrence Berkeley National Laboratory. White radiation was used to yield a voxel resolution of 1.3 μm. The image acquisition was accomplished with a 50 μm LuAg scintillator, a 5x lens, and an sCMOS PCO Edge camera. The catalyst was mounted on the top of a ceramic holder, which is placed inside a quartz tube. The tube was installed onto a rotation stage and went through a furnace. The top of the holder with the catalyst was located inside the furnace. N_2 was purged inside the quartz tube and continued flowing at 100 standard cubic centimeters per minute during the whole scanning process. For each scan, 1313 images were collected with an exposure time of 100 ms per image while the sample was rotated through 180 degrees. For in situ heating X-ray CT, the sample was heated from room temperature to 950 ℃ with 10 ℃ per minute, and held at 150 ℃, 250 ℃, 350 ℃, 450 ℃, 550 ℃, 650 ℃, 750 ℃, 850 ℃, 950 ℃ for a scanning. Three scans were accomplished at the point of 950 ℃. The sample was then naturally cooled down to room temperature and held at this point for final measurement. The image stacks obtained from the first and last scans were segmented by Trainable Weka Segmentation, a machine learning analysis tool. A median filter was used to process the segmented result of the last scan images to decrease the impact of image noise. Dragonfly 4.1 was used to create the three-dimensional structures.

3.2.7 Nitrogen physisorption

Nitrogen physisorption was performed in a Micromeritics 3Flex Surface and Catalyst Analyzer. The samples were vacuumed for 7h before the measurement (vacuum at 90 ℃ for 1h and then at 200 ℃ for 6h). The surface area was calculated by the Barrett-Emmett-Teller (BET) method.

3.3 Performance comparison of Initial and Re-pyrolyzed Catalysts

The advantage of re-pyrolysis of M-N-C catalysts to the electrocatalytic performance has been partially studied and reported by our group previously[43]. By testing initial Fe-N-C catalysts and re-pyrolyzed Fe-N-C catalysts under NH_3 in both acid and alkaline media via linear sweep voltammetry on rotating ring disk electrode, it was found that the re-pyrolysis process under ammonia increased the diffusion current density and decreased the peroxide yield but did not change the half-wave potential. Improved performances in both media were expected to be as a result of the removal of surface oxides and residual iron nanoparticles and the formation of a beneficial chemical composition with a large amount of aliphatic and graphitic carbon and nitrogen, particularly in the iron coordinated environment and the pyridinic nitrogen. The previous study was done *ex situ,* where the chemistry of the material was characterized after each step of the synthesis, including the re-pyrolysis. In-situ chemical observation during the re-pyrolysis step avoids the contamination of air exposure to the surface chemistry. Here, a set of electrochemical RRDE data tested with freshly synthesized Fe-N-C catalysts via the same recipe is given in **Figure 3-1**, showing improvement with re-pyrolysis.
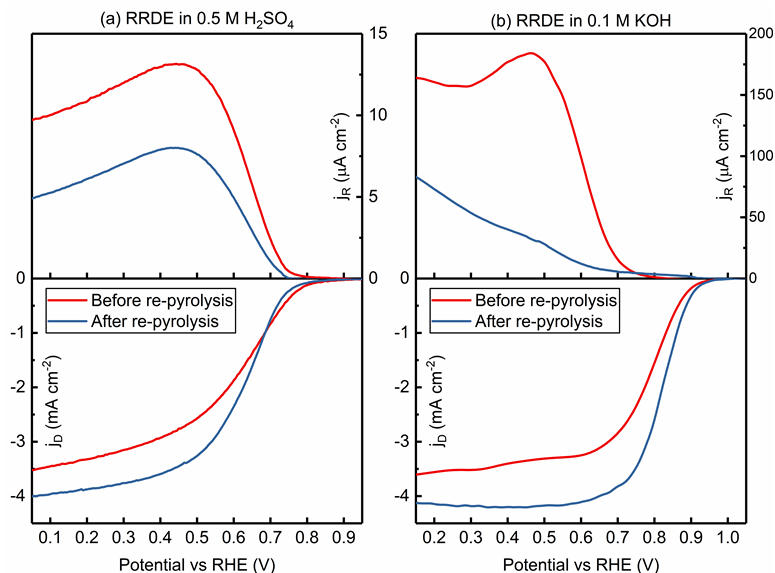
Figure 3-1 The polarization data of Fe-N-C materials before and after re-pyrolysis.

(a) in 0.5 M sulfuric acid and (b) in 0.1 M KOH. Both were tested on RRDE with 1600 rpm rotation speed and 5 mV s^{-1} scanning rate.

3.4 Transformation of Surface Chemistry during Re-pyrolysis

Figure 3-2 follows the changes in Fe-N-C chemistry by *in situ* XPS with heating under ultra-high vacuum conditions. A low energy survey spectra including the binding energy region captures all of the relevant XPS transitions - iron (Fe 2p around 710 eV), fluorine (F 1s around 686 eV), oxygen (O 1s around 532 eV), nitrogen (N 1s around 399 eV) and carbon (C 1s around 284 eV) - between 850 eV to 250 eV. F 1s peak originates from the use of hydrofluoric acid to etch silicon dioxide during synthesis. Some HF molecules may remain trapped in pores even after rigorous washing to a neutral pH and drying at low temperature (80 ℃ to 150 ℃ in conventional lab ovens). Comparing the results of the initial 150 ℃ and the final 150 ℃, it was found that, after heating, surface concentration of O 1s and F 1s decreased from 5.73 ± 0.15 % to 2.55 ± 0.18 % and from 0.62 ± 0.07 % to 0.09 ± 0.09 % respectively. Considering the minimum detection limit of XPS of 0.1 at%[86], it can be concluded that the fluorine disappears after heating. The decrease in the amount of oxygen may be due to the removal of pre-adsorbed molecules as

67

well as changes in the carbon chemistry. The latter was observed in the previous study where the amount of surface oxides decreased after re-pyrolysis[43]. The removal of pre-adsorbed species can be implied from the decrease in the intensity of the peak corresponding to the O 1s region (binding energy larger than 535 eV) as shown in **Figure 3-3k**, corresponding to physically adsorbed water[87] and carbon dioxide[88]. **Figure 3-2c** also indicates that the surface concentration of Fe did not change during re-pyrolysis, with the same initial and final atomic percentages of 0.33%. This suggests that iron distribution between the surface (sampling depth for Fe 2p is ~4.5 nm[89]) and deeper layers were not affected during the re-pyrolysis. This indicates that there was no noticeable transfer of iron between the material surface (calculated as ~4.5 nm, three times of inelastic mean free path[89]) or within. Because the surface "cleaning" occurs through desorption of adsorbed gas and removal of surface oxides, the C at% increased from 89.8 ± 0.3 % at room temperature to 93.9 ± 0.4 % after cooling down to 150 ℃ after re-pyrolysis. The change in the amount of nitrogen can be estimated from the surface concentration of N and N / C ratio. N amount was recorded at ~3.5 at% initially, then increased to a maximum of ~3.8 % during re-pyrolysis at around 550 ℃, and decreased to ~3.3% after the sample had cooled down to 150 ℃. N/C ratio reaches a maximum between 450-650 ℃. This observation will be further discussed in an interpretation of the chemistry of nitrogen from high-resolution N 1s spectra.
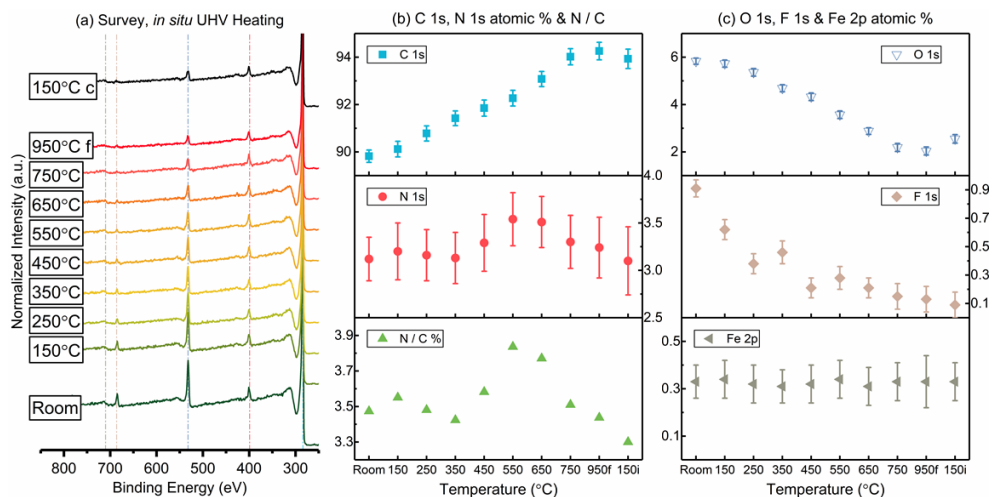
Figure 3-2 Survey XPS of Fe-N-C catalyst in situ heating in ultra-high vacuum condition.

(a) Survey spectra ranging from 850 eV to 250 eV. (b) Element composition results of C and N, in addition to the calculated ratio of N / C. (c) Element composition results of O, F and Fe. The term "950 ºC f" refers to "flash", unrestricted ramping rate from 750 ºC to 950 ºC without holding. The term "150 ºC c" refers to "cool", holding at 150 ºC for test after natural cooling. The 5 vertical lines in (a) refer to Fe 2p, F 1s, O 1s, N 1s and C 1s from left to right respectively.
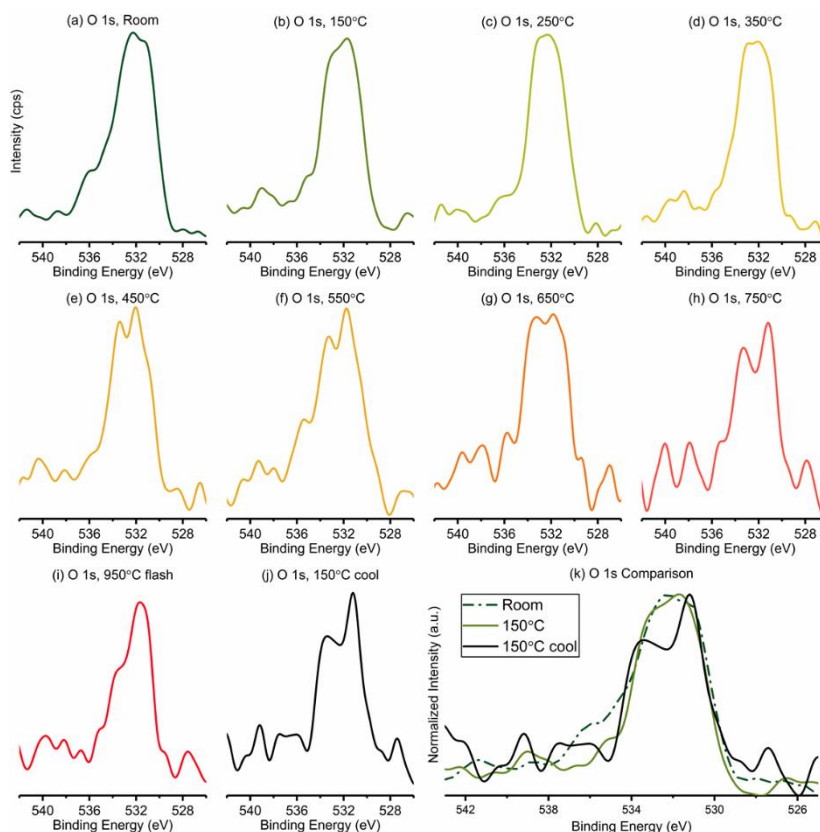
Figure 3-3 O 1s XPS at different temperature points after in situ re-pyrolysis.

(a) Room temperature; (b) 150 °C; (c) 250 °C; (d) 350 °C; (e) 450 °C; (f) 550 °C; (g) 650 °C; (h) 750 °C; (i) 950 °C flash; (j) 150 °C cool; (k) comparison among room temperature, 150 ºC and 150 ºC cool. All spectra were processed by FFT smoothing with cutoff frequency of 1 Hz from the raw data, due to the noise from short time data acquisition (around 3 minutes).

The changes in high-resolution C 1s during *in situ* UHV heating are shown in **Figure 3-4**, while all C 1s spectra curve fittings are shown in **Figure 3-6**. The atomic concentrations of each C chemical state are listed in **Figure 3-5**, based on the corrected calculation of total C atomic concentration at every temperature point. The zoomed-in lowest binding energy region of overlapped spectra in **Figure 3-6k** shows a continuous binding energy shift to higher values with increasing temperature. To compare spectra during heating and after cooling to the initial spectrum, the difference spectra were obtained by normalizing the spectra to the same area and subtracting the initial spectrum from the subsequent as shown in **Figure 3-4c**. From a comparison of the C 1s spectra at initial room temperature, 150 ℃ before re-pyrolysis, and 150 ℃ after cooling in **Figure 3-4c**, a positive 0.2 eV shift of maximum peak from 284.5 eV to 284.7 eV can be seen. This shift and the corresponding difference plot can be further divided into two binding energy regions of change in carbon chemistry. The first is the decrease of peaks around 284.5-284.7 eV and an accompanying increase in the peak around 285-285.5 eV. This change is due to the rearrangement of the carbonaceous framework, as the graphitic carbon[23,90] (*i.e.* sp^2 hybridization) signal at 284.5 eV decreased while the amorphous carbon[23,91] (*i.e.* sp^3 hybridization) signal at 284.8 eV or higher increased. Also, as **Figure 3-4e** shows, the total amount of sp^2 and sp^3 carbon did not change significantly during re-pyrolysis (~60.2 % and ~57.8 % for initial 150 ℃ and final 150 ℃, respectively). Hence, the re-pyrolysis process converted graphitic C (decrease from 39.4 ± 3.7 % to 14.7 ± 3.5 %) into the amorphous state (an increase from 21.0 ± 4.0 % to 43.1 ± 4.3 %), resulting in a more porous carbonaceous material structure. This facilitates the mass transport of ions and molecules during the reaction, due to increasing diffusion current density which was described in **Figure 3-2** previously. A minor effect is the slight increase of the intensity of C 1s of the region within 286 eV binding energy,

the position where C-N contributes, from 13.9 ± 1.3 % for the initial150 ℃ sampling to 14.9 ±

2.0 % for the final 150 ℃ sampling. From changes in the amount of elemental oxygen, we have

speculated that during re-pyrolysis, surface carbon oxides were being removed from the surface.

Concomitantly, the amount of carbon-oxygen species does not change, as **Figure 3-4f** shows.
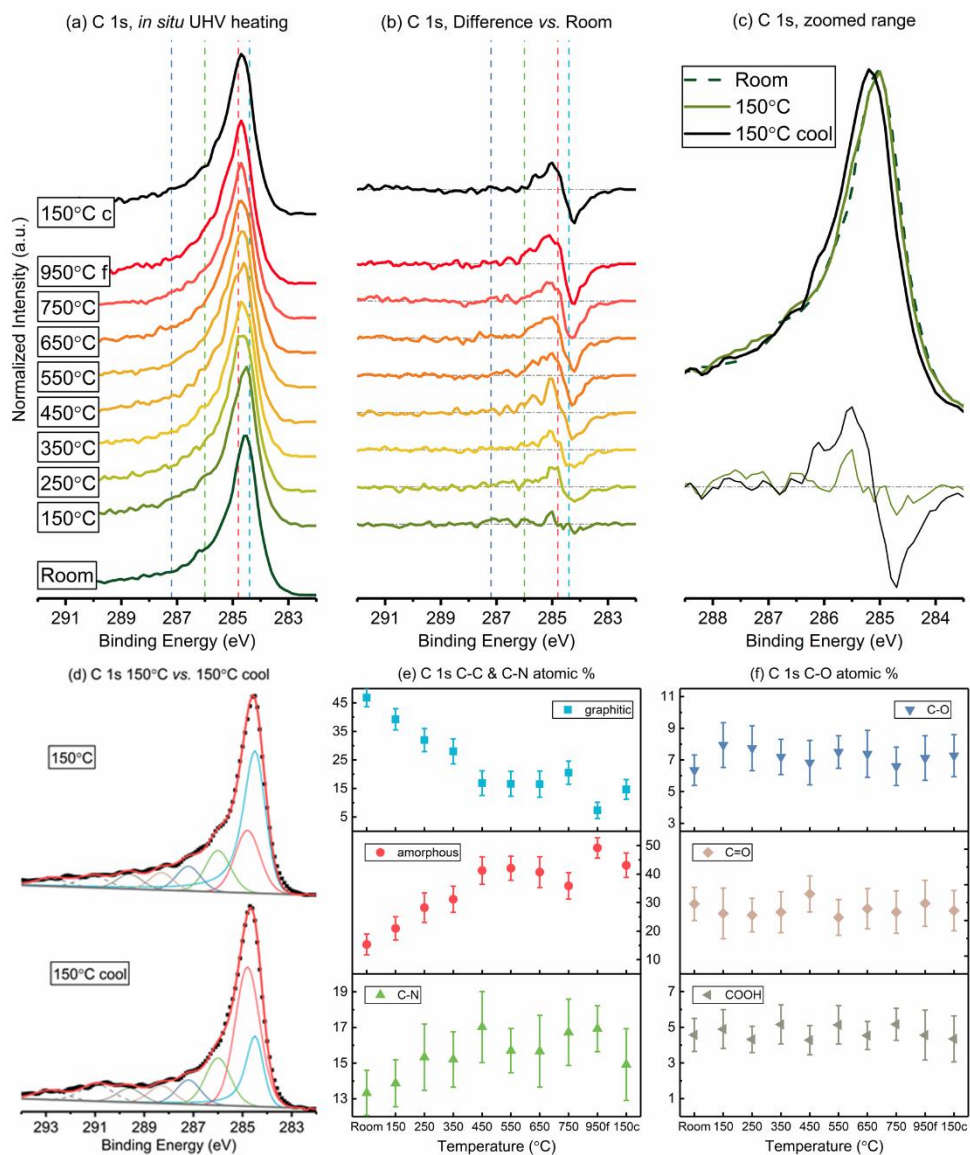
Figure 3-4 C 1s XPS of in situ UHV heating Fe-N-C catalyst.

(a) C 1s spectra measured while holding at every 100 ℃. (b) Difference plots of spectra *versus* the one measured at room temperature (c) C 1s spectra in zoomed range from binding energy of 288.5 eV to 283.5 eV. (d) Curve fit plots of 150℃ and 150℃-cool. (e) Fitting results of graphitic C, amorphous C and C-N. (f) Fitting results of C-O, C=O and COOH.
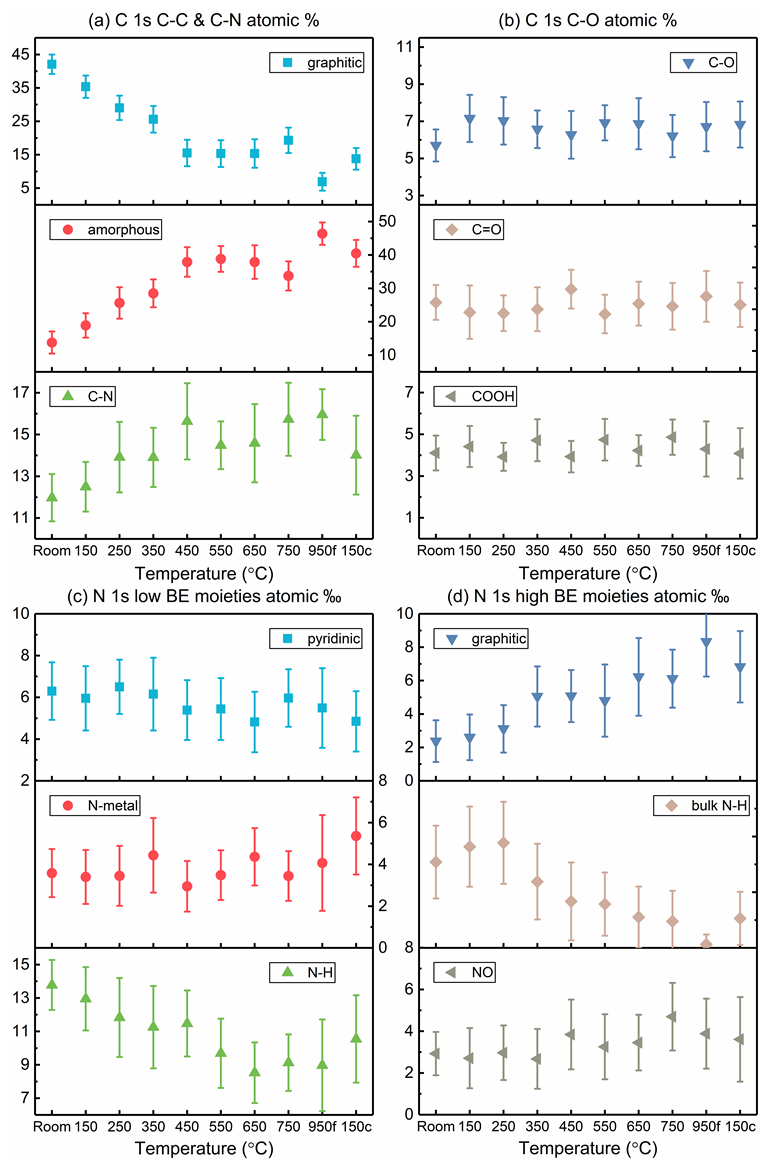
Figure 3-5 Fitting results of C 1s and N 1s as atomic concentration after correction with the corresponding element atomic concentration.

(a)(b) C 1s, (c)(d) N 1s. For easier reading, the unit for N 1s is listed as permille.
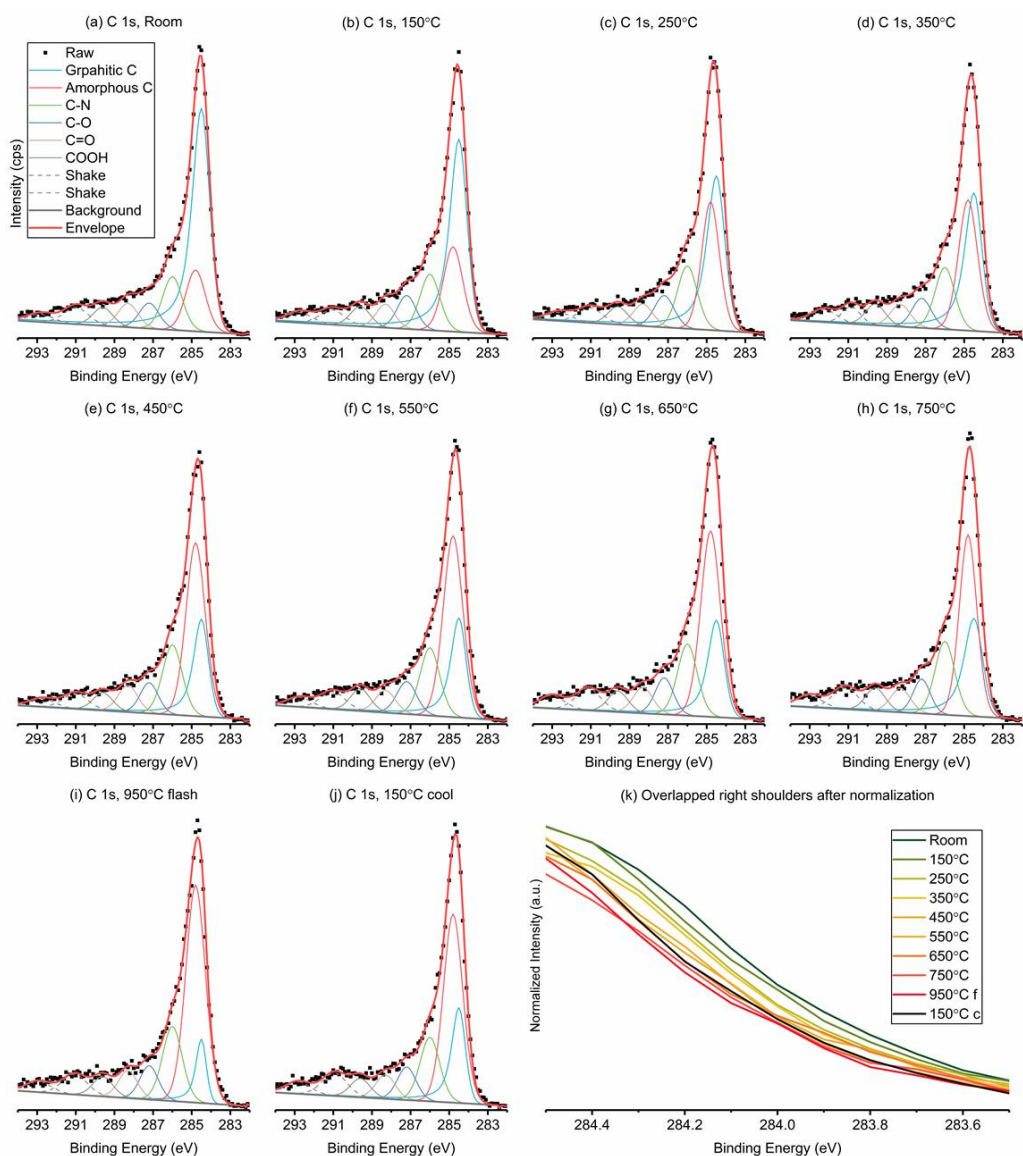
Figure 3-6 C 1s XPS with curve fitting at different temperature points after in situ re-pyrolysis.

(a) Room temperature; (b) 150 °C; (c) 250 °C; (d) 350 °C; (e) 450 °C; (f) 550 °C; (g) 650 °C; (h) 750 °C; (i) 950 °C flash; (j) 150 °C cool; (k) Overlapped right shoulders after normalization.

The changes in high-resolution N 1s during *in situ* UHV heating are shown in **Figure 3-7**, with N 1s spectra curve fittings shown in **Figure 3-8**. The atomic concentrations of each N moiety is listed in **Figure 3-5**, based on the corrected calculation of total N atomic concentration at every temperature point. Upon heating to ~450℃ there is no change in nitrogen chemistry. At ~ 450℃, regions around 397.5 eV and around 399.7 eV start experiencing a decrease in intensity. According to our previously reported density functional theory calculation results[23,24,84] and other

reported N 1s results[11,92,93], the smaller binding energy range change is due to the removal of edge pyridinic N and unstable imine N, and the second region is where a decrease of hydrogenated N-H (including pyrrolic N and hydrogenated pyridinic N) would contribute to. The curve fit results shown in **Figure 3-7d-f** provide quantitative insight into changes in N chemistry. It can be found that after re-pyrolysis, the amount of pyridinic N decreases slightly from 19.1 ± 4.9 % to 15.0 ± 4.5 % while the amount of metal-N_x increases from 10.9 ± 4.1 % to 16.6 ± 5.7 %, with a high standard deviation indicating a heterogeneous composition. The amount of surface N-H decreases significantly from 41.5 ± 6.1 % to 32.7 ± 8.1 % while the amount of graphitic N increases from 8.3 ± 4.4 % to 21.2 ± 6.6 %. Moreover, bulk N-H which has a much higher core level shift[84] around 402.8 eV also has the most significant decrease from 11.6 ± 4.6 % to 3.3 ± 3.0 %. In conclusion, the re-pyrolysis process gave a more balanced nitrogen-carbon structure: a small reduction in edge pyridinic nitrogen sites prone to protonation and hydrogenation, stabilization of metal-N, a dramatic decrease in both surface and bulk hydrogenated sites N-H, and a higher amount of graphitic N. Small amounts of hydrogenated N should result in a more selective ORR mechanism with a smaller amount of nitrogen atoms contributing to the peroxide yielding reaction. Coincidentally, an increase in graphitic N will improve the surface ionic conductivity and increase the diffusion current density[85], as described in **Figure 3-2** previously.
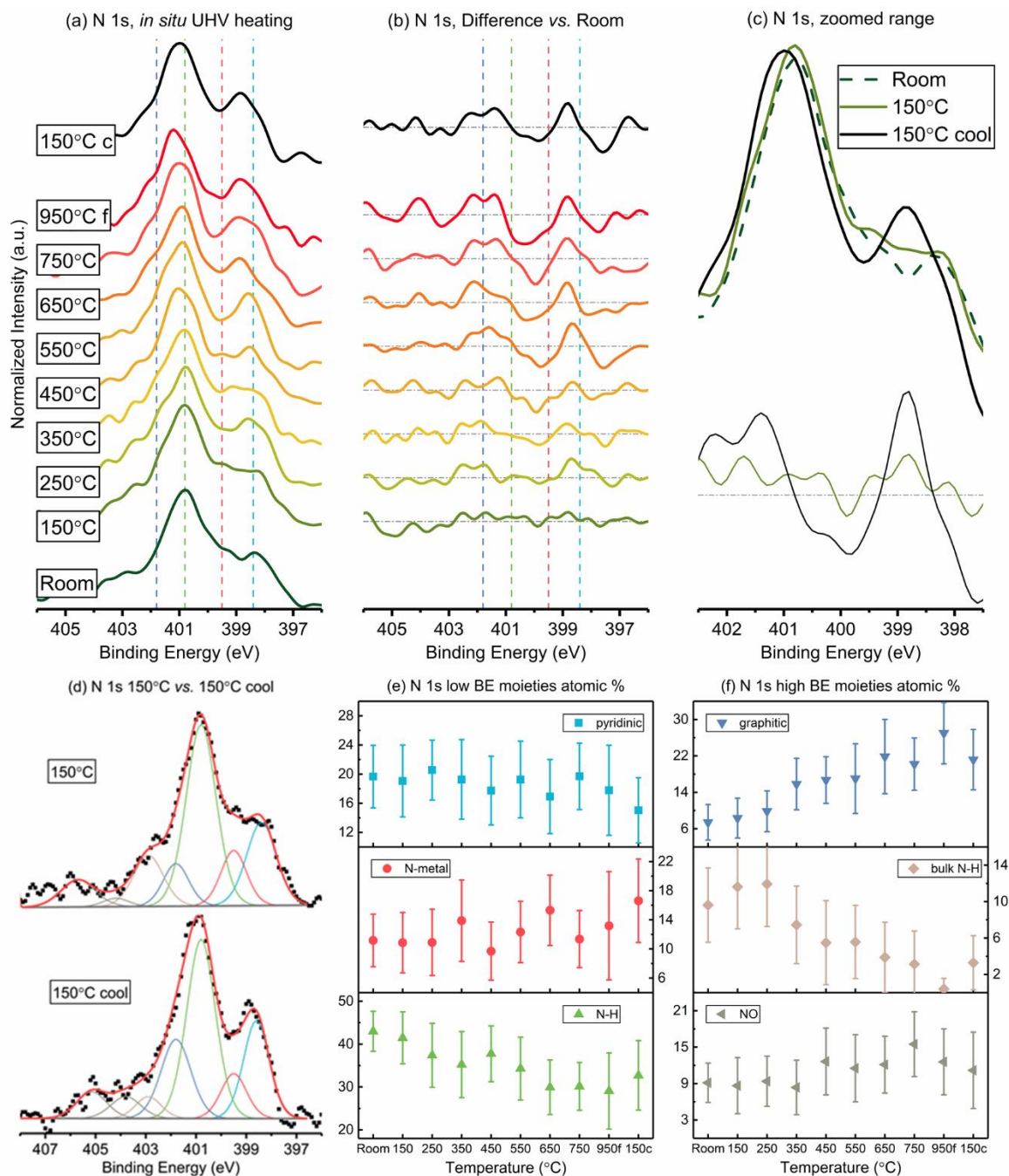
Figure 3-7 N 1s XPS of in situ UHV heating Fe-N-C catalyst.

(a) N 1s spectra measured while holding at every 100 ℃. (b) Difference plots of spectra *versus* the one measured at room temperature. (c) N 1s spectra in zoomed range from binding energy of 402.5 eV to 397.5 eV. (d) Curve fit plots of 150℃ and 150℃-cool. (e) Fitting results of pyridinic N, N-metal and N-H. (f) Fitting results of graphitic N, bulk N-H and NO.
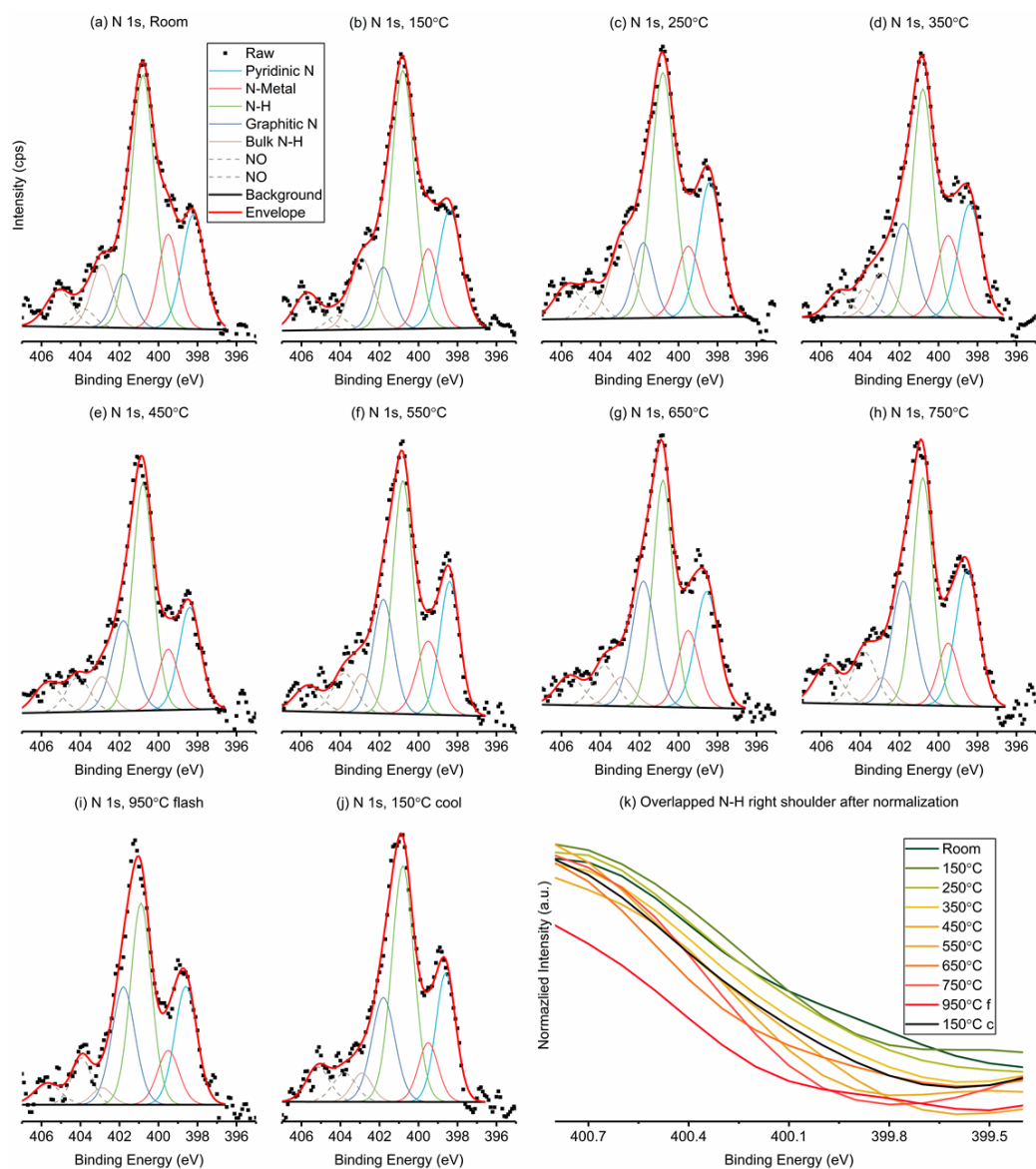
Figure 3-8 N 1s XPS with curve fitting at different temperature points after in situ re-pyrolysis.

(a) Room temperature; (b) 150 °C; (c) 250 °C; (d) 350 °C; (e) 450 °C; (f) 550 °C; (g) 650 °C; (h) 750 °C; (i) 950 °C flash; (j) 150 °C cool; (k) Overlapped N-H right shoulder after normalization. All spectra were processed by fast Fourier transform smoothing with cutoff frequency of 2.5 Hz from the raw data.

3.5 Morphoglical and Spectroscopic Transforamiton during Re-pyrolysis

To help explain the changes of X-ray photoelectron spectra during re-pyrolysis, *in situ* UHV

heating STEM experiments were performed and displayed in **Figure 3-9** for two different

regions. For the cluster / single atom region shown in **Figure 3-9a**, there is a bright area in the

center portion of the top row which could be a small agglomeration of iron atoms. With the

76

temperature increasing, this agglomeration continuously disintegrates and it diffuses into the carbonaceous structure, becoming smaller clusters or single atoms (easily recognized in the enlarged images). The diffusion rate becomes quite fast at 950 ℃. During the natural cooling progress to room temperature, these diffused iron atoms did not re-agglomerate but remained dispersed. Moreover, from the bottom row, which shows the zoomed-in region, it can be found that the diffusion occurred not only on the surface but also within the carbonaceous matrix, explaining why there was no apparent change of Fe atomic percentage during re-pyrolysis in XPS survey spectra as **Figure 3-2a** shows. After re-pyrolysis, some Fe clusters stayed hexagonal or cubic shape. It is still unknown whether these clusters are bonded with neighboring C / N atoms or not. However, this series of STEM images could explain why the graphite C concentration decreases while the amorphous C concentration increases after re-pyrolysis, as well as the decreasing amounts of Fe-N$_4$ moieties.

Another interesting finding from STEM imaging is the nanoparticle/carbide region and is shown in **Figure 3-9b**. A 30 nm size nanoparticle consisting of iron and, most likely carbon as well, could be found in the center of the photos surrounded by a thick layer of graphite (where the lattice can be recognized in the enlarged photos), which may explain why it was not etched by the acid during the synthesis. This kind of nanoparticle existence in M-N-C catalysts has been reported by several research groups (*e.g.* Wu *et al.* & Chung *et al.*[8,94] of Los Alamos National Lab, Wu *et al.*[95] of University at Buffalo, Strickland *et al.*[79] of Northeastern University, Li *et al.*[96] of University of Montpellier and Möller *et al.*[97] of TU Berlin) even with the use of different synthesis precursors and pyrolysis parameters. Similarly to **Figure 3-9a**, the continuous diffusion of iron atoms to form a small cluster and single atom during the re-pyrolysis is observed. To compare, the nanoparticle also has a similar diffusion progress, but the obvious decrease occurs

only at 950 ℃. After heating, this large nanoparticle decreases in size to 10nm. The area of the particle was 27 times smaller than that at the initial state, releasing vast amounts of iron atoms back into the carbonaceous structure. The fresh Fe could transform into either iron clusters or single atom sites, but most likely Fe-N$_2$ sites according to the change of N 1s XPS described previously.
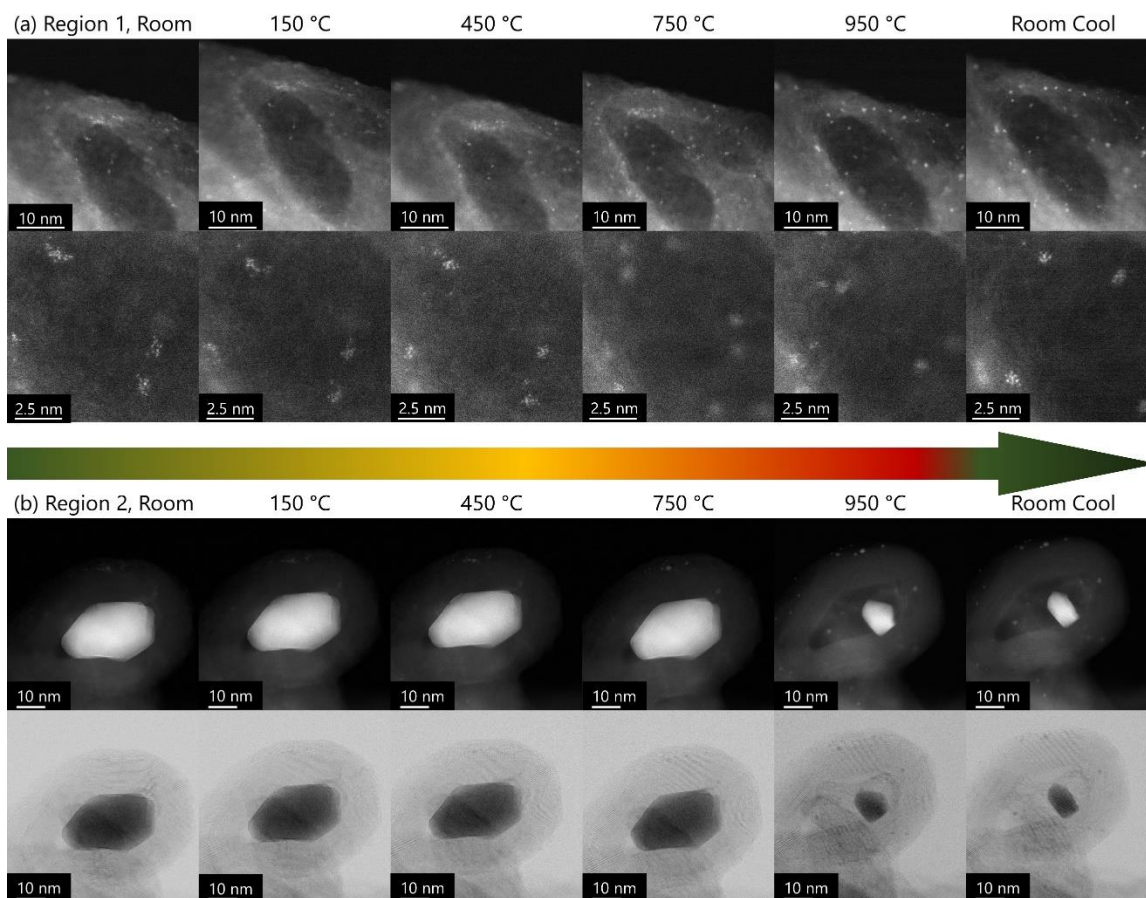
Figure 3-9 STEM photos of in situ UHV heating Fe-N-C catalysts.

(a) The cluster / single atom region. The bottom row is the zoomed-in dark center part of the top row. (b) The nanoparticle/carbide region. The bottom row is the corresponding bright field version of the top row.

To investigate how nitrogen distributes with iron during the re-pyrolysis, low-voltage STEM imaging and simultaneous electron energy loss spectroscopy (EELS) was done to observe the transformation during the *in situ* re-pyrolysis process. The transformation of an iron cluster-rich area was shown in **Figure 3-10**, with the bright scattered spots in the STEM images showing the

iron atoms diffused over the carbonaceous matrix surface when the temperature was elevated. However, from the comparison among different EELS elemental mappings, it can be found that all C, N, and Fe elements were uniformly distributed in this area before the re-pyrolysis as shown in **Figure 3-10a** and did not present obvious changes during the process. The overlaid EELS signals of Fe and N further demonstrate that the iron atoms were well surrounded by N during the whole process. (Similar findings were observed in different cluster-rich areas (**Figure 3-11**, **Figure 3-12**, and **Figure 3-13**). EEL spectra of reference samples were shown in **Figure 3-14** and used to compare with the spectrum of the catalysts. The different phenomena of Fe between STEM and EELS results were caused by the limited resolution of EELS mapping (one pixel = 0.33 nm^2 to 0.44 nm^2), but also indicated that the transformation of the iron clusters shown in **Figure 3-9a** is smaller than the EELS resolution. The calculated correlation between iron and nitrogen also did not show obvious changes on the EELS resolution scale during the re-pyrolysis process (**Figure 3-15**).

The transformation of an iron particle was also observed during this experiment (**Figure 3-16**). The particle size was reduced by 55 % (according to the threshold calculation) after undergoing the re-pyrolysis process. Also, the percentage of iron that is correlated with the nitrogen increased 10.1%, indicating that more iron atoms diffused away from the nanoparticle and coordinated with N sites. **Figure 3-17** shows the zoom-in area near the particles after the sample was re-pyrolyzed. Some uniformly dispersed iron clusters were found on the carbon support, surrounded by nitrogen. Considering the shrinkage of Fe nanoparticles, the newly formed clusters near the nanoparticle most likely arose from the Fe diffusion.
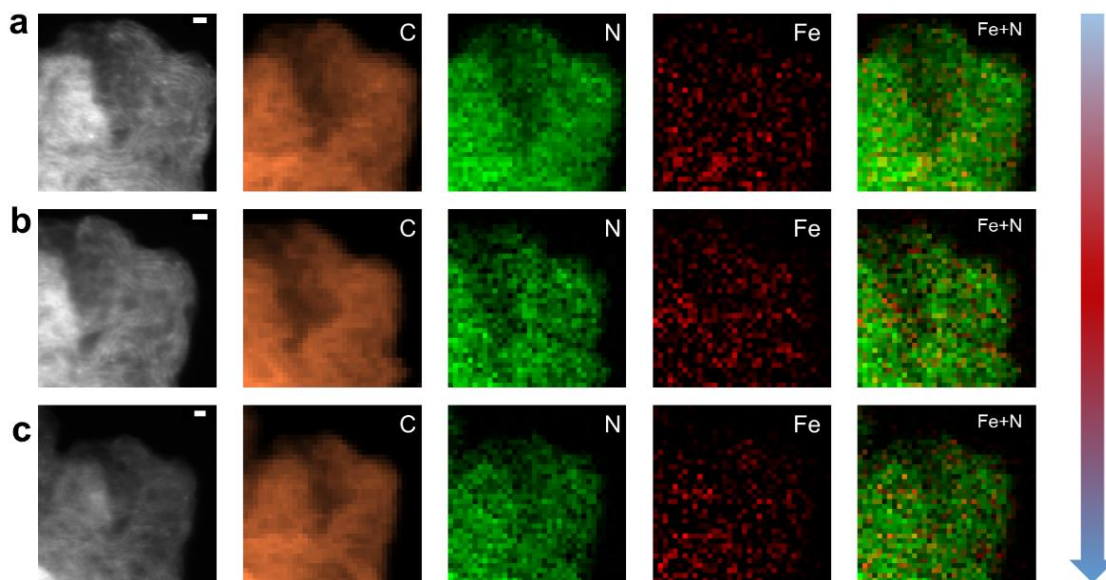
Figure 3-10 STEM of an iron cluster-rich area (Area I) and the corresponding EELS mapping pictures of in situ UHV heating Fe-N-C.

(a) the pristine sample. The pixel size is 0.36 nm x 0.36 nm in EELS mapping. (b) sample pyrolyzed to 950 ℃. The pixel size is 0.33 nm x 0.33 nm in EELS mapping. (c) sample cold down from 950 ℃. The pixel size is 0.33 nm x 0.33 nm – 0.44 nm x 0.44 nm in EELS mapping. Scale bar: 1 nm
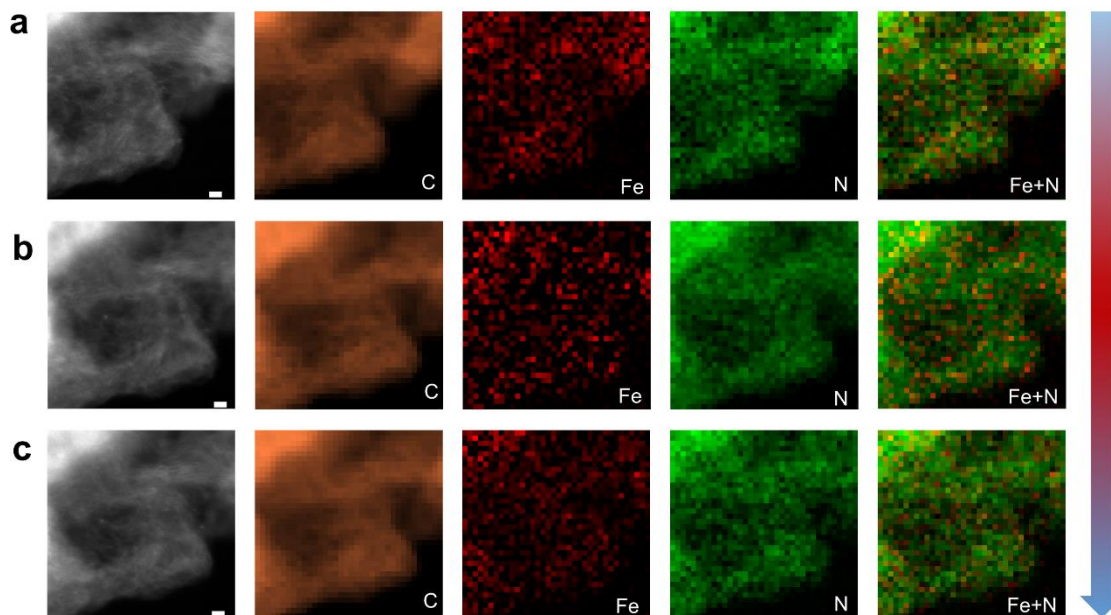
Figure 3-11 STEM photos of a cluster-rich area (Area II) and corresponding EELS mapping pictures of in situ UHV heating Fe-N-C.

(a) the pristine sample, (b) sample pyrolyzed to 950 ℃, and (c) sample cold down from 950 ℃. The pixel size is 0.44 nm x 0.44 nm in EELS mapping. Scale bar: 1 nm
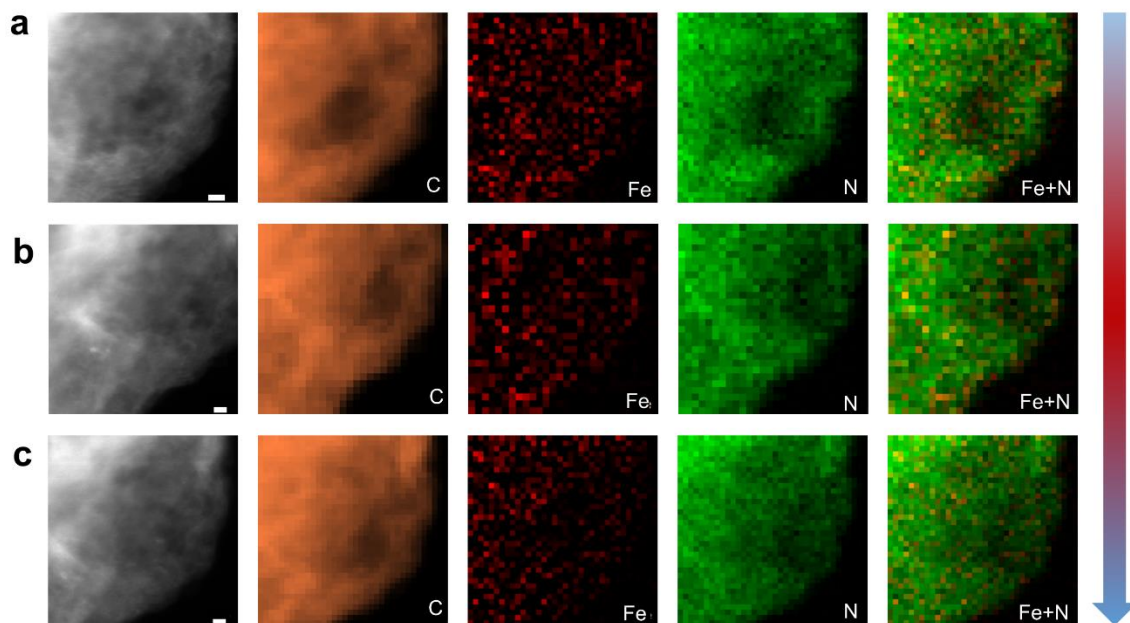
Figure 3-12 STEM photos of a cluster-rich area (Area III) and corresponding EELS mapping pictures of in situ UHV heating Fe-N-C.

(a) the pristine sample, (b) sample pyrolyzed to 950 ℃, and (c) sample cold down from 950 ℃. The pixel size is 0.33 nm x 0.33 nm – 0.57 nm x 0.57 nm in EELS mapping. Scale bar: 1 nm
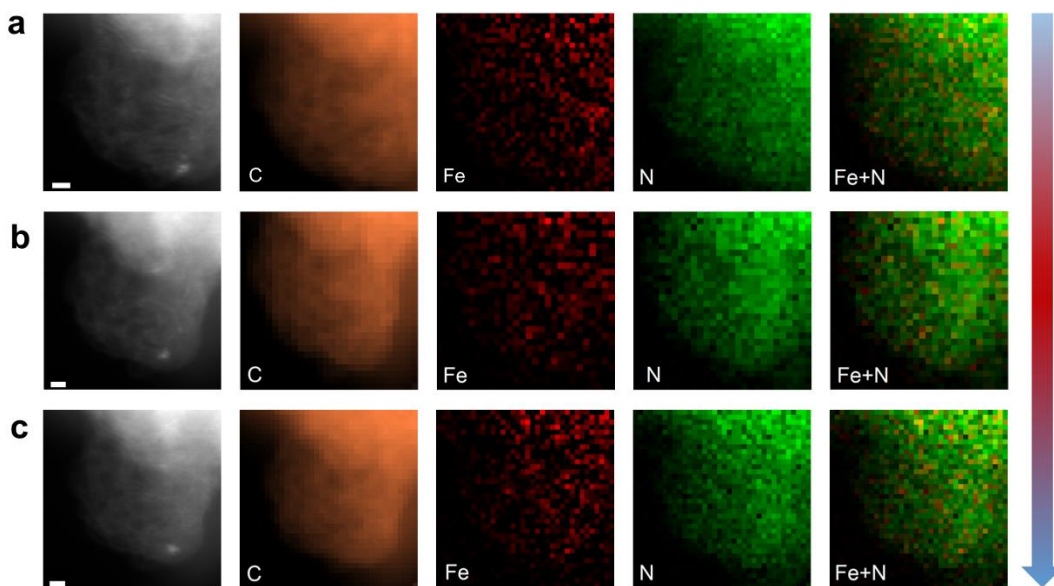
Figure 3-13 STEM photos of a cluster-rich area (Area IV) and corresponding EELS mapping pictures of in situ UHV heating Fe-N-C.

(a) the pristine sample, (b) sample pyrolyzed to 950 ℃, and (c) sample cold down from 950 ℃. The pixel size is 0.28 nm x 0.28 nm - 0.43
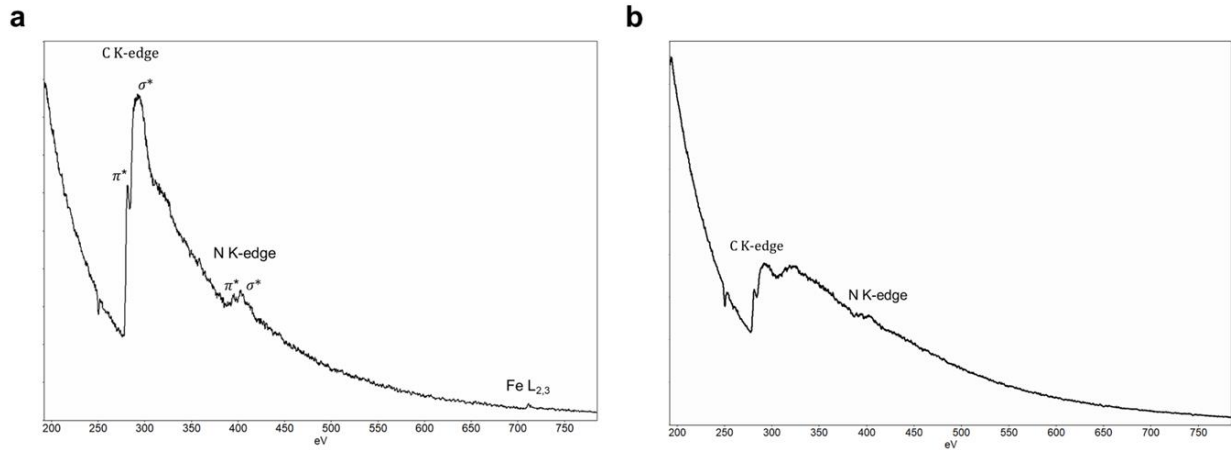
Figure 3-14 EEL spectra of reference sample.

(a) iron (II) phthalocyanine, (b) 29H, 31H-phthalocyanine
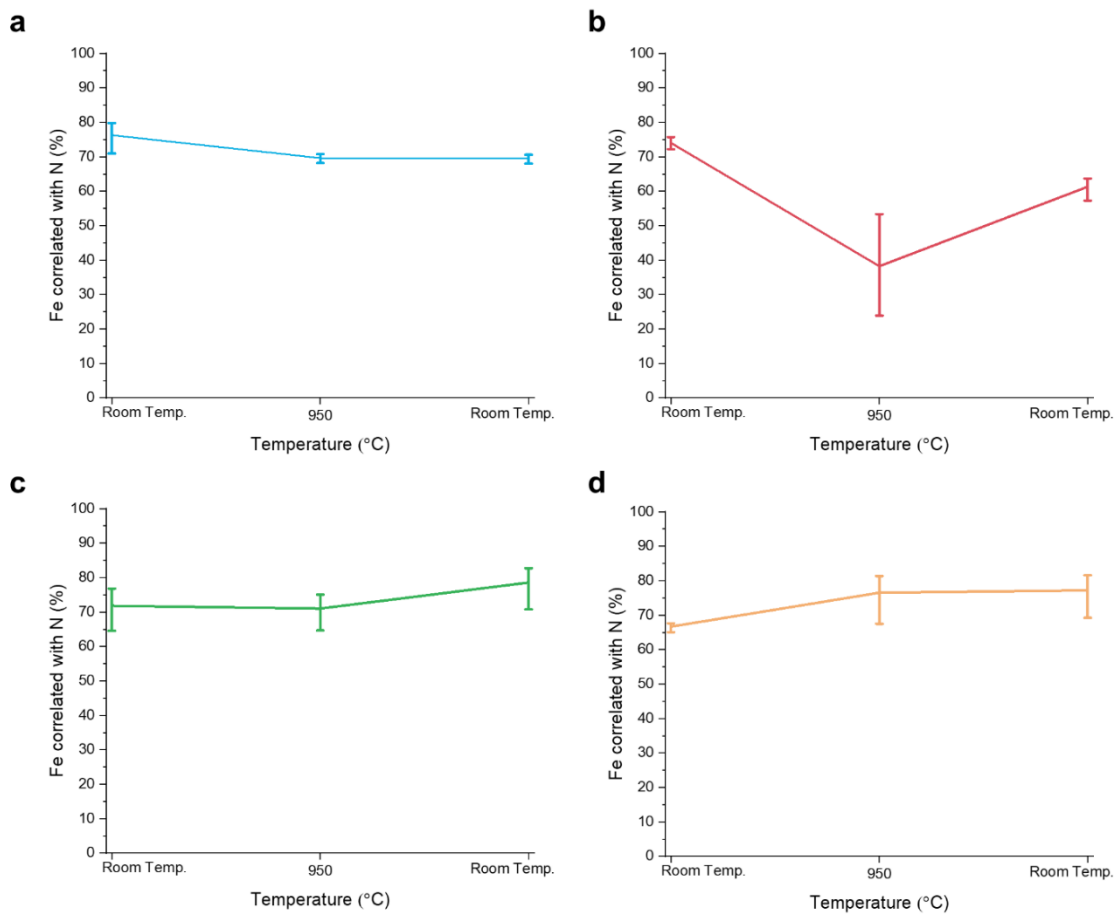
Figure 3-15 The percentage of Fe correlated with N over the total amount of Fe.

(a) Area I, (b) Area II, (c) Area III and (d) Area IV.
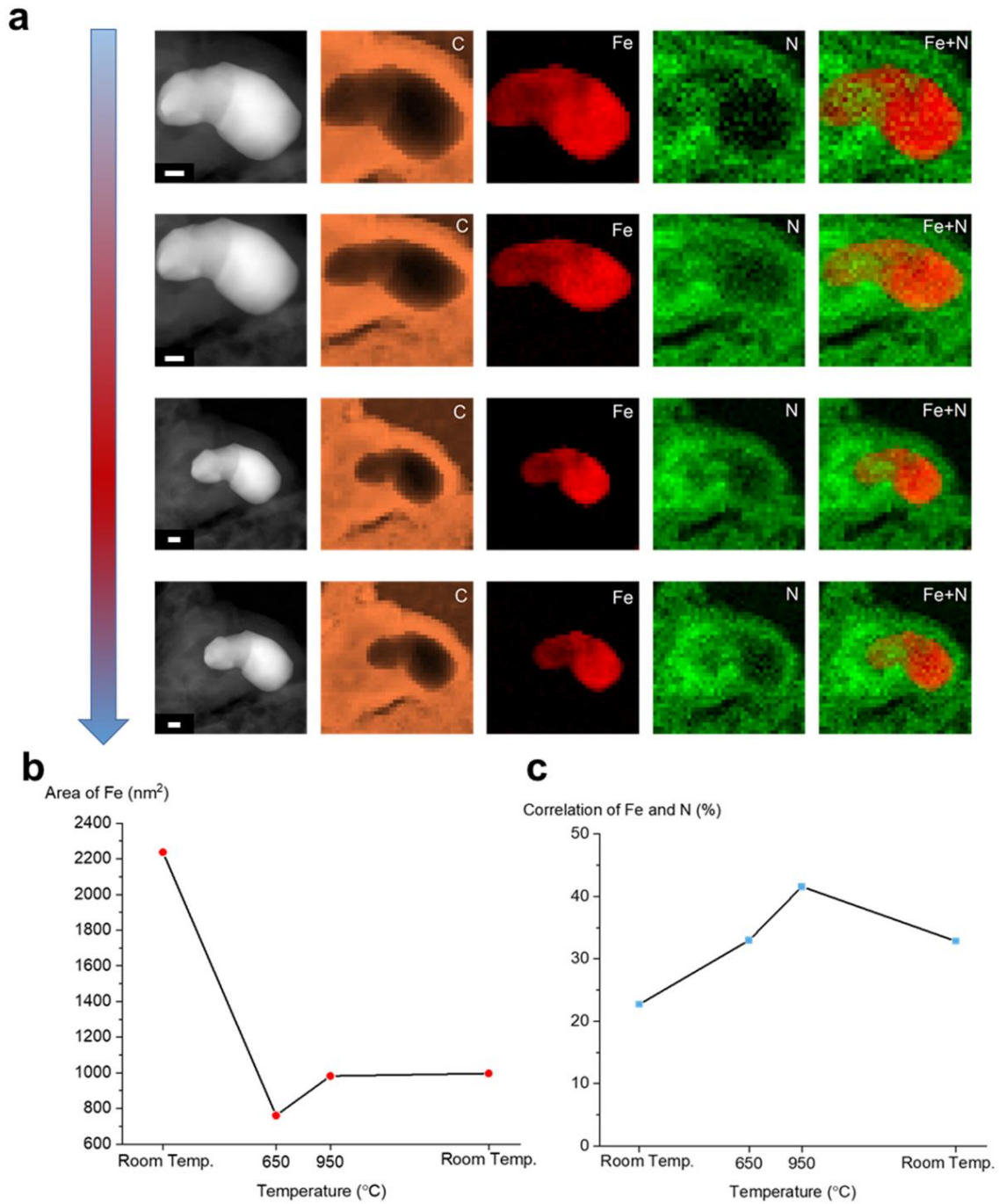
Figure 3-16 Transformation of a pre-existing iron particle during re-pyrolysis process.

(a) STEM photos and corresponding EELS mapping pictures of *in situ* UHV heating Fe-N-C. (b) the transformation of the iron particle area, (c) The percentage of Fe correlated with N over the total amount of Fe. The pixel size is 2.2 nm x 2.2 nm – 3.6 nm x 3.6 nm in EELS mapping.
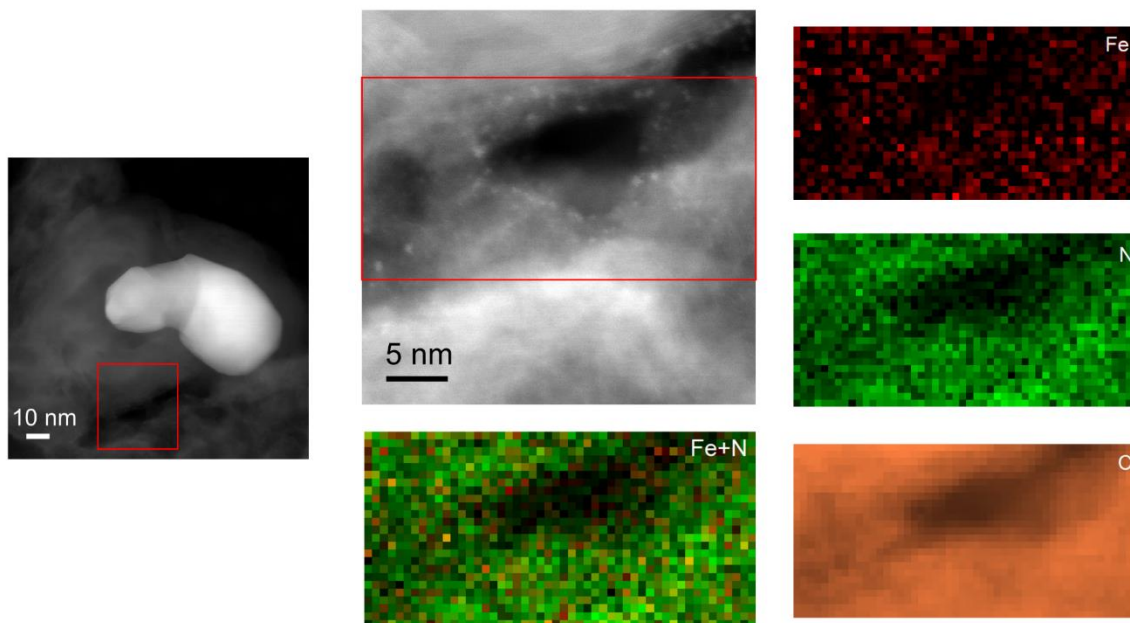
Figure 3-17 Zoom-in area of the area near the pre-existing iron particle after the re-pyrolysis process and its corresponding EELS mapping.

Note: The pixel size is 0.64 nm x 0.64 nm in EELS mapping.

To further investigate the diffusion of iron during re-pyrolysis, the energy dispersive X-ray spectra mapping of *in situ* re-pyrolysis was performed in another area with a low magnification due to the limited spatial resolution, as **Figure 3-18** shows. To avoid electron beam contamination as well as emission interference at high temperatures, EDS mapping imaging was done at the initial 250 ℃ and final 250º C for analysis. Most Fe atoms were found to allocate uniformly, behaving like a bright cloud under STEM after the re-pyrolysis. The cracking progress of the pre-existing Fe nanoparticles into atomically dispersed Fe sites is confirmed by the comparison between the 250 ℃ and 950 ℃ figures. The EDS mapping indicates that C, N and Fe are homogeneously distributed as Fe-N-C after the re-pyrolysis except for the two 10 nm iron nanoparticles that remained. In addition, the silicon signal of two nanoparticles was also found: one being adjacent to the iron nanoparticles while the other being independent. These were most likely protected by (or incorporated in) the carbonaceous matrix and were not etched by HF during the materials synthesis process. It is surface concentration was too low to be

detected in the XPS survey spectra. Moreover, this series of low magnitude STEM figures also indicate that the main carbonaceous structure remained stable during the re-pyrolysis progress, which would be further confirmed by the X-ray computed tomography to be discussed later.
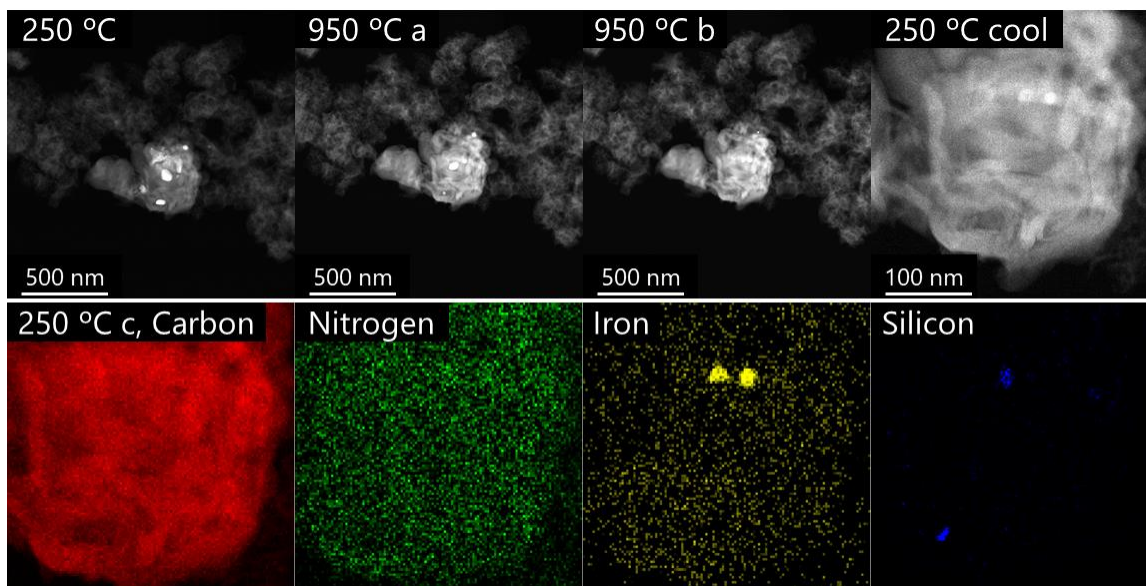
Figure 3-18 STEM images and corresponding EDS mapping of in situ UHV heating Fe-N-C.

The top row shows the initial state at 250 ºC, the continuous change of nanoparticles at 950 ºC and the final 250 ºC after cooling down. The bottom low shows the EDS mapping info at 250 ºC after cooling down. The term "250 ºC c" refers to "250 ºC cool", meaning the test was done after the sample colds down to 250 ºC for test.

Considering the apparent nanoparticle transformation during the re-pyrolysis process, *in situ* N_2 heating XRD as well as *ex situ* XRD was performed to check the possible change of crystal structure. The corresponding patterns are displayed in **Figure 3-19** and **Figure 3-20** respectively. The signals of AlN, α-Al_2O_3 and graphite were clearly found due to the design of the *in situ* heating setup. The shift of nearly all XRD peaks including the one of Fe-N-C around 26.3º to smaller 2θ angles during heating was attributed to the thermal expansion of the crystal lattice[98]. The only exception is the signal around 28º assigned to the (002) of graphite which belongs to the graphite dome. The graphite dome was utilized to protect and isolate the internal high-temperature N_2 and the external cooling air. After excluding the ambient diffraction patterns, it

was found that there was neither the appearance of new peaks nor the disappearance of pre-existing peaks during or after the re-pyrolysis, while any changes of 26.3º signal for Fe-N-C was too difficult to estimate due to the peak width. Briefly, *in situ* heating XRD indicates that the re-pyrolysis process does not result in large crystal formation/decomposition for Fe-N-C catalysts.
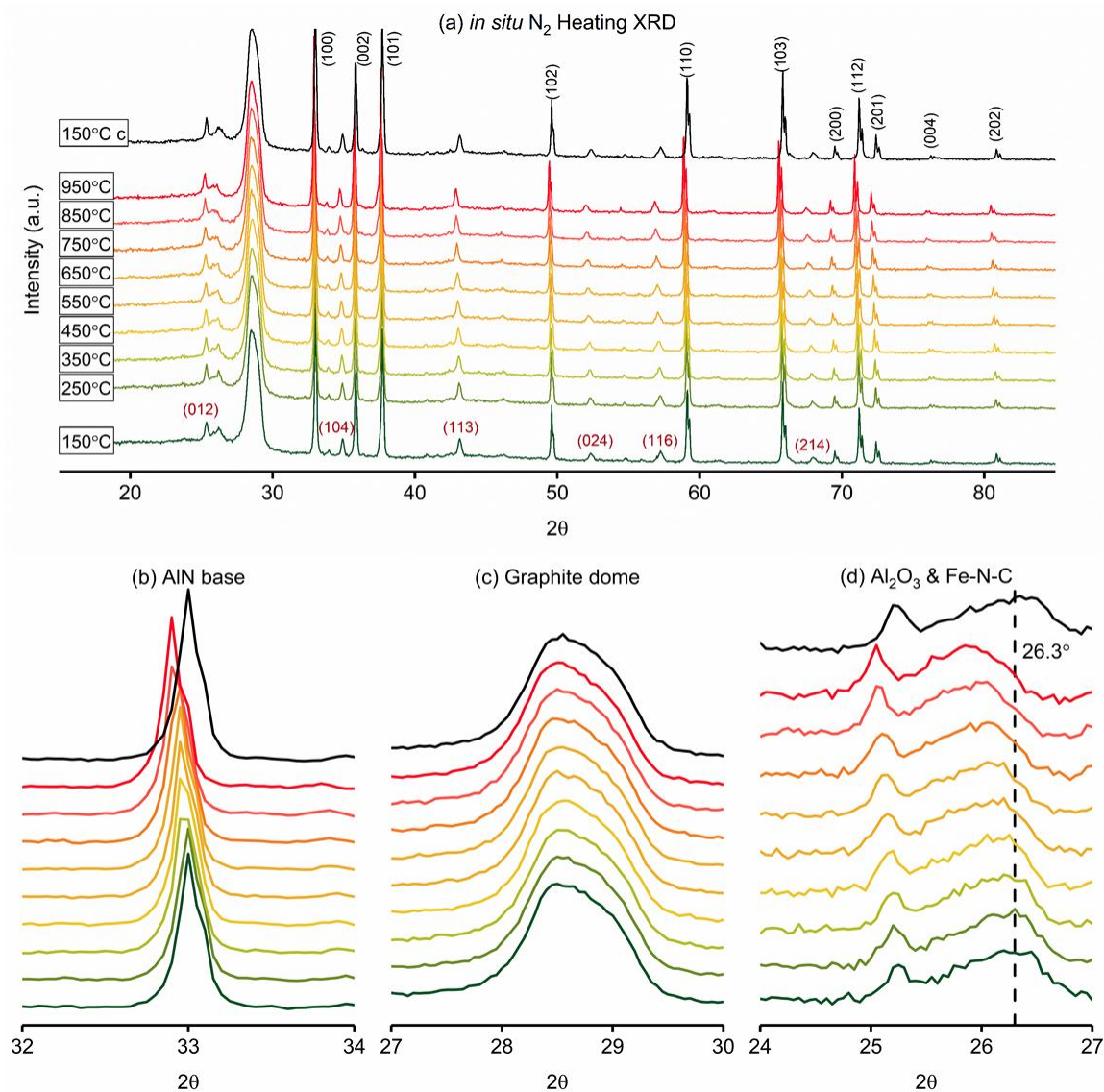
Figure 3-19 XRD patterns of in situ N2 heating Fe-N-C catalyst.

The catalyst was pressed on the silica/alumina tape, heated on AlN base, and isolated by graphite dome. (a) Full scan; (b) Zoomed range from 32º to 34º showing (100) of AlN base, which was heated together with Fe-N-C; (c) Zoomed range from 27º to 30º showing (002) of graphite dome, which was cooled by air blowing; (d) High resolution narrow scan from 24º to 27º showing (012) of α-Al_2O_3 and Fe-N-C. The corresponding AlN peaks (black color) refer to JCPDS 25-1133. The corresponding α-Al_2O_3 peaks (red color) refer to ICDD 001-1243.
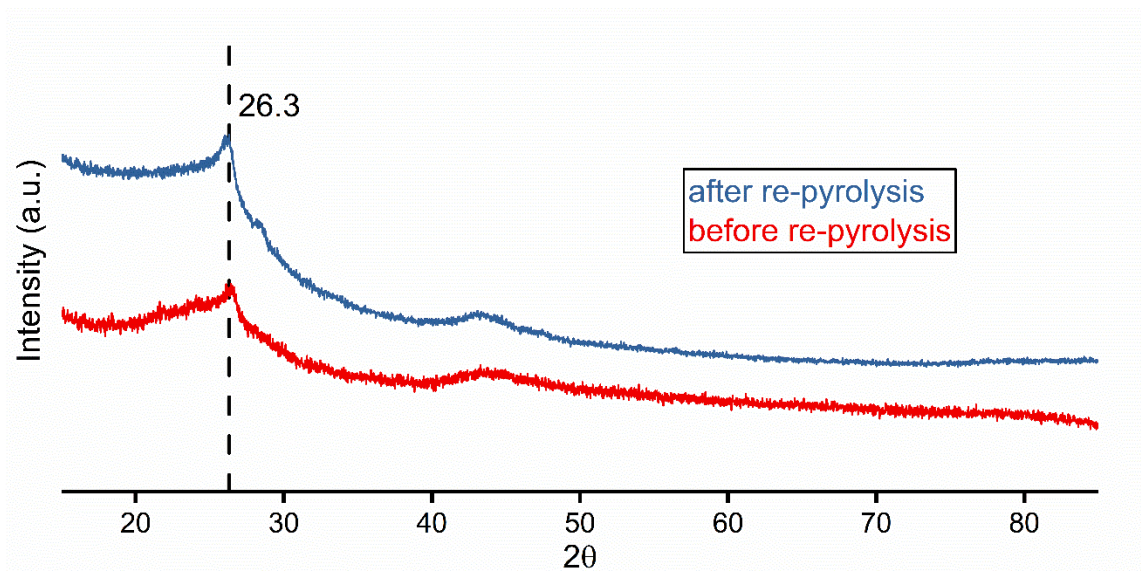
Figure 3-20 XRD patterns of Fe-N-C catalysts before and after re-pyrolysis.

The possible morphology change during the re-pyrolysis was investigated by *in situ* N_2 heating X-ray computed tomography, as **Figure 3-21** - **Figure 3-22**shows. No significant morphology change (e.g., appearance/disappearance of the pathway, emergence of substantial pores, etc.) was observed during the scanning, although some trivial changes, such as the breaking or formation of small clusters in some areas, happened with the temperature changes. The porosity values in thru-plane direction were calculated in a chosen area (shown as the 3-D structure) of the sample in pristine and final states. The plots of the porosity with the depth in the thru-plane direction show a similar tendency. The porosity increases slightly after the re-pyrolysis process. The difference between the porosity values arises from the image noise difference. The evaporation of the materials in some areas may also contribute to the increase in porosity after the re-pyrolysis. The specific surface area of the pyrolyzed sample and the samples re-pyrolyzed at 450 ℃, 750 ℃, and 950 ℃ were calculated with Brunauer–Emmett–Teller (BET) isotherm (**Figure 3-23** and Table 3-1). All catalysts showed high surface area (659.7803 m²/g - 931.0143 m²/g) with the isotherms indicating a presence of micropores and mesopores.
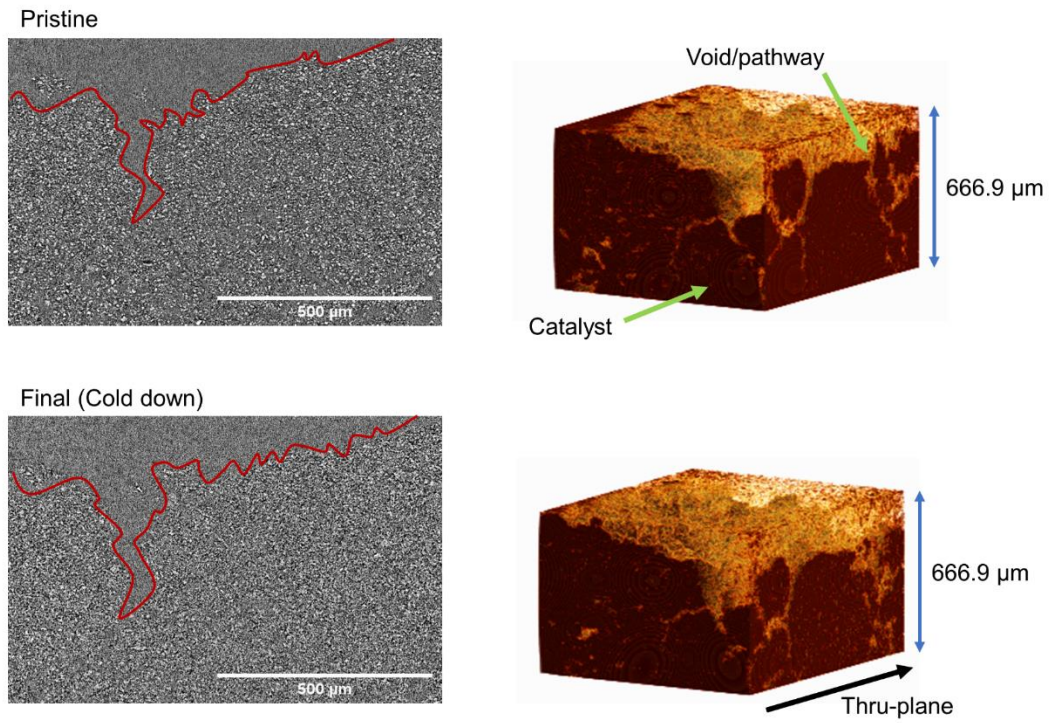
Figure 3-21 X-ray CT cross-section images and 3D structures of the sample at the beginning and after the in situ N_2 heating.
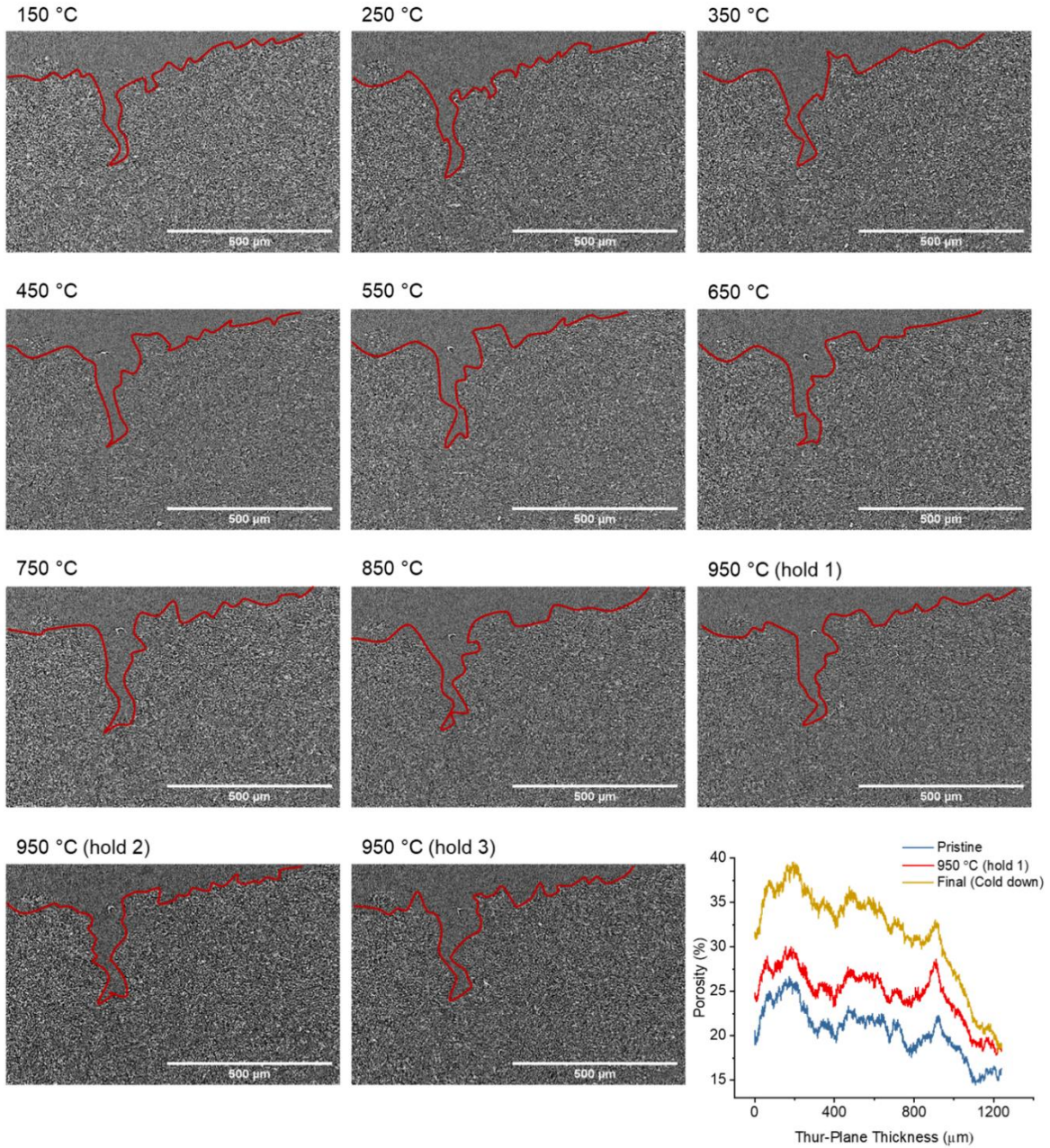
Figure 3-22 X-ray CT cross-section images of the sample during in situ N2 heating and porosity plots of the sample at pristine, 950 °C and after cold down.
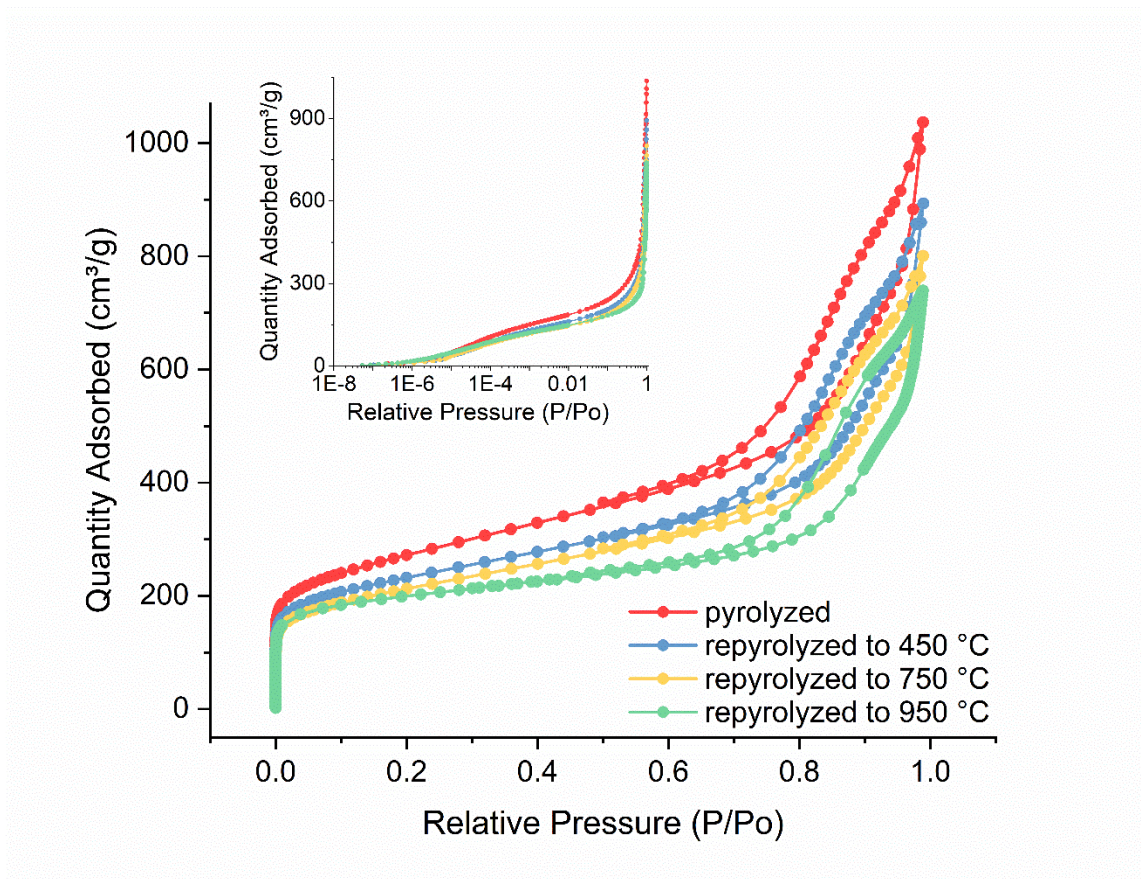
Figure 3-23 Adsorption isotherm plots of N2 on the samples pyrolyzed/re-pyrolyzed at different temperatures.

Note: The inset graph is the semi-log isotherm plots.

Table 3-1 Physicochemical properties of the Fe–N–C catalysts the samples pyrolyzed/re-pyrolyzed at different temperatures

Sample Description	BET surface area (m^2/g)
Pyrolyzed Fe-N-C	931.01
Re-pyrolyzed Fe-N-C (450 °C)	793.19
Re-pyrolyzed Fe-N-C (750 °C)	727.07
Re-pyrolyzed Fe-N-C (950 °C)	659.78

3.6 Stability of the Chemical State

To check the stability of the chemical state of M-N-C after re-pyrolysis, a repeated re-pyrolysis was processed and analyzed with *in situ* heating XPS, as **Figure 3-24** shows. Similarly, different spectra were obtained by the normalization to the same area and the subtraction of the initial spectrum from the final spectrum. The difference spectra between 1st and 2nd re-pyrolysis were

also done by subtracting the 1st spectrum from the 2nd one. It can be found that C 1s spectra has

no apparent change between 150 ℃ 1st time and 150 ℃ 2nd time, implying that the carbonaceous

structure (the M-N-C catalyst "backbone" material) became quite stable after the re-pyrolysis. N

1s spectra also changed, but it can be attributed to a slightly more significant decrease of

pyridinic N during the repeated re-pyrolysis. However, the absolute value of this increase was

similar to the noises. Hence, this small change could be regarded as negligible, implying that the

M-N-C materials becomes stabilized after re-pyrolysis and does not require further heat

treatment. However, considering the XPS facility limitation of the Kratos AXIS Supra which can

only continuously stay at 800 ℃ and instantly go up to 1000 ℃ (*i.e.* "flash" as described), it is

still unknown how the C 1s and N 1s spectra would change after 30 to 60 minutes of holding at

950 ℃.
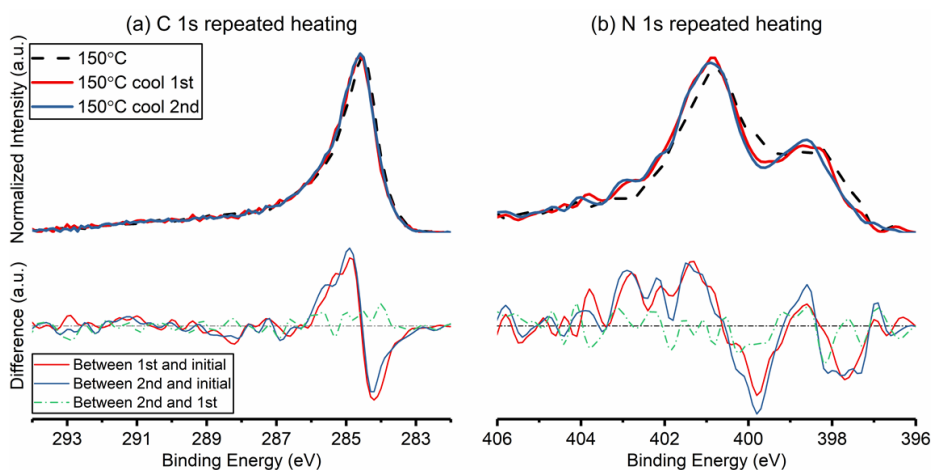
Figure 3-24 XPS for in situ heating and repeated in situ heating and the corresponding differences versus initial 150 ℃.

(a) C 1s. (b) N 1s. The repeated heating followed the same ramping and cooling procedure.

3.7 Electrochemical performance of the catalysts re-pyrolyzed to different temperatures

The electrochemical performance of the pyrolyzed sample (after HF etching) as well as the samples re-pyrolyzed at 450 ℃, 750 ℃, and 950 ℃ was assessed with a rotating ring disk electrode setup (**Figure 3-25**). For comparison, the electrochemical performance of Pt/C standard is also provided (**Figure 3-26**). The re-pyrolyzed samples show increased half-wave potential and decreased peroxide generation. The improved half-wave potential can be attributed to the increase in the Fe-N_x active site density. The decrease in peroxide yield is due to a more reasonable ratio of N-H (including the pyrrolic N and protonated pyridinic N) and pyridinic N. Moreover, higher capacitance is achieved through re-pyrolysis of the catalyst. This indicates that re-pyrolysis can increase the accessible surface area and decrease the concentration of graphitic carbon.
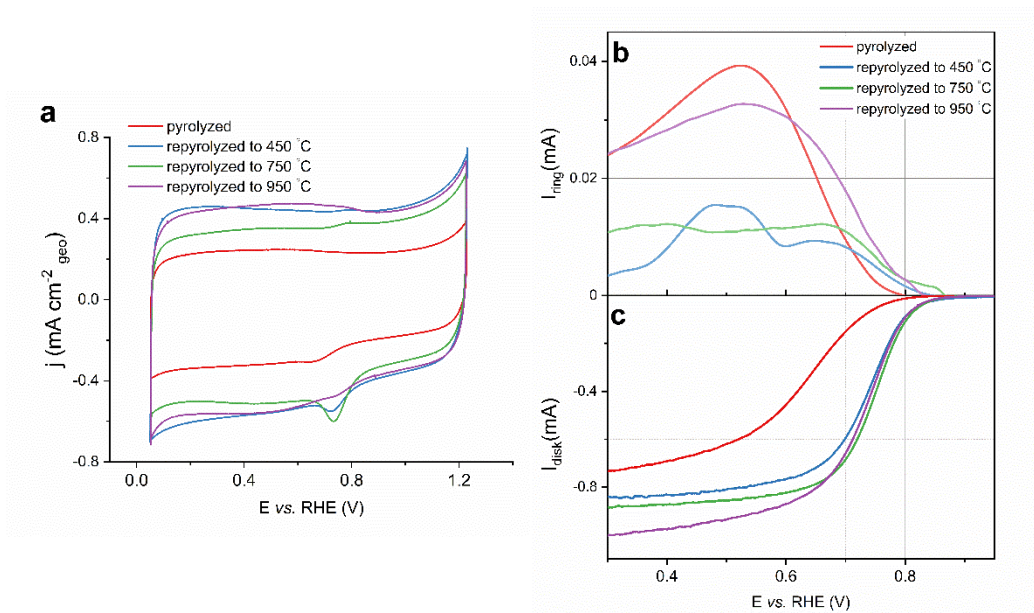
Figure 3-25 Electrochemistry data for the samples pyrolyzed/re-pyrolyzed to different temperatures.

92

The electrolyte is O_2-saturated 0.1 M $HClO_4$. (a) cyclic voltammetry in N_2-saturated electrolyte and a scan rate of 20 mV s^{-1}, (b) ring current density and (c) disk current density in O_2-saturated electrolyte, 900 rpm and 20 mV s^{-1} scanning rate. The sample loading on the electrode was of 175 µg cm^{-2} $_{geo}$ and the electrode surface was of 0.247 cm^2.
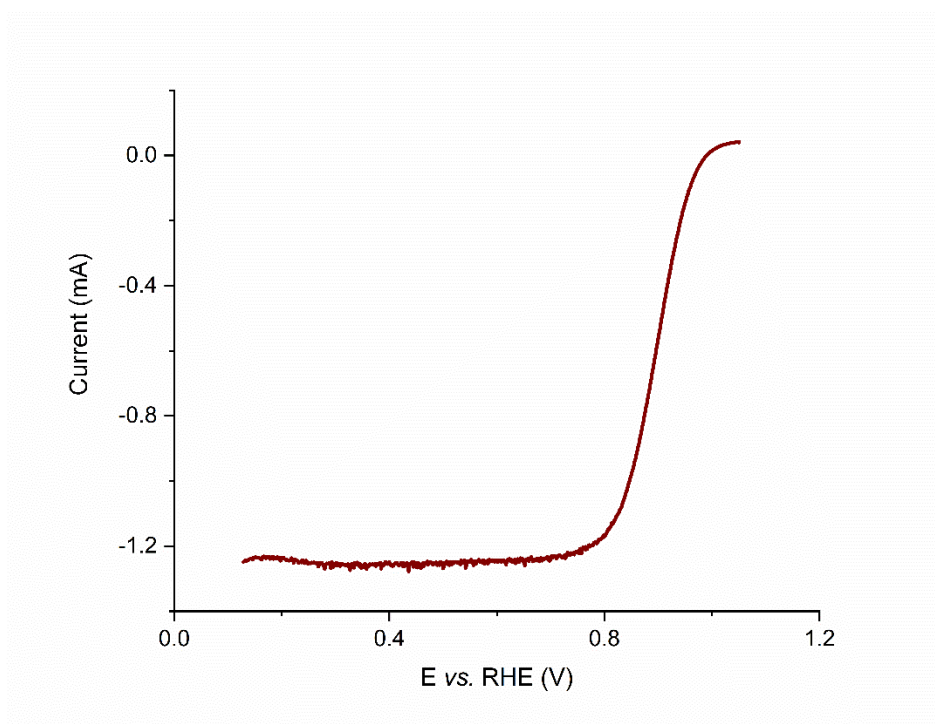
Figure 3-26 Electrochemistry data for the 10 wt.% Pt/C (Sigma Aldrich) standard.

The electrolyte is O_2-saturated 0.1 M $HClO_4$, with a 900 rpm rotation rate and 20 mV s^{-1} scanning rate. The sample loading on the electrode was of 40 µg Pt /cm^2 $_{geo}$ and the electrode surface was of 0.247 cm^2. The half-wave potential is 0.885 V.

3.8 Summary

The combination of several *in situ* UHV / N_2 heating characterization methods performed on a general Fe-N-C material successfully revealed why the re-pyrolysis procedure improves the electrochemical performance of M-N-C materials as well as detailing the chemical and materials synthesis phenomena that occurs during the re-pyrolysis process. (i) The *in situ* XPS indicates that the re-pyrolysis leads to the complete evaporation of the potentially harmful solvent, a negligible Fe concentration change on the catalyst surface, the amorphization of C, and the rearrangement/optimization of multitudinous N sites. (ii) The *in situ* TEM imaging demonstrates that the re-pyrolysis results in the elimination of undesired Fe nanoparticles, the dispersion (*via* surface diffusion or vapor-phase processes) of Fe atoms, the increase of Fe-N_x sites, and a more

uniform distribution of Fe-N$_x$ sites. (iii) The *in situ* STEM-EELS, in *situ* XRD and *in situ* X-ray CT point out that the re-pyrolysis will not cause noticeable crystal phases formation (metallic, oxide or carbide nanoparticles) and does not lead to substantial morphological changes of carbonaceous framework (no new poses, cracks or delaminate formation). In addition, our discovery from *in situ* STEM-EDS implies that the impurities present in precursors, which could not be detected by bulk spectroscopies, may cause severe agglomeration of iron during synthesis. Fortunately, it can be reversed by the re-pyrolysis process to a large degree and potentially eliminated. Given the evidence, the process of re-pyrolysis can be classified as a materials purification step of the synthesis procedure.

In summary, the re-pyrolysis provides numerous synthetic advantages and is recommended to be utilized for all metal-nitrogen-carbon (M-N-C) electrocatalysts, no matter the precursors or synthesis parameters. The next stage will be to bring more efforts in investigating how the re-pyrolysis could affect specific commercial carbons and whether it could influence platinum-group-metal electrocatalysts as well.

Chapter 4 Evolution of Metal-Organic Framework (MOF) to Metal-Nitrogen-Carbon Catalysts by Pyrolysis

4.1 Overview

Metal-nitrogen moieties (M-N$_x$) embedded in the carbon matrix of M-N-C materials have been recognized as the most essential active sites[27,29,99,100]. Significant efforts have been made to disperse the metal species well in the carbon matrix to get a higher density of active sites, as catalyst activity is proportional to the number of active sites. Besides the M-N$_x$ sites, well designed carbonaceous materials are also essential for the M-N-C catalysts, as their pore space ensures gaseous and liquid permiability and the solid part provides electronic conductivity. The way to obtain the M-N-C catalysts with sufficient M-N$_x$ sites and specialty carbonaceous materials is through pyrolyzing precursors. The selected precursors are rich in carbon, as well as nitrogen, and usually include metal species. Typical materials used as precursors are macrocyclic compounds[101,102], polymer[8,43], metal-organic framework (MOF)[18,103] and the mixture of the above with templating agents[17,104]. MOF-derived catalysts show a large potential for high catalytic activity. This potential comes from its porous structure with a high surface area. Zeolitic imidazolate framework (ZIF) materials are usually the type of MOFs used as precursors to make M-N-C catalysts. Previous studies showed that the half-wave potential for the ORR of the catalysts synthesized from iron doped ZIF-8 with a surface area of 969 m^2 g^{-1} reached 0.82 V in acid media[105]. The catalysts derived from Co-based MOF with a surface area of 1359 m^2 g^{-1} exhibit a half-wave potential of around 0.85 V in alkaline media[106]. Recently, a great deal of effort has been made to disperse the metal on ZIF-8 materials by using chemical vapor deposition (CVD) during pyrolysis. With CVD, iron salt vapor can be transported over ZIF-8

derived Zn-N-C materials, transmetalating the Zn sites with Fe, yielding an Fe-N-C catalyst with well dispersed Fe-N$_4$ sites[107]. CVD can also be conducted in a way that deposited N-doped carbon on the prepared Fe-N-C catalysts, yielding highly stable pyridinic N-coordinated FeN$_4$ sites, significantly improving the durability of the catalyst[108].

General interest in pyrolyzing MOFs to make catalysts is based on the hypothesis that the favorable porous structure of MOFs can sustain heat treatment. The high porosity and the surface area of the structure should facilitate molecular transport and provides the possibility for the active sites to be highly dispersed. However, the above hypothesis might not always be correct. Some synthesized M-N-C catalysts derived from MOF-based materials and their corresponding morphological information, as well as the ORR activity in the acid electrolyte are summarized in Supplementary Material (Table 4-1). From the (scanning) transmission electron microscopy images in previous studies[106,109], the hexagonal shape of the MOFs observed by microscopy before the pyrolysis did not persist after the pyrolysis.

The reason why pyrolyzed precursors only partially maintain their original MOF structure remains unclear. The pyrolysis process is currently a "Pandora's box" – the structure of the product is only revealed after the process is done and the materials are characterized. Also, the extent to which the morphological properties affect the electrochemical performance of MOF-derived catalysts remains ambiguous. These hinder the rational design of the MOF-based catalysts. Herein, we observed the pyrolysis of the MOF materials by a combination of *in situ* and *ex situ* techniques to reveal the transformation from the morphological and spectroscopic perspective. Two commercial ZIFs with the same structures (ZIF-8 named Basolite® Z1200 from Sigma-Aldrich© and ZIF-67 from PlasmaChem©) were used as precursors in the study. ZIFs are MOFs that are comprised of tetrahedrally coordinated metal ions and imidazole ligands. ZIF-8,

coordinated with zinc ions, and ZIF-67, coordinated with cobalt ions, share the same sodalite

topology. ZIF-8 **Figure 4-1a**) has been combined with other precursors to form ideal transition

metal-N-C catalysts [109-113]. ZIF-67 (**Figure 4-1d**) can be used as a sole precursor since it contains

cobalt, as well as carbon and nitrogen source. Ideally, cobalt can bond with nitrogen and form

$Co-N_x$ active sites after pyrolysis [106,114,115]. With commercial chemicals, fewer interfering factors,

like unknown contaminations and unexpected operation errors, are involved. Thus, the pathway

of MOF leading to the carbonaceous materials *via* pyrolysis can be better understood. The direct

observation and thorough analysis of "the birth of catalysts" are the foundation for the rational

design of M-N-C.

Table 4-1 Morphological information and the performance in acid media of previously reported MOF-derived catalysts

Published Year	Precursor	Pyrolysis	Morphological change	Surface area (BET)	Half-wave potential	Note	Ref.
2016	Co/Zn(mIm)$_2$	1st pyrolysis to 1000 °C under Ar. 2nd pyrolysis to 950 °C under NH$_3$	Highly porous carbon structure without visible metal nanoparticles. Shape partially remained	1563 m^2·g^{-1}	0.76 V (vs. RHE) 400 µg/cm^2 0.5 M H$_2$SO$_4$	Acid etched between two pyrolysis	116
2017	nitrogen-doped graphene aerogel supported Co-MOF	Heated to 750 °C under Ar. Then Kept at 100 °C in air for 24hr	Structure destroyed, particles and graphitic carbon formed.	1359 m^2·g^{-1}	-	-	106
2019	Co-ZIF-8@surfactant (F127)	Heated to 900 °C under N$_2$	Structure remained. Metal: atomically dispersed.	825 m^2·g^{-1}	0.84 V (vs. RHE)	-	117

Year	Material	Process	Structure	Surface area	Performance	Notes	Ref
					800 µg/cm^2 0.5 M H_2SO_4		
2019	5Fe-1uIm-3mIm (dual-ligand)	Heated to 1100 °C under N_2.	Structure remained. Metal: atomically dispersed.	801 m^2·g^{-1}	0.86 V (vs. RHE) 800 µg/cm^2 0.5 M H_2SO_4	5% Fe in total metal moles	118
2019	ZIF-8+Phen+Co(Ac)$_2$·4H$_2$O	Heated to 1050 °C under Ar	Structure remained	315 - 430 m^2·g^{-1}	-	0.5 wt% Co	119
2019	MIL-100(Fe)+ZIF-8	Heated to 1000 °C under N_2. Cold down under NH_3 from 800 °C and N_2 from 500 °C	Single particle incorporated in carbon shell. Some hexagonal shape remained	755 m^2·g^{-1}	0.79 V (vs. RHE) 500 µg/cm^2 0.5 M H_2SO_4	Mass ratio MIL/ZIF=1: 40, Catalysts were acid etched	120
2020	Zn(mIm)$_2$	Heated to 1000 °C under N_2. Cold down under NH_3 from 900 °C	sponge-like structure appeared. Hexagonal shape disappeared	763 m^2·g^{-1}	-	ZIF-derived carbon	109
2020	Mn-doped ZIF-8	Step pyrolysis to 800 °C for 2hr then to 1100 °C for 1 hr under Ar. 2nd pyrolysis to 1100 °C under Ar	Structure remained. Metal: atomically dispersed.	1511 m^2·g^{-1}	0.815 V (vs. RHE) 800 µg/cm^2 0.5 M H_2SO_4	Acid etched between two pyrolysis	112

Year	Precursor	Treatment	Structure	Surface area	Performance	Note	Ref
2020	$Zn(NO_3)_2 \cdot 6H_2O$ + $FeSO_4 \cdot 7H_2O$ + 2-methylimidazole	Heated to 900 °C under Ar	Structure remained.	$1164.6 \ m^2 \cdot g^{-1}$	-	molar ratio of Zn^{2+}/Fe^{2+} = 20:1	[111]
2021	ZIF-8 $(Zn(NO_3)_2 \cdot 6H_2O$+2-methylimidazole)+$FeCl_3$	ZIF-8 heated to 1050 °C under Ar to get Zn-N-C. Then deposited FeCl3 to Zn-N-C at 750 °C under Ar	Structure remained. Metal: atomically dispersed.	$807 - 1593 \ m^2 \cdot g^{-1}$	0.85 V (vs. RHE) 800 µg/cm^2 0.5 M H_2SO_4	Chemical vapor deposition (CVD)	[107]
2022	Fe_2O_3@ZIF-8+ NH_4Cl +ZIF-8	Fe2O3@ZIF-8 heated to 800 °C under Ar to get Fe-N-C. Ground Fe-N-C with NH_4Cl to get Fe-AC. Deposited ZIF-8 to Fe-AC at 1100 °C under Ar	Structure remained. Metal: atomically dispersed.	$668.6 \ m^2 \cdot g^{-1}$	0.846 V (vs. RHE) 600 µg/cm^2 0.5 M H_2SO_4	CVD at the 2nd step	[108]

4.2 Methods

4.2.1 Materials synthesis

ZIF-8 was purchased from Sigma-Aldrich$^©$ (Basolite$^®$ Z1200), while ZIF-67 was purchased from PlasmaChem$^©$. The *ex situ* samples were pyrolyzed under Ar with a ramping rate of 10 C/min. The acid etched pyrolyzed products were done by etching the pyrolyzed samples with 3M HCl overnight followed by being washed until the pH reached neutral.

4.2.2 Scanning transmission electron microscope (STEM)

The *in situ* heating STEM experiments were done in a vacuum environment. The Protochips Fusion Select[TM] was used where there is one heating chip (E-FHDC, Protochips, Inc.) applied and the $\varphi = 8$ μm holes were covered by holey carbon thin films. The MOF materials were dispersed in the ethanol solvent with ultrasound bath. The resulting sample suspension was then dropped onto the heating chip by pipette. After the sample had dried on the chip, an optical microscope was used to check whether the powder sample was on the chip windows.

The sample for *ex situ* STEM experiments was dispersed in ethanol solvent by ultrasound bath. The resulting suspension was then dropped on the holey carbon-coated copper grid. The sample was dried before doing the STEM.

STEM was performed on a JEOL JEM-ARM300CF microscope with probe correctors and a 300 kV cold field emission gun. All reported temperatures were calculated by the measured electrical resistance of the heater. Energy dispersive X-ray spectroscopy (EDS) was done at the pristine state, 250 °C, and at the final state. The EDS was done with 100 mm^2 dual silicon drift detectors.

4.2.3 *In situ* X-ray nano-computed tomography (nano-CT)

The *in situ* heating X-ray nano-CT experiments were done with the transmission X-ray microscope from beamline 32-ID of the Advanced Photon Source (APS) at Argonne National Laboratory (ANL). Monochromatic X-ray of 8 keV energy was applied. A 50 nm outermost zone width Fresnel zone plate was used as an objective lens and a phase-ring placed in the back focal plane of the zone plate was used to perform imaging in Zernike phase contrast mode. The voxel size is 21.3 nm.

Samples were mounted on the graphite pin, which was mounted onto a high-accuracy air-bearing rotary stage. The top part of the pin was enveloped by an inductive furnace with X-ray transparent window. The N_2 gas flew through the furnace during the whole experiment. Scans were performed for pyrolysis process at pristine state, 200 °C, 400 °C, 600 °C, 850 °C, 980 °C, 1050 °C and at the final state after cooling down to room temperature. However, the images taken at high temperatures were not reconstructed since the rotating center was changing during the scan due to the intense vibrations. The temperature stepping ramp rate was used with 10 °C·s^{-1} and 15 min hold time at each temperature.

The data was reconstructed with TomoPy and ASTRA toolbox[53-55,121]. Image processing was done with Dragonfly 2022.1 Software (Object Research Systems (ORS) Inc, Montreal, Canada, 2020; software available at http://www.theobjects.com/dragonfly). The semantic segmentation is done with UNet++ architecture [122,123].

4.2.4 X-ray diffraction (XRD)

The *ex situ* XRD is performed on Rigaku SmartLab with Cu Kα source. High-temperature *in situ* powder XRD was done at beamline12.2.2 of the Advanced Light Source (ALS) at Lawrence Berkeley National Laboratory (LBNL) in an environmental cell previously reported[57,58,124-126]. Around 1 mg of the powder sample was introduced into a 0.7 mm outer diameter quartz capillary provided by Hilgenberg GmbH, Germany. The gas was delivered by a set of mass flow controllers and is delivered to the sample by a tungsten carbide injection capillary. The quartz capillary and the tungsten carbide capillary were both mounted and enclosed inside a silicon carbide cylinder with two holes allowing X-ray beam to pass. The cylinder was heated with two infrared lamps (Osram 64635HLX) and served as a furnace. A pattern with a LaB6 standard NIST 660b was acquired for setup calibration before the experiment. The setup temperature is

controlled using a S-type thermocouple placed next to the sample. Prior to performing experiments with the MOF samples, a temperature calibration curve was done using Pt as standard material all along the temperature range. The reported temperature was the average temperature during the 30 s exposure time. All experiments were performed with an incident X-ray beam of 25 keV and a spot size of 30 x 30 μm^2.

The XRD data was collected when the precursor material was heated from room temperature to 1035 °C at the rate of 10 °C·min^{-1}, held at 1035 °C for 30 min, and cooled to room temperature under 5% H_2 and 95% Ar atmosphere. The gas was flowing at 10 NmL·min^{-1}. The patterns containing Debye diffraction rings were processed on-the-fly using Dioptas software[59] to yield intensity as a function of 2 Theta. The relative crystallinity was calculated by integrating area under the peaks and compared the integration to the one calculated based on the pristine spectrum. PDXL software was also used to analyze the data.

4.2.5 Thermogravimetric analysis (TGA)

TGA characterization was performed on a simultaneous thermal analyzer (Netzsch STA 449 F3 Jupiter). The precursor materials were mounted in ceramic crucibles. Blank experiments were performed for background corrections. All samples were heated under Ar from 80 °C to 1020 °C with the rate of 10 °C·min^{-1}. NETZSCH Proteus Thermal Analysis was used to analyze the data.

4.2.6 Raman spectroscopy

The Raman spectra were obtained on a Horiba LabRAM HR Evolution confocal Raman microscope with 633 nm laser and 600 g/mm grating. 100x objective was applied. Twenty-five individual 20s spectra were accumulated. CasaXPS software was used to analyze the data. All data was fitted with four peaks based on publications[127,128].

4.2.7 X-ray Absorption Spectroscopy (XAS)

XAS data were collected at the 10-BM beamline of APS at ANL [129]. The sample was mixed with some binder and pressed as a pellet. The pellet was then sealed in a holder with Kapton tapes. The products of pyrolyzed ZIF-8 were measured at the Zn K-edge (9659 eV) in transmission mode. The products of pyrolyzed ZIF-67 were measured at Co K-edge (7709 eV) in fluorescence mode. The data was processed and modeled using the Demeter XAS software package[130]. The EXAFS amplitude reduction factor S_0^2 was determined based on the fitting of standard reference material. The fits were performed in k-weight = 1,2,3 with a Fourier Transform range and fitting window indicated in the EXAFS fitting result tables.

4.2.8 X-ray Photoelectron Spectroscopy (XPS)

XPS was performed on a Kratos AXIS Supra spectrometer with a monochromatic Al Kα source. Ar ion was used to etch the sample surface for 30 s with 500 eV Ar250 + cluster setup after the surface was characterized. CasaXPS software was used to analyze the data. The fitting was using 70% Gaussian/30% Lorentzian setup based on previous calculations and publications [23,24,43,84,85,131].

4.2.9 Inductively Coupled Plasma-Mass Spectrometry (ICP-MS)

ICP-MS was done on the ThermoFisher iCAP RQ ICP-MS system. The powder samples were digested in aqua regia over several days, and then diluted to ppb concentration levels in 1 vol.% nitric acid in Milli-Q water. The standard calibration curves were prepared by diluting an elemental standard in 1 vol.% nitric acid in Milli-Q water and then performing a series of auto-dilutions in the system.

4.2.10 Nitrogen physisorption

Nitrogen physisorption was done in a Micromeritics 3Flex Surface and Catalyst Analyzer. The samples were vacuumed at 90 °C for 1 h and then at 200 °C for 6 h before the measurement. The surface area was calculated by the Barrett-Emmett-Teller (BET) method. The pore size distribution was obtained with the non-local density functional theory model (NLDFT).

4.2.11 Electrochemical measurement

The electrochemical experiments were done with a rotating ring disk electrode (RRDE) setup. The catalyst inks (9.88 $\mu g \cdot \mu L^{-1}$) were prepared by mixing samples, 5 wt.% Nafion solution (Sigma-Aldrich) and 1:1 MilliQ H_2O (18.2 $M\Omega$)/Isopropanol (Sigma-Aldrich) under sonication. 2×10 μL of the catalyst ink was drop cast on the working electrode (glassy carbon electrode, $S_{geo} = 0.247$ cm^2 with a platinum ring) while the electrode was rotating slowly. The electrode was dried under heat-flux (and while maintaining rotation) between each deposition. A final layer of 800 $\mu g \cdot cm^{-2}$ loadings was derived. The catalyst was activated in an N_2-saturated electrolyte through 100 cycles at 500 $mV \cdot s^{-1}$ between 0.05 and 1.23 V vs. RHE, followed by 3 cycles at 20 $mV \cdot s^{-1}$ and linear sweep voltammetry between 0.05 and 1.05 V vs. RHE at 20 $mV \cdot s^{-1}$ (as a baseline correction). Then, linear sweep voltammetry between 0.05 and 1.05 V vs. RHE at 20 $mV \cdot s^{-1}$ was measured at 900 rpm and 1600 rpm at O_2-saturated electrolyte. The data was corrected from the ohmic losses in solution and the baseline obtained in N_2-saturated electrolyte.

4.3 Precursors Selection and Characterization

As verified by X-ray diffraction (XRD), ZIF-8 (**Figure 4-1b**) and ZIF-67 (**Figure 4-1e**) are both pure crystalline products. The pattern of the ZIF-8 correlates well with the structure reported by Yaghi's group [132]. In the pattern of the ZIF-67, extra peaks were observed at 2θ keV $\approx 37.8°$,

39.6°, and 46.1° (X-ray energy was converted to 8keV from 25 keV based on Bragg's law) compared to the standard simulated XRD pattern structure [133]. Those peaks might correspond to Co(OH)2 (PDF# 00-030-0443) and CoN (PDF# 01-083-8039), which was probably in coexistence with the cobalt source materials used to synthesize the ZIF-67 and will be discussed in the in situ XRD results. Thermogravimetric analysis (TGA) was performed to examine the sample mass changes during the pyrolysis. The derivative thermogravimetry (DTG) profile reveals transforming temperature points, which were later used as the observation points for in situ experiments (**Figure 4-1c** and **Figure 4-1f**). For ZIF-8, the DTG curve shows a sharp peak at 625 °C, which should be due to Zn evaporation after the ZIF-8 melting and decomposition [134]. The sample mass of the ZIF-8 kept decreasing after 625 °C and did not reach a plateau. The DTG curve of ZIF-67 exhibits continuous peaks from around 490 °C to 615 °C. This should correspond to ZIF-67 melting and decomposition [135,136].
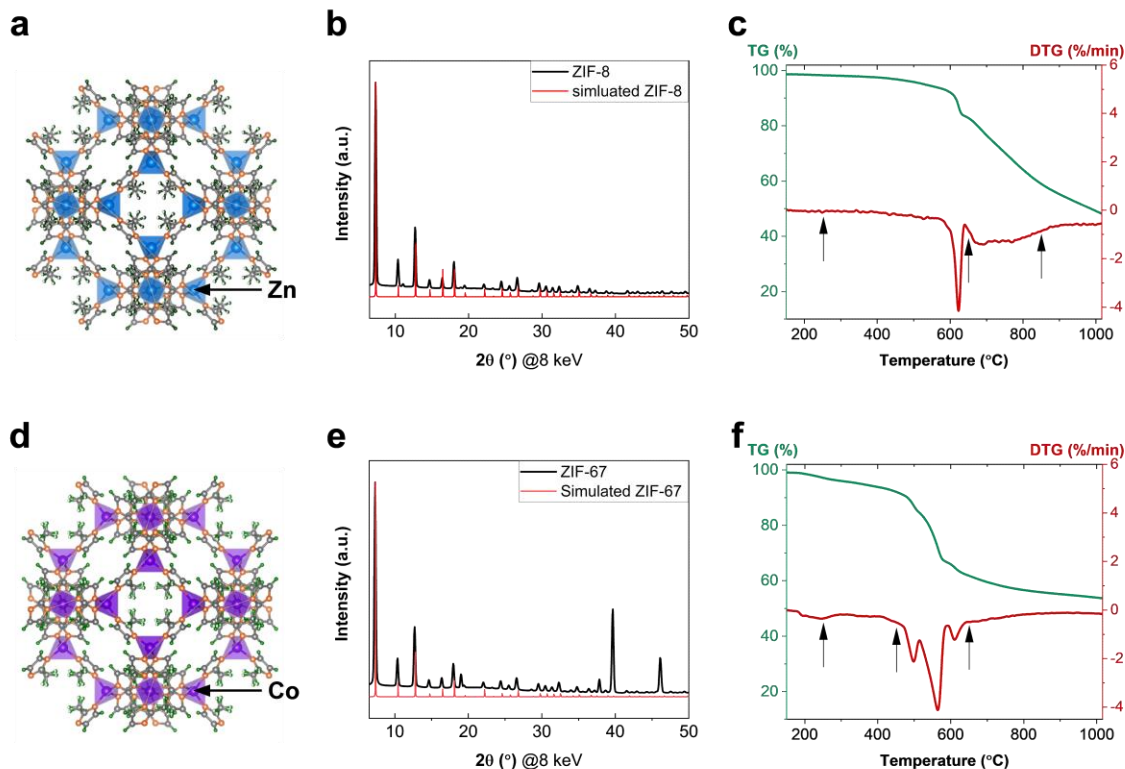
Figure 4-1 Characterization of the ZIF-8 and ZIF-67.

(a) the crystal structure of ZIF-8. (b) X-ray diffraction patterns of ZIF-8 and simulated pattern (CCDC-602542). The X-axis of the pristine ZIF-8 data has been converted from 25 keV (0.4959 Å) to Cu kα (1.5406 Å). (c) TGA profile of ZIF-8 under Ar atmosphere. Arrows show the temperature points during the process chosen to be study in the *in situ* STEM experiment. (d) the crystal structure of ZIF-67. (e) X-ray diffraction patterns of ZIF-67 and simulated pattern (CCDC-671073). The X-axis of the pristine ZIF-67 data has been converted from 25 keV (0.4959 Å) to Cu kα (1.5406 Å). (f) TGA profile of ZIF-67 under Ar atmosphere. Arrows show the temperature points during the process chosen to be study in the *in situ* STEM experiment.

4.4 Transformation of ZIF-8 during Pyrolysis

The pyrolysis step is critical for converting MOFs into M-N-C catalysts, and often leads to severe morphological transformations. *In situ* scanning transmission electron microscopy (STEM) experiments performed under a vacuum environment reveal the change of the precursor morphology within a selected field of view. In the pristine images of the ZIF-8, hexagonal facets were clearly shown (**Figure 4-2a** and **Figure 4-3**). The corresponding energy-dispersive X-ray spectroscopy (EDS) indicates that Zn, N, and C are all distributed uniformly (**Figure 4-4**). When the temperature was elevated, the overall shape of the materials did not show apparent changes (**Figure 4-2a and Figure 4-5**). With image thresholding, the percentage change of area of ZIF-8

106

shown in the STEM from all temperatures can be quantified. The captured area of the materials

in the region of interest (ROI) decreased by 34.7% at 650 °C and then by 45.2% at 850 °C

compared to the pristine image (Table 4-2). Only half of the area of the material is left in the ROI

after finishing the pyrolysis process. The EDS mapping reveals that very little of the Zn was left

after pyrolysis. A zoom-in ROI showing a hexagonal facet of the ZIF-8 is also provided (**Figure

4-6**, **Figure 4-7**, **Figure 4-8**, and **Figure 4-9**). The structure became loose and more porous when

the temperature was increased to 650 °C. At 850 °C, the structure transformed into a more

fibrous and disordered state, and turbostratic carbon as well as some clusters (most likely zinc)

appeared. After the sample was pyrolyzed to 1050 °C and after cool down, the structure became

more open. Also, more bright dots were shown, indicating some metal clusters formed. These

bright dots are most likely zinc clusters (**Figure 4-10** - **Figure 4-11**). The *in situ* nano-CT

experiments reveal the changes in the materials in three-dimensional views. No noticeable

transformation was observed before 650 °C. When comparing the volume of an ROI calculated

based on the segmentation results, the materials shrank by 23.8% (Table 4-3 **and Figure 4-12**).

This is consistent with the results gained from thresholding STEM images. More representative

cross-section images from the *in situ* nano-CT experiments are shown in **Figure 4-13** - **Figure

4-14**.
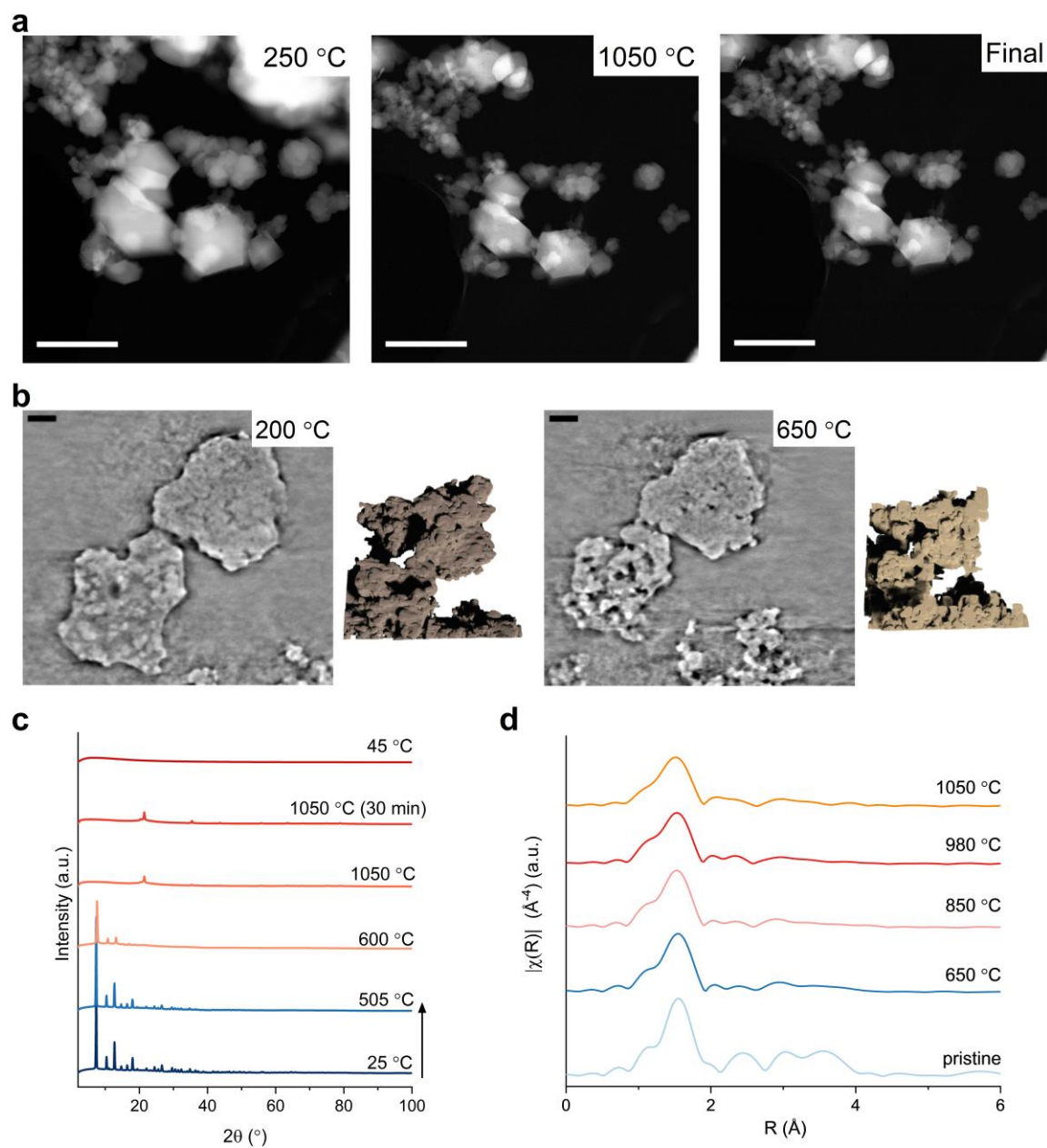
Figure 4-2 *In situ* transformation of the ZIF-8 during pyrolysis.

(a) *In situ* STEM experiment under vacuum. HAADF-STEM images for ZIF-8 during pyrolysis at 250 °C, 1050 °C and after cold down are shown. Scale bar: 500 nm. (b) *In situ* nano-CT experiment under N_2 environment. Grayscale images and the three-dimensional volume renderings of the identical location of ZIF-8 during pyrolysis at 200 °C and 650 °C are shown. Scale bar: 1,000 nm. (c) *In situ* XRD experiment under flowing 5% H_2 + 95% Ar. Selected XRD patterns of ZIF-8 recoded at selected temperatures are shown. The X-axis has been converted from 25 keV (0.4959 Å) to Cu kα (1.5406 Å). The arrow indicates the reaction progress. (d) *Ex situ* EXAFS of the ZIF-8 and ZIF-8 pyrolyzed at 650 °C, 850 °C, 980 °C and 1050 °C under Ar environment.
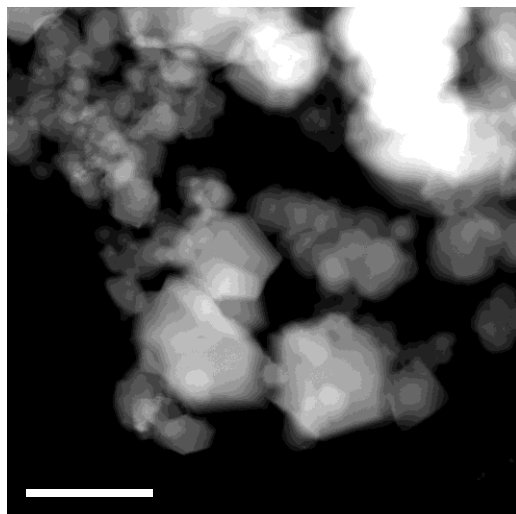
Figure 4-3 Enlarged STEM image of the pristine ZIF-8。

Pristine

$$\frac{C}{Zn}$$
$$\overline{N}$$

500 nm
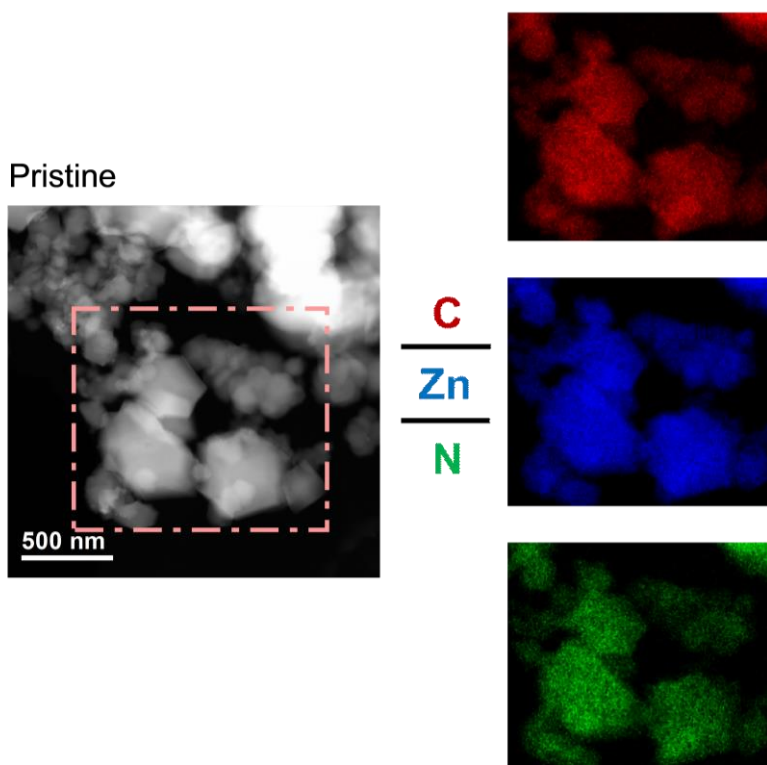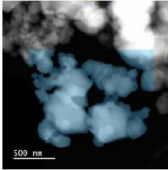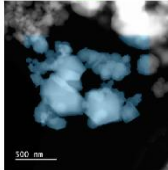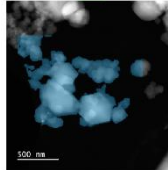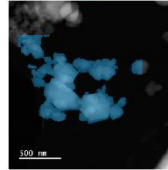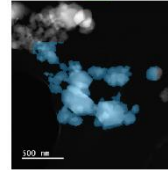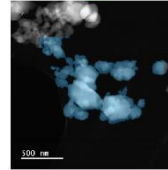
Figure 4-4 EDS mapping of the pristine ZIF-8 at the beginning of the in situ heating experiment.
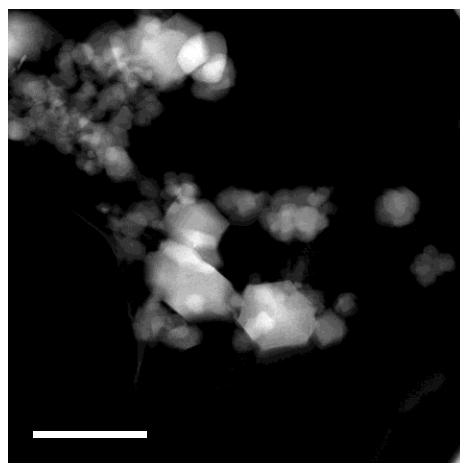
Figure 4-5 Enlarged STEM images of the ZIF-8 at 1050 °C during the in situ heating experiment.

Table 4-2 Observation of the Transformation in *in situ* STEM experiment of ZIF-8

	25 ⁰C	250 ⁰C	600 ⁰C	850 ⁰C	1050 ⁰C	Cold down
*Scale bar: 500 nm						
Resolution (µm/pixel)	0.01	0.0065	0.0065	0.0065	0.0065	0.0065
pixels chosen (rectangle)	18120	42872	42872	42872	42872	42872
Area chosen (rectangle)	1.81	1.81	1.81	1.81	1.81	1.81
pixels label	12382	25063	19170	16123	14732	14641
Calculated area label (µm²)	1.24	1.06	0.81	0.68	0.62	0.62
Area changes compared to 25 ⁰C	-	-14.52%	-34.68%	-45.16%	-50.00%	-50.00%

Area changes compared to 250 ⁰C	-	-	-23.51%	-35.67%	-41.22%	-41.58%
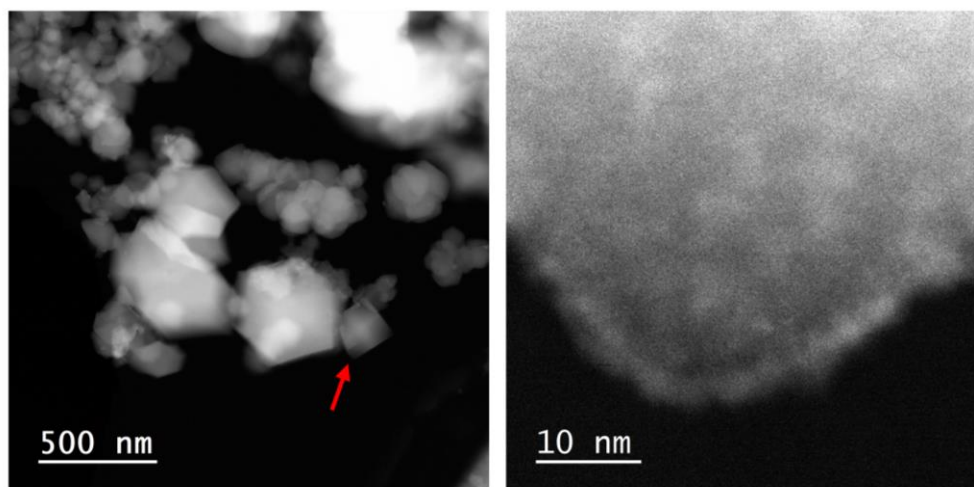
Figure 4-6 Enlarged STEM images of the ZIF-8 at 250 °C during the in situ heating experiment.

The red arrow points out the area that the second image shows.
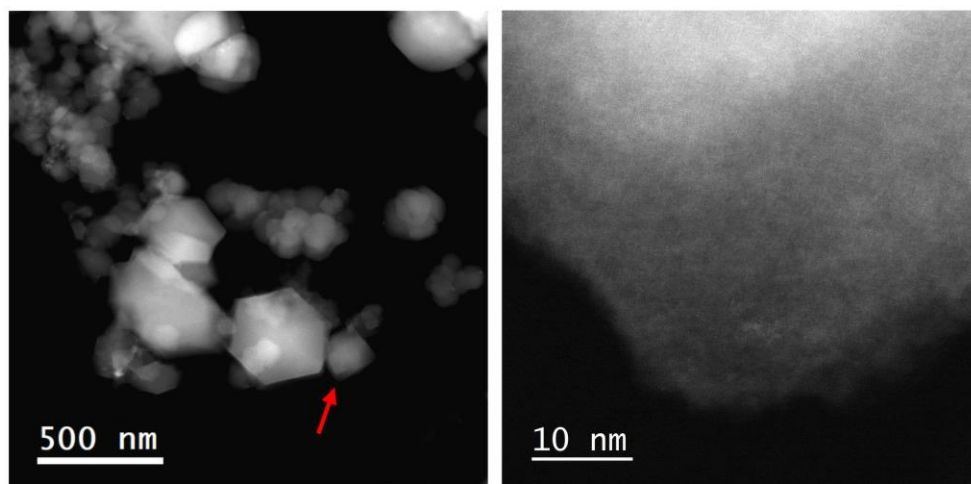
Figure 4-7 Enlarged STEM images of the ZIF-8 at 650 °C during the in situ heating experiment.

The red arrow points out the area that the second image shows.
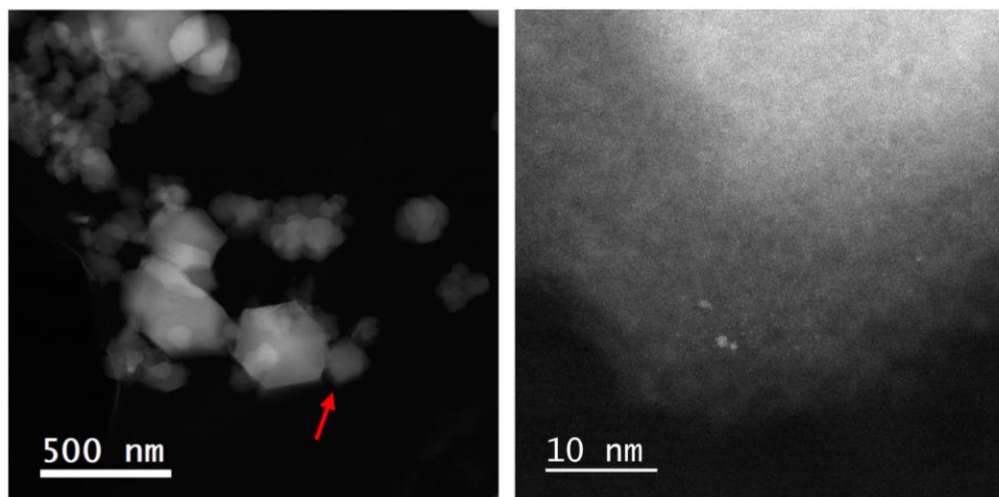
Figure 4-8 Enlarged STEM images of the ZIF-8 at 850 °C during the in situ heating experiment.

The red arrow points out the area that the second image shows.
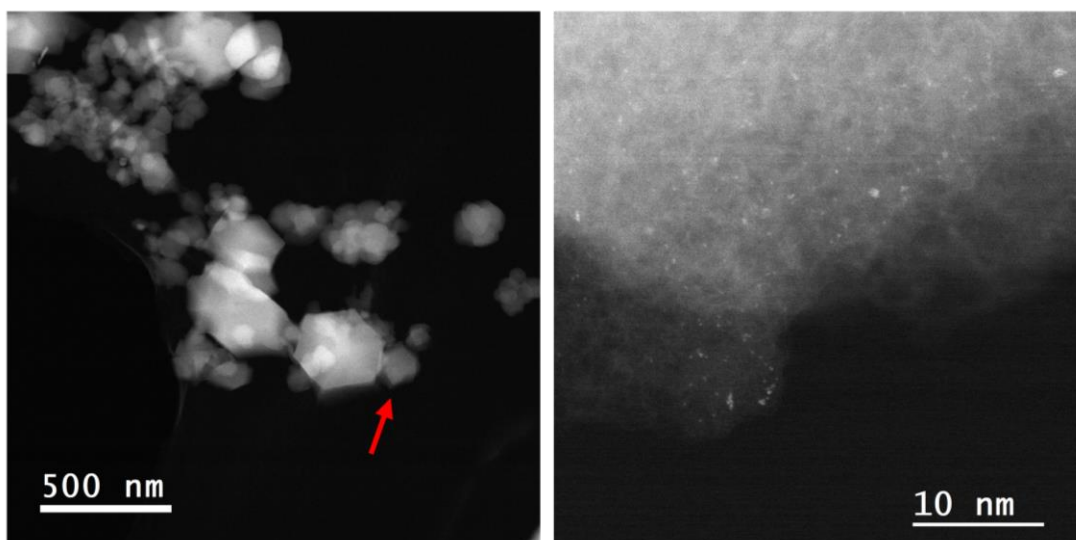
Figure 4-9 Enlarged STEM images of the ZIF-8 pyrolyzed to 1050 °C and then cold down during the in situ heating experiment.

The red arrow points out the area that the second image shows.
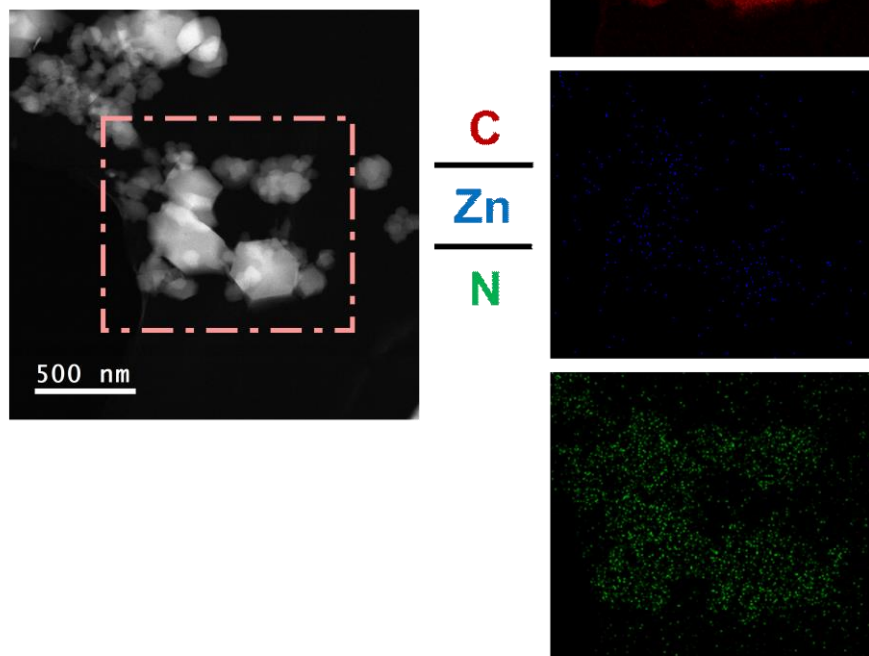
Figure 4-10 EDS mapping of the pyrolyzed ZIF-8 at the end of the in situ heating experiment. (Region I)
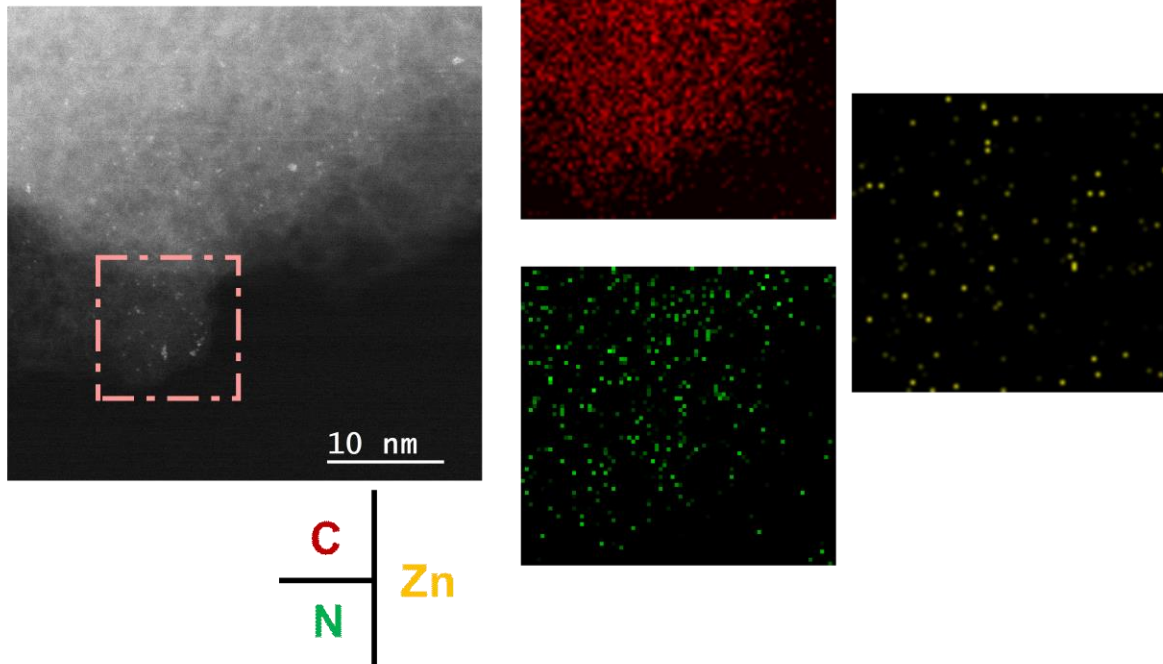
Figure 4-11 EDS mapping of the pyrolyzed ZIF-8 at the end of the in situ heating experiment. (Region II)

a

b
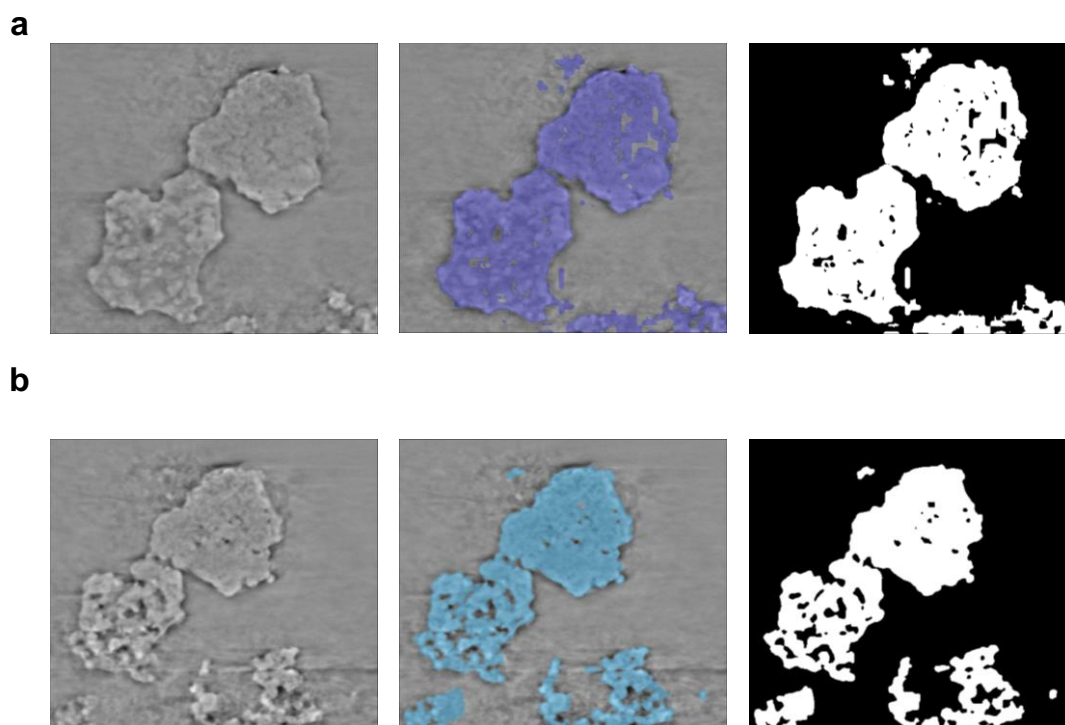
Figure 4-12 Segmentation results shown on the representative cross-section image of the ROI of the *in situ* nano-CT experiment of ZIF-8.

(a) sample at 200 °C; (b) sample at 650 °C. The field of view is 10.6925 µm x 9.6915 µm.

Table 4-3 Voxels labeled as catalysts in the ROI from the *in situ* nano-CT data of ZIF-8

Temperature	Voxel Labeled	Calculated Volume
200 °C	19,278,348	186.3 µm^3
650 °C	14,693,895	142.0 µm^3

*Size of ROI: 10.6926 µm × 9.4785 µm × 7.9875 µm

200 °C

400 °C

650 °C
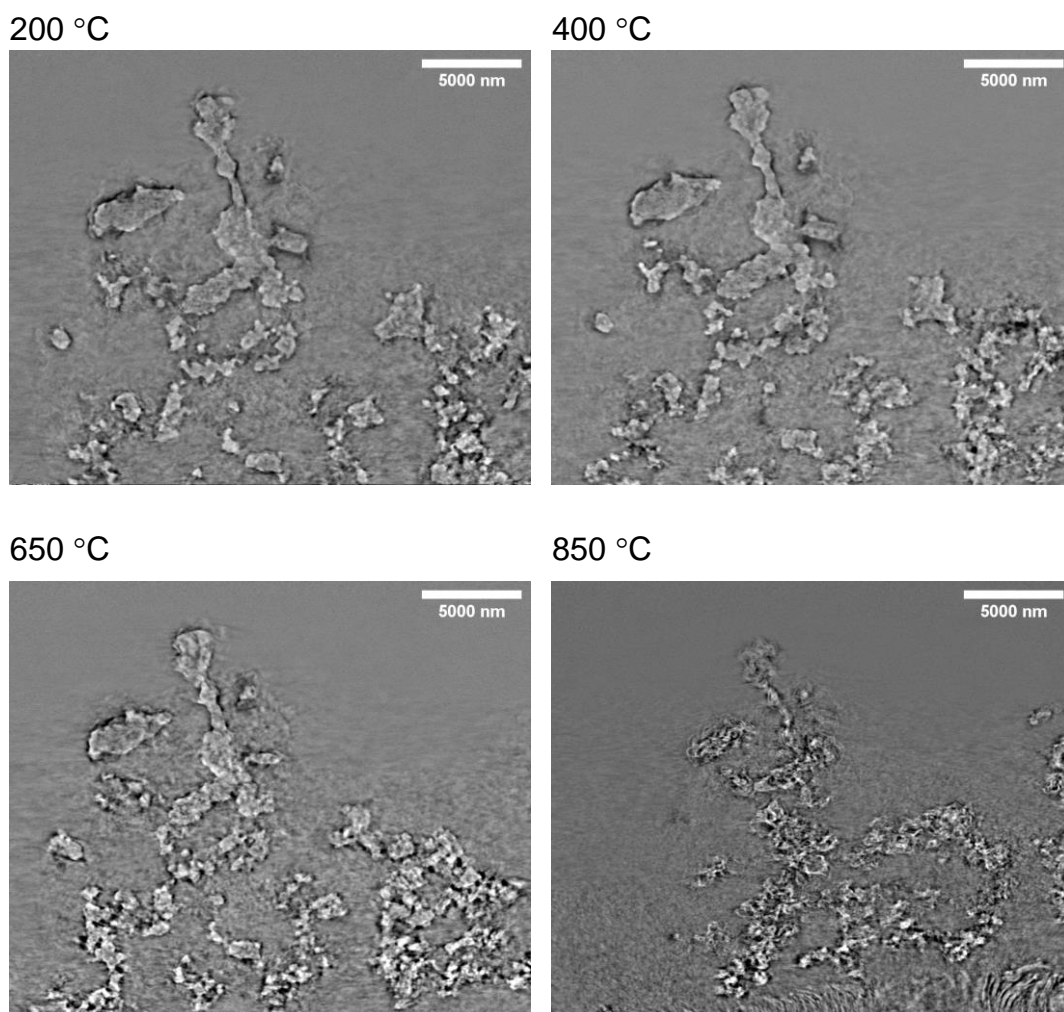
850 °C

Figure 4-13 Representative cross-section images of the in situ nano-CT experiment of ZIF-8 (Region I).

Note: The sample vibrated a lot at 850 °C

116
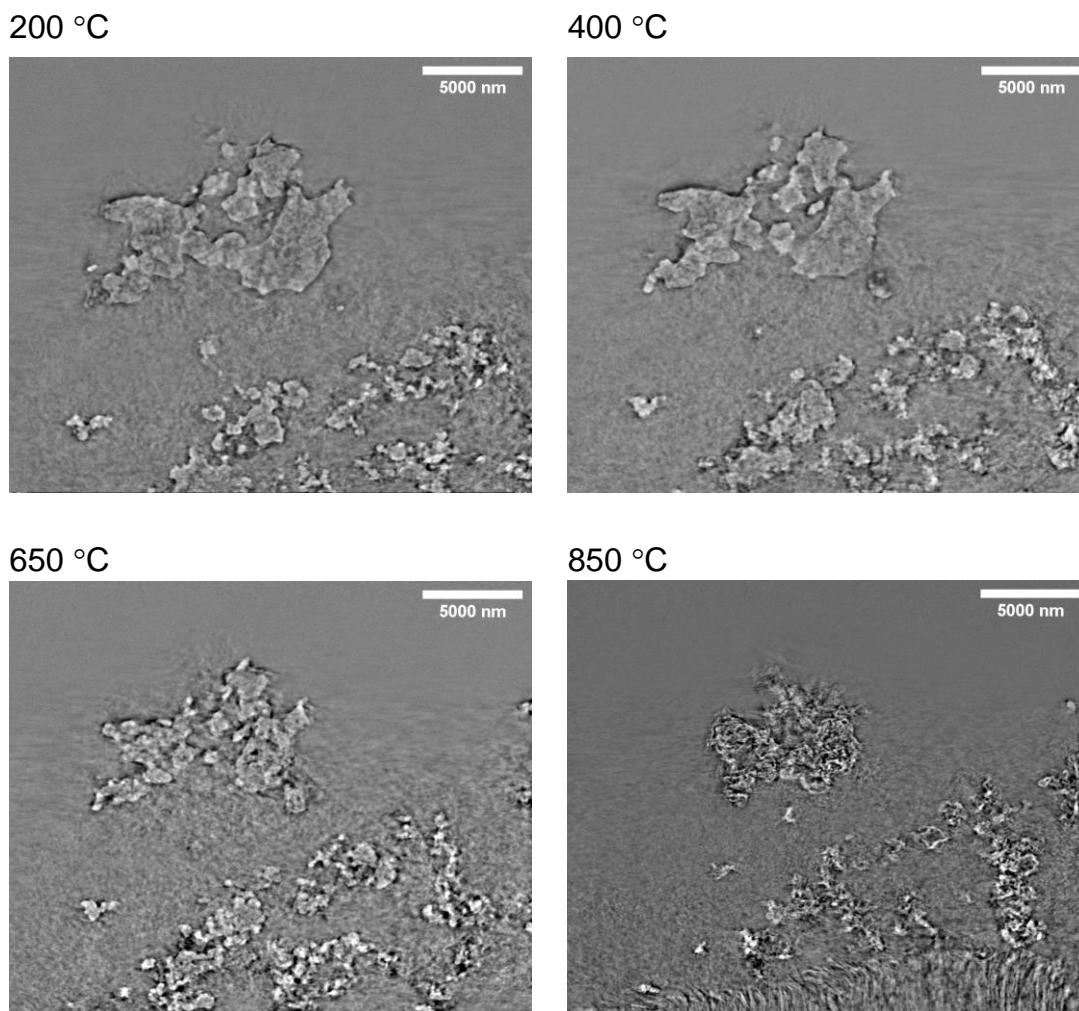
Figure 4-14 Representative cross-section images of the in situ nano-CT experiment of ZIF-8 (Region II).

Note: The sample vibrated a lot at 850 °C

Crystal structure transformations were observed by performing *in situ* XRD experiment during

the pyrolysis. The evolution patterns of ZIF-8 were collected at the rate of 10 °C min^{-1} and under

a flowing gas stream composed of 5% H_2 and 95% Ar (**Figure 4-2c** and **Figure 4-15**). The

atmosphere used here contains hydrogen to remove oxygen and avoid oxidation in the system.

Based on catalytic performance of the samples pyrolyzed in different atmosphere reported in the

previous publication [17,45,137], the hydrogen amount used here should not provide enough chemical

potential to significantly change the pyrolysis process when comparing the samples pyrolyzed in

pure Ar/N$_2$. Note that all reflections are shifted toward lower 2θ compared to the reference patterns due to thermal expansion. All reflections related to pristine MOF structure started disappearing at around 520 °C, indicating decomposition or amorphization. With the temperature increase to 640 °C, the reflections disappeared, and only flat patterns remained (**Figure 4-16**). There was a reflection at 2θ≈ 21.5° appearing at 970 °C, which later disappeared when the temperature decreased. This reflection probably belongs to α-cristobalite ($P4_12_12$, PDF# 00-039-1425), belonging to the sample-containing SiO$_2$ capillary. From the *ex situ* data of the pyrolyzed ZIF-8 (**Figure 4-17**), this reflection was not observed, indicating that the SiO$_2$ is not inside the samples. No other new reflection appeared when comparing the final pattern with the pristine one, confirming that no other crystalline structure was formed during the pyrolysis. The sample became totally amorphous after the experiment. The process of amorphization at the lower temperature can be better demonstrated with the relative crystallinity changes with temperatures in ZIF-8 (**Figure 4-18**). The relative crystallinity of ZIF-8 was reduced to 53%, when the sample was pyrolyzed to around 600 °C. This number later decreased to zero at around 640 °C, indicating that the sample was totally amorphized[138]. The decrease in the relative crystallinity can be attributed to the local ZnN$_4$ tetrahedron deformation, meaning that the long-range-order structure has been transformed into the short-range-order one.
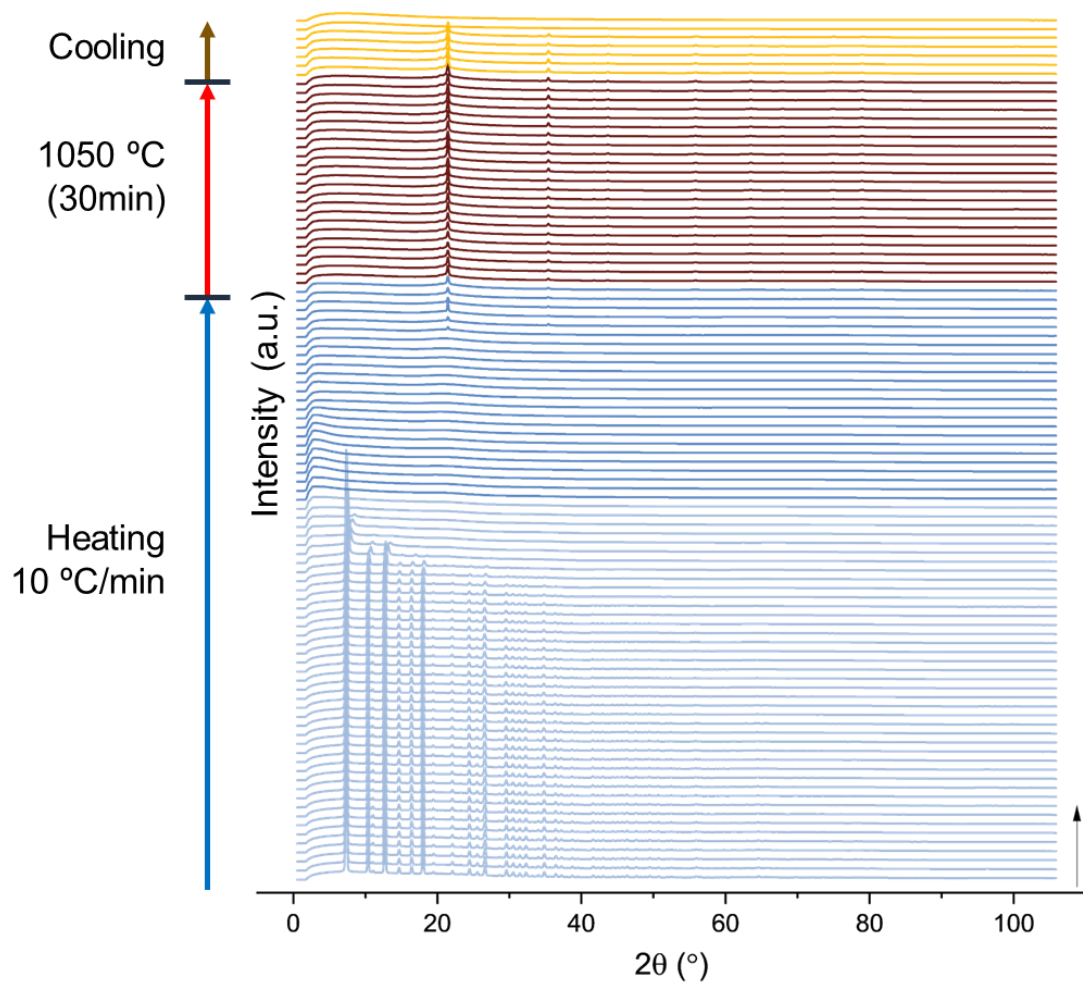
Figure 4-15 *In situ* XRD data of ZIF-8.

Note: X-axis (2 Theta) was converted from 25 keV (0.4959 Å) to Cu Kα (1.5406 Å)
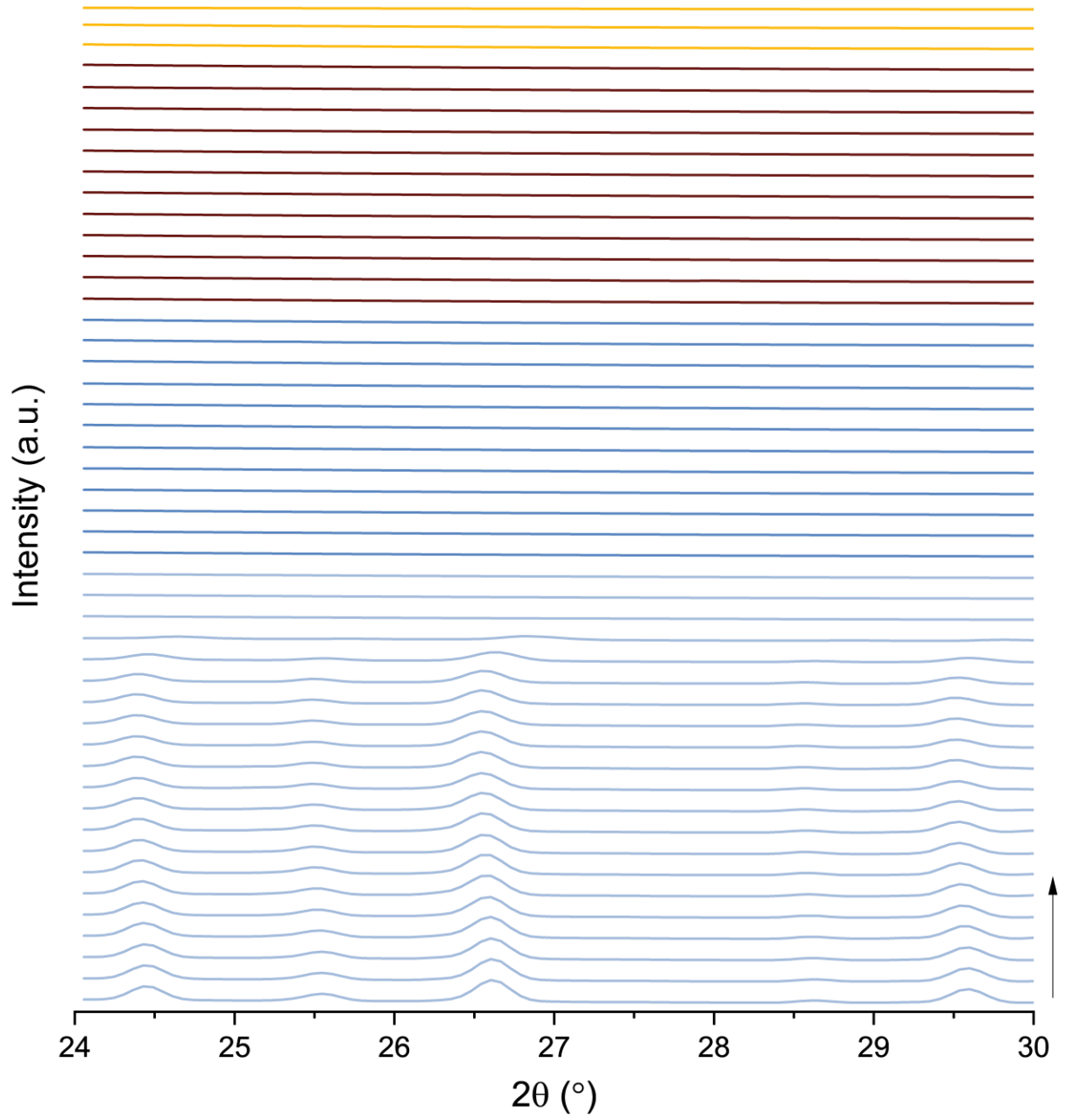
Figure 4-16 *In situ* XRD data of ZIF-8 zooming into 24° to 30°.

Note: X-axis (2 Theta) was converted from 25 keV (0.4959 Å) to Cu Kα (1.5406 Å)
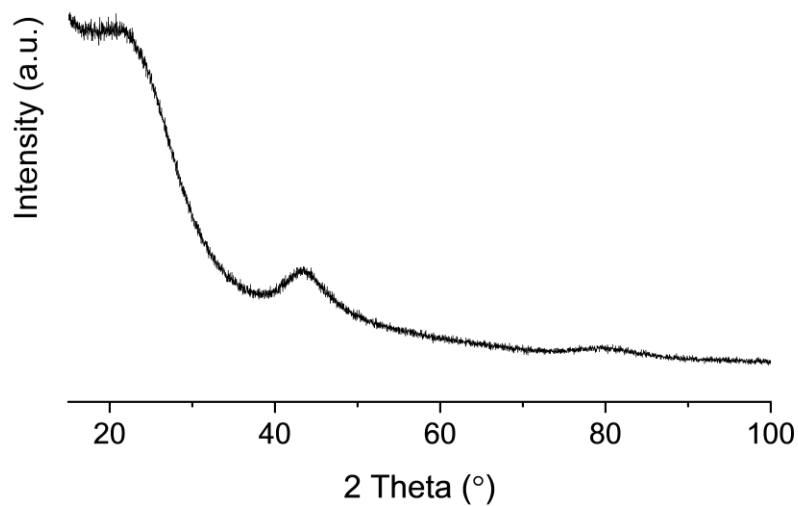
Figure 4-17 *Ex situ* XRD data of ZIF-8 pyrolyzed to 1050 °C.

Note: Measurement was done with Cu Kα (1.5406 Å)
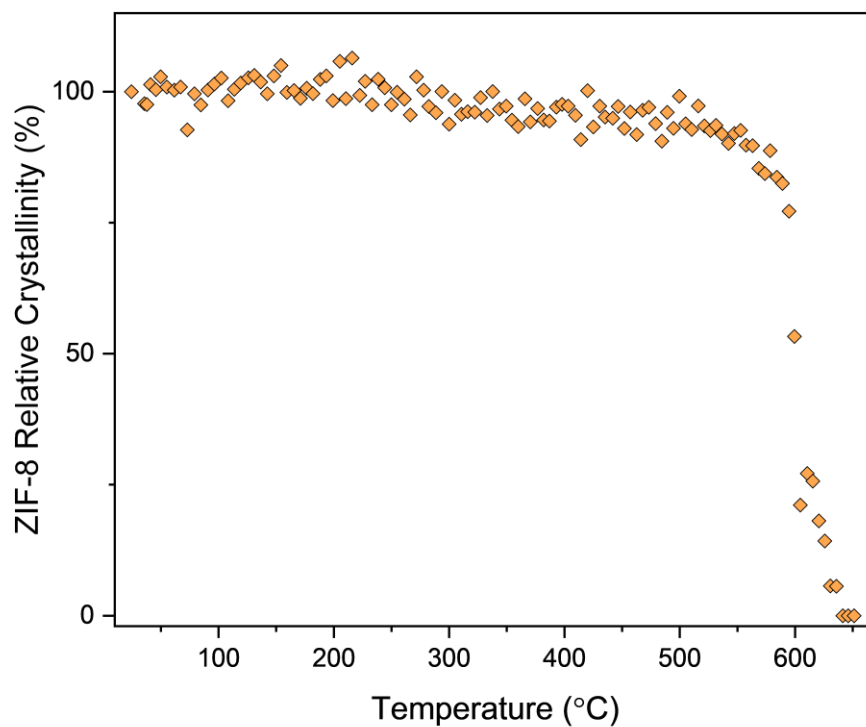
Figure 4-18 ZIF-8 relative crystallinity as a function of the temperature.

Note: The relative crystallinity was calculated by integrating area under the peaks of the in situ XRD spectra and compared the integration to the one calculated based on the pristine spectrum.

To get more information about the structural changes, *ex situ* XAS at the Zn K-edge was measured on the ZIF-8 pyrolyzed to 650 °C, 850 °C, 980 °C, and 1050 °C under Ar atmosphere. The pronounced peaks at 1.55Å in Zn K-edge R space plots (**Figure 4-2d**) can be assigned to the Zn-N shell. It revealed that some Zn remained in the sample after pyrolysis, and they are bonded with N to form $Zn-N_x$ sites (x=4.5±0.5, Table 4-4**, Figure 4-19**). The XANES data (**Figure 4-20**) of pristine ZIF-8 shows features at 9666.1 eV and 9673.7 eV, which should be associated with tetrahedral ZnN_4. The former feature appears due to the Zn 1_s → Zn 4_p transitions, while the latter feature reflects the multiple scattering of the mid-range order structure [27,139,140]. After pyrolysis, a peak at ca. 9669 eV showed up as the only feature, which indicates the the existence of ZnN_4 (D_{4h} symmetry). This feature shifted to lower energy when comparing the sample pyrolyzed to 650 °C to those at higher temperatures. This change was caused by the variation in the degree of distortion of the D_{4h} symmetry. Given the fact that square planar ZnN_4 should cause a peak at around 9667 eV, the above phenomenon indicates that Zn^{2+} were sitting closer to the porphyrin-like N_4 plane when the temperature was increased[141].
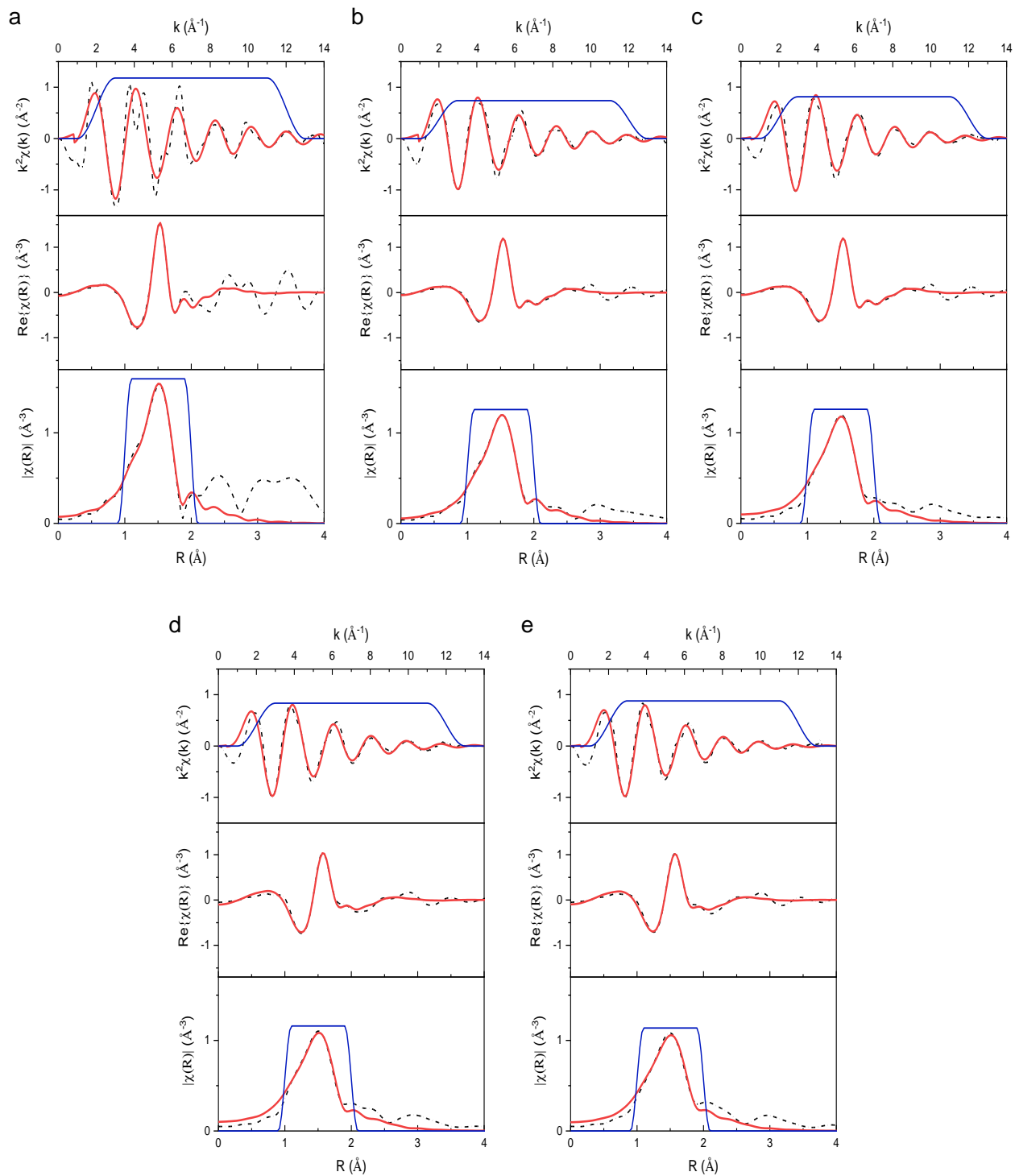
Figure 4-19 EXAFS fits of ZIF-8 pyrolyzed at different temperatures under Ar.

(a) pristine ZIF-8, (b) ZIF-8 pyrolyzed to 650 °C, (c) ZIF-8 pyrolyzed to 850 °C, (d) ZIF-8 pyrolyzed to 980 °C, and (e) ZIF-8 pyrolyzed to 1050 °C showing $k^2 \chi(k)$ (top), real part (middle) and magnitude (bottom) of $\chi(R)$. Data in black short dash dot line, fits in red solid line, and windows in blue solid line.

Table 4-4 EXAFS Fitting results for the ZIF-8 and the pyrolyzed products

	Pristine	650 °C	850 °C	980 °C	1050 °C
N_N	4.3±0.5	3.8±0.2	4.5±0.5	4.5±0.5	4.5±0.5
r_{Co-N}	1.56±0.01	1.56±0.01	1.54±0.03	1.54±0.03	1.54±0.04
σ^2_{Co-N}	0.0038±0.0015	0.0055±0.0008	0.0071±0.0016	0.0082±0.0025	0.0090±0.0025
k range (Å^{-1})	$2 \leq k \leq 12$ (dk=2)	$2 \leq k \leq 12$ (dk=2)	$2 \leq k \leq 12$ (dk=2)	$2 \leq k \leq 12$ (dk=2)	$2 \leq k \leq 12$ (dk=2)
R range (Å)	$1 \leq R \leq 2$ (dR=0.2)	$1 \leq R \leq 2$ (dR=0.2)	$1 \leq R \leq 2$ (dR=0.2)	$1 \leq R \leq 2$ (dR=0.2)	$1 \leq R \leq 2$ (dR=0.2)

* S_0^2 is set to 0.8. bond length: Å
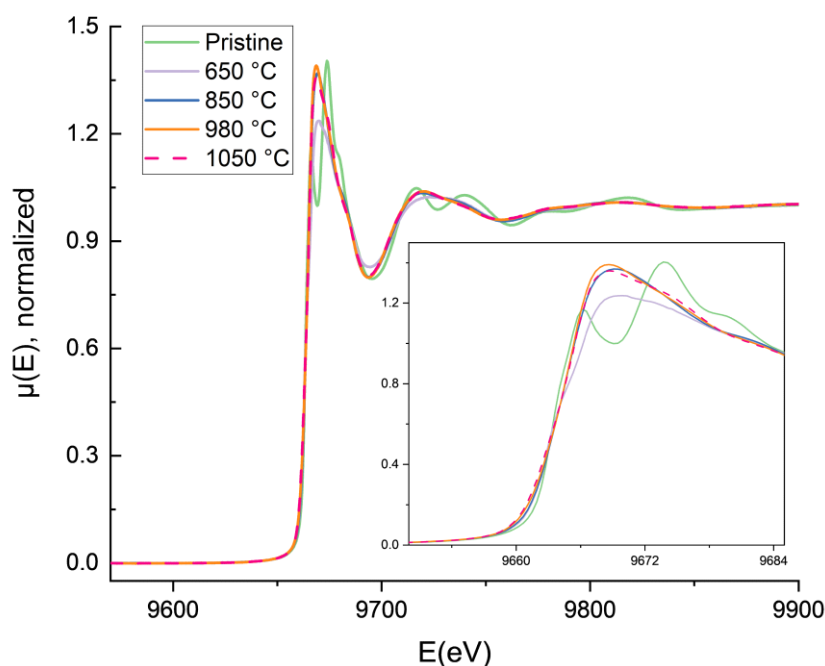
Figure 4-20 XANES of ZIF-8 pyrolyzed at different temperatures under Ar.

Ex situ Raman spectroscopy was used to understand the evolution of MOFs to carbonaceous materials. The ZIF-8 pyrolyzed to 650 °C, 850 °C, 980 °C, and 1050 °C under Ar atmosphere were measured (**Figure 4-21** - **Figure 4-22,** Table 4-5). The sample pyrolyzed to 650 °C (**Figure 4-21**) has not fully transformed into carbonaceous material; thus, the corresponding Raman spectrum is complicated by the bands assigned to methyl group vibration, D band, and G+D' band[78,127]. The G band comes from the vibration of the E_{2g} symmetry of ideal graphitic lattice

while the D' band comes from the vibration of the E_{2g} symmetry of disordered graphitic lattice. D' band is always appeared as a shoulder of G band and here they were fitted together. When the samples were pyrolyzed to 850 °C, 980 °C, and 1050 °C, the corresponding Raman can then be convolved into four peaks associated with G+D' band (~1593 cm^{-1}), distorted carbon (~1504 cm^{-1}), D band (~1346 cm^{-1}) and the sp^2 carbon outside of the graphene network (~1220 cm^{-1}) (**Figure 4-22**)[78,128]. The increased peak intensity at ~1220 cm^{-1} suggests that the carbon matrix of the sample pyrolyzed to 980 °C contains higher out-of-the-plane carbon compared to the sample pyrolyzed to a lower temperature. Once the temperature reached 980 °C, further increasing the pyrolysis temperature did not have much effect on the carbon matrix. The ratio of the intensities of the D band and G+D' band are both around 1.35 of the ZIF-8 pyrolyzed to 980 °C and 1050 °C (**Figure 4-22d**).
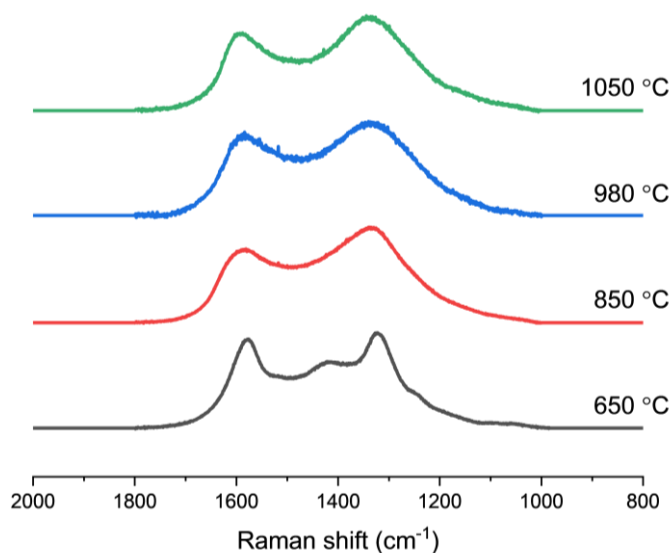
Figure 4-21 Raman spectra of pyrolyzed ZIF-8 pyrolyzed at different temperatures.
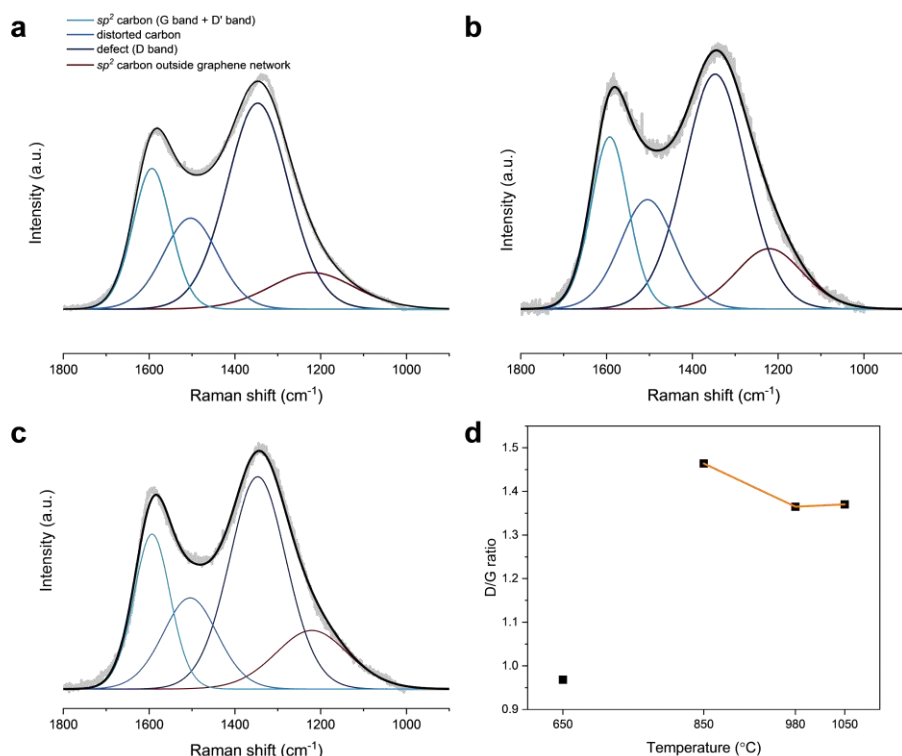
Figure 4-22 Fitted Raman spectra of pyrolyzed ZIF-8.

(a) ZIF-8 pyrolyzed to 850 °C, (b) ZIF-8 pyrolyzed to 980 °C, (c) ZIF-8 pyrolyzed to 1050 °C, (d) D/G ratio of ZIF-8 pyrolyzed to different temperatures. Note: D/G ratio refers to the intensity ratio of D band and G+D' band.

Table 4-5 D/G ratio from Raman results of the pyrolyzed ZIF-8

Temperature (°C)	I_D	I_G	I_D/I_G
650	3861.15	3987.05	0.96842
850	2315.451	1581.726	1.46388
980	528.233	386.989	1.36498
1050	1091.701	796.704	1.37027

From the morphological and structural characterization of the ZIF-8 and its pyrolyzed products, the pyrolyzed ZIF-8 can be an excellent soft template for the M-N-C catalysts. It overall retains the favorable porous structure of MOF (which would be confirmed with N_2 absorption later), contains carbon mainly with an open structure, and its metal did not agglomerate but spread out

uniformly on the matrix. The ZIF-8 pyrolyzed to 980 °C and 1050 °C should have similar

performance in terms of being a precursor for salt deposition for ORR.

4.5 Transformation of ZIF-67 during Pyrolysis

Similar characterizations have been carried out to study the transformation of ZIF-67 during pyrolysis (**Figure 4-23**). *In situ* STEM experiments reveals the morphological transformation of the ZIF-67 pyrolysis at the nanoscale. Hexagonal facets were clearly shown in the 250 °C images (**Figure 4-23a** and **Figure 4-24**). EDS indicates that Co, N, and C are all distributed uniformly (**Figure 4-25** - **Figure 4-26**). However, when the temperature reached 450 °C, metallic species started agglomerating and forming clusters of ~20 nm (**Figure 4-23a**, **Figure 4-27**, and **Figure 4-28**). These metal nanoclusters later grew into clusters of ~100 nm during the pyrolysis (**Figure 4-29**). This phenomenon is different from what was observed when pyrolyzing ZIF-8. The EDS taken after the pyrolysis confirmed that the nanoclusters were cobalt (**Figure 4-30**). The melting point and the vaporization point of the cobalt are over 1500 °C when the vapor pressure is higher than 1×10^{-7} atm [142]. The Co evaporation temperature would increase if there were atmosphere existing and the pressure were lower. Thus, after ZIF-67 melted and decomposed, the cobalt stayed in the solid state in our experiment. The cobalt clusters then migrated due to the heating. Several clusters aggregated to become stable, and thus the cobalt cluster size grew [143]. The cobalt clusters started catalyzing the carbon graphitization once the temperature reached over 1000 °C [144,145]. The porous structure thus collapsed due to the carbon graphitization, which should result in the surface area decrease (discussed later with N_2 absorption results). From the STEM, the carbon phase in the pyrolyzed product was combined with the graphitic carbon and the amorphous carbon (**Figure 4-29**). Some of the graphitic carbon wrapped the metal particle, making the particle hard to be removed by the acid etching and causing decreased porosity. The STEM images showed the precursor material area after pyrolysis inside an ROI decreased by 58.1% compared to the one pyrolyzed up to 250 °C (Table 4-6). *In situ* nano-CT experiments

reveals the changes of the materials in three-dimensions. The volume of the same ROI decreased

from around 148.4 μm^3 to 45.7 μm^3, which corresponds to percentage volume change of 69.2%

after the temperature increased from 200 °C to 980 °C (**Figure 4-31** and Table 4-7). More

representative cross-section images from the *in situ* nano-CT experiments are shown in the

Figure 4-32 - **Figure 4-33**.
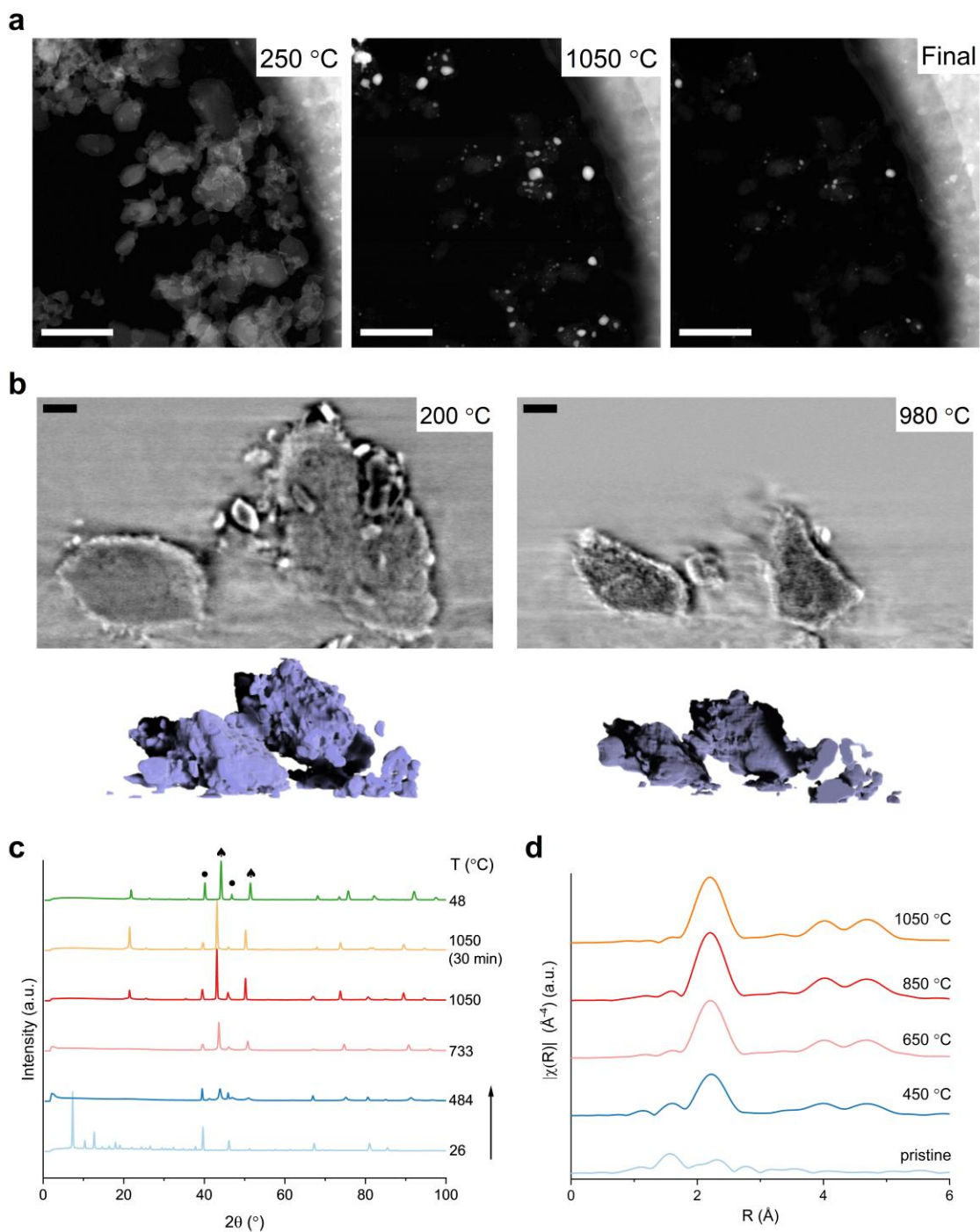
Figure 4-23 Transformation of the ZIF-67 during pyrolysis.

(a) *In situ* STEM experiment under vacuum. HAADF-STEM images for ZIF-67 during pyrolysis at 250 °C, 1050 °C and after cold down are shown. Scale bar: 500 nm. (b) *In situ* nano-CT experiment under N_2 environment. Grayscale images and the three-dimensional volume renderings of identical location of the ZIF-8 during pyrolysis at 200 °C and 980 °C are shown. Scale bar: 1,000 nm. (c) *In situ* XRD experiment under flowing 5% H_2 + 95% Ar. Selected XRD patterns of ZIF-67 recoded at selected temperatures are shown. ♠ represents Co, ● represents CoN. The X-axis has been converted from 25 keV (0.4959 Å) to Cu kα (1.5406 Å). The arrow indicates the reaction progress. (d) *Ex situ* EXAFS of the ZIF-67 and ZIF-67 pyrolyzed at 650 °C, 850 °C, 980 °C and 1050 °C under Ar environment.
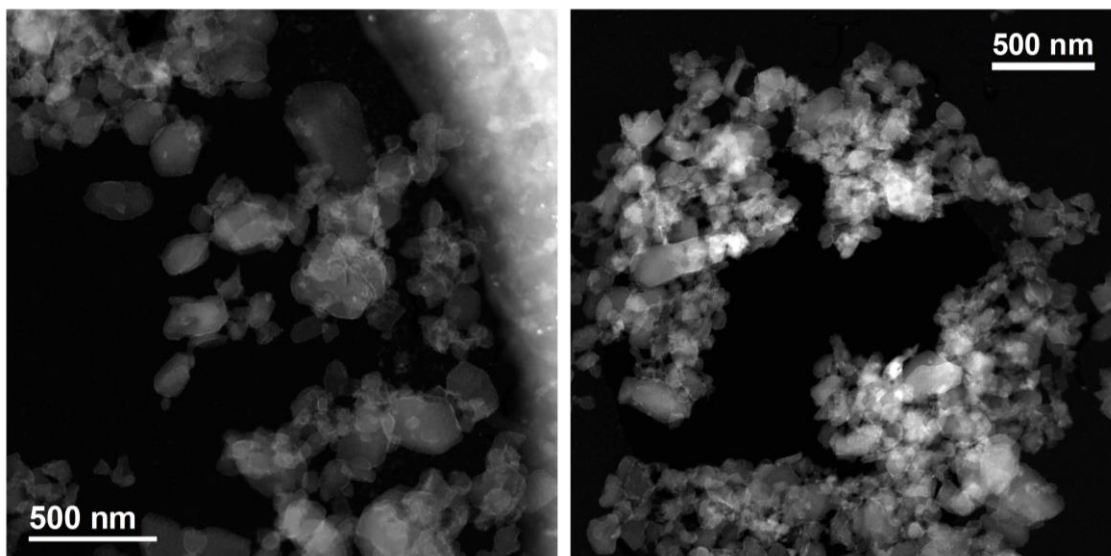
Figure 4-24 Enlarged STEM images of the ZIF-67 at 250 °C during the *in situ* heating experiment.
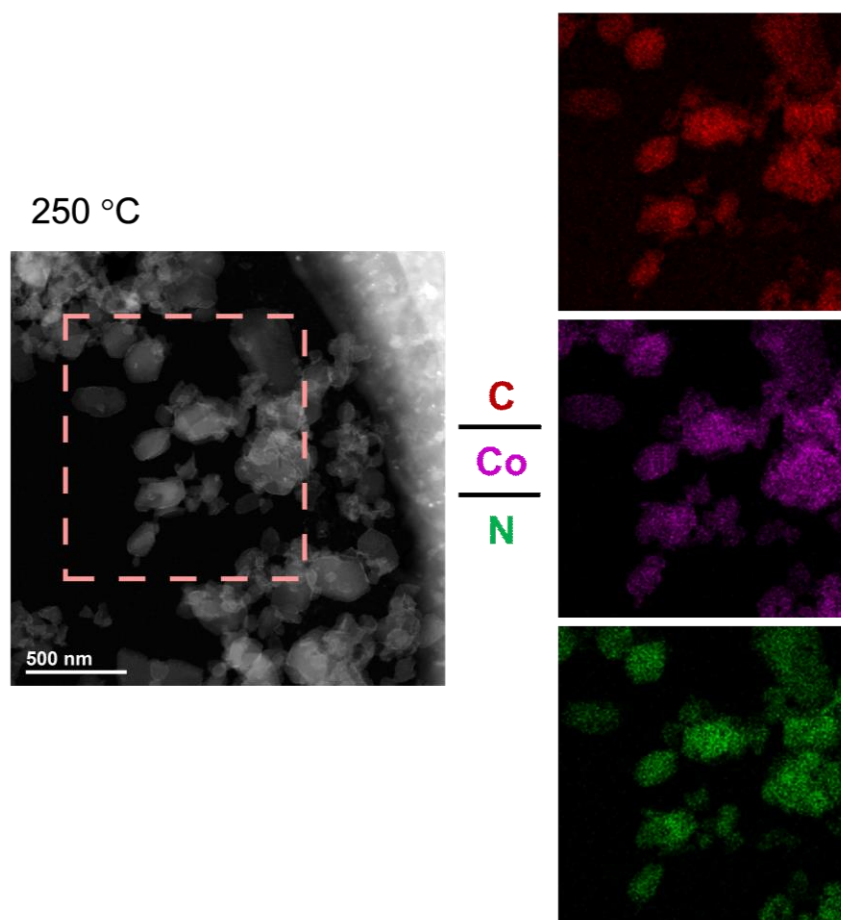
Figure 4-25 EDS mapping of the pristine ZIF-67 at 250 °C of the *in situ* heating experiment. (Region I)
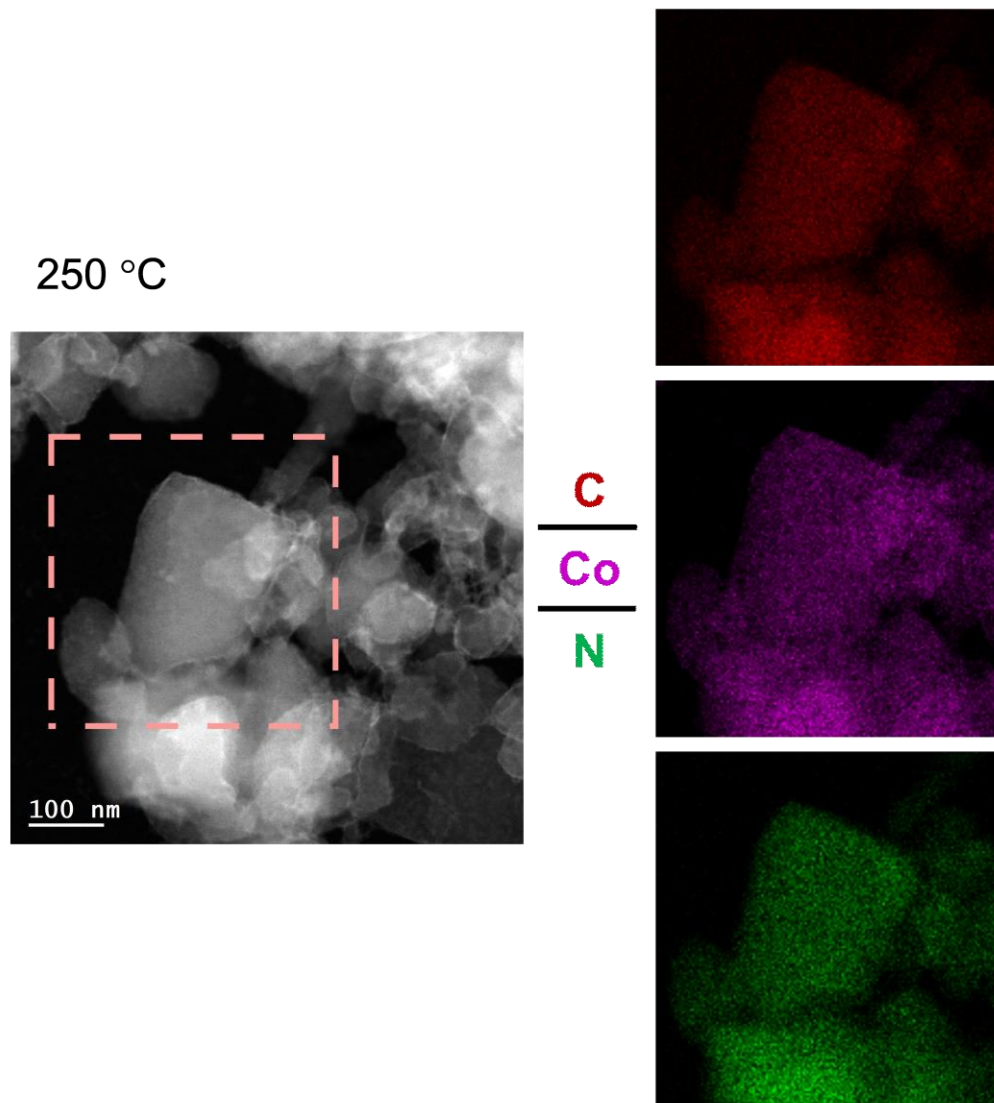
Figure 4-26 EDS mapping of the pristine ZIF-67 at 250 °C of the *in situ* heating experiment. (Region II)
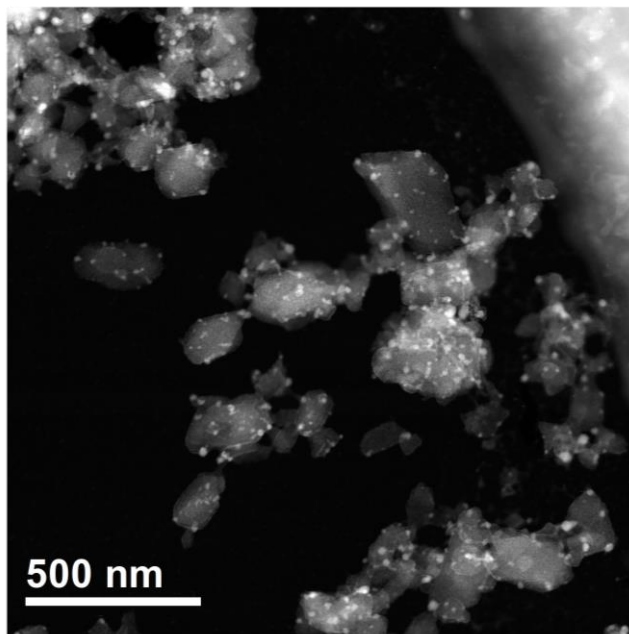
Figure 4-27 Enlarged STEM images of the ZIF-67 at 450 °C during the *in situ* heating experiment.
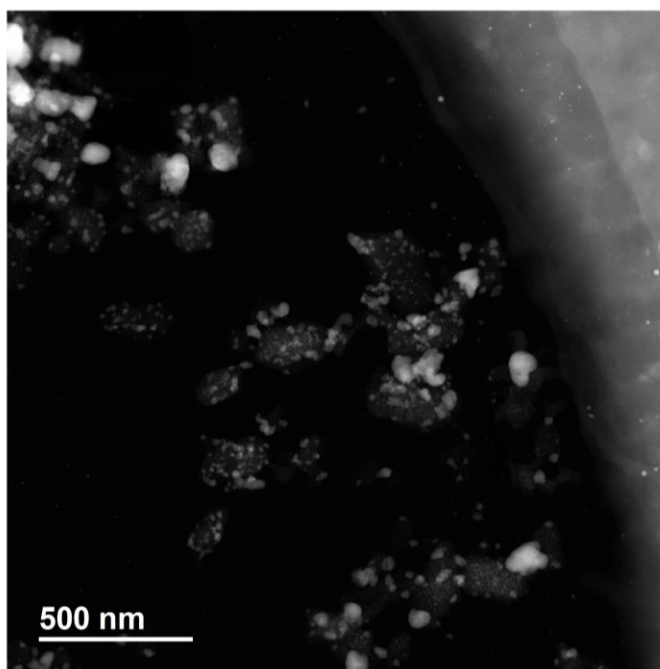
Figure 4-28 Enlarged STEM images of the ZIF-67 at 650 °C during the in situ heating experiment.
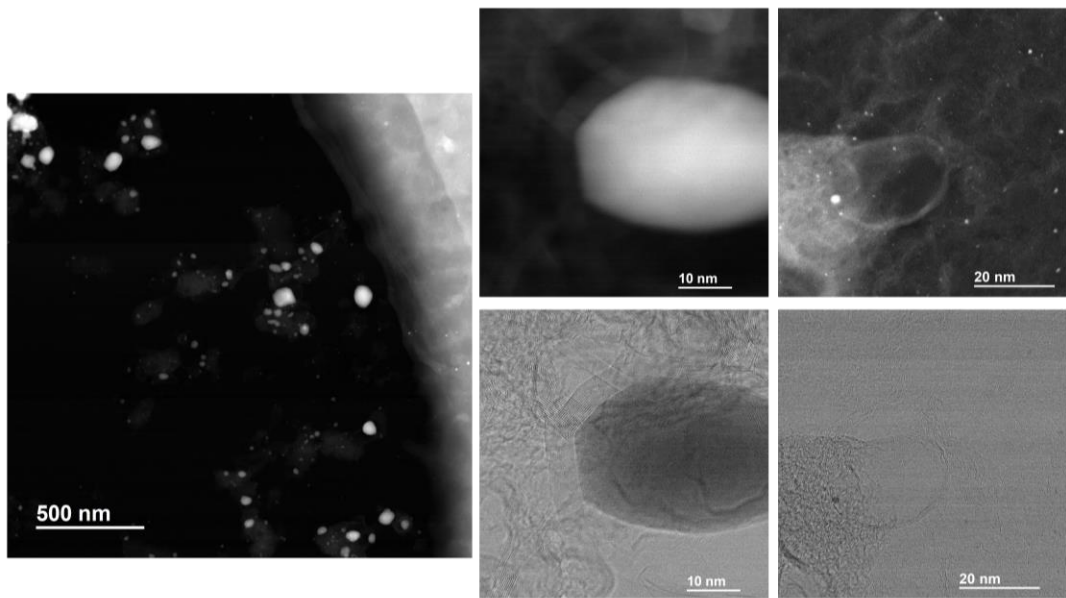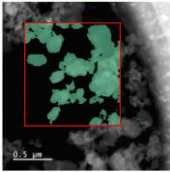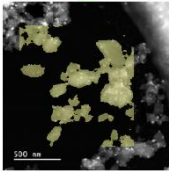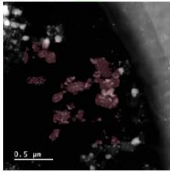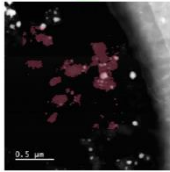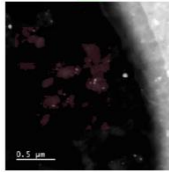
Figure 4-29 Enlarged STEM images of the ZIF-67 at 1050 °C during the *in situ* heating experiment.

Figure 4-30 EDS mapping of the pyrolyzed ZIF-67 at the end of the *in situ* heating experiment.

	250 ⁰C	450 ⁰C	650 ⁰C	1050 ⁰C	Cold down
Scale bar: 0.5 µm					
Resolution (µm/pixel)	0.01	0.0084	0.01	0.01	0.01
pixels chosen (rectangle)	16368	23236	16368	16368	16368
Area chosen (rectangle)	1.64	1.64	1.64	1.64	1.64
pixels label	16368	23236	16368	16368	16368
Calculated area label (μm^2)	1	0.62	0.39	0.32	0.36
Area changes compared to 250 ⁰C	-	-27.91%	-54.65%	-62.79%	-58.14%

a

b
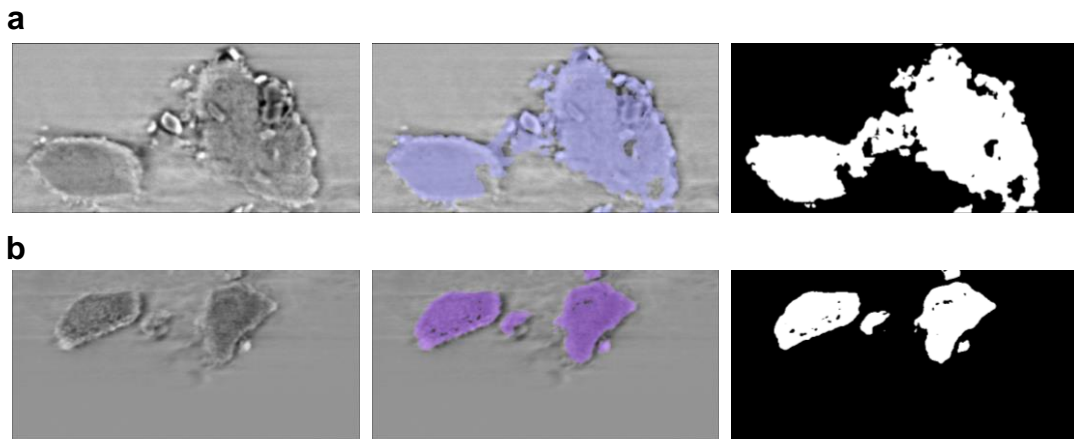
Figure 4-31 Segmentation results shown on the representative cross-section image of the ROI of the *in situ* nano-CT experiment of ZIF-67.

(a) at 200 °C; (b) at 980 °C. The field of view is 13.2699 µm x 6.4113 µm.

Table 4-7 Voxels labeled as catalysts in the ROI from the in situ nano-CT data of ZIF-67

Temperature	Voxel Labeled	Calculated Volume
200 °C	15,355,222	148.4 µm^3
980 °C	4,726,258	45.7 µm^3

Size of ROI: 13.2486 µm × 6.4752 µm × 9.7767 µm
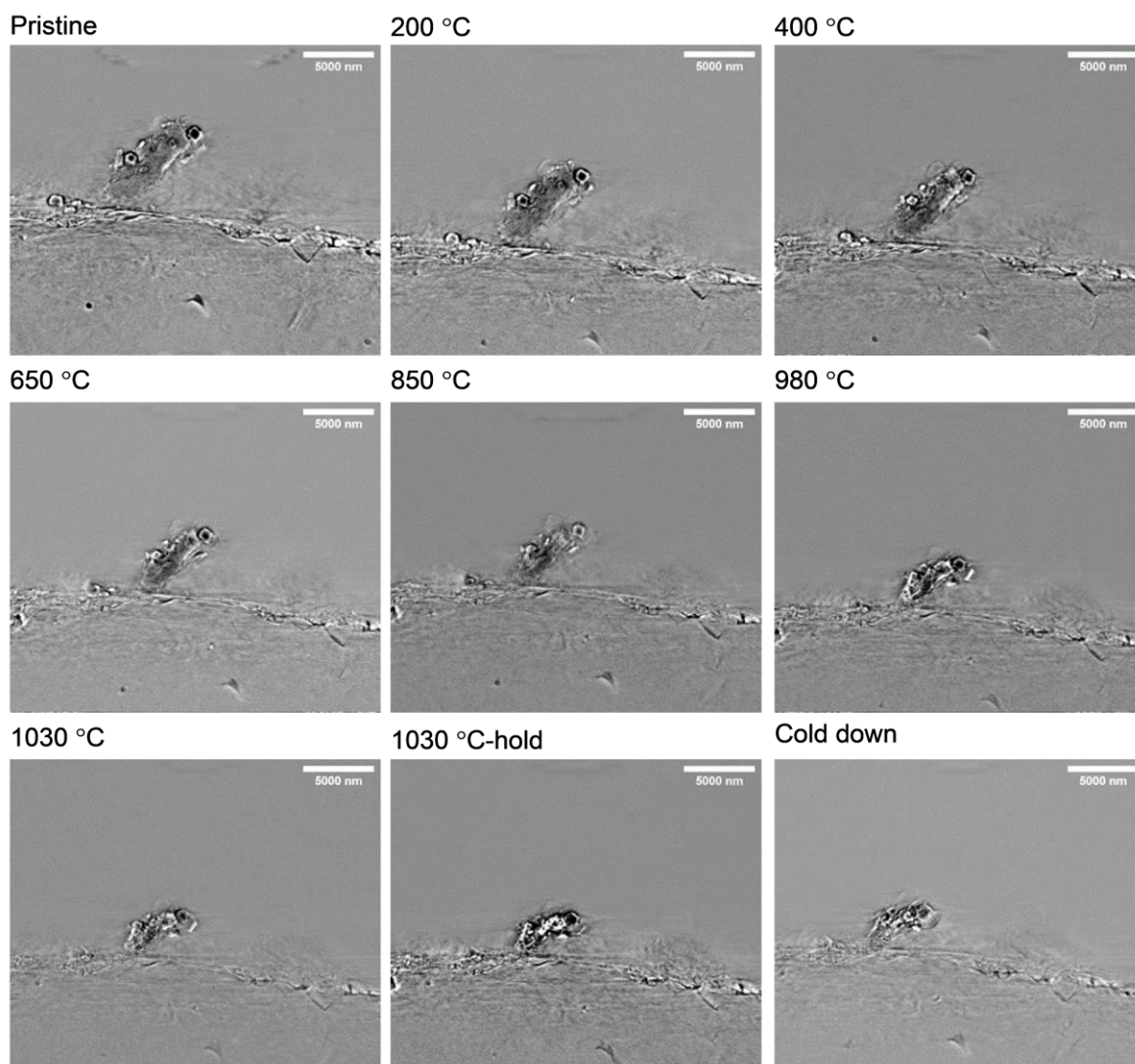
Figure 4-32 Representative cross-section images of the *in situ* nano-CT experiment of ZIF-67 (Region I).

Note: The sample vibrated intensely starting at 850 °C

136
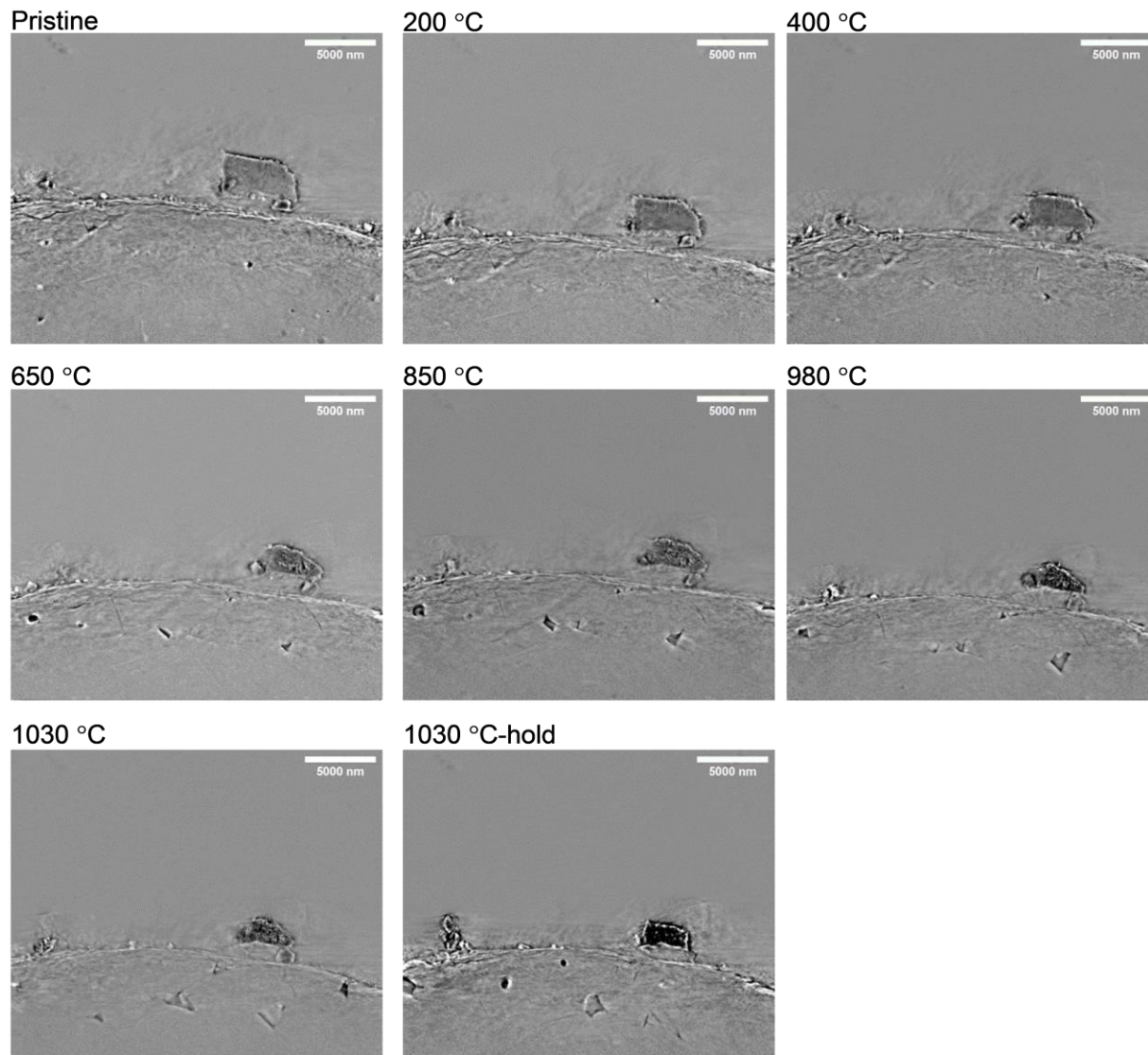
Figure 4-33 Representative cross-section images of the *in situ* nano-CT experiment of ZIF-67 (Region II).
Note: The sample vibrated intensely starting at 850 °C

The *in situ* XRD experiment of ZIF-67 was performed with a heating rate of 10 °C min^{-1} and under flowing 5% H_2 and 95% Ar atmosphere (**Figure 4-23c** and **Figure 4-34** - **Figure 4-38**). Note that all reflections are shifted toward lower 2θ compared to the reference patterns due to thermal expansion. All 2θ were reported based on the X-ray energy of 8 keV (converted from 25 keV based on Bragg's law). The main reflection of ZIF-67 (011) at $2\theta_{8\text{ keV}} \approx 7.30°$ disappeared at 446 °C, which is consistent with the aforementioned melting and decomposition point from the

TGA result (**Figure 4-1f**). The reflections at $2\theta_{8\,keV} \approx 37.8°$, $39.6°$, and $46.1°$ are assigned to Co(OH)$_2$ (PDF# 00-030-0443) and CoN (PDF# 01-083-8039). The ZIF-67 occupied 65.3 wt.%. With the temperature increasing, Co(OH)$_2$ decomposed. The reflection at $2\theta_{8\,keV} \approx 43.9°$ appeared when the samples pyrolyzed to 467 °C, and the reflection at $2\theta \approx 50.8°$ became pronounced above 625 °C. These reflections are assigned to cubic Co (111) and (200) reflections, respectively (PDF# 00-015-0806). The reflections at $2\theta_{8\,keV} \approx 47.0°$ and $41.1°$ can be assigned to hexagonal Co (PDF# 04-007-8518), which is not thermally stable above 450 °C and probably was transformed to the cubic structure at higher temperature[146,147]. CoN (PDF# 01-083-8039), which reflections appeared in the precursor's spectrum, was still present after pyrolysis. The reflection at $2\theta_{8\,keV} \approx 21.8°$, which also appeared in the ZIF-8 spectrum, can be attributed to α-cristobalite ($P4_12_12$, PDF# 00-039-1425) belonging to the capillary. The *ex situ* measurement of the ZIF-67 pyrolyzed at 1050 °C did not detect this reflection (**Figure 4-39**), suggesting that the sample did not include SiO$_2$. The reflection at $2\theta_{8\,keV} \approx 26.4°$ that appeared at approximately 992 °C with a crystallite size of around 0.36 nm (FWHM=0.3820) corresponds to the graphite (002) reflection (PDF# 00-041-1487) (**Figure 4-40**). During the pyrolysis, the crystal structure of ZIF-67 transformed to mainly Co metal (48.2 wt.%) and some cobalt nitrite (15.5 wt.%) existed. The Co metal catalyzed the graphitization, causing the carbon matrix to be destroyed. This phenomenon has also been observed in a previous study [145].
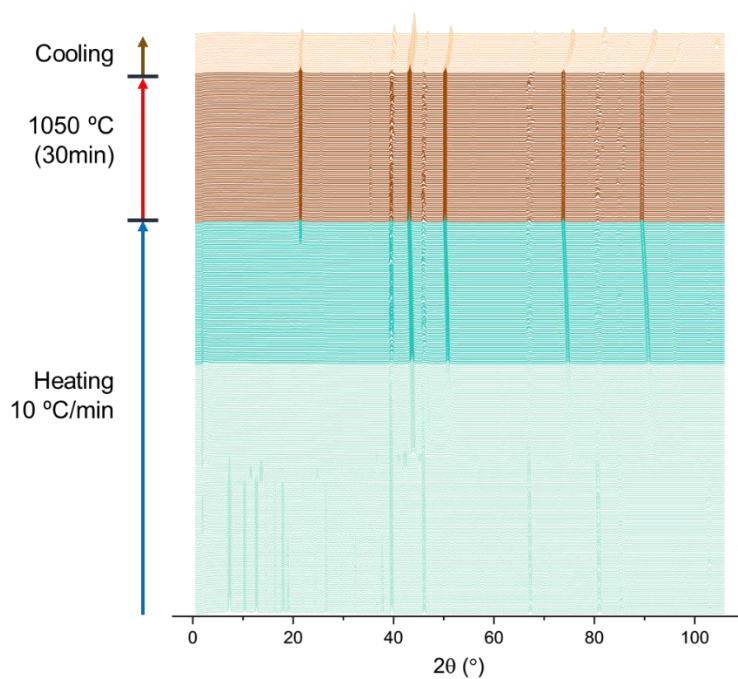
Figure 4-34 *In situ* XRD data of ZIF-67.

Note: X-axis (2 Theta) was converted from 25 keV (0.4959 Å) to Cu Kα (1.5406 Å)
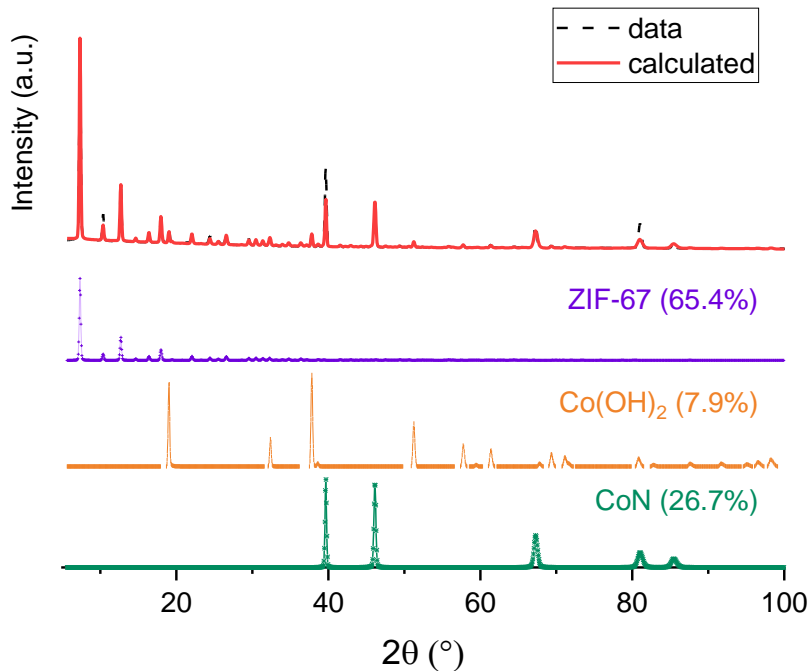
Figure 4-35 Rietveld refinement results of the pristine ZIF-67 XRD data.

Note: X-axis (2 Theta) was converted from 25 keV (0.4959 Å) to Cu Kα (1.5406 Å)
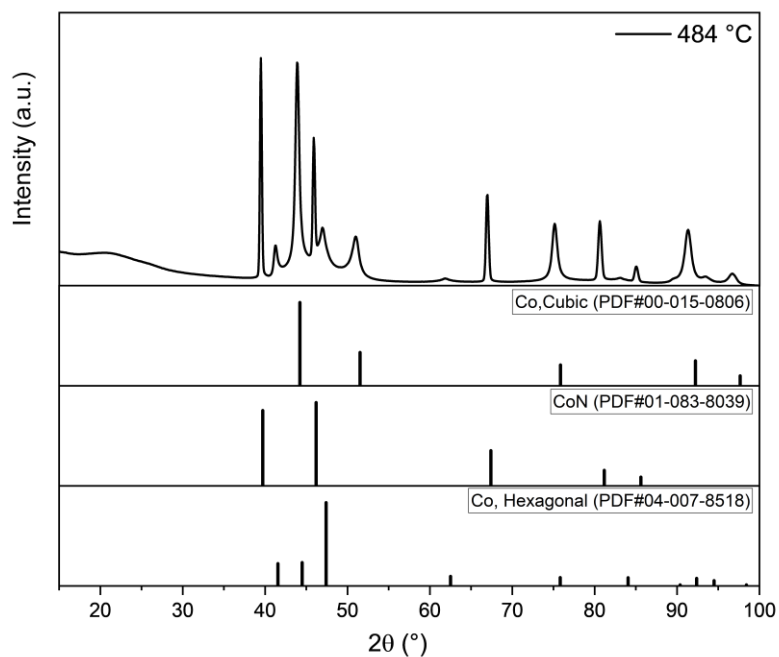
Figure 4-36 XRD data of ZIF-67 at 484 °C from the *in situ* experiment and the corresponding PDF cards.

Note: X-axis (2 Theta) is transferred to Cu Kα from 25 keV
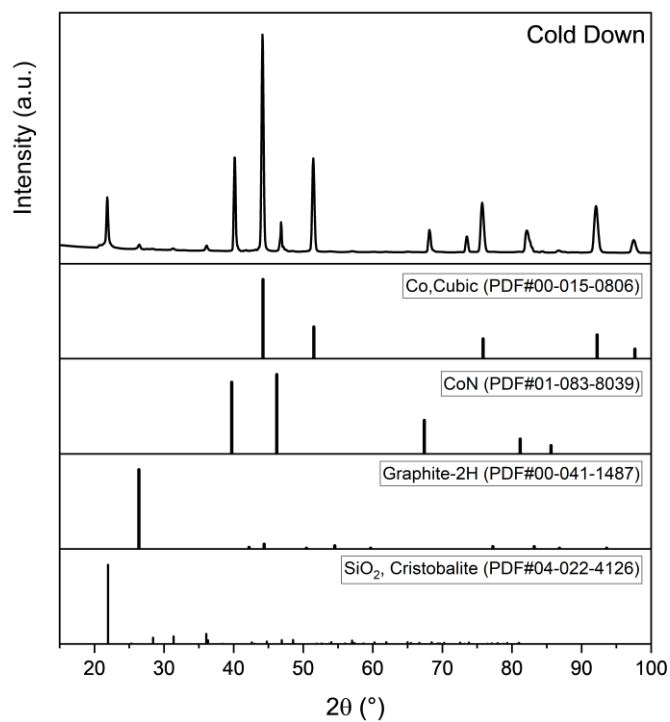
Figure 4-37 XRD data of ZIF-67 after cold down from the *in situ* experiment and the corresponding PDF cards.

Note: X-axis (2 Theta) is transferred to Cu Kα from 25 keV

140
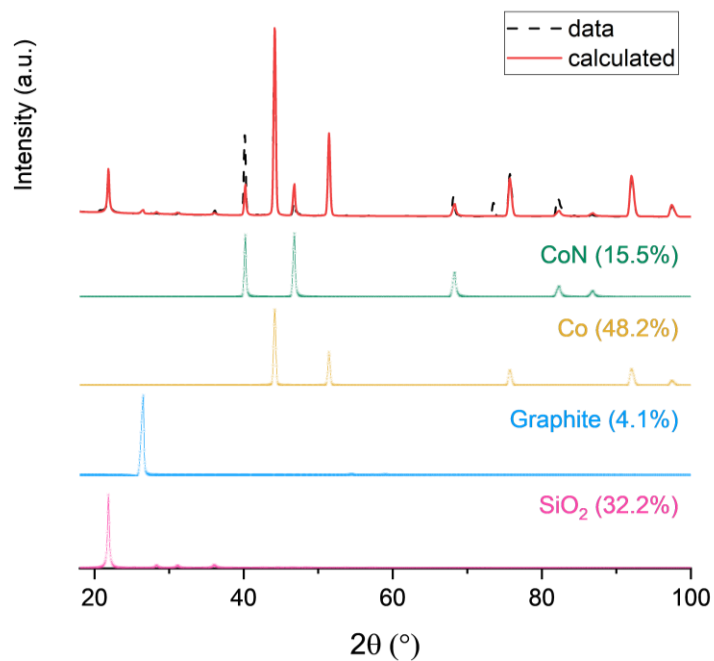
Figure 4-38 Rietveld refinement results of the XRD data of ZIF-67 after cold down from the *in situ* experiment.

Note: X-axis (2 Theta) was converted from 25 keV (0.4959 Å) to Cu Kα (1.5406 Å)
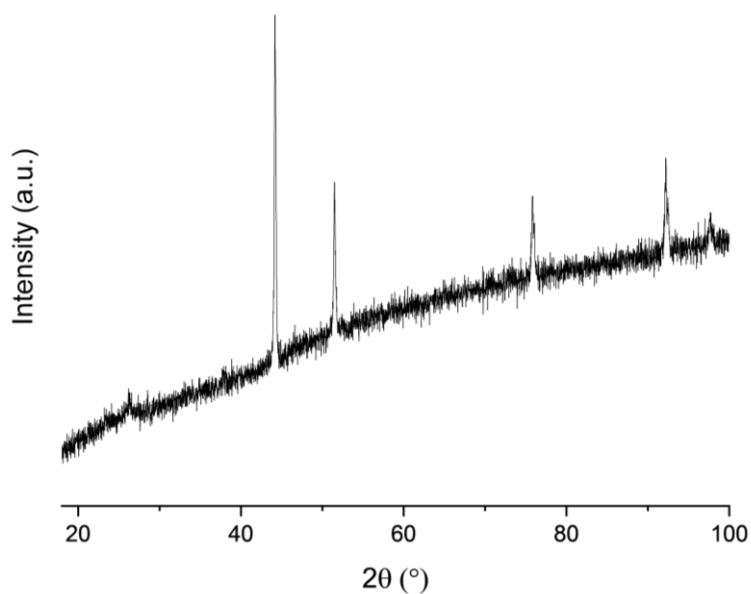
Figure 4-39 *Ex situ* XRD data of ZIF-67 pyrolyzed to 1050 °C.
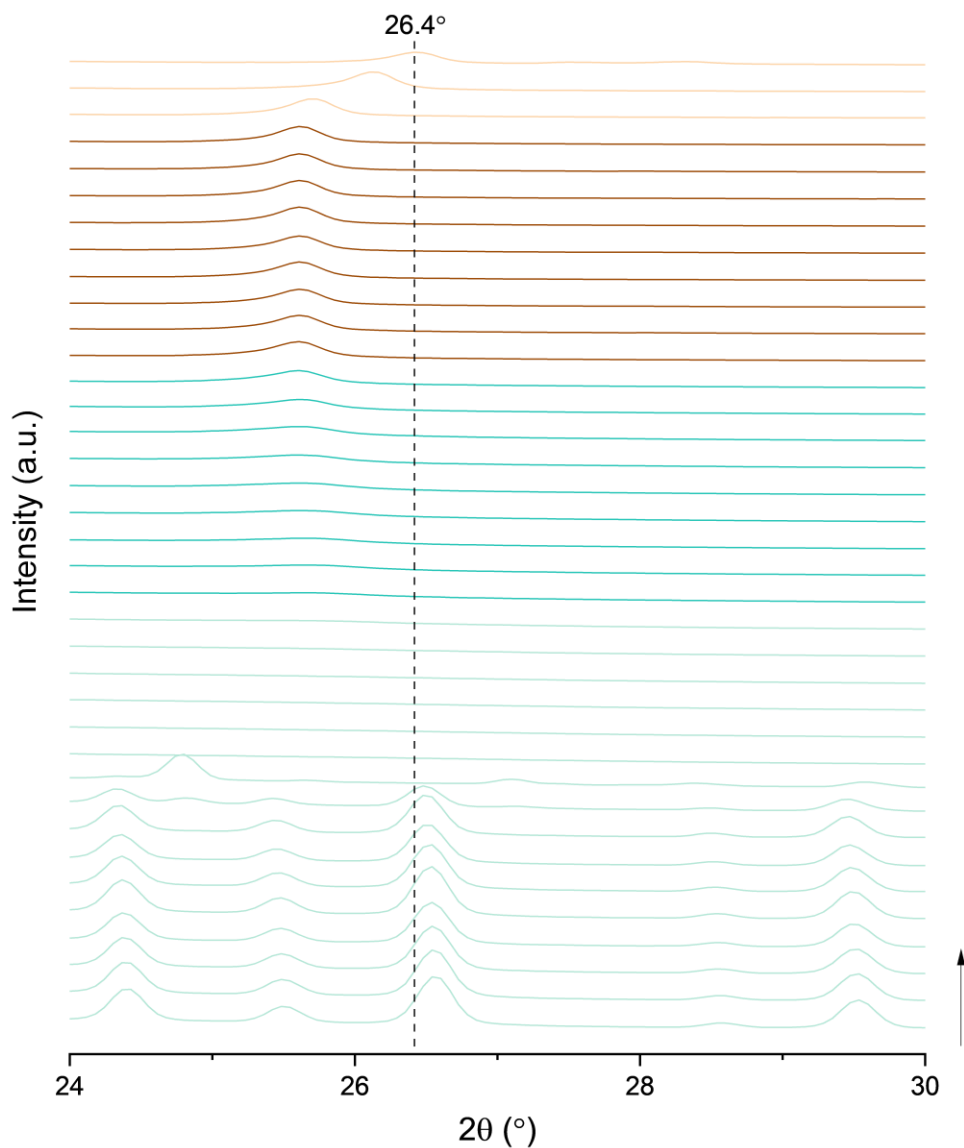
Figure 4-40 *In situ* XRD data of ZIF-67 zooming into 24° to 30°.

Note: X-axis (2 Theta) was converted from 25 keV (0.4959 Å) to Cu Kα (1.5406 Å)

Ex situ XAS at the Co K-edge was measured on the ZIF-67 pyrolyzed to 450 °C, 650 °C, 850 °C, and 1050 °C under Ar atmosphere. The most pronounced peak at 1.55Å in the FT-EXAFS of the pristine ZIF-67 is associated with the Co-N bonding. After the sample was pyrolyzed, the features at 2.21Å related to the Co-Co shell became dominant (**Figure 4-1d**, **Figure 4-41**, and Table 4-8). This correlates with the appearance of the metal particles in the STEM images. The

XANES data (**Figure 4-42**) of pristine ZIF-67 demonstrates features at 7710 eV and 7728 eV. The former one is associated with the Co 1s→3d transition, while the latter one is associated with the Co 1s→4p transition[148]. The data of pristine ZIF-67 included a sharper peak arising from the white line compared to the data of the sample pyrolyzed to 450 °C. This indicates that the Co was in the oxidation state of +2. This could be from the ZIF-67 itself [149]. Combining the results from XRD, this can also be from the $Co(OH)_2$ existed in the pristine ZIF-67. [150,151]. When the sample pyrolyzed to 650 °C and above, the XANES spectra demonstrated the same features revealing the nature of metallic Co particles of the cobalt in the samples [152].
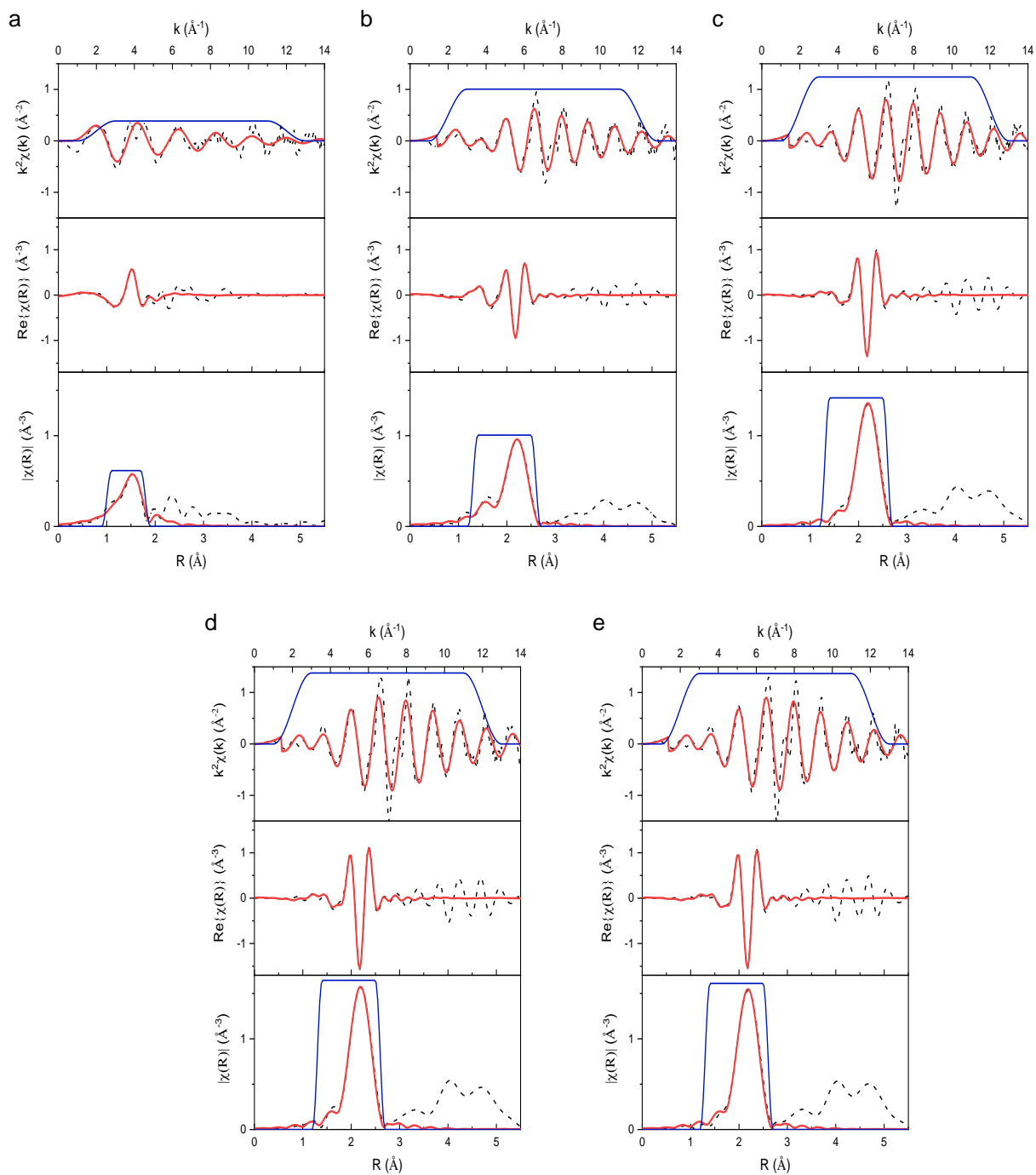
Figure 4-41 EXAFS fits of ZIF-67 pyrolyzed at different temperatures under Ar.

(a) pristine ZIF-67, (b) ZIF-67 pyrolyzed to 450 °C, (c) ZIF-67 pyrolyzed to 650 °C, (d) ZIF-67 pyrolyzed to 850 °C, and (e) ZIF-67 pyrolyzed to 1050 °C showing $k^2 \chi(k)$ (top), real part (middle) and magnitude (bottom) of $\chi(R)$. Data in black short dash dot line, fits in red solid line, and windows in blue solid line.

144

Table 4-8 EXAFS Fitting results for the ZIF-67 and the pyrolyzed products

	Pristine	450 °C	650 °C	850 °C	1050 °C
N_{Co}	2.1±0.3	0.4±0.2	-	-	-
r_{Co-Co}(Å)	1.57±0.04	1.54±0.02	-	-	-
σ^2_{Co-Co}	0.0040±0.0025	0.0051±0.0015	-	-	-
N_N	-	2.1±0.4	2.9±0.3	3.1±0.3	3.2±0.3
r_{Co-N}	-	2.21±0.01	2.21±0.01	2.21±0.01	2.21±0.01
σ^2_{Co-N}	-	Set to 0.003	0.0051±0.0008	0.0044±0.0008	0.0049±0.0008
k range $(Å^{-1})$	2≤k≤12 (dk=2)	2≤k≤12 (dk=2)	2≤k≤12 (dk=2)	2≤k≤12 (dk=2)	2≤k≤12 (dk=2)
R range (Å)	1≤R≤1.8 (dR=0.2)	1.3≤R≤2.6 (dR=0.2)	1.3≤R≤2.6 (dR=0.2)	1.3≤R≤2.6 (dR=0.2)	1.3≤R≤2.6 (dR=0.2)

* S_0^2 is set to 0.8. bond length: Å
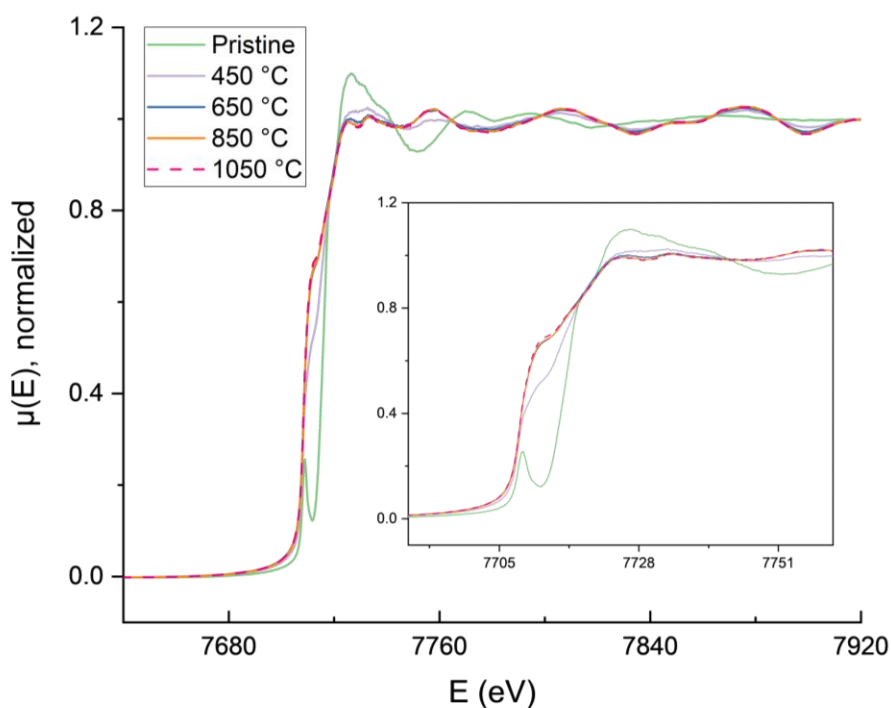
Figure 4-42 XANES of ZIF-67 pyrolyzed at different temperatures under Ar.

Ex situ Raman spectroscopy was used to understand the evolution of MOF to carbonaceous

materials (**Figure 4-43** - **Figure 4-44**, Table 4-9). Similar to that of low-temperature treated ZIF-

8, the spectrum of the sample pyrolyzed to 450 °C demonstrates the features corresponding to the methyl group vibration, as well as the D band and G+D' band. The samples pyrolyzed to 650 °C and above can be considered carbonaceous materials. The intensity of the G+D' band increased as the temperature raised. The ratio of the intensities of the D band and G+D' band in the sample pyrolyzed to 1050 °C is less than one, indicating that more graphitic carbon exists than the defected or disordered carbon in the materials. These results agree with the conclusion gained from the results of *in situ* STEM and XRD experiments. It is also worth noticing that the spectrum of the sample pyrolyzed to 1050 °C contains a sharp D' band (~ 1615 cm^{-1}) (**Figure 4-44**). This means more defected-induced graphitic feature (armchair or zigzag edge in the graphitic carbon structure[153]) existed in the samples. The appearance of the sharp D' band indicates that a significant amount of graphitic carbon exists in the samples pyrolyzed to 1050 °C.
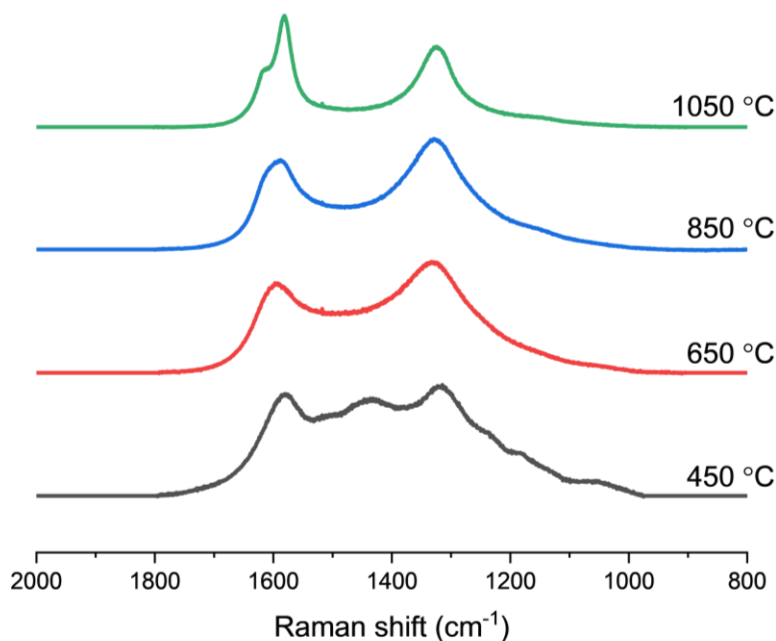
Figure 4-43 Raman spectra of pyrolyzed ZIF-67 pyrolyzed at different temperatures.
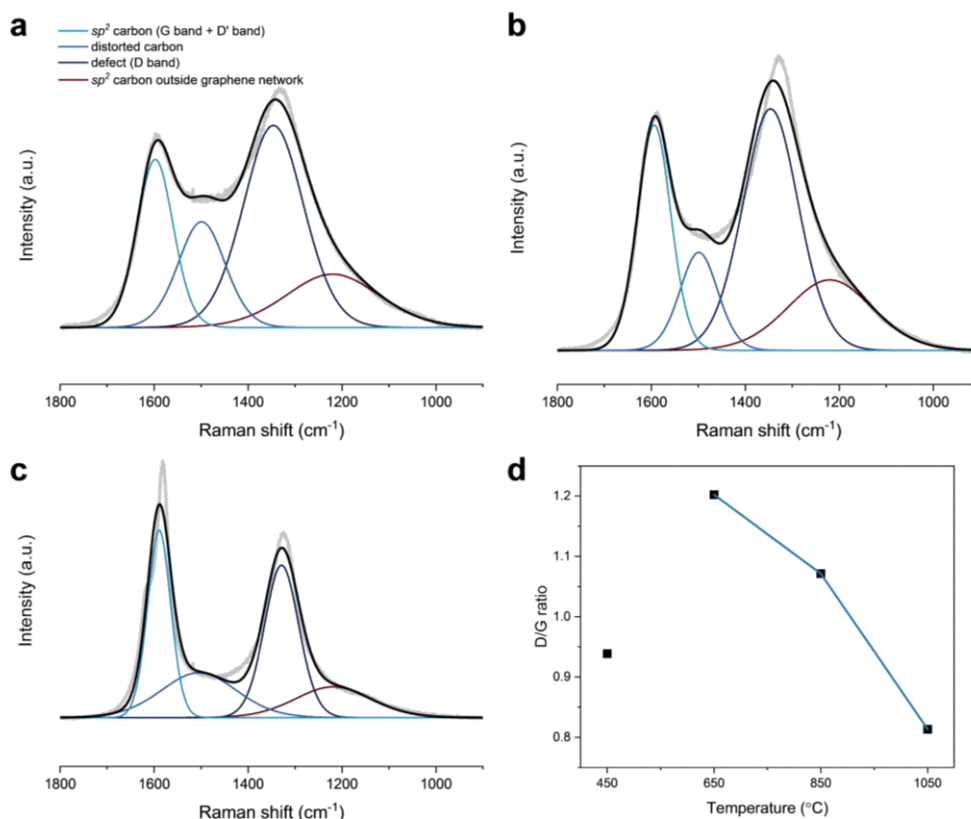
Figure 4-44 Fitted Raman spectra of pyrolyzed ZIF-67.

(a) ZIF-67 pyrolyzed to 650 °C, (b) ZIF-67 pyrolyzed to 850 °C, (c) ZIF-67 pyrolyzed to 1050 °C, (d) D/G ratio of ZIF-67 pyrolyzed to different temperatures. Note: D/G ratio refers to the intensity ratio of D band and G+D' band. For the ZIF-67 pyrolyzed to 1050 °C, the highest intensity was used.

Table 4-9 D/G ratio from Raman results of the pyrolyzed ZIF-67

Temperature (°C)	I_D	I_G	I_D/I_G
450	2041.38	2174.98	0.93857
650	1777.157	1478.342	1.20213
850	3539.112	3303.052	1.07147
1050	1564.783	1923.827	0.81337

From the morphological and structural characterization of the ZIF-67 and its pyrolyzed products, the pyrolyzed ZIF-67 lost the favorable porous structure of MOF. The reason that the structure collapsed was the carbon graphitization, which was catalyzed by the Co cluster that formed during the pyrolysis. In our case, the final catalyst of pyrolyzing ZIF-8 has no metallic particle

and thus catalyzed graphitization was not observed. This phenomenon indicates that other transition metals, including iron, nickel, etc., might cause the same issue, if they remain in the matrix and agglomerate. The Co catalyzed graphitization process is due to the heteroepitaxial growth. The carbon solubility is 3.41% atom in Co at 1000 °C[154]. This means the carbon diffused into the Co bulk easily. As a consequent, the Co precipitated a descent amount of carbon on the surface and thus the graphitic carbon formed [155]. Also, the Co has a strong interaction with graphene [156], meaning that the graphitic carbon layers (which is multiple layers of graphene) could be attached to the Co particle surface firmly. On the other hand, due to the existence of the cobalt nanoparticles, the pyrolyzed product of ZIF-67 might have a high peroxide yield during ORR, which is confirmed later with the electrochemical testing results.

4.6 Confirmation of Structure Evolution

To learn more about the evolution of the surface chemistry and the to confirm the porous network structures evolution envisaged from the previous STEM results, the samples pyrolyzed to 975 °C were acid-etched to remove the particles (**Figure 4-45a** and **Figure 4-45b**). The samples were not pyrolyzed over 1000 °C to avoid the formation of too much graphitic carbon, which might cause difficulties in removing particles (**Figure 4-46**). XPS was performed to understand the surface chemistry of the precursors (ZIF-8 and ZIF-67), samples pyrolyzed to 975 °C, as well as the sample before and after acid etching (**Figure 4-45c** - **Figure 4-45d**). Ar-etching was used to understand the chemistry of the content beneath the surface. The surface chemistry changes mainly occurred during the pyrolysis process. The atomic concentration of the C 1s on the ZIF-8 sample surface increased by 30.7% after pyrolysis, while the N 1s and the Zn 2p decreased by 76.1% and 92.1%, separately. The decrease of the Zn 2p atomic concentration confirms that the metal species evaporated during the heat treatment. After acid etching, the

atomic concentration on the sample surfaces of Zn 2p further decreased and the O 1s increased slightly. This indicates that some of the metal species etched away, and the surface absorbed some water during the etching. The atomic concentration of C 1s, N 1s and Zn 2p did not change much, meaning that the contents are uniform on the sample and few nanometers inside the surface. The Ar-etched surface showed a decreased atomic concentration of the O 1s, meaning the absorbed water only existed on the sample surface. For the ZIF-67, the atomic concentration of the C 1s has similar changes as the ZIF-8 sample after pyrolysis and acid etching. The atomic concentration of O 1s did not change significantly on ZIF-67 surface after pyrolysis and dropped a little bit after the acid-etching. This means the structure of the pyrolyzed ZIF-67 had low surface area and thus absorbed less water. However, there was a large decrease of the N 1s and Co 2p concentration on the surface of the ZIF-67, which can be a sign of the structure collapse. Most of the nitrogen and Co might be beneath the sample surface in a collapsed structure. The carbon and graphitic carbon wrapped the metal and the nitrogen ligands. This consists with what we observed during the *in situ* STEM experiments. After acid etching, the Co 2p concentration decreased even more, indicating the removal of the Co on the surface. The high-resolution C 1s and N 1s XPS spectra with curve fitting reveal the carbon framework and N moiety composition (**Figure 4-47** - **Figure 4-52**). The typical M-N-C carbon framework appeared after the samples were pyrolyzed. Metal-N is the most favorable site since it prefers the four-electron pathway[23]. The atomic concentration of metal-N of the pyrolyzed ZIF-67 increased by 66.32% after Ar etching. This indicates that most of the metals are embedded inside the samples. Pyridine N and N-H (including pyrrolic N and hydrogenated pyridinic N) are favorable for the first and second steps of the two-electron pathway[23]. The ratio of these above sites is related to the efficiency of this pathway. The ratio was close to one for the acid-etched pyrolyzed ZIF-8. However, the ratio

of the pyrolyzed ZIF-67 before and after acid-etching was 0.87 and 0.78, respectively. Inductively Coupled Plasma-Mass Spectrometry (ICP-MS) was also done to access the quantity of metal element inside the final catalysts before and after acid etching. The Zn in pyrolyzed ZIF-8 was 0.52 wt.% while the number decreased to 0.27 wt.% after acid etching. The Co in pyrolyzed ZIF-67 was 64.98 wt.% while the number hugely dropped to 1.80 wt.% after acid etching.

N_2 absorption was applied to probe the changes in the pyrolyzed product before and after the acid etching step. The isotherms of the ZIF-8 samples showed abrupt increases at a low relative pressure (**Figure 4-45e**). This indicates the existence of the micropores. There was no significant difference in the surface area and the pore size distribution of the samples after acid etching (surface area: 1,171.8 m² g^{-1}) compared to the one before (surface area: 1,219.9 m² g^{-1}). Thus, the acid etching did not affect significantly the pyrolyzed ZIF-8 samples. The isotherms of the ZIF-67 samples displayed typical type-IV isotherms with a type H4 hysteresis loop in the range of P/P0 > 0.4, indicating the presence of mesopores. The sample after acid etching showed a higher surface area (surface area: 158.0 m² g^{-1}) and increased pore volume (**Figure 4-53**) compared to the one before etching (surface area: 51.8 m² g^{-1}). This can be due to the removal of the cobalt nanoparticles.
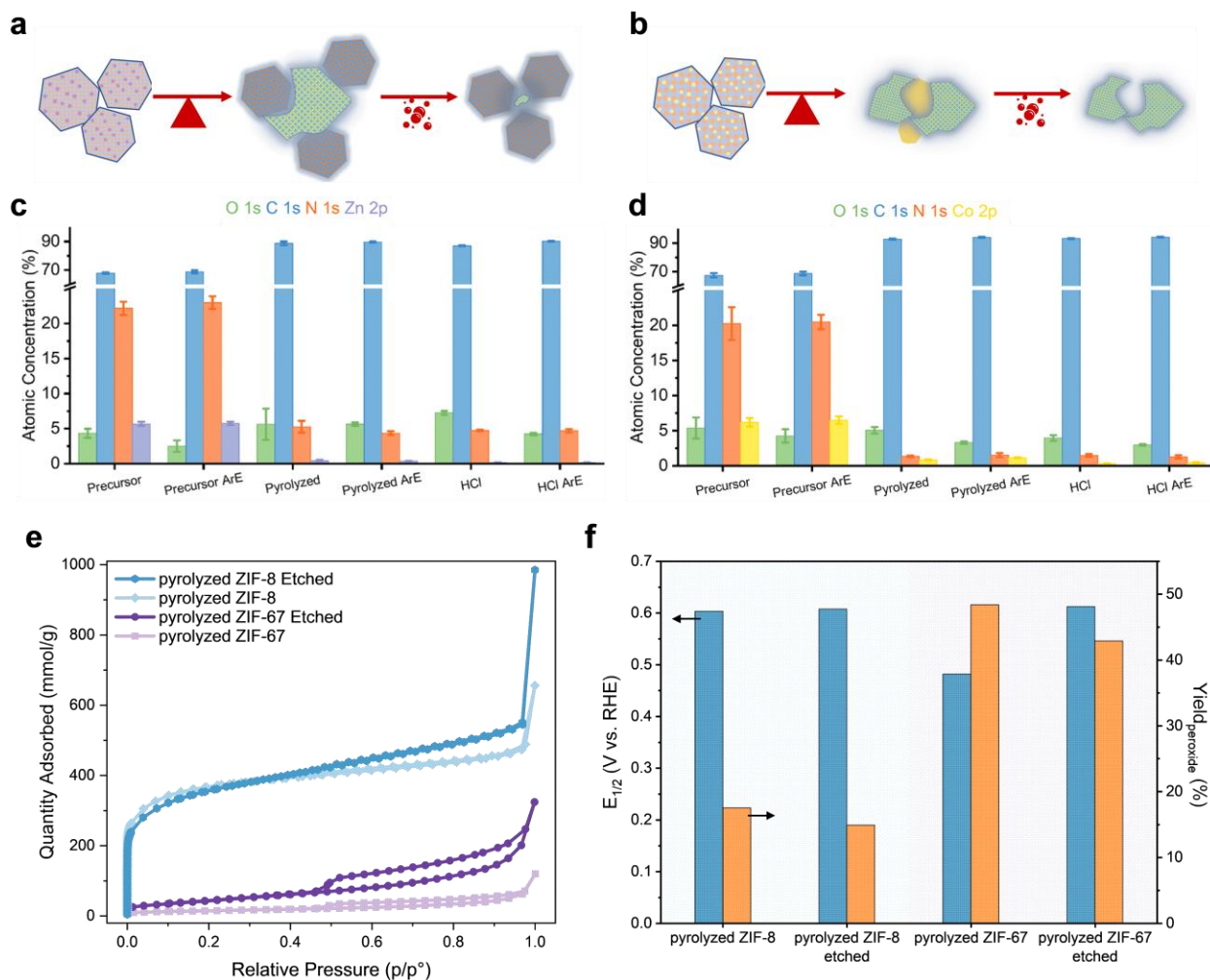
Figure 4-45 Comparison of pyrolyzed ZIF-8 and ZIF-67 before and after acid etching. Samples were pyrolyzed to 975 °C.

(a) – (b) A schematic of transformations of precursors during pyrolysis and acid etching of ZIF-8 (a) and ZIF-67 (b). (c) Atomic concentration of different elements gained from XPS of ZIF-8, pyrolyzed ZIF-8 before and after acid etching (HCl), as well, as acid etching after Ar beam etching (HCl ArE). (d) Atomic concentration of different elements gained from XPS of ZIF-67, pyrolyzed ZIF-67 before and after acid etching (HCl), as well, as acid etching after Ar beam etching (HCl ArE). (e) Adsorption isotherm plots of N_2 on the pyrolyzed ZIF-8 and ZIF-67 before and after acid etching (980 °C). (f) Half-wave potential and peroxide yield gained from RRDE experiment for the pyrolyzed sample before and after acid etching. Disk and ring current density were collected under 1600 rpm rotating speed. The sample loading on the electrode was of 800 µg cm^{-2} $_{geo}$ and the electrode surface was of 0.247 cm^2. The electrolyte is O_2-saturated 0.1 M HClO$_4$.
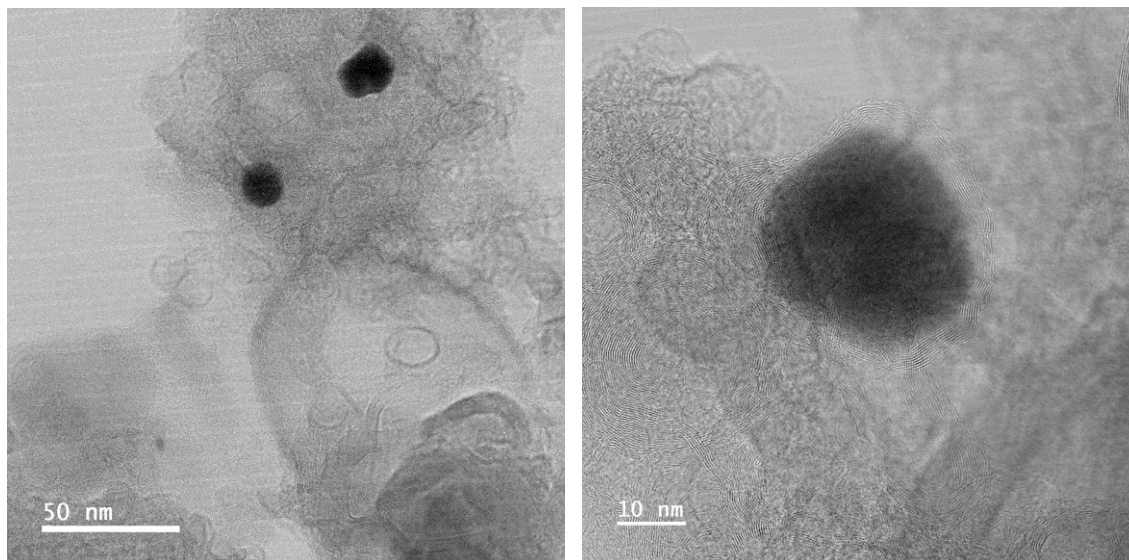
Figure 4-46 STEM images of ZIF-67 pyrolyzed to 1050 °C and acid etched.
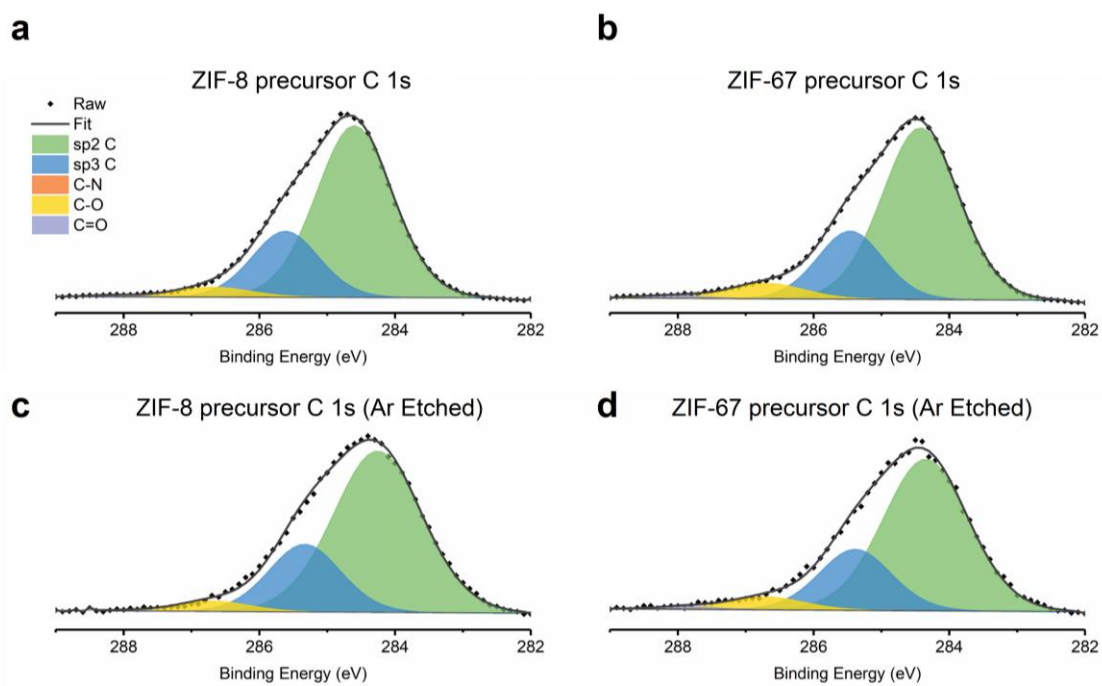
Figure 4-47 Curve fitted XPS C 1s spectra of ZIF-8 and ZIF-67 (precursors).
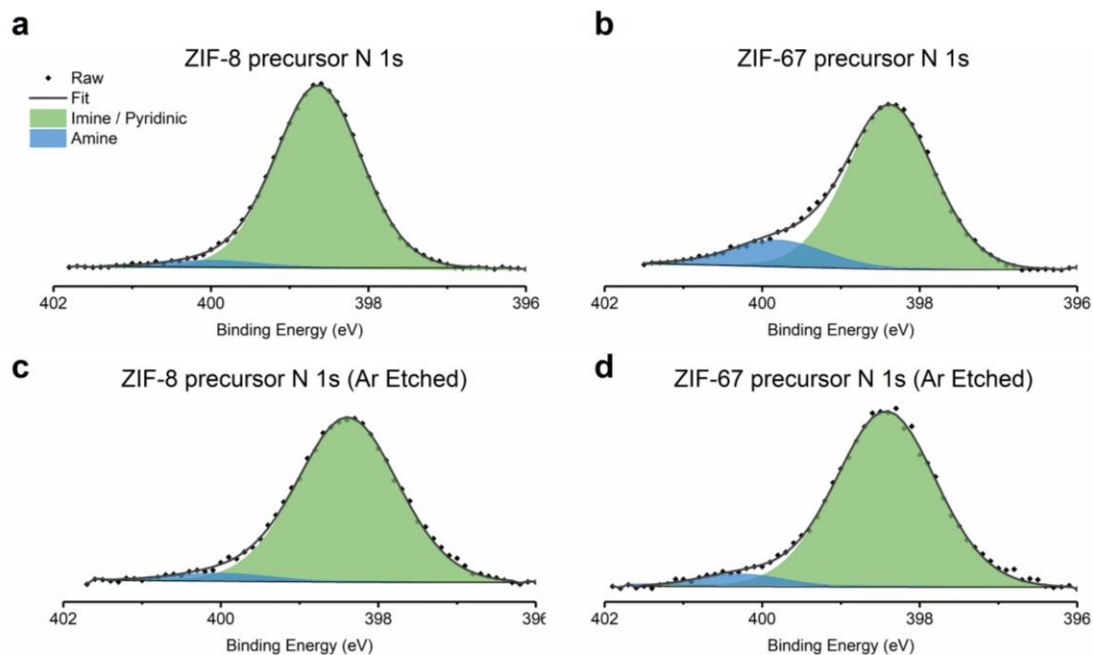
Figure 4-48 Curve fitted XPS N 1s spectra of ZIF-8 and ZIF-67 (precursors).
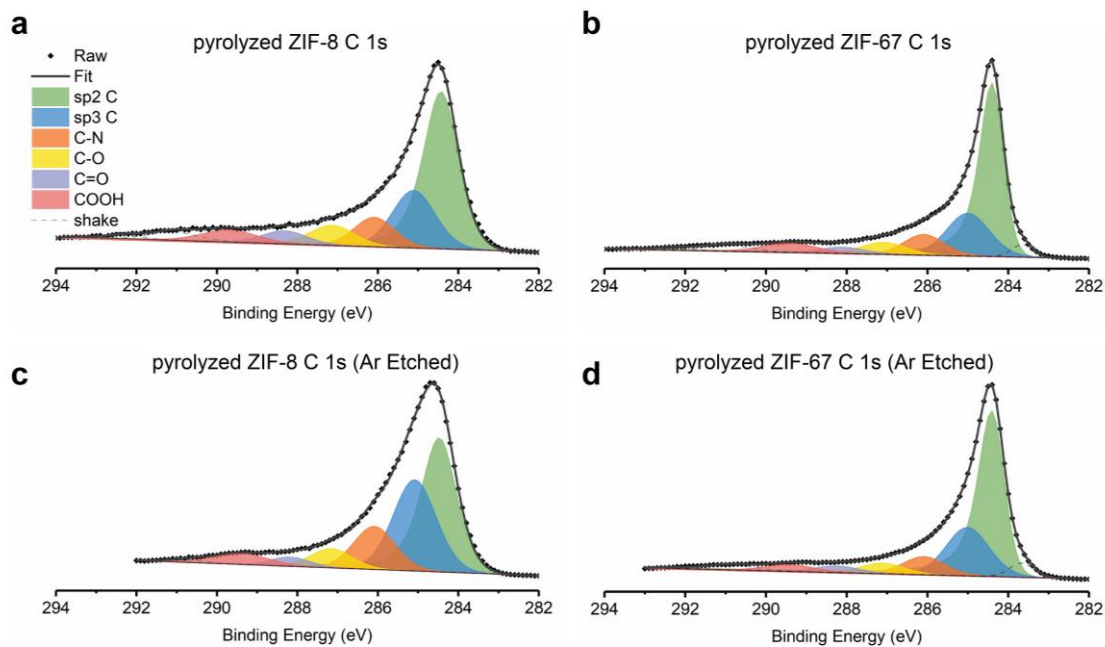
Figure 4-49 Curve fitted XPS C 1s spectra of pyrolyzed ZIF-8 and ZIF-67 (975 °C, Ar).
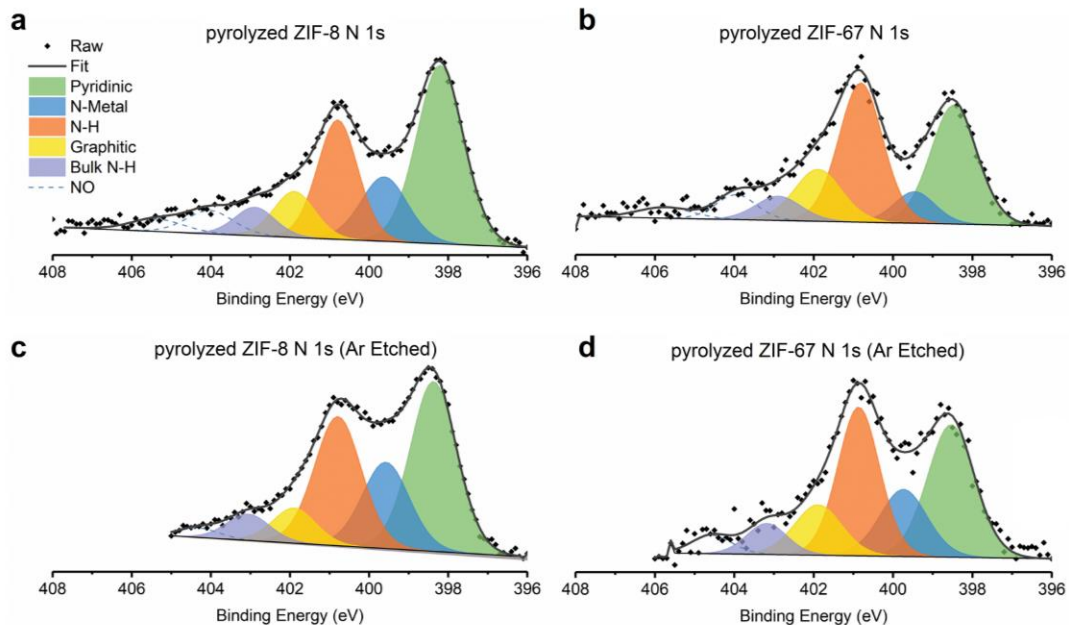
Figure 4-50 Curve fitted XPS N 1s spectra of pyrolyzed ZIF-8 and ZIF-67 (975 °C, Ar).
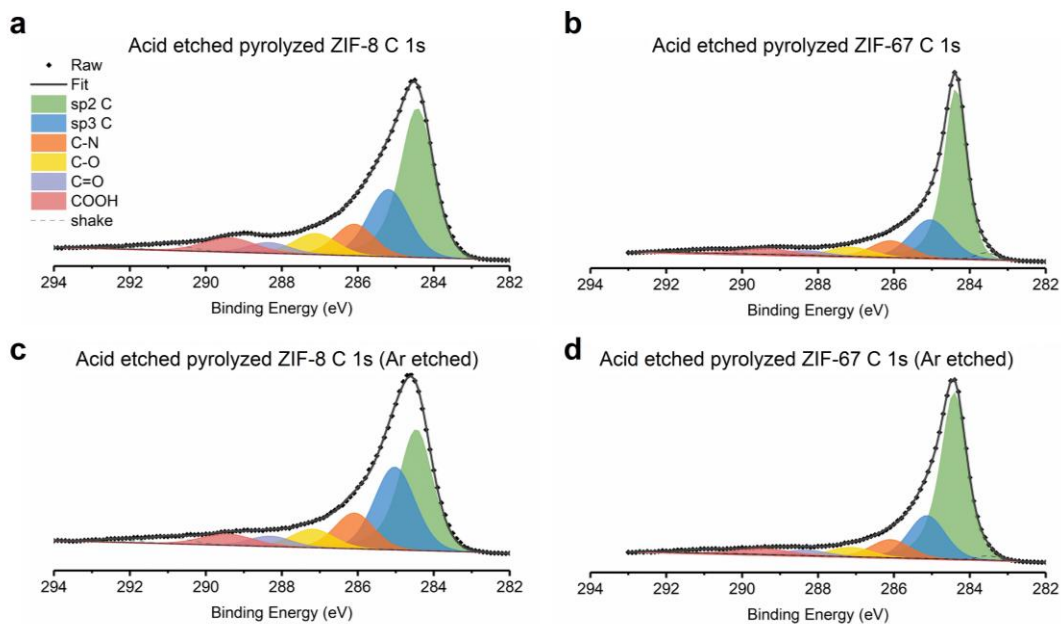
Figure 4-51 Curve fitted XPS C 1s spectra of pyrolyzed ZIF-8 and ZIF-67 (975 °C, Ar) after acid etching.
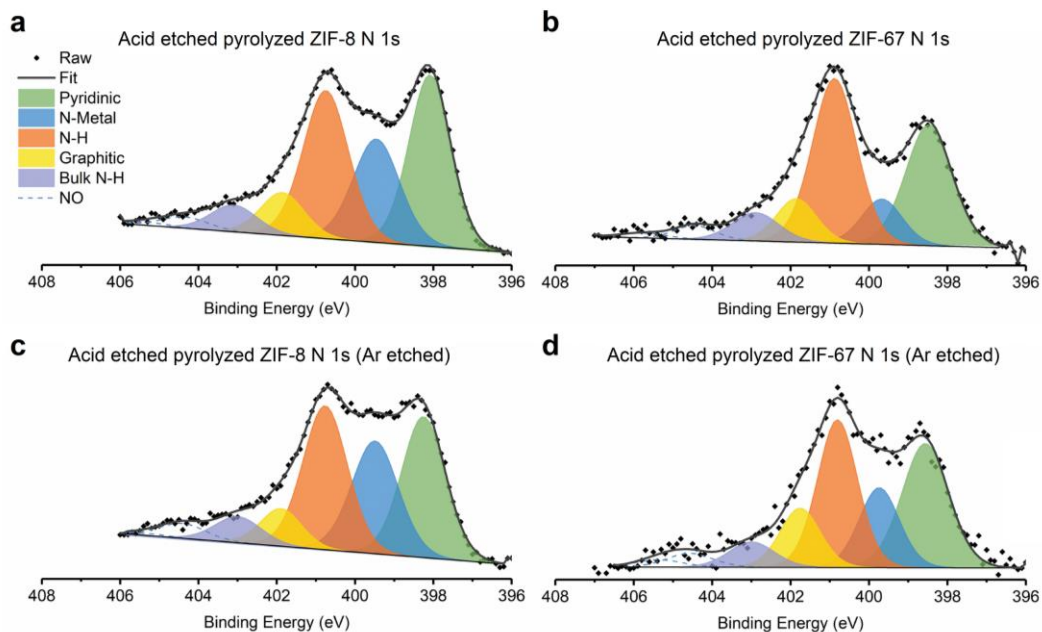
Figure 4-52 Curve fitted XPS N 1s spectra of pyrolyzed ZIF-8 and ZIF-67 (975 °C, Ar) after acid etching.
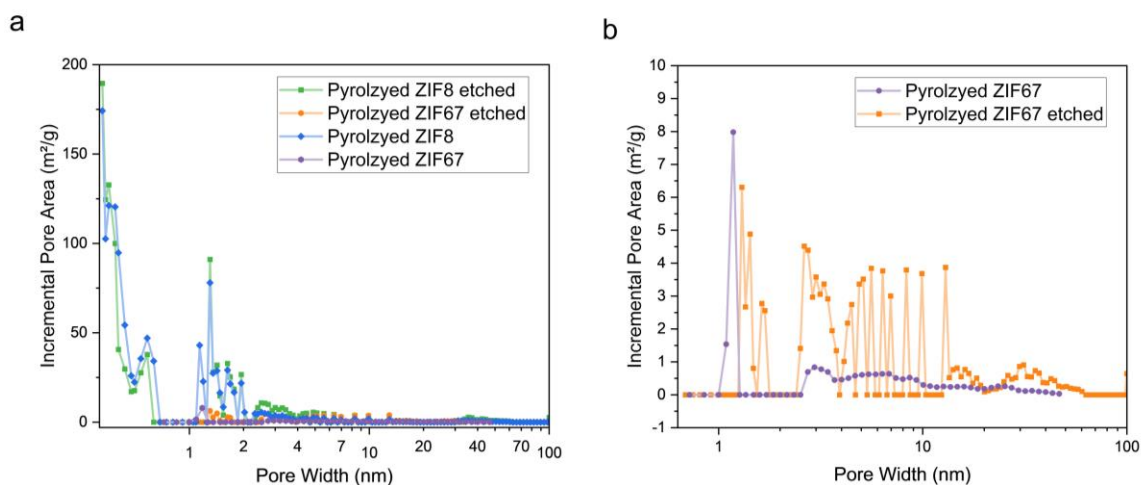
Figure 4-53 NLDFT pore size distribution (under 2 nm) of pyrolyzed ZIF-8 and ZIF-67 before and after acid etching.

(a) pyrolyzed ZIF-8 and ZIF-67 before and after acid etching. The samples were pyrolyzed to 975 °C. (b) zoom-in plot for the pyrolyzed ZIF-67.

4.7 Electrochemical Activities

The electrochemical activity of the samples pyrolyzed at different temperatures was assessed

with a rotating ring disk electrode setup (**Figure 4-45f**, **Figure 4-54** - **Figure 4-61**). Overall, the

cyclic voltammetry (CV) curves of the samples pyrolyzed to higher temperatures demonstrated a quasi-rectangular shape. The capacitance of the ZIF-8 pyrolyzed to 1050 °C was lower than the ones pyrolyzed at 850 °C and 980 °C, which indicates an eventual collapse of the pristine porous structure. This phenomenon can also be attributed to the existence of more disordered graphitic carbon and the decreased volume of pores. However, the half-wave potential of the ZIF-8 pyrolyzed to 1050 °C, although very similar to the one of the samples pyrolyzed to 980 °C, is the highest. This is probably due to the metal-N active site formation happening at high temperatures. For ZIF-67, the sample pyrolyzed to 450 °C had a very low capacitance, indicating that the carbon substrate and the active sites had not formed. With the pyrolysis temperature increased, the capacitance first increased and then decreased. That is due to the existence of metallic cobalt, which blocked some of the pores in the sample. The half-wave potential of the pyrolyzed ZIF-8 is higher than the pyrolyzed ZIF-67. However, the half-wave potential of the pyrolyzed-67 increased from 0.48 V to 0.61 V after acid etching, while the half-wave potential of the pyrolyzed ZIF-8 remained roughly the same. This is due to the increase of the capacitance and of the surface area after the removal of the metal particles. The peroxide yield of the pyrolyzed ZIF-67 is much higher compared to the pyrolyzed ZIF-8. The reason is that the product of pyrolyzed ZIF-67 contained more inactive metallic cobalt (embedded in the carbon structure) and probably cobalt carbide. This led to insufficient existence of the M-N$_x$ sites in the sample, which can further reduce the peroxide to water. Thus, the pyrolyzed ZIF-67 could not efficiently reduce the peroxide, whose generation was catalyzed by the N-H sites in the final catalysts. The same conclusion can be drawn from the experiment done under 1600 rpm and 900 rpm.
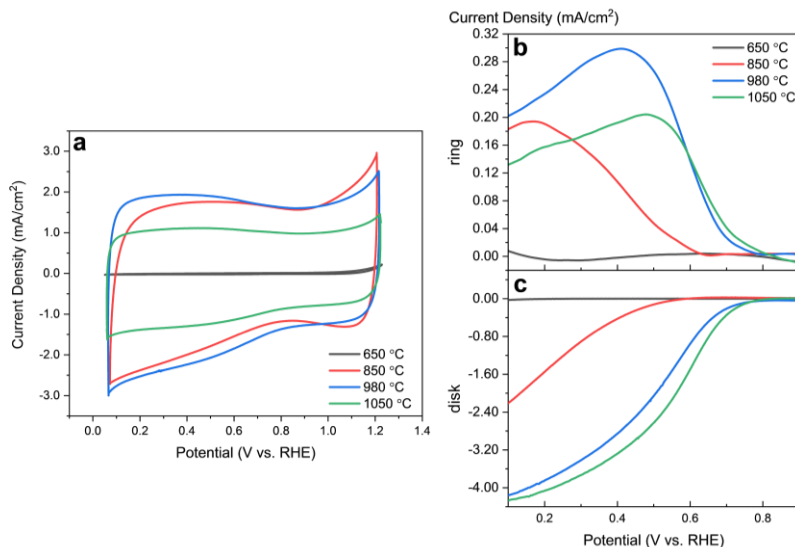
Figure 4-54 Electrochemistry data for the ZIF-8 pyrolyzed at different temperatures with a rotating speed of 1600 rpm.

Disk and ring current density were collected under 1600 rpm rotating speed. The sample loading on the electrode was of 800 µg cm^{-2} $_{geo}$ and the electrode surface was of 0.247 cm^2. The electrolyte is O_2-saturated 0.1 M $HClO_4$. (a) cyclic voltammetry in N_2-saturated electrolyte and a scan rate of 20 mV s^{-1}, (b) ring current density and (c) disk current density in O_2-saturated electrolyte and a scan rate of 20 mV s^{-1}.
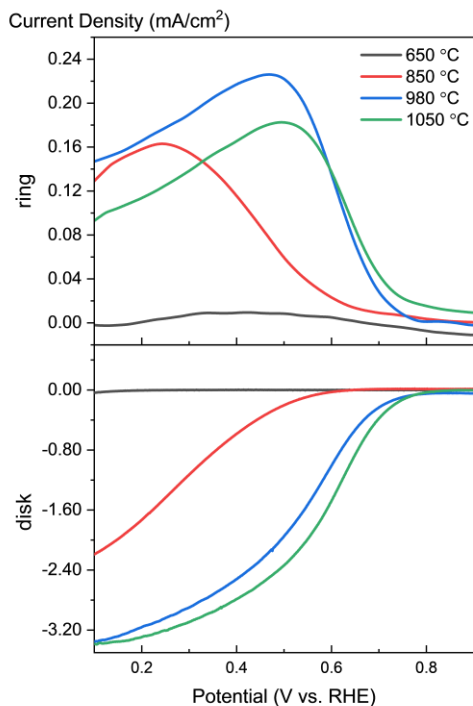
Figure 4-55 RRDE data for the ZIF-8 pyrolyzed at different temperatures with a rotating speed of 900 rpm.

The sample loading on the electrode was of 800 µg cm^{-2} $_{geo}$ and the electrode surface was of 0.247 cm^2. The electrolyte is O_2-saturated 0.1 M $HClO_4$. (a) ring current density and, (b) disk current density in O_2-saturated electrolyte and a scan rate of 20 mV s^{-1}.
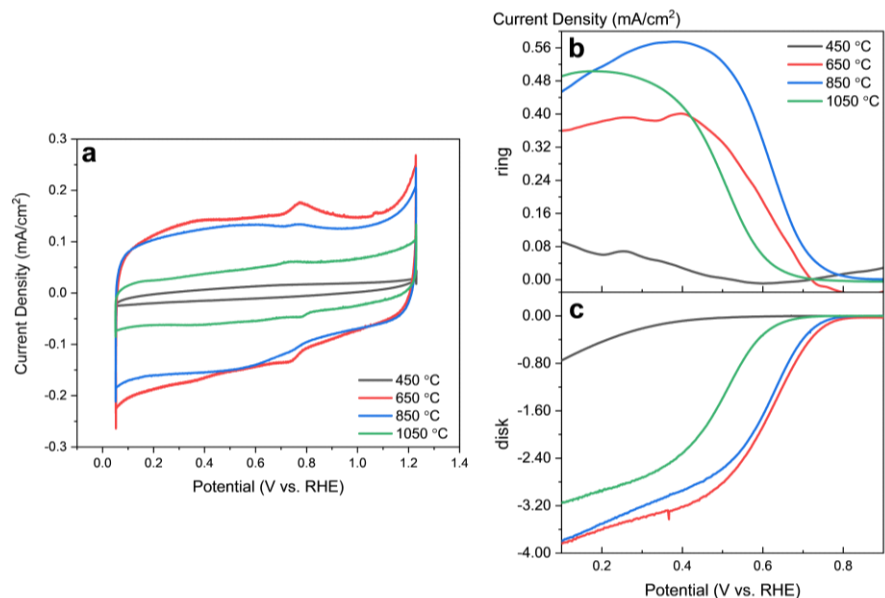
Figure 4-56 Electrochemistry data for the ZIF-67 pyrolyzed at different temperatures with a rotating speed of 1600 rpm.

Disk and ring current density were collected under 1600 rpm rotating speed. The sample loading on the electrode was of 800 µg cm^{-2}_{geo} and the electrode surface was of 0.247 cm^2. The electrolyte is O_2-saturated 0.1 M $HClO_4$. (a) cyclic voltammetry in N_2-saturated electrolyte and a scan rate of 20 mV s^{-1}, (b) ring current density and (c) disk current density in O_2-saturated electrolyte and a scan rate of 20 mV s^{-1}.
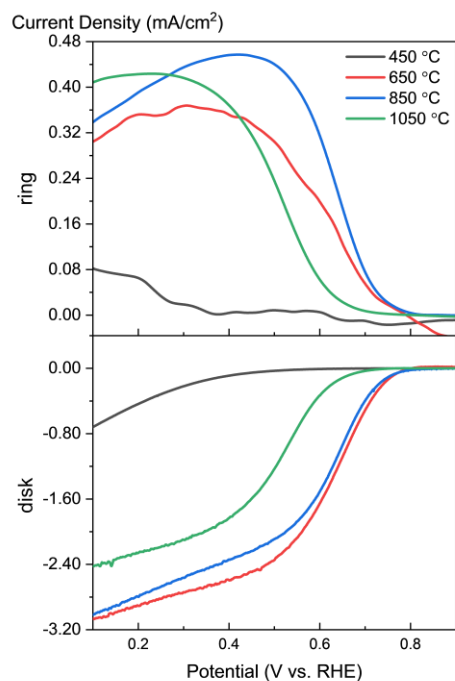
Figure 4-57 RRDE data for the ZIF-67 pyrolyzed at different temperatures with a rotating speed of 900 rpm.

The sample loading on the electrode was of 800 µg cm^{-2}_{geo} and the electrode surface was of 0.247 cm^2. The electrolyte is O_2-saturated 0.1 M $HClO_4$. (a) ring current density and, (b) disk current density in O_2-saturated electrolyte and a scan rate of 20 mV s^{-1}.

158
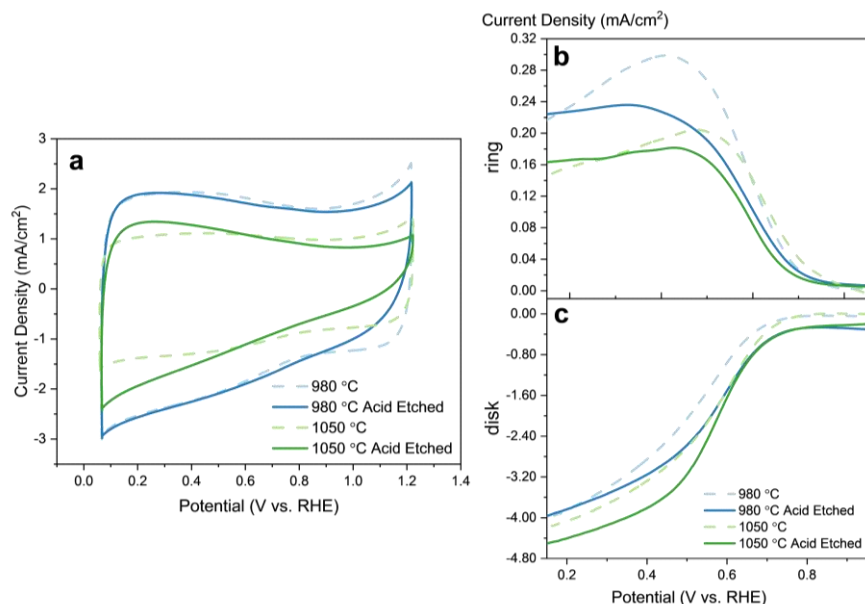
Figure 4-58 Electrochemistry data for the pyrolyzed ZIF-8 before and after etching with a rotating speed of 1600 rpm.

Samples were pyrolyzed to 980 ℃ and 1050 ℃. Disk and ring current density were collected under 1600 rpm rotating speed. The sample loading on the electrode was of 800 µg cm^{-2} $_{geo}$ and the electrode surface was of 0.247 cm^2. The electrolyte is O$_2$-saturated 0.1 M HClO$_4$. (a) cyclic voltammetry in N$_2$-saturated electrolyte and a scan rate of 20 mV s^{-1}, (b) ring current density and (c) disk current density in O$_2$-saturated electrolyte and a scan rate of 20 mV s^{-1}.

Figure 4-59 RRDE data for the pyrolyzed ZIF-8 before and after etching with a rotating speed of 900 rpm.

Samples were pyrolyzed to 980 ℃ and 1050 ℃. The sample loading on the electrode was of 800 µg cm^{-2} $_{geo}$ and the electrode surface was of 0.247 cm^2. The electrolyte is O$_2$-saturated 0.1 M HClO$_4$. (a) ring current density and, (b) disk current density in O$_2$-saturated electrolyte and a scan rate of 20 mV s^{-1}.

159

Figure 4-60 Electrochemistry data for the pyrolyzed ZIF-67 before and after etching with a rotating speed of 1600 rpm.

Samples were pyrolyzed to 850 °C and 1050 °C. Disk and ring current density were collected under 1600 rpm rotating speed. The sample loading on the electrode was of 800 µg cm^{-2} $_{geo}$ and the electrode surface was of 0.247 cm^2. The electrolyte is O$_2$-saturated 0.1 M HClO$_4$. (a) cyclic voltammetry in N$_2$-saturated electrolyte and a scan rate of 20 mV s^{-1}, (b) ring current density and (c) disk current density in O$_2$-saturated electrolyte and a scan rate of 20 mV s^{-1}.
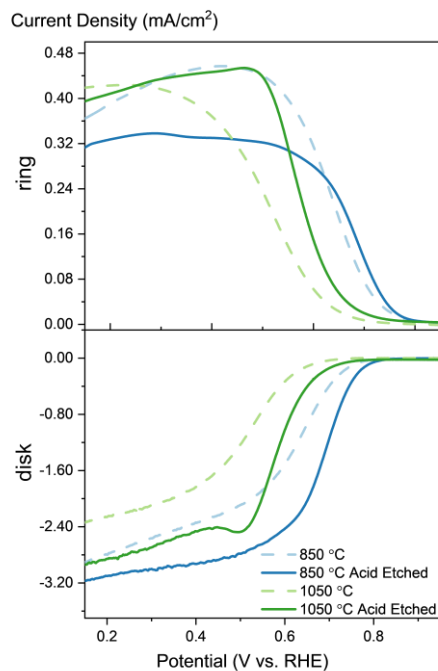
Figure 4-61 RRDE data for the pyrolyzed ZIF-67 before and after etching with a rotating speed of 900 rpm.

Samples were pyrolyzed to 850 °C and 1050 °C. The sample loading on the electrode was of 800 µg cm^{-2} $_{geo}$ and the electrode surface was of 0.247 cm^2. The electrolyte is O$_2$-saturated 0.1 M HClO$_4$. (a) ring current density and, (b) disk current density in O$_2$-saturated electrolyte and a scan rate of 20 mV s^{-1}.

160

4.8 Comparison of pyrolyzed ZIF-8 and pyrolyzed ZIF-67

Combining all the characterization results, the transformation from the MOF precursors to the M-N-C catalysts was directly observed. The most pronounced difference between the pyrolyzed product of ZIF-8 and ZIF-67 was the formation of the metallic particles (**Figure 4-62**). The metallic particles, though can be active for the ORR, would not be dispersed well during the pyrolysis and thus the metal active sites density was low. Furthermore, the Co particles catalyzed the carbon graphitization process easily due to the high carbon solubilities in cobalt. The most crucial advantage of ZIF-8 being a precursor is the well-dispersed Zn after the process. However, the Zn concentration inside the sample was low since it evaporated at the early stage of the pyrolysis. This indicates that not many metal-related active sites existed in the final catalysts. This would significantly affect the performance. Thus, ZIF-8 has a promise to be a great templating precursor for ORR, as it can serve as a template for deposition of transition metal species, such as Fe that are active towards ORR[107,108,157].
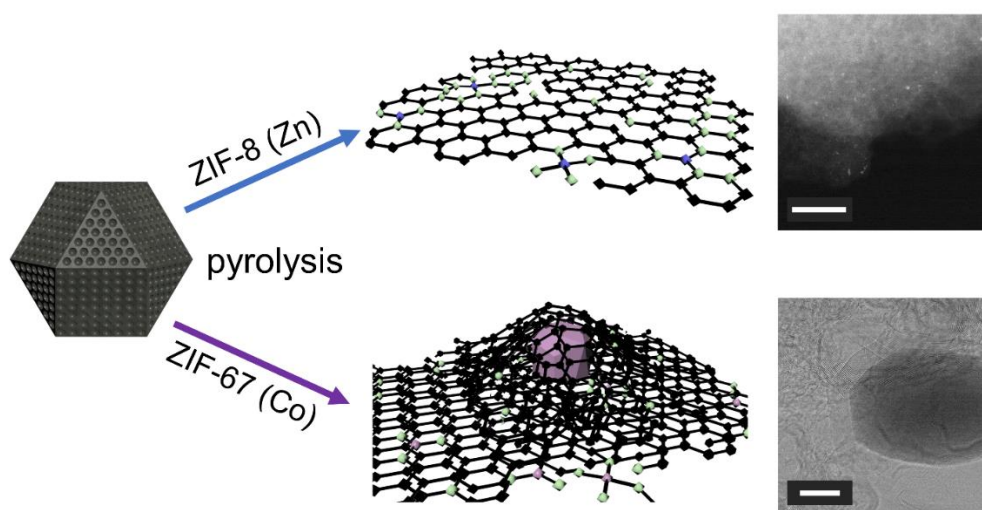
Figure 4-62 Schematic figure on pyrolyzing ZIF-8 and ZIF-67 to over 1000 ℃.

Blue, purple, green, and black spheres represent Zn, Co, N and C atoms/particle, respectively. The TEM on top is the Zn-MOF pyrolyzed to 1050 ℃ and cold down under vacuum. The TEM at the bottom is the ZIF-67 pyrolyzed to 1050 ℃ under vacuum. The scale bars on both TEM images are 10 nm.

4.9 Summary

In conclusion, MOF has a favorable porous structure that benefits catalytic activity. To make it conductive and to form M-N-C catalysts, pyrolysis is an essential step. However, pyrolyzing transition metal doped MOFs can cause metallic particles to form during the pyrolysis. This metal formation not only decreases the concentration of the active sites but also catalyzes the carbon graphitization at high temperatures. The graphitization process causes the favorable structure to collapse, and thus the usage of MOF as precursors loses its meaning. ZIF-8 is a promising MOF since its doping metal, Zn, evaporates at the early stage of the pyrolysis. However, the evaporation of metal indicates insufficient metal-N active sites, which limits the performance of the remaining products as catalysts. To maintain the porous structure of MOFs, controlling the metal species and preventing them from agglomerating is the key.

Chapter 5

Conclusion and Outlook

5.1 Conclusion

The pyrolysis leads to the morphological, phase and chemical transformation of the precursors to M-N-C catalysts. The above transformation can be detected separately but are related to each other. The morphological transformation indicates that the metal dispersion can be related to the temperature and the weight percentage of the metal. Under high temperature (>900 °C with certain temperature holding time and >1000 °C without holding temperature), the metallic particles would catalyze the carbon graphitization event. The Raman spectroscopy proved that the catalysts made by pyrolyzing over 1000 °C contains a high amount of graphitic carbon. The graphitization would cause the metal to be further encapsulated by the graphitic carbon and probably form metal carbide. The formation of this kind of encapsulated metallic particles or carbide would collapse the pristine structure of the precursors. Thus, even the pristine structure is of high porosity, it would be damaged when the metallic particles form. Unfortunately, Co and Fe tends to catalyze the carbon graphitization easily, due to the carbon solubility or some interaction with carbon, and the Fe-N-C and the Co-N-C have been proved to be the M-N-C catalysts with best performance. On the other hand, the surface chemical transformation revealed that most of the active sites and carbon framework has formed on the surface before 900 °C. Based on the corresponding RRDE results, highly graphitization of the carbon would harm the catalytic performance, due to the decrease of the M-N$_x$ sites and the morphology. Thus, no matter what precursors are chosen, the temperature control should be accurate and careful. It would be

better to choose a temperature lower than 900 °C to avoid the metallic particle formation and the carbon graphitization event.

When the metallic particle formed or when some organic solvent left on the catalyst surface brought adverse effects, a re-pyrolysis process can help. The repyrolysis process can disintegrate the metallic particles and release metal atom (iron in this study), which was probably due to the interaction between graphitic carbon and the metal. The repyrolysis also turns part of the graphitic carbon on the surface into amorphous, and remove the potentially harmful solvent left on the surface from the etching step.

5.2 Outlook

The studies provide a thorough analysis of the pyrolysis process. There is something that can be done in the future based on the results of the studies in this thesis. The suggestions for future work can be raised from two directions.

i) Things can be done to provide better analysis to pyrolysis process.

ii) Things can be done to rationally design M-N-C catalysts.

For the first direction, the following suggestions can be made. Firstly, more studies should be done to understand the effect of the holding time during the low temperature range. TGA and the evolved gas analysis should be able to help. Another thing is to understand better about the metal-carbon interaction during the pyrolysis when synthesizing the catalysts with new precursors. Raman spectroscopy and STEM-EDS/EELS should be able to help. Also, better applying nano-CT with phase mode should be able to reveal more information about the process. Last but not the least, even though STEM can give researchers an idea about whether the metal is dispersed well morphologically, it is a tool showing the sample morphology at a small field of

view. Technology like XRD should be conducted to support any conclusions made from a TEM/STEM image.

For the second direction, the following suggestions can be made based on the results of the studies. Firstly, when designing the precursors, the metal interaction with the carbon should be taken into account. Also, temperature chosen should be more careful. Based on the results shown in the thesis, a temperature of over 1000 °C is unnecessary, and will have an adverse effect on the catalysts. When increasing the weight percentage of the metal, temperature would be even more important since the metallic particles would be easy to form. Recently, synthesizing M-N-C catalysts with soft-template using chemical vapor deposition method is arising attention. Even with this method, a high temperature is not necessary since the Zn in ZIF-8 has evaporated below 700 °C and the iron atom has been released when temperature hits above 600 °C. Researchers should also consider how to uniformly heat the materials when scaling up if a low temperature is applied.

Overall, pyrolysis is an important step in synthesizing M-N-C catalysts and should not be treated as Blackbox. The thesis revealed the box and provided suggestions for future work. The M-N-C catalysts can be designed more rationally based on direct evidence and analysis of the pyrolysis.

Reference

1   bp Statistical Review of World Energy. (2022).
2   Davis, S. J. *et al.* Net-zero emissions energy systems. *Science* **360**, eaas9793, doi:10.1126/science.aas9793 (2018).
3   Rogelj, J. *et al.* Zero emission targets as long-term global goals for climate protection. *Environmental Research Letters* **10**, 105007, doi:10.1088/1748-9326/10/10/105007 (2015).
4   Yoshida, T. & Kojima, K. Toyota MIRAI Fuel Cell Vehicle and Progress Toward a Future Hydrogen Society. *Interface magazine* **24**, 45-49, doi:10.1149/2.f03152if (2015).
5   Sealy, C. The problem with platinum. *Materials Today* **11**, 65-68, doi:10.1016/s1369-7021(08)70254-2 (2008).
6   Debe, M. K. Electrocatalyst approaches and challenges for automotive fuel cells. *Nature* **486**, 43-51, doi:10.1038/nature11115 (2012).
7   Lefèvre, M., Proietti, E., Jaouen, F. & Dodelet, J.-P. Iron-Based Catalysts with Improved Oxygen Reduction Activity in Polymer Electrolyte Fuel Cells. *Science* **324**, 71-74, doi:10.1126/science.1170051 (2009).
8   Wu, G., More, K. L., Johnston, C. M. & Zelenay, P. High-Performance Electrocatalysts for Oxygen Reduction Derived from Polyaniline, Iron, and Cobalt. *Science* **332**, 443-447, doi:10.1126/science.1200832 (2011).
9   Wang, X. *et al.* MOF derived catalysts for electrochemical oxygen reduction. *J. Mater. Chem. A* **2**, 14064-14070, doi:10.1039/c4ta01506a (2014).
10   Karthikayini, M. P., Thirupathi, T., Wang, G., Ramani, V. K. & Raman, R. K. Highly Active and Durable Non-Precious Metal Catalyst for the Oxygen Reduction Reaction in Acidic Medium. *Journal of The Electrochemical Society* **163**, F539-F547, doi:10.1149/2.1001606jes (2016).
11   Zhao, Y. *et al.* Few-layer graphdiyne doped with sp-hybridized nitrogen atoms at acetylenic sites for oxygen reduction electrocatalysis. *Nature Chemistry* **10**, 924-931, doi:10.1038/s41557-018-0100-1 (2018).
12   Patniboon, T. & Hansen, H. A. N‐Doped Graphene Supported on Metal‐Iron Carbide as a Catalyst for the Oxygen Reduction Reaction: Density Functional Theory Study. *ChemSusChem* **13**, 996-1005, doi:10.1002/cssc.201903035 (2020).
13   Vezzù, K. *et al.* Fe-carbon nitride "Core-shell" electrocatalysts for the oxygen reduction reaction. *Electrochimica Acta* **222**, 1778-1791, doi:10.1016/j.electacta.2016.11.093 (2016).
14   Maiyalagan, T., Jarvis, K. A., Therese, S., Ferreira, P. J. & Manthiram, A. Spinel-type lithium cobalt oxide as a bifunctional electrocatalyst for the oxygen evolution and oxygen reduction reactions. *Nature Communications* **5**, doi:10.1038/ncomms4949 (2014).
15   Asset, T., Maillard, F. & Jaouen, F. Electrocatalysis with Single‐Metal Atom Sites in Doped Carbon Matrices. *Supported Metal Single Atom Catalysis*, 531-582 (2022).
16   Pylypenko, S., Olson, T. S., Carroll, N. J., Petsev, D. N. & Atanassov, P. Templated Platinum/Carbon Oxygen Reduction Fuel Cell Electrocatalysts. *The Journal of Physical Chemistry C* **114**, 4200-4207, doi:10.1021/jp909418m (2010).

17   Serov, A. *et al.* Nano-structured non-platinum catalysts for automotive fuel cell application. *Nano Energy* **16**, 293-300, doi:https://doi.org/10.1016/j.nanoen.2015.07.002 (2015).

18   Proietti, E. *et al.* Iron-based cathode catalyst with enhanced power density in polymer electrolyte membrane fuel cells. *Nature Communications* **2**, 416, doi:10.1038/ncomms1427 (2011).

19   Ma, S., Goenaga, G. A., Call, A. V. & Liu, D.-J. Cobalt Imidazolate Framework as Precursor for Oxygen Reduction Reaction Electrocatalysts. *Chemistry – A European Journal* **17**, 2063-2067, doi:https://doi.org/10.1002/chem.201003080 (2011).

20   Wu, G. *et al.* Performance Durability of Polyaniline-derived Non-precious Cathode Catalysts. *ECS Transactions* **25**, 1299, doi:10.1149/1.3210685 (2009).

21   Chen, S.-A. & Lin, L.-C. Polyaniline Doped by the New Class of Dopant, Ionic Salt: Structure and Properties. *Macromolecules* **28**, 1239-1245, doi:10.1021/ma00108a062 (1995).

22   Shui, J., Chen, C., Grabstanowicz, L., Zhao, D. & Liu, D.-J. Highly efficient nonprecious metal catalyst prepared with metal–organic framework in a continuous carbon nanofibrous network. *Proceedings of the National Academy of Sciences* **112**, 10629-10634 (2015).

23   Artyushkova, K., Serov, A., Rojas-Carbonell, S. & Atanassov, P. Chemistry of Multitudinous Active Sites for Oxygen Reduction Reaction in Transition Metal–Nitrogen–Carbon Electrocatalysts. *The Journal of Physical Chemistry C* **119**, 25917-25928, doi:10.1021/acs.jpcc.5b07653 (2015).

24   Matanovic, I., Artyushkova, K. & Atanassov, P. Understanding PGM-free catalysts by linking density functional theory calculations and structural analysis: Perspectives and challenges. *Current Opinion in Electrochemistry* **9**, 137-144, doi:10.1016/j.coelec.2018.03.009 (2018).

25   Kramm, U. I. *et al.* On an Easy Way To Prepare Metal–Nitrogen Doped Carbon with Exclusive Presence of MeN4-type Sites Active for the ORR. *Journal of the American Chemical Society* **138**, 635-640, doi:10.1021/jacs.5b11015 (2016).

26   Santori, P. G. *et al.* Effect of Pyrolysis Atmosphere and Electrolyte pH on the Oxygen Reduction Activity, Stability and Spectroscopic Signature of FeNx Moieties in Fe-N-C Catalysts. *Journal of The Electrochemical Society* **166**, F3311-F3320, doi:10.1149/2.0371907jes (2019).

27   Jia, Q. *et al.* Experimental Observation of Redox-Induced Fe–N Switching Behavior as a Determinant Role for Oxygen Reduction Activity. *ACS Nano* **9**, 12496-12505, doi:10.1021/acsnano.5b05984 (2015).

28   Jia, Q. Y. *et al.* Spectroscopic insights into the nature of active sites in iron-nitrogen-carbon electrocatalysts for oxygen reduction in acid. *Nano Energy* **29**, 65-82, doi:10.1016/j.nanoen.2016.03.025 (2016).

29   Zitolo, A. *et al.* Identification of catalytic sites for oxygen reduction in iron- and nitrogen-doped graphene materials. *Nature Materials* **14**, 937-942, doi:10.1038/nmat4367 (2015).

30   Chung, H. T. *et al.* Direct atomic-level insight into the active sites of a high-performance PGM-free ORR catalyst. *Science* **357**, 479-484, doi:10.1126/science.aan2255 (2017).

31   Li, J. *et al.* Evolution Pathway from Iron Compounds to Fe1(II)–N4 Sites through Gas-Phase Iron during Pyrolysis. *Journal of the American Chemical Society* **142**, 1417-1423, doi:10.1021/jacs.9b11197 (2020).

32   Aiyappa, H. B. *et al.* Oxygen Evolution Electrocatalysis of a Single MOF‐Derived Composite Nanoparticle on the Tip of a Nanoelectrode. *Angewandte Chemie International Edition* **58**, 8927-8931, doi:10.1002/anie.201903283 (2019).

33   Honda, K., Waki, Y., Matsumoto, A., Kondo, B. & Shimai, Y. Amorphous carbon having higher catalytic activity toward oxygen reduction reaction: Quinone and carboxy groups introduced onto its surface. *Diamond and Related Materials* **107**, 107900, doi:https://doi.org/10.1016/j.diamond.2020.107900 (2020).

34   Qiu, K. & Guo, Z. X. Hierarchically porous graphene sheets and graphitic carbon nitride intercalated composites for enhanced oxygen reduction reaction. *Journal of Materials Chemistry A* **2**, 3209-3215, doi:10.1039/C3TA14158F (2014).

35   Erable, B. *et al.* Iron-Nicarbazin derived platinum group metal-free electrocatalyst in scalable-size air-breathing cathodes for microbial fuel cells. *Electrochimica Acta* **277**, 127-135, doi:10.1016/j.electacta.2018.04.190 (2018).

36   Serov, A., Artyushkova, K. & Atanassov, P. Fe-N-C Oxygen Reduction Fuel Cell Catalyst Derived from Carbendazim: Synthesis, Structure, and Reactivity. *Advanced Energy Materials* **4**, 1301735, doi:10.1002/aenm.201301735 (2014).

37   Wang, L., Sofer, Z. & Pumera, M. Will Any Crap We Put into Graphene Increase Its Electrocatalytic Effect? *ACS Nano* **14**, 21-25, doi:10.1021/acsnano.9b00184 (2020).

38   Gewirth, A. A., Varnell, J. A. & Diascro, A. M. Nonprecious Metal Catalysts for Oxygen Reduction in Heterogeneous Aqueous Systems. *Chemical Reviews* **118**, 2313-2339, doi:10.1021/acs.chemrev.7b00335 (2018).

39   Zagal, J. H. & Koper, M. T. M. Reactivity Descriptors for the Activity of Molecular MN4 Catalysts for the Oxygen Reduction Reaction. *Angewandte Chemie International Edition* **55**, 14510-14521, doi:10.1002/anie.201604311 (2016).

40   He, Y. *et al.* Highly active atomically dispersed CoN4 fuel cell cathode catalysts derived from surfactant-assisted MOFs: carbon-shell confinement strategy. *Energy & Environmental Science* **12**, 250-260, doi:10.1039/c8ee02694g (2019).

41   Deng, Y. *et al.* g-C3N4 promoted MOF derived hollow carbon nanopolyhedra doped with high density/fraction of single Fe atoms as an ultra-high performance non-precious catalyst towards acidic ORR and PEM fuel cells. *Journal of Materials Chemistry A* **7**, 5020-5030, doi:10.1039/c8ta11785c (2019).

42   Rojas-Carbonell, S. *et al.* Effect of pH on the Activity of Platinum Group Metal-Free Catalysts in Oxygen Reduction Reaction. *ACS Catalysis* **8**, 3041-3053, doi:10.1021/acscatal.7b03991 (2018).

43   Artyushkova, K. *et al.* Correlations between Synthesis and Performance of Fe-Based PGM-Free Catalysts in Acidic and Alkaline Media: Evolution of Surface Chemistry and Morphology. *ACS Applied Energy Materials* **2**, 5406-5418, doi:10.1021/acsaem.9b00331 (2019).

44   Primbs, M. *et al.* Establishing reactivity descriptors for platinum group metal (PGM)-free Fe–N–C catalysts for PEM fuel cells. *Energy & Environmental Science*, doi:10.1039/d0ee01013h (2020).

45   Reshetenko, T. *et al.* Electron and proton conductivity of Fe-N-C cathodes for PEM fuel cells: A model-based electrochemical impedance spectroscopy measurement.

Electrochemistry Communications **118**, 106795, doi:https://doi.org/10.1016/j.elecom.2020.106795 (2020).

46   Osmieri, L. *et al.* Utilizing ink composition to tune bulk-electrode gas transport, performance, and operational robustness for a Fe–N–C catalyst in polymer electrolyte fuel cell. *Nano Energy*, 104943 %@ 102211-102855 (2020).

47   Varipore™: A Powerful Manufacturing Platform for Fuel Cell and Electrolyzer Applications. *ECS Meeting Abstracts*, doi:10.1149/ma2019-02/37/1734 (2019).

48   Xie, J. *et al.* Selective Aerobic Oxidation of Alcohols over Atomically-Dispersed Non-Precious Metal Catalysts. *ChemSusChem* **10**, 359-362, doi:https://doi.org/10.1002/cssc.201601364 (2017).

49   Barnard, H. S. *et al.* Synchrotron X-ray Micro Tomography at the Advanced Light Source: In-Situ Sample Environments for Advanced Aerospace Materials. *Microscopy and Microanalysis* **24**, 444-445, doi:10.1017/s1431927618014472 (2018).

50   Serov, A. *et al.* Nano-structured platinum group metal-free catalysts and their integration in fuel cell electrode architectures. *Applied Catalysis B: Environmental* **237**, 1139-1147, doi:10.1016/j.apcatb.2017.08.067 (2018).

51   Arganda-Carreras, I. *et al.* Trainable Weka Segmentation: a machine learning tool for microscopy pixel classification. *Bioinformatics* **33**, 2424-2426, doi:10.1093/bioinformatics/btx180 (2017).

52   Normile, S. J. & Zenyuk, I. V. Imaging ionomer in fuel cell catalyst layers with synchrotron nano transmission x-ray microscopy. *Solid State Ionics* **335**, 38-46 (2019).

53   Gürsoy, D. A., De Carlo, F., Xiao, X. & Jacobsen, C. TomoPy: a framework for the analysis of synchrotron tomographic data. *Journal of Synchrotron Radiation* **21**, 1188-1193, doi:10.1107/s1600577514013939 (2014).

54   Pelt, D. M. *et al.* Integration of TomoPy and the ASTRA toolbox for advanced processing and reconstruction of tomographic synchrotron data. *Journal of Synchrotron Radiation* **23**, 842-849, doi:10.1107/s1600577516005658 (2016).

55   De Carlo, F. *et al.* Scientific data exchange: a schema for HDF5-based storage of raw and analyzed data. *Journal of synchrotron radiation* **21**, 1224-1230 (2014).

56   De Andrade, V. *et al.* Nanoscale 3D imaging at the advanced photon source. *SPIE Newsroom* **10**, 006461 (2016).

57   Doran, A. *et al.* Compact low power infrared tube furnace for in situ X-ray powder diffraction. *Review of Scientific Instruments* **88**, 013903, doi:10.1063/1.4973561 (2017).

58   Schlicker, L. *et al.* Transmission in situ and operando high temperature X-ray powder diffraction in variable gaseous environments. *Review of Scientific Instruments* **89**, 033904, doi:10.1063/1.5001695 (2018).

59   Prescher, C. & Prakapenka, V. B. DIOPTAS: a program for reduction of two-dimensional X-ray diffraction data and data exploration. *High Pressure Research* **35**, 223-230, doi:10.1080/08957959.2015.1059835 (2015).

60   Lua, A. C., Yang, T. & Guo, J. Effects of pyrolysis conditions on the properties of activated carbons prepared from pistachio-nut shells. *Journal of Analytical and Applied Pyrolysis* **72**, 279-287, doi:10.1016/j.jaap.2004.08.001 (2004).

61   Zlotorowicz, A., Jayasayee, K., Dahl, P. I., Thomassen, M. S. & Kjelstrup, S. Tailored porosities of the cathode layer for improved polymer electrolyte fuel cell performance. *Journal of Power Sources* **287**, 472-477, doi:10.1016/j.jpowsour.2015.04.079 (2015).

62   Maser, J. Book Review: Soft X-rays and Extreme Ultraviolet Radiation: Principles and Applications. *Microscopy and Microanalysis* **7**, 536-536, doi:10.1007/s10005-001-0023-1 (2001).

63   Van Veen, J. A. R., Colijn, H. A. & Van Baar, J. F. On the effect of a heat treatment on the structure of carbon-supported metalloporphyrins and phthalocyanines. *Electrochimica Acta* **33**, 801-804, doi:10.1016/s0013-4686(98)80010-8 (1988).

64   Shen, M., Wei, C., Ai, K. & Lu, L. Transition metal–nitrogen–carbon nanostructured catalysts for the oxygen reduction reaction: From mechanistic insights to structural optimization. *Nano Research* **10**, 1449-1470, doi:10.1007/s12274-016-1400-7 (2017).

65   Shen, V. K., Siderius, D.W., Krekelberg, W.P., and Hatch, H.W., Eds., . NIST Standard Reference Simulation Website *NIST Standard Reference Database Number 173*, doi:10.18434/T4M88Q.

66   Richner, G., Van Bokhoven, J. A., Neuhold, Y.-M., Makosch, M. & Hungerbühler, K. In situ infrared monitoring of the solid/liquid catalyst interface during the three-phase hydrogenation of nitrobenzene over nanosized Au on TiO2. *Physical Chemistry Chemical Physics* **13**, 12463, doi:10.1039/c1cp20238c (2011).

67   Cameron, G. G. & Fortune, J. D. Determination of activation energies from TGA and TVA traces. *European Polymer Journal* **4**, 333-342, doi:10.1016/0014-3057(68)90021-9 (1968).

68   Wang, H., Li, G., Ma, J. & Zhao, D. The effect of methane decomposition on the formation and magnetic properties of iron carbide prepared from oolitic hematite. *RSC Advances* **7**, 3921-3927, doi:10.1039/c6ra26166c (2017).

69   Nikitenko, S. I. *et al.* Tailoring the Properties of Fe−Fe3C Nanocrystalline Particles Prepared by Sonochemistry. *The Journal of Physical Chemistry B* **108**, 7620-7626, doi:10.1021/jp036376r (2004).

70   Choi, M., Kim, M., Lee, K., Song, J. & Kim, J. The effects of Fe nano-powders on compaction behaviors and magnetic properties of SMCs. *Journal of Magnetism and Magnetic Materials* **480**, 33-39 (2019).

71   Ye, Y. F. *et al.* Atomic-scale distorted lattice in chemically disordered equimolar complex alloys. *Acta Materialia* **150**, 182-194, doi:10.1016/j.actamat.2018.03.008 (2018).

72   Chang, W.-S., Wei, Y., Guo, J.-M. & He, F.-J. Thermal Stability of Ni-Fe Alloy Foils Continuously Electrodeposited in a Fluorborate Bath. *Open Journal of Metal* **02**, 18-23, doi:10.4236/ojmetal.2012.21003 (2012).

73   Hoekstra, J. *et al.* Base Metal Catalyzed Graphitization of Cellulose: A Combined Raman Spectroscopy, Temperature-Dependent X-ray Diffraction and High-Resolution Transmission Electron Microscopy Study. *The Journal of Physical Chemistry C* **119**, 10653-10661, doi:10.1021/acs.jpcc.5b00477 (2015).

74   He, Z. *et al.* Iron Catalysts for the Growth of Carbon Nanofibers: Fe, Fe3C or Both? *Chemistry of Materials* **23**, 5379-5387, doi:10.1021/cm202315j (2011).

75   Sajitha, E. P. *et al.* Synthesis and characteristics of iron nanoparticles in a carbon matrix along with the catalytic graphitization of amorphous carbon. *Carbon* **42**, 2815-2820, doi:10.1016/j.carbon.2004.06.027 (2004).

76   Stinespring, C. D. & Wormhoudt, J. C. Surface studies relevant to silicon carbide chemical vapor deposition. *Journal of Applied Physics* **65**, 1733-1742, doi:10.1063/1.342947 (1989).

77   Kouketsu, Y. *et al.* A new approach to develop the Raman carbonaceous material geothermometer for low-grade metamorphism using peak width. *Island Arc* **23**, 33-50, doi:10.1111/iar.12057 (2014).

78   Sadezky, A., Muckenhuber, H., Grothe, H., Niessner, R. & Pöschl, U. Raman microspectroscopy of soot and related carbonaceous materials: Spectral analysis and structural information. *Carbon* **43**, 1731-1742, doi:https://doi.org/10.1016/j.carbon.2005.02.018 (2005).

79   Strickland, K. *et al.* Anion Resistant Oxygen Reduction Electrocatalyst in Phosphoric Acid Fuel Cell. *ACS Catalysis* **8**, 3833-3843, doi:10.1021/acscatal.8b00390 (2018).

80   Workman, M. J. *et al.* Platinum group metal-free electrocatalysts: Effects of synthesis on structure and performance in proton-exchange membrane fuel cell cathodes. *Journal of Power Sources* **348**, 30-39, doi:10.1016/j.jpowsour.2017.02.067 (2017).

81   Yang, H.-J. *et al.* Superior Selectivity and Tolerance towards Metal-Ion Impurities of a Fe/N/C Catalyst for CO2 Reduction. *ChemSusChem* **12**, 3988-3995, doi:10.1002/cssc.201901330 (2019).

82   Türk, K. K. *et al.* Novel multi walled carbon nanotube based nitrogen impregnated Co and Fe cathode catalysts for improved microbial fuel cell performance. *International Journal of Hydrogen Energy* **43**, 23027-23035, doi:https://doi.org/10.1016/j.ijhydene.2018.10.143 (2018).

83   Asset, T. *et al.* Investigating the Nature of the Active Sites for the CO2 Reduction Reaction on Carbon-Based Electrocatalysts. *ACS Catalysis* **9**, 7668-7678, doi:10.1021/acscatal.9b01513 (2019).

84   Matanovic, I. *et al.* Core Level Shifts of Hydrogenated Pyridinic and Pyrrolic Nitrogen in the Nitrogen-Containing Graphene-Based Electrocatalysts: In-Plane vs Edge Defects. *The Journal of Physical Chemistry C* **120**, 29225-29232, doi:10.1021/acs.jpcc.6b09778 (2016).

85   Chen, Y., Matanovic, I., Weiler, E., Atanassov, P. & Artyushkova, K. Mechanism of Oxygen Reduction Reaction on Transition Metal–Nitrogen–Carbon Catalysts: Establishing the Role of Nitrogen-containing Active Sites. *ACS Applied Energy Materials* **1**, 5948-5953, doi:10.1021/acsaem.8b00959 (2018).

86   Shard, A. G. Detection limits in XPS for more than 6000 binary systems using Al and Mg Kα X-rays. *Surface and Interface Analysis* **46**, 175-185, doi:10.1002/sia.5406 (2014).

87   Knipe, S. W., Mycroft, J. R., Pratt, A. R., Nesbitt, H. W. & Bancroft, G. M. X-ray photoelectron spectroscopic study of water adsorption on iron sulphide minerals. *Geochimica et Cosmochimica Acta* **59**, 1079-1090, doi:https://doi.org/10.1016/0016-7037(95)00025-U (1995).

88   Yang, C. *et al.* Carbon Dioxide Adsorption on CeO2(110): An XPS and NEXAFS Study. *ChemPhysChem* **18**, 1874-1880, doi:10.1002/cphc.201700240 (2017).

89   Seah, M. P. & Dench, W. A. Quantitative electron spectroscopy of surfaces: A standard data base for electron inelastic mean free paths in solids. *Surface and Interface Analysis* **1**, 2-11, doi:10.1002/sia.740010103 (1979).

90   Jackson, S. T. & Nuzzo, R. G. Determining hybridization differences for amorphous carbon from the XPS C 1s envelope. *Applied Surface Science* **90**, 195-203, doi:https://doi.org/10.1016/0169-4332(95)00079-8 (1995).

91   Fujimoto, A., Yamada, Y., Koinuma, M. & Sato, S. Origins of sp3C peaks in C1s X-ray Photoelectron Spectra of Carbon Materials. *Analytical Chemistry* **88**, 6110-6114, doi:10.1021/acs.analchem.6b01327 (2016).

92   Matter, P. H., Zhang, L. & Ozkan, U. S. The role of nanostructure in nitrogen-containing carbon catalysts for the oxygen reduction reaction. *Journal of Catalysis* **239**, 83-96, doi:https://doi.org/10.1016/j.jcat.2006.01.022 (2006).

93   Liu, J., Song, P. & Xu, W. Structure-activity relationship of doped-nitrogen (N)-based metal-free active sites on carbon for oxygen reduction reaction. *Carbon* **115**, 763-772, doi:https://doi.org/10.1016/j.carbon.2017.01.080 (2017).

94   Chung, H. T., Won, J. H. & Zelenay, P. Active and stable carbon nanotube/nanoparticle composite electrocatalyst for oxygen reduction. *Nature Communications* **4**, 1922, doi:10.1038/ncomms2944 (2013).

95   Wu, G. *et al.* Carbon nanocomposite catalysts for oxygen reduction and evolution reactions: From nitrogen doping to transition-metal addition. *Nano Energy* **29**, 83-110, doi:https://doi.org/10.1016/j.nanoen.2015.12.032 (2016).

96   Li, J. *et al.* The Challenge of Achieving a High Density of Fe-Based Active Sites in a Highly Graphitic Carbon Matrix. *Catalysts* **9**, 144 (2019).

97   Möller, T. *et al.* Efficient CO2 to CO electrolysis on solid Ni–N–C catalysts at industrial current densities. *Energy & Environmental Science* **12**, 640-647, doi:10.1039/C8EE02662A (2019).

98   Oezaslan, M., Hasché, F. & Strasser, P. In Situ Observation of Bimetallic Alloy Nanoparticle Formation and Growth Using High-Temperature XRD. *Chemistry of Materials* **23**, 2159-2165, doi:10.1021/cm103661q (2011).

99   Kramm, U. I. *et al.* Structure of the catalytic sites in Fe/N/C-catalysts for O2-reduction in PEM fuel cells. *Physical Chemistry Chemical Physics* **14**, 11673, doi:10.1039/c2cp41957b (2012).

100   Tylus, U. *et al.* Elucidating Oxygen Reduction Active Sites in Pyrolyzed Metal–Nitrogen Coordinated Non-Precious-Metal Electrocatalyst Systems. *The Journal of Physical Chemistry C* **118**, 8999-9008, doi:10.1021/jp500781v (2014).

101   Cook, A. H. 325. Catalytic properties of the phthalocyanines. Part I. Catalase properties. *Journal of the Chemical Society (Resumed)*, 1761, doi:10.1039/jr9380001761 (1938).

102   Jasinski, R. A New Fuel Cell Cathode Catalyst. *Nature* **201**, 1212-1213, doi:10.1038/2011212a0 (1964).

103   Strickland, K. *et al.* Highly active oxygen reduction non-platinum group metal electrocatalyst without direct metal–nitrogen coordination. *Nature Communications* **6**, 7343, doi:10.1038/ncomms8343 (2015).

104   Serov, A., Robson, M. H., Smolnik, M. & Atanassov, P. Tri-metallic transition metal–nitrogen–carbon catalysts derived by sacrificial support method synthesis. *Electrochimica Acta* **109**, 433-439, doi:https://doi.org/10.1016/j.electacta.2013.07.104 (2013).

105   Wang, X. *et al.* Directly converting Fe-doped metal–organic frameworks into highly active and stable Fe-N-C catalysts for oxygen reduction in acid. *Nano Energy* **25**, 110-119, doi:10.1016/j.nanoen.2016.04.042 (2016).

106   Xia, W. *et al.* High-Performance Energy Storage and Conversion Materials Derived from a Single Metal–Organic Framework/Graphene Aerogel Composite. *Nano Letters* **17**, 2788-2795, doi:10.1021/acs.nanolett.6b05004 (2017).

107   Jiao, L. *et al.* Chemical vapour deposition of Fe–N–C oxygen reduction catalysts with full utilization of dense Fe–N4 sites. *Nature Materials* **20**, 1385-1391, doi:10.1038/s41563-021-01030-2 (2021).

108   Liu, S. *et al.* Atomically dispersed iron sites with a nitrogen–carbon coating as highly active and durable oxygen reduction catalysts for fuel cells. *Nature Energy* **7**, 652-663, doi:10.1038/s41560-022-01062-1 (2022).

109   Wang, H. *et al.* Capacitive deionization using carbon derived from an array of zeolitic-imidazolate frameworks. *Nano Energy* **77**, 105304, doi:https://doi.org/10.1016/j.nanoen.2020.105304 (2020).

110   Wang, Q. *et al.* Evolution of Zn(II) single atom catalyst sites during the pyrolysis-induced transformation of ZIF-8 to N-doped carbons. *Science Bulletin* **65**, 1743-1751, doi:https://doi.org/10.1016/j.scib.2020.06.020 (2020).

111   Chen, X. *et al.* Metal–organic framework-derived mesoporous carbon nanoframes embedded with atomically dispersed Fe–Nx active sites for efficient bifunctional oxygen and carbon dioxide electroreduction. *Applied Catalysis B: Environmental* **267**, 118720, doi:https://doi.org/10.1016/j.apcatb.2020.118720 (2020).

112   Chen, M. *et al.* Atomically Dispersed MnN4 Catalysts via Environmentally Benign Aqueous Synthesis for Oxygen Reduction: Mechanistic Understanding of Activity and Stability Improvements. *ACS Catalysis* **10**, 10523-10534, doi:10.1021/acscatal.0c02490 (2020).

113   Karapinar, D. *et al.* Electroreduction of CO_2 on Single‐Site Copper‐Nitrogen‐Doped Carbon Material: Selective Formation of Ethanol and Reversible Restructuring of the Metal Sites. *Angewandte Chemie International Edition* **58**, 15098-15103, doi:10.1002/anie.201907994 (2019).

114   Xia, W. *et al.* Well-defined carbon polyhedrons prepared from nano metal–organic frameworks for oxygen reduction. *J. Mater. Chem. A* **2**, 11606-11613, doi:10.1039/c4ta01656d (2014).

115   Zhang, M., Dai, Q., Zheng, H., Chen, M. & Dai, L. Novel MOF-Derived Co@N-C Bifunctional Catalysts for Highly Efficient Zn-Air Batteries and Water Splitting. *Advanced Materials* **30**, 1705431, doi:10.1002/adma.201705431 (2018).

116   Chong, L. *et al.* Investigation of Oxygen Reduction Activity of Catalysts Derived from Co and Co/Zn Methyl-Imidazolate Frameworks in Proton Exchange Membrane Fuel Cells. *ChemElectroChem* **3**, 1541-1545, doi:https://doi.org/10.1002/celc.201600163 (2016).

117   He, Y. *et al.* Highly active atomically dispersed CoN4 fuel cell cathode catalysts derived from surfactant-assisted MOFs: carbon-shell confinement strategy. *Energy & Environmental Science* **12**, 250-260, doi:10.1039/c8ee02694g (2019).

118   Zhang, H. *et al.* Atomically Dispersed Iron Cathode Catalysts Derived from Binary Ligand-Based Zeolitic Imidazolate Frameworks with Enhanced Stability for PEM Fuel Cells. *Journal of The Electrochemical Society* **166**, F3116-F3122, doi:10.1149/2.0141907jes (2019).

119   Sun, Y. *et al.* Activity–Selectivity Trends in the Electrochemical Production of Hydrogen Peroxide over Single-Site Metal–Nitrogen–Carbon Catalysts. *Journal of the American Chemical Society* **141**, 12372-12381, doi:10.1021/jacs.9b05576 (2019).

120   Wang, H. *et al.* Engineering Fe–Fe₃C@Fe–N–C Active Sites and Hybrid Structures from Dual Metal–Organic Frameworks for Oxygen Reduction Reaction in H_2–O_2 Fuel Cell. *Advanced Functional Materials* **29**, 1901531, doi:10.1002/adfm.201901531 (2019).

121   De Andrade, V. *et al.* Fast X-ray Nanotomography with Sub-10 nm Resolution as a Powerful Imaging Tool for Nanotechnology and Energy Storage Applications. *Advanced Materials* **33**, 2008653, doi:https://doi.org/10.1002/adma.202008653 (2021).

122   Zhou, Z., Rahman Siddiquee, M. M., Tajbakhsh, N. & Liang, J.   3-11 (Springer International Publishing, 2018).

123   Zhou, Z., Siddiquee, M. M. R., Tajbakhsh, N. & Liang, J. UNet++: Redesigning Skip Connections to Exploit Multiscale Features in Image Segmentation. *IEEE Transactions on Medical Imaging* **39**, 1856-1867, doi:10.1109/TMI.2019.2959609 (2020).

124   Kunz, M. *et al.* A beamline for high-pressure studies at the Advanced Light Source with a superconducting bending magnet as the source. *Journal of Synchrotron Radiation* **12**, 650-658, doi:doi:10.1107/S0909049505020959 (2005).

125   Hardy, D. A. *et al.* Prussian Blue Iron–Cobalt Mesocrystals as a Template for the Growth of Fe/Co Carbide (Cementite) and Fe/Co Nanocrystals. *Chemistry of Materials* **31**, 8163-8173, doi:10.1021/acs.chemmater.9b02957 (2019).

126   Bekheet, M. F. *et al.* Steering the Methane Dry Reforming Reactivity of Ni/La2O3 Catalysts by Controlled In Situ Decomposition of Doped La2NiO4 Precursor Structures. *ACS Catalysis* **11**, 43-59, doi:10.1021/acscatal.0c04290 (2021).

127   Tanaka, S. *et al.* Adsorption and Diffusion Phenomena in Crystal Size Engineered ZIF-8 MOF. *The Journal of Physical Chemistry C* **119**, 28430-28439, doi:10.1021/acs.jpcc.5b09520 (2015).

128   Wu, G. *et al.* Nitrogen-Doped Graphene-Rich Catalysts Derived from Heteroatom Polymers for Oxygen Reduction in Nonaqueous Lithium–O2 Battery Cathodes. *ACS Nano* **6**, 9764-9776, doi:10.1021/nn303275d (2012).

129   Kropf, A. J. *et al.*   (AIP).

130   Ravel, B. & Newville, M. ATHENA, ARTEMIS, HEPHAESTUS: data analysis for X-ray absorption spectroscopy using IFEFFIT. *Journal of Synchrotron Radiation* **12**, 537-541, doi:doi:10.1107/S0909049505012719 (2005).

131   Artyushkova, K. *et al.* Density functional theory calculations of XPS binding energy shift for nitrogen-containing graphene-like structures. *Chemical Communications* **49**, 2539, doi:10.1039/c3cc40324f (2013).

132   Park, K. S. *et al.* Exceptional chemical and thermal stability of zeolitic imidazolate frameworks. *Proceedings of the National Academy of Sciences* **103**, 10186-10191, doi:10.1073/pnas.0602439103 (2006).

133   Banerjee, R. *et al.* High-Throughput Synthesis of Zeolitic Imidazolate Frameworks and Application to CO_2 Capture. *Science* **319**, 939-943, doi:doi:10.1126/science.1152516 (2008).

134   Nozari, V. *et al.* Ionic liquid facilitated melting of the metal-organic framework ZIF-8. *Nature Communications* **12**, 5703, doi:10.1038/s41467-021-25970-0 (2021).

135   Hu, Y., Song, X., Zheng, Q., Wang, J. & Pei, J. Zeolitic imidazolate framework-67 for shape stabilization and enhanced thermal stability of paraffin-based phase change materials. *RSC Advances* **9**, 9962-9967, doi:10.1039/c9ra00874h (2019).

136   Han, X. *et al.* Exploring the Roles of ZIF-67 as an Energetic Additive in the Thermal Decomposition of Ammonium Perchlorate. *Energy & Fuels* **35**, 4447-4456, doi:10.1021/acs.energyfuels.0c03878 (2021).

137   Workman, M. J., Serov, A., Tsui, L.-k., Atanassov, P. & Artyushkova, K. Fe–N–C Catalyst Graphitic Layer Structure and Fuel Cell Performance. *ACS Energy Letters* **2**, 1489-1493, doi:10.1021/acsenergylett.7b00391 (2017).

138   Venna, S. R., Jasinski, J. B. & Carreon, M. A. Structural Evolution of Zeolitic Imidazolate Framework-8. *Journal of the American Chemical Society* **132**, 18030-18033, doi:10.1021/ja109268m (2010).

139   Rossi, G., D'Acapito, F., Amidani, L., Boscherini, F. & Pedio, M. Local environment of metal ions in phthalocyanines: K-edge X-ray absorption spectra. *Physical Chemistry Chemical Physics* **18**, 23686-23694, doi:10.1039/c6cp04022e (2016).

140   Dadlani, A. *et al.* Revealing the Bonding Environment of Zn in ALD Zn(O,S) Buffer Layers through X-ray Absorption Spectroscopy. *ACS Applied Materials & Interfaces* **9**, 39105-39109, doi:10.1021/acsami.7b06728 (2017).

141   Li, F. *et al.* Identifying the structure of Zn-N$_2$ active sites and structural activation. *Nature Communications* **10**, 2623, doi:10.1038/s41467-019-10622-1 (2019).

142   Wachi, F. M. & Gilmartin, D. E. Vapor Pressure and Heat of Vaporization of Cobalt. *The Journal of Chemical Physics* **57**, 4713-4716, doi:10.1063/1.1678140 (1972).

143   Akhtar, M. K., Lipscomb, G. G. & Pratsinis, S. E. Monte Carlo Simulation of Particle Coagulation and Sintering. *Aerosol Science and Technology* **21**, 83-93, doi:10.1080/02786829408959698 (1994).

144   Fu, R. *et al.* Formation of Graphitic Structures in Cobalt- and Nickel-Doped Carbon Aerogels. *Langmuir* **21**, 2647-2651, doi:10.1021/la047344d (2005).

145   Goldie, S. J., Jiang, S. & Coleman, K. S. Cobalt nanoparticle catalysed graphitization and the effect of metal precursor decomposition temperature. *Materials Advances* **2**, 3353-3361, doi:10.1039/d1ma00125f (2021).

146   Nishizawa, T. & Ishida, K. The Co (Cobalt) system. *Bulletin of Alloy Phase Diagrams* **4**, 387-390, doi:10.1007/BF02868089 (1983).

147   Sewak, R., Dey, C. C. & Toprek, D. Temperature induced phase transformation in Co. *Scientific Reports* **12**, 10054, doi:10.1038/s41598-022-14302-x (2022).

148   Pattengale, B. *et al.* Exceptionally Long-Lived Charge Separated State in Zeolitic Imidazolate Framework: Implication for Photocatalytic Applications. *Journal of the American Chemical Society* **138**, 8072-8075, doi:10.1021/jacs.6b04615 (2016).

149   SantaLucia, D. J., Hu, W., Wang, D., Huang, J. & Berry, J. F. Postsynthetic Treatment of ZIF-67 with 5-Methyltetrazole: Evolution from Pseudo-Td to Pseudo-Oh Symmetry and Collapse of Magnetic Ordering. *Inorganic Chemistry* **61**, 6056-6062, doi:10.1021/acs.inorgchem.2c00066 (2022).

150   Deng, T. *et al.* Atomic-level energy storage mechanism of cobalt hydroxide electrode for pseudocapacitors. *Nature Communications* **8**, 15194, doi:10.1038/ncomms15194 (2017).

151   Gajdek, D. *et al.* Structural Changes in Monolayer Cobalt Oxides under Ambient Pressure CO and O2 Studied by In Situ Grazing-Incidence X-ray Absorption Fine Structure Spectroscopy. *The Journal of Physical Chemistry C* **126**, 3411-3418, doi:10.1021/acs.jpcc.1c10284 (2022).

152   Cheng, G., Carter, J. D. & Guo, T. Investigation of Co nanoparticles with EXAFS and XANES. *Chemical Physics Letters* **400**, 122-127, doi:https://doi.org/10.1016/j.cplett.2004.10.095 (2004).

153   Malard, L. M., Pimenta, M. A., Dresselhaus, G. & Dresselhaus, M. S. Raman spectroscopy in graphene. *Physics Reports* **473**, 51-87, doi:https://doi.org/10.1016/j.physrep.2009.02.003 (2009).

154   Sung, C.-M. & Tai, M.-F. Reactivities of transition metals with carbon: Implications to the mechanism of diamond synthesis under high pressure. *International Journal of Refractory Metals and Hard Materials* **15**, 237-256, doi:https://doi.org/10.1016/S0263-4368(97)00003-6 (1997).

155   Dahal, A. & Batzill, M. Graphene–nickel interfaces: a review. *Nanoscale* **6**, 2548-2562, doi:10.1039/C3NR05279F (2014).

156   Eom, D. *et al.* Structure and Electronic Properties of Graphene Nanoislands on Co(0001). *Nano Letters* **9**, 2844-2848, doi:10.1021/nl900927f (2009).

157   Li, J. *et al.* Evolution Pathway from Iron Compounds to $Fe_1(II)–N_4$ Sites through Gas-Phase Iron during Pyrolysis. *Journal of the American Chemical Society* **142**, 1417-1423, doi:10.1021/jacs.9b11197 (2020).